SYNTHESIS AND KINETIC PROCESSES IN DESIGNED POLYMERS

BY

KALI A. MILLER

DISSERTATION

Submitted in partial fulfillment of the requirements
for the degree of Doctor of Philosophy in Chemistry
in the Graduate College of the
University of Illinois at Urbana-Champaign, 2019

Urbana, Illinois

Doctoral Committee:

Professor Paul V. Braun, Chair
Associate Professor Christopher M. Evans
Professor Jeffrey S. Moore
Professor Steven C. Zimmerman

ABSTRACT

Traditional polymers have been long used for commercial products from polyester shirts to polyvinyl chloride (PVC) pipes or even polytetrafluoroethane (Teflon) non-stick coatings. As the needs of our society grow and change, innovative solutions must be created to overcome the challenges that industry faces today. New polymers must be designed and engineered to perform specialized functions, improve on existent properties, or respond to changes in the environment. This thesis focuses on the synthesis and characterization of such polymer systems, with specific considerations for their kinetic processes. Selected material systems are individually described in paragraphs below, with applications in membranes and protective coatings, degradable materials, transport and concentration, and biocompatibility.

Silicon photonic microring resonators have emerged as a promising technology for the sensitive detection of toxic and regulated substances. By functionalizing the surface of silicon photonic microring resonators with polymer brushes, we find that small molecules can selectively partition into the surface-confined sensing region of the optical resonators. This strategy leads to response enhancements in excess of 1000% percent, relative to non-functionalized sensors, for representative targets including 4-methylumbelliferyl phosphate, a simulant for highly toxic organophosphates, Bisphenol A, an industrial pollutant, as well as other small organic analytes of interest. Additionally, brush-modified resonators can be used utilized as a platform for the in-situ characterization of hydrophobic, hydrophilic, and stimuli-responsive polymer brush surfaces. Diffusion and partitioning of small molecules into the brushes was observed in real-time and conformation changes were quantified by measuring and fitting shifts in the resonance wavelength. With these techniques, we showed not only quantification of solvent compatibilities based on small molecule transport through the brush interface, but also extraction of polymer brush pK_a as a function of brush length and solvent conditions. Thus, we also demonstrate that our technique allows for accessible characterization of diverse polymer layers in the present of complex analyte solvent interactions.

The simultaneous growth in waste plastics, 3D-printing, and implantable biomaterials has challenged chemists to develop new polymers able to meet the demands of real-world applications. In particular, there is increasing demand for smart polymers that change their shape or properties or degrade in response to environmental stimuli. A renewed interest in degradable polymers,

especially for biomedical and engineering applications has led to an extensive search for new mechanisms to breakdown polymers. Herein, we introduce the 3-iodopropyl acetal moiety as a simple cleavable unit that undergoes acid catalyzed hydrolysis to liberate HI and acrolein stoichiometrically. We show that integrating this unit into linear and network polymers gives a class of macromolecules that undergo a new mechanism of degradation with an acid amplified, sigmoidal rate. This trigger-responsive self-amplified degradable polymer undergoes accelerated rate of degradation and agent release.

Fast relaxation imaging (FReI) is introduced as a novel technique to detect protein unfolding in situ by imaging changes in fluorescence resonance energy transfer (FRET) after temperature jump perturbations. Unlike bulk measurements, diffraction-limited epifluorescence imaging combined with fast temperature perturbations reveals the impact of local environment effects on protein-biomaterial compatibility. Our experiments investigated a crowding sensor protein and phosphoglycerate kinase to quantify the confinement effect of the cross-linked hydrogel and reveal the effect of noncovalent interactions of the protein with the polymer surface. Additionally, we demonstrate that a biomedically-relevant zwitterionic polymer in solution can interact with proteins directly through utilizing fluorescence techniques. Polymer-dependent changes in the tryptophan fluorescence spectra of three structurally-distinct proteins reveal that the polymer interacts directly with all three proteins and changes both the local polarity near tryptophan residues and the protein conformation. Thermal denaturation studies show that the protein melting temperatures decrease and that protein folding cooperativity increases upon interaction with the polymer. We demonstrate the exact extent of the changes is protein-dependent, as some proteins exhibit increased stability, whereas others experience decreased stability at high polymer concentrations. These results suggest that the polymer is not universally protein-repellent and that its efficacy in biotechnological applications will depend on the specific proteins used.

Vibrational resonances of microelectromechanical systems can serve as means for assessing physical properties of ultrathin coatings in sensors and analytical platforms. Most such technologies exist in largely two-dimensional configurations with a limited total number of accessible vibration modes and modal displacements, thereby placing constraints on design options and operational capabilities. Our study presents a set of concepts in 3D microscale platforms with vibrational resonances excited by Lorentz-force actuation for purposes of measuring properties of thin-film coatings. Nanoscale films including photodefinable epoxy,

cresol novolak resin, and polymer brush with thicknesses as small as 270 nm serve as the test vehicles for demonstrating the advantages of these 3D MEMS for detection of multiple physical properties, such as modulus and density, within a single polymer sample. The stability and reusability of the structure are demonstrated through multiple measurements of polymer samples using a single platform, and *via* integration with thermal actuators, the temperature-dependent physical properties of polymer films are assessed. Numerical modeling also suggests the potential for characterization of anisotropic mechanical properties in single or multilayer films. The findings establish unusual opportunities for interrogation of the physical properties of polymers through advanced MEMS design.

Nanoantenna-based surface-enhanced infrared absorption is a powerful platform for the detection of biological and chemical species due to its ability to strongly enhance infrared absorption of a relatively narrow band of vibrational modes. However, SEIRA only detects molecules within order of 100 nm of the nanoantenna, and thus requires diffusion of analyte into the local vicinity of the nanoantenna to provide enhanced sensing. Here, we demonstrate the use of a polyacrylamide hydrogel film with imbedded radial chemical gradient to locally concentrate analytes in the local vicinity of SEIRA-active nanoantenna to improve the detection limit over that provided by SEIRA along. Using a positive charge gradient, embedded in a hydrogel film, a nerve agent simulant, 4-methylumbelliferyl phosphate, was concentrated 15-fold above a SEIRA active array of nanoantenna. The combined effect of molecular concentration and SEIRA resulted in the potential ability to detect the agent of interest at concentrations two orders of magnitude below that provided by ATR using a conventional, gradient-free substrate.

ACKNOWLEDGEMENTS

First of all, I'd like to express my sincere gratitude to my advisor, Professor Paul Braun, for his support and guidance throughout my time at the University of Illinois. Thank you for your endless encouragement to always reach for my goals, no matter how challenging. Many thanks to members of the Braun Group for enlightening discussions and enjoyable moments, shared in and outside the lab. Thank you to my mentors in the group for helping me start out on the right foot: Marta Hatzell, Hyung-Jun Koo, Neil Krueger, Kristopher Waynant, and Chunjie Zhang. Thank you to my fellow responsive polymers subgroup researchers for always being there for experimental assistance and helpful discussions: Mohammad Ali, Daniel Bacon-Brown, Hao Chen, Eric Epstein, Ravi Kollarigowda, Shuqi Lai, Kewang Nan, Tsung-han Tsai, and Shiyan Zhang. I also want to thank Julia Kohanek, Brian Mosby, Christian Ocier, Corey Richards, Jungwoo Shin, Kaitlin Tyler, and Runyu Zhang for their support. Special thanks to our research program coordinator, Erica Malloch, for help ordering research supplies and answering my many questions. Additionally, I had the great pleasure of mentoring and working with three talented undergraduate students: Mary Grace Haugen, Elizabeth Murphy, and Nathan Reed.

I also want to express gratitude to my committee members. Thank you to Professor Jeffrey Moore for pushing me to ask the right questions and strive to be the best scientist that I can be. Thank you to Professor Christopher Evans for always agreeing to meet with me for insightful discussions and never-ending guidance. Thank you to Professor Joaquín Rodríguez-López for serving as a temporary committee member for my preliminary exam and the constant encouragement through the ups and downs of my PhD. Lastly, a very special thank you to Professor Steven Zimmerman for being my advisor away from home. You have been my role model not just as an amazing scientist and a caring teacher, but also as a champion for diversity and inclusion that has shown me that there is always much to learn.

Part of what has made my time at Illinois so memorable is the faculty that have had the great honor of knowing. They have served as educators, mentors, and collaborators, and inspirations to help shape me into the person that I am today. Thank you to Professors Gretchen Adams, Ryan Bailey, Peter Beak, Dana Dlott, Randy Ewoldt, Gregory Girolami, Martin Gruebele, Kami Hull, Deborah Leckband, Yi Lu, Douglas Mitchell, Catherine Murphy, Ralph Nuzzo, and Chad Rienstra. Additionally, thank you to the international collaborators I have had the opportunity

to work with: Professor Harald Giessen and Frank Neubrech from the University of Stuttgart in Germany and Dr. Dan Daniel and Alfred Ting at A*STAR in Singapore.

I am grateful to the National Science Foundation for financial support throughout my PhD. This has allowed me the freedom to pursue my own research interests and has provided me with the unique opportunity to establish many interdisciplinary projects. Additionally, I am grateful to Dr. Brian Pate from the Defense Threat Reduction Agency for financial support and insightful discussions during our monthly project reviews. I would like to thank the Beckman Institute, Institute for Genomic Biology, Materials Research Laboratory, Microanalysis Laboratory, and NMR Laboratory for access to world-class instrumentation and staff expertise that was critical to success in my projects. In particular, thank you to Austin Cyphersmith, Dean Olsen, Scott Robinson, Mayandi Sivaguru, Julio Soares, Kevin Tucker, Leilei Yin, and Dainwen Zhang.

My colleagues at Illinois have been critical to my success. Special thanks to Caitlin Davis, Lydia Kisley, and Alex Stanton for teaching me just as much about life as science (and we've talked about a lot of science). Thank you to Carrie Levinn, Kimberly Lundberg, Tim Moneypenny, Elena Montoto, Sarah Pearlmutter, and Ryan Roony for sticking together from day one. Thanks to Julio Serrano for all the ceaseless encouragement and motivation throughout my PhD. This also would not have been possible without support and thought-provoking conversations with Syeda Tajin Ahmed, Brenda Andrade, Katie Chiang, Mayank Garg, Robby Goldman, Libby Haywood, Deborah Liu, Hector Lopez, Ephraim Morado, Adam Nelson, Arif Nelson, Zully Perez, Shampa Samanta, Samya Sen, Jordan Sickle, Perez Sierra, Michael Stablein, David Stevens, Alif Laila Tisha, Brittany Walker, Shannon Wetzler, and Jose Zavala.

Lastly, I would like to thank my family for their support during my time in graduate school. Even when I doubted myself, their confidence in my abilities always pulled me through. I'd like to express my sincere gratitude to my sister, Shannon Miller, for being there for me through thick and thin. My extended family is too large to list in entirety, but thank you to the Artus, Foreman, Miller, Miklovic, Pharr, and Prechodko families. I hope we continue to get closer through the years. A huge thank you to my new family, Anthony, Lucille, and Rick Griffin. I can't to see what new adventures lie ahead for us. Finally, thank you to my ACS volunteering family (in particular, Peter Dorhout, Harry Elston, Marta Gmurczyk, John Palmer, Joe Pickel, Ralph Stuart, and Marinda Wu) and my childhood friends who are like family (Elizabeth Deutsch, Angela Fang, Amanda Jones, Michele Mackowiak, and Sara Thomas).

CONTRIBUTIONS

Throughout my time in graduate school, I have had the good fortune of working on many collaborative projects with students, staff, and faculty from different departments, labs, institutions, and even countries. As such, I would like to briefly summarize my contributions to each project. For the project in chapter 2, I synthesized a majority of the polymer-coated substrates and assisted with experimental design, data interpretation, and manuscript writing. For the project in chapter 3, I synthesized many of the brush-coated substrates, assisted with experimental design, and led data interpretation efforts, focus of project scope, and writing of the manuscript. For the project in chapter 4, I led efforts for the design and fabrication of the hydrogel systems, derivation of fitting equations and experimental setup for rheology experiments (with the help of Professor Ewoldt's group), rate analysis of all data, workup of previously-obtained GPC data, the preparation of the manuscript and supplemental material, and paper revision efforts. For the project in chapter 5, I assisted with experimental design (especially the FRAP experiments), data interpretation, and manuscript writing. For the project in chapter 6, I led polymer synthesis and characterization efforts (NMR and DLS studies with the help of Elizabeth Murphy) and assisted in experimental design, data interpretation, and manuscript writing. For the project in chapter 7, I synthesized and characterized the polymer-coated substrates and assisted with data interpretation, project scope, and manuscript writing. For the project in chapter 8, I assisted with hydrogel-coated substrate fabrication and characterization, experimental design, data interpretation, and manuscript writing. For the project listed in the appendix, I designed survey questions and wrote the IRB with the help of Kaitlin Tyler, designed and led the workshop, and led data workup, manuscript writing, and paper revision efforts.

TABLE OF CONTENTS

CHAPTER 1: INTRODUCTION

1.1 Design of functional polymers

1.1.1 Polymer architectures

The term polymer refers to molecules that have many repeating units, known as monomers. These repeating units can vary greatly in size, from on the order of 1,000 g/mol (commonly termed oligomers) to approximately infinite (network polymers). Understanding the physical properties of a polymer (mechanical strength, solubility, brittleness) requires knowledge of the length of polymer chains. Chain length is often expressed in terms of molecular weight of the polymer chain. However, almost no synthetic polymers will have a single molecular weight because there will be a distribution of shorter and longer chains within one sample. The molecular weight must therefore necessarily be described as an average molecular weight calculated from the molecular weights of all the chains in a sample. This value is commonly determined by gel permeation chromatography (GPC), size exclusion chromatography (SEC), and nuclear magnetic resonance (NMR) techniques. The molecular weight and dispersity of the sample can be influenced drastically by synthesis method. Additionally, the synthesis method and chosen monomers can impact the polymer physical properties just as much as the chain length. This variety lends to a multitude of possibilities for static and dynamic function that can be adapted from polymers found in nature, polymers that have been designed to have a specific new function, or both.[1-3]

Polymers that are made up of a single repeating unit are termed homopolymers. Alternatively, polymers can be made up of many different types of repeating units and configurations (Figure 1.1). Polymers that are made up of different repeating units are termed copolymers. If the monomers of a single type are grouped together, then this is known as a block copolymer. The monomers of a single type can be regularly distributed in an alternating fashion or randomly distributed. Polymers also don't have to have their repeating units arranged in a linear chain. There are many types of branched polymers, with hyperbranched, graft, star, and dendrimer being the most common. These branched polymers may even be made up of copolymers. These polymers can be utilized in their bulk form, dissolved in a solvent, or chemically bound to a surface (commonly called a polymer brush). Additionally, there are other more complex architectures that exist that provide access to functions that would otherwise not be possible. For example, polymer networks consist of individual polymer chains that are linked together by chemical bonds. These networks can be made up of copolymers, swollen in a solvent to achieve new properties, or even comprised of two different interpenetrating networks. Each of these polymer structures has unique properties that can be exploited for applications ranging from consumer products (packaging, fabrics, adhesives) to demanding specialty uses (bulletproof vests, artificial joints, switchable devices).[4-9]

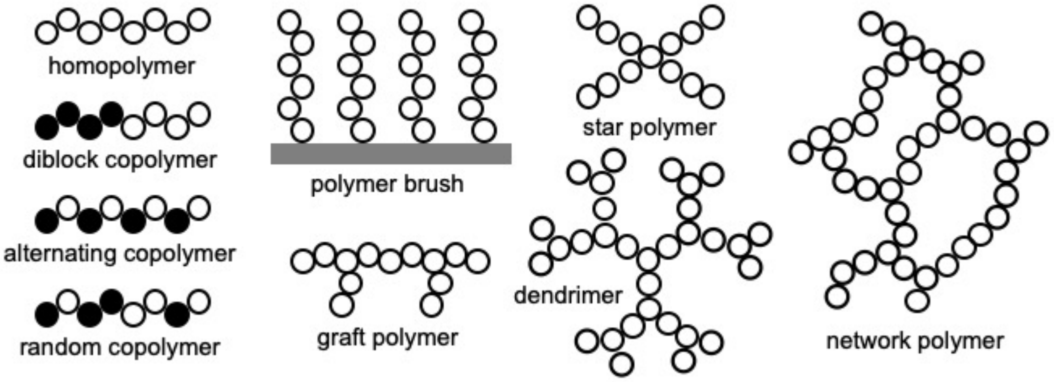

Figure 1.1 Schematic representation of common polymer architectures: homopolymers, copolymer variations, polymer brush and grafted polymers, star polymers, dendrimers, and network polymers.

1.1.2 Synthetic methods

To achieve these architectures, variety of synthetic methods can be employed depending on the desired molecular composition and experimental conditions needed for a specific application. Briefly, step-growth and chain-growth are the two most common classifications (Figure 1.2). Step-growth polymers are defined as polymers that are formed by a stepwise reaction between monomers, usually through functional groups that contain heteroatoms. In this case, any two monomer units can react, including the ends of oligomeric chains. Thus, step-growth polymers increase in size at a slow rate and reach moderately high sizes only at very high conversion due to the entropic costs associated with this reaction. Condensation and addition mechanisms are common types of step-growth polymerization. Alternatively, there is also chain growth polymerization where the polymer chain starts forming on one end and monomers must get added to another end due to their reactivity. In this case, the backbone made up entirely of interconnected carbon chains rather than linked through heteroatoms. Radical, cationic, and anionic mechanisms are common types of chain-growth polymerization.[10]

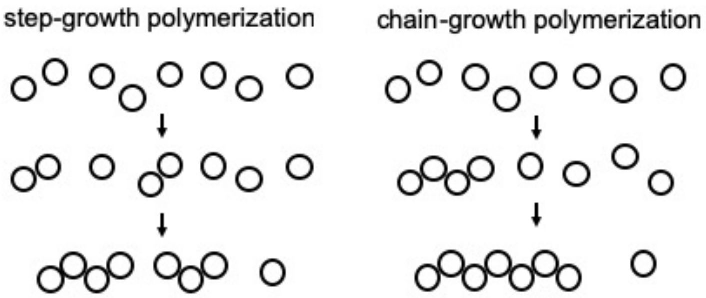

Figure 1.2 Schematic representation of step-growth and chain-growth polymer synthesis methods.

1.1.3 Triggered function

Responsive materials are capable of altering their shapes or properties upon exposure to an external trigger. There are many examples of triggers that cause a responsive behavior and they all can be understood as a chemical or physical reaction with this stimulus. For example, heat can be used to rapidly change their shape in thermal-active memory polymers due to "memorization" of an original shape. Heat can also be used to change the properties of polymers that have a lower critical solution temperature (LCST). Alternatively, light can be used to facilitate polymer degradation due to sensitive functional groups that can undergo spontaneous reactions. pH-sensitive polymers are materials that change in volume to swell or collapse when the pH of the surrounding medium changes, through the mechanism of charge repulsions. Self-healing material systems have the ability to repair their own damage by mechanisms such as mixing of previously-separated reactive materials or creation of new reactive units. Other stimuli include magnetic or electric fields, sound, ionic strength, or binding events that trigger a reaction cascade.[11-15]

Stimuli-responsive materials are often used interchangeably with the term "smart" materials because it encompasses the idea that these materials have the potential to create a new paradigm for how materials are used for both consumer and specialty applications. For example, smart materials could adapt to surrounding environments, regulate transport of molecules, quickly change wettability and adhesion properties, or even interconvert chemical and biochemical signals into optical, electrical, thermal, and mechanical signals. These materials have increasing importance in applications such as drug delivery, tissue engineering, biosensing and diagnostics, smart coatings and optical systems, microelectromechanical systems, and coatings. The enthusiastic interest and creative advances in this topic demonstrate that this marks the beginning of the development of smart materials.[16-20]

1.1.4 Static function

In addition to stimuli-responsive functionality, another focus in developing advanced material technologies is the advancement static function. In this case, a material system is developed with innate function that is exploited throughout its lifetime, without a specific trigger. For example, superhydrophobic or superhydrophilic coatings have potential in the protection of optical devices (anti-fogging) or self-cleaning, stain-resistant, and water-resistant products.[21,11] Additionally, anti-biofouling surface coatings prevent non-specific interactions (such as adsorption of biomolecules) onto the surface of materials. This can be applied to fields from engineered nanomaterials, biomedical devices and implants, and marine biofouling.[23,24] Other examples of current applications of polymers with either extreme or traditional static functionality include advanced functional membranes, corrosion resistant coatings, or electronic materials.[25-27]

1.2 Selected applications and current challenges

1.2.1. Small molecule transport and concentration

The detection of low-concentration target analytes has long been a challenge for nanoscale sensors: if the desired analyte is only transported across the sensor by diffusion, the probability that a molecule will interact the sensor scales with the solution concentration.[28] There are many relevant chemical agents that must be detected at low concentrations, including organophosphates, pesticides, industrial toxins, and environmental toxins (for example, nerve agent soman with $IC_{50} = 5 \times 10^{-6}$ M).[29] As such, new devices and technologies are needed that can quickly identify and/or degrade agents into less toxic substances. Surface attraction has been used to drive diffusion against conventional gradients and gravity since the early 90’s.[30] In this method, ionic, hydrophobic, or other noncovalent interactions are exploited to bring an analyte closer in space to the sensor to improve both the sensitivity and response time.[31,32] Depending on the analyte of interest, one general solution is to coat the sensor surface with a polymer of complementary functionality such that the analyte would selectively prefer the polymer layer to other environments (Figure 1.3). Here, the analyte will partition from either the air or liquid and, as driven by noncovalent attractions, concentrate within the polymer layer that is directly over the sensor surface.

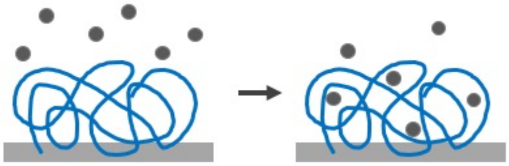

Figure 1.3 A schematic illustration of the partitioning of molecules from the external environment into a polymer layer over the sensor by noncovalent interactions.

Alternatively, chemical compounds may be segregated and concentrated into specific regions on a surface. This can be accomplished by post-modification of a polymer backbone such that the concentration of specific functional groups varies over distance.[33-35] These embedded chemical potential gradients create interactions with the target molecule and serve as the driving force for molecular transport across the polymer surface. Gradient technology has the potential to be further developed for catalytic remediation and detection at points of concentration or for lab-on-a-chip devices that incorporate directional transport. Gradient systems that are innately mobile (i.e. that do not need plasticizer to concentrate on a reasonable time scale) are of particular interest due to their utility in real-world applications.

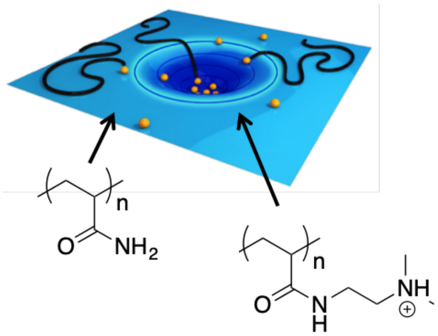

Figure 1.4 A schematic illustration of the directed transport of molecules by a two-dimensional radially symmetric enthalpy gradient. Molecules outside of the gradient exhibit only random diffusion and the curved blue surface represents the enthalpy profile of the molecule in the medium. Adapted with permission from: Zhang, C.; Sitt, A.; Koo, H.-J.; Waynant, K. V.; Hess, H.; Pate, B. D.; Braun, P. V. Autonomic Molecular Transport by Polymer Films Containing Programmed Chemical Potential Gradients. *J. Am. Chem. Soc.* **2015**, *137* (15), 5066-5073. Copyright 2015 American Chemical Society.

1.2.2 Membranes and protective coatings

Biological membranes are an integral part of living cells and efficiently fulfill a large number of mass and energy transport functions. These materials can transport and separate individual chemical components selectively within the cell by utilizing ligands, electrical potential gradients, or even without an external driving force. Membranes used in various applications can vary widely in their structure, function, and mode of operation. However, the fundamental concept is the same: exploiting physical interactions (size, shape, charge) or chemical interactions (hydrogen bonding, hydrophobicity, binding) to drive selective interactions and thus separations between mixtures.[36] Using these concepts, the practical application of synthetic membranes began approximately 100 years ago. These membranes are much larger compared to nano-sized biological membranes, averaging thicknesses in the hundreds of nanometers or several micrometers. Additionally, synthetic membranes are usually much less complex compared to their biological counterpart in order to make them commercially relevant for industrial processes. Today, synthetic membranes are used to produce clean water, to purify industrial waste and recover valuable products, to fractionate macromolecular mixtures in the food and drug industries, or to separate gases and vapors.[37,38] Developing research utilizes advanced polymer systems to create key components in energy conversion and storage systems (such as batteries and fuel cells) or in biomedical applications such as drug delivery systems or sensors and diagnostic devices.[39-41]

Similar to membranes, coating technologies are thin polymer layers that exploit physical and chemical interactions for a desired purpose. Additionally, a major consideration in coating processes is a balance between effectiveness and simplicity or scalability. Industrially-relevant coating applications include surface protection and modification, decorative finishes, or special functions for commodities and merchandise. Functional coatings change the properties of the substrate to improve adhesion, wettability, corrosion resistance, or wear resistance. In other cases, the coating adds a new property such as electrical conductivity or a magnetic response.[42-46] As demand increases for such specialty applications, new materials must be developed to meet these challenges. One widely-investigated strategy is the use of polymer brushes for both membrane and coating applications.[47-50] Surface anchored polymer chains provide mechanical strength and the ability to withstand a variety of post processing steps. Additionally, the distance between the grafting points can be designed as smaller than the end-to-end distance of the polymer chain. This provides a unique properties and behaviors that are vastly different from those accessible using analogous bulk materials, especially with the utilization of complex architectures such as dendritic brush sytems.[51] Current research continues to push the boundaries of what is possible with these new functional materials well as developing accurate characterization platforms to monitor their performance in the presence of commercially relevant analyte-solvent systems.

1.2.3 Polymer degradation

Polymer degradation results from an irreversible change which leads to failure in the molecular structure of the chain and breakdown into smaller components. Polymers degrade by several different mechanisms, depending on the polymer structure and conditions of exposure. In commercial materials, failure may be even be defined as losing mechanical, structural, electrical, or aesthetic properties rather than complete breakdown of the chains.[52] The major factors causing polymer degradation are heat, mechanical energy, radiation, and ozone. Understanding these factors can help engineer polymers that are much more commercially relevant such that they are durable, chemically and biologically inert, and have a low cost of production.[53,54] Unfortunately, some of these most useful features result in accumulation in the environment if not recycled properly. To prevent bioaccumulation, there is much recent work on developing new mechanisms and triggers for the breakdown of polymers that could be incorporated into degradable consumer products, even the development of new enzymatic or microbial degradation mechanisms.[55,56] However, there the delicate balance between stability and degradability must be explored for each system. For example, the changing substituents neighboring the linking groups between monomers could help tune reactivity.[57-59] Due to this tunability in design, such polymers also have promising emerging applications beyond consumer products, such as controlled release in drug delivery, water treatment, and as temporary 3D printing scaffolds.[60-64]

1.2.4 Polymer-protein interactions

Proteins have proven to have tremendous potential in biological pharmaceuticals and drug targets due to their highly specific and complex set of functions and biocompatibility. Commonly-used materials include silicon for its use in biosensors and biodegradability into orthosilicic acid,[66-70] metal oxides due to their wide range of structures and optical, electrical, and magnetic properties,[71,72] polyethylene glycol or zwitterionic organic modifications to encourage nonfouling behaviors,[73-78] hydrophobic coatings that combat bacterial growth,[79-82] and hydrogels for protein delivery in tissue engineering.[83-87] However, a major challenge in exploiting the unique functions of proteins in engineered devices and delivery systems is their compatibility with these materials. Incompatible materials can disrupt protein structures and lead to aggregation, biofouling, or degradation that reduce device performance. Complicating this problem is that protein-hydrogel interactions are governed by a complex combination of factors including solvation environment, hydrophobic and noncovalent interactions, charge repulsion, and crowding. This challenge motivates the need for in situ approaches for identifying material properties that affect protein function.[65]

1.3 Analysis methods for designed polymer systems

1.3.1 Silicon photonic microring resonators[1]

Silicon photonic microring resonators, which belong to a larger class of whispering gallery resonators,[88] are chip-integrated optical structures that are responsive to changes in the local refractive index near the sensor surface. In these devices, shown schematically in Figure 1.5, light from an adjacent linear waveguide can be coupled into the microring cavity only under conditions of optical resonance, as defined by: coupled into the cavity via an adjacent linear waveguide positioned within the evanescent field. Optical modes are supported along the circumference of the cavity according to the resonance condition:

$$m\lambda = 2\pi r n_{eff} \tag{1.1}$$

where m is an integer, λ is wavelength of light, r is the radius of the resonator, and n_{eff} is the effective refractive index sampled by the optical mode. Light is confined into the resonator via total internal reflection and interacts with the environment through an exponentially-decaying optical profile that has a 1/e decay length of 63 nm.[89]

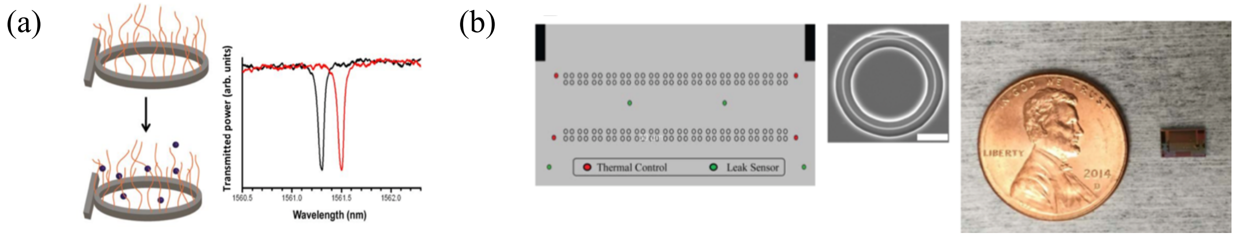

Figure 1.5 (a) Schematic diagram of polymer brush-modified microring resonator. Analyte localization within the polymer brush changes the local refractive index leading to a shift in resonance wavelength. A representative transmission spectra shows a decrease in optical power past the resonator at the resonance wavelength. A change in local refractive index accompanying analyte partitioning causes a shift in the resonance. (b) Representative layout of a micoring resonator chip, with an SEMs image of a single ring (scale bar 10 μm). An optical micrograph with a penny for scale reference.

---

[1] Reproduced with permission from: Stanton, A. L. D.; Miller, K. A.; Braun, P. V.; Bailey, R. C. Polymer Brush-Modified Microring Resonators for Partition-Enhanced Small Molecule Chemical Detection. *ChemistrySelect* **2017**, *2 (4)*, 1521-1524. Copyright 2017 Wiley-VCH Verlag GmbH & Co. KGaA, Weinheim.

These devices are fabricated at the wafer scale on silicon-on-insulator wafers at a commercial silicon foundry using standard deep UV photolithography. High fidelity fabrication leads to high Q factor cavities which leads to a dramatic increase in the effective optical path length and dramatic sharpening of the resonance to an extremely narrow spectral dispersion (FWHM ≈ 50 picometers). As the refractive index near the resonator changes, in this case due to the localization of analytes via partitioning into the polymer brush, the local refractive index is changed, resulting in a shift in the resonance wavelengths of modes supported by the cavity. This provides the signal transduction mechanism.

This technology, which has been previously demonstrated for the detection of a range of biomolecular targets,[90–93] is being commercialized by Genalyte, Inc. as the Maverick detection platform. In the current configuration, each sensor array chip is 4 x 6 mm in size and features 132 individually-addressable, 30 μm-diameter sensors. The entire chip is coated with a fluoropolymer cladding layer and selectively removed to expose only 128 of the rings to solution. The remaining sensors can be used to correct for thermal drift. Each microring is optically addressed via input and output grating couplers, which are connected to either end of the linear coupling waveguide. In this way, all optical interfaces are done in the far field with light coupled from free-space into and off of the chip from the laser and then to a detection photodiode. No end coupling using fiber optics is required. Resonance measurements are made by sweeping the output of a tunable external cavity diode laser centered at 1.56 μm through a suitable spectral range and detecting resonances as dips in the optical power transmitted through the coupling waveguide past the microring sensor.

During detection experiments, the shift in resonance wavelength is determined in real-time with solutions being flowed across the sensor chip via an automated fluid handling system that delivers fluid through a laser cut Mylar gasket, which defined two channels per sensor array chip. Four microring resonators are monitored to determine both either bare- or polymer-modified sensor response, while four occluded rings were used for real-time temperature correction. The sensor responses are measured in real-time and extracted resonance wavelength shifts averaged over a suitable time period are plotted for exposure to different small molecule analytes.

1.3.2 Rate law analysis[2]

There are many intertwining factors to consider when studying a chemical reaction, including the chemical properties of the reactants and expected product, reaction conditions, reaction mechanism, and rate of reaction. An understanding of kinetics is fundamental to all reactions and rate laws can be used to predict the relationship between the rate of a reaction and the concentrations of the reactants.[94] A rate law is an equation that explicitly relates these factors together in a way that can be used to characterize a system and predict future reactivity. In these expressions, component concentrations are represented as bracketed capital letters and the orders of reaction are expressed in exponent numbers. The three most common orders of reaction are zero, first, and second. Briefly, the rate of zero order reactions is independent of reactant concentration, the rate of first order reactions is dependent on only one reactant concentration, and the rate of second order reactions is dependent on two reactants.

These same principles can be applied to systems in which there are more complicated mechanisms of reaction. For example, many polymer degradations are autocatalytic reactions and this rate law can be expressed as:[95,95]

$$r = k_1[R] + k_2[R][P]\,, \tag{1.2}$$

where R is the reactant, P is the product, and k_1 and k_2 are the rate constants that describe the non-autocatalytic and autocatalytic mechanisms, respectively. In this case, k_1 is first order with respect to the reactant but k_2 is dependent on both the reactant and product concentration. When analyzing polymer systems, it is common to track the disappearance of the reactant by NMR. In order to derive an expression that relates reaction completion to rate constants, this equation be written as

$$-\frac{dc}{dt} = k_1 c + k_2 c(c_0 - c)\,, \tag{1.3}$$

---

[2] Reproduced with permission from: Miller, K. A.; Morado, E. G.; Samanta, S. R.; Walker, B. A.; Nelson, A. Z.; Sen, S.; Tran, D. T.; Whitaker, D. J.; Ewoldt, R. H.; Braun, P. V.; Zimmerman, S. C. Acid-Triggered, Acid-Generating, and Self-Amplifying Degradable Polymers. *J. Am. Chem. Soc.* **2019**, *141 (7)*, 2838-2842. Copyright 2019 American Chemical Society.

where c represents the concentration of the degradable moiety with its initial value being c_0. To express the rate as a function of the initial concentration and a measured concentration as a function of time, integration of Equation 1.3 leads to the following rate law

$$\ln\left[\frac{k_1 + k_2c_0 - k_2c}{c}\right] = (k_1 + k_2c_0)t + \ln\left[\frac{k_1}{c_0}\right]. \tag{1.4}$$

Note: a plot of $\ln[(k_1 + k_2c_0 - k_2c)/c]$ versus time can be shown for visual representation to give a straight line based on the relationship provided in Equation 1.4. Finally, rearrangement and simplification of Equation 1.4 leads to

$$\frac{c}{c_0} = \frac{k_1 + k_2c_0}{k_1\, e^{(k_1+k_2c_0)t} + k_2c_0}, \tag{1.5}$$

which is an explicit equation for reaction conversion as a function of time. This equation can be used to fit k_1 and k_2 by least-squares regression of the normalized degrading agent concentration that is obtained by means such as NMR.

In the case of hydrogel systems where the concentration cannot easily be observed by NMR, k_1 and k_2 can be extracted from the normalized storage modulus. Using the phantom model of rubber elasticity[97,98] and assuming a network functionality of $f = 4$ (as expected for a bifunctional crosslinker), the plateau modulus G_0 and the number density of elastically active crosslinks (μ) are related by $G_0 = (v - \mu)k_BT = \mu k_BT$, where $v = \mu \cdot f/2$ is the number density of elastically active network strands and k_BT is the thermal energy.[99-102] In the case of fitting G/G_0 (Given that $\mu \equiv N_Ac$),

$$c = \frac{G}{k_BTN_A} \text{ and } c_0 = \frac{G_0}{k_BTN_A}\ . \tag{1.6}$$

Substituting Equation 1.6 into 1.5, an equation can be obtained that can be directly relates modulus to k_1 and k_2:

$$\frac{G}{G_0} = \frac{k_1 + \frac{k_2G_0}{k_BTN_A}}{k_1\, e^{\left(k_1+\frac{k_2G_0}{k_BTN_A}\right)t} + \frac{k_2G_0}{k_BTN_A}}\ . \tag{1.7}$$

1.3.3 Fluorescence techniques to interrogate protein interactions

Fluorescence is the light emitted by a molecule following the absorption of electromagnetic energy. This phenomenon typically arises from the transition of the excited species from first excited electronic singlet level to its ground electronic level.[103,104] These basic principles can be exploited to interrogate protein structure by monitoring the protein fluorescence spectra. For example, one recent study monitored the fluorescence spectra of a tryptophan moiety that was present in several proteins of complementary structure.[73] By exposing these proteins to different bulk polymer solutions, fluorescence intensity, peak shift, and temperature effects were monitored to gain insight on protein-polymer interactions.

In order to measure diffusion of fluorescent probes in polymer thin films, different strategies must be employed. One of the most accessible methods to characterize this is fluorescence recovery after photobleaching (FRAP). In this technique, the diffusion of fluorescently labeled molecules can be studied by photobleaching molecules in a region of interest (ROI) and then monitoring the fluorescence recovery as the bleached molecules within the ROI exchange with the surrounding unbleached molecules.[105] This technique is of particular interest compared to other fluorescent methods because it does not require excessively specialized equipment, analytical tools, or probes, and can be applied to dye-coated polymer surfaces even at longer time scales.[106] In the FRAP measurements, the time-dependent intensity change in the region of interest can be normalized to the prebleach intensity ($I(t)/I_0$) such that the bleaching recovery can be analyzed with the analytical expression[65,107]

$$\frac{I(t)}{I_0} = A\left[1 - e^{-(t/\tau_D)^{\alpha}}\right] \tag{1.8}$$

where A is the fraction of fluorophores that recover from the bleach and τ_D is the characteristic diffusion time it takes a molecule to diffuse across the bleached spot. Here, α represents any non-Brownian anomalous diffusion, where $\alpha = 1$ represents Brownian diffusion and $\alpha < 1$ indicates anomalous subdiffusion. The results can be related to the diffusion coefficient, D, by[65,107]

$$D = \frac{\omega^2}{4\tau_D} \tag{1.9}$$

where ω is the bleach spot radius.

Another technique that has been developed to probe polymer-protein thin film interactions in situ is fast relaxation imaging (FReI), which can be used to quantify the equilibrium thermodynamic and kinetic signatures of proteins. In this technique, changes in fluorescence resonance energy transfer (FRET) are observed on a conventional epifluorescence microscope platform. Changes in protein folding and stability are imaged by monitoring differences in FRET following a temperature jump perturbation.[108] FReI has been used to study how local microenvironments influence the structure, thermal stability, and folding of model proteins in live cells.[109,110] More recently, this has been applied biomaterial interfaces using a setup show in Figure 1.6.[65] In this case, the donor AcGFP1 is excited directly by blue LED light. The emission from the AcGFP1 donor and mCherry acceptor fluorescence is split onto two separate halves of the CMOS detector with a dichroic, similar to a traditional FRET microscope. A temperature jump is induced with a 2 μm infrared laser.

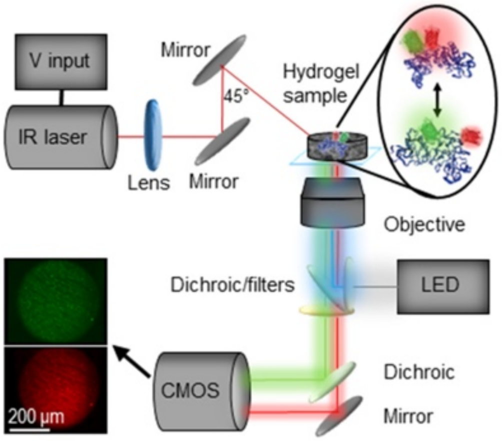

Figure 1.6 Experimental setup of the FReI microscope. Reproduced with permission from: Kisley, L.; Serrano, K. A.; Kong, X.; Gruebele, M.; Leckband, D. E. Direct Imaging of Protein Stability and Folding Kinetics in Hydrogels. *ACS Appl. Mater. Interfaces* **2017**, *9 (26)*, 21606-21607. Copyright 2017 American Chemical Society.

1.3.4 Resonant microelectromechanical systems

Microelectromechanical systems (MEMS) are systems that consist of small-scale electrical and mechanical components for specific purposes. Although a universal definition is lacking, MEMS products possess a number of distinctive features: miniature embedded systems, involve one ore many micromachine components, enable higher level functions, integrate smaller functions into one package with greater utility. Additionally, these systems often bring cost benefits through low unit pricing or cutting service and maintenance costs.[111,112] Recently MEMS technology has extended its boundaries to include optical, radio-frequency, nano, and even biological devices. Typical dimensions for a MEMS component varies from 1 μm to a few hundred micrometers, with the overall size less than 1 mm.[113] A subset of MEMS technology are systems with tailored mechanical vibratory resonances that can address a range of applications in mass detection, microscale rheology, energy harvesting, wearable sensors, and soft robotics.[114] These technologies function by monitoring how interactions with the environment influence the resonant behavior (e.g., the resonant frequency) of the device. As such, the device performance will depend on the resonant characteristics of the device.[115]

1.3.5 Surface-enhanced infrared absorption spectroscopy

Mid-infrared spectroscopy is a powerful technique that excites the vibrational transitions present in almost all organic molecules. Although fluorescence or refractive index change based sensors are essential for rapid detection, vibrational spectroscopy methods have typically been employed as probes of molecular structure.[116] In recent years, however, there have been many advances in 3D spatial mapping, [117] angstrom-scale resolution,[118] and real-time sensing applications[119] that begin to merge real-time sensing and molecular identification. For example, when gold nanowires are tailored to act as plasmonic nanoantennas for surface-enhanced infrared absorption (SEIRA) spectroscopy, they are capable of enormous enhancement even from less than one attomol of molecules.[120] Thus, SEIRA shows much promise for studying transport and diffusion on thin film polymer surfaces at appropriately low concentrations with spatial resolution.

Gold nanoantennas function by oscillating in resonance with specific IR frequencies.[121,122] Briefly, the molecular vibration of interest can be matched with the plasmonic excitation of a nanoantenna, thus enhancing the signal of that vibration. For example, the signature peaks from a monolayer of octadecanethiol (2850-2863 cm^{-1} and 2915-2936 cm^{-1}) normally cannot be distinguished by infrared spectroscopy. However, upon functionalization of a nanoantenna surface and measurement, bot peaks can be distinguished later quantified using the SIERA method (Figure 1.7). Many relevant chemical agents have unique functional group absorption band, including organophosphates, pesticides, industrial toxins, and environmental toxins. The advantage of SIERA over other possible sensor designs is its high sensitivity, small sensing volumes, and high integration density for robust detection. However, since the dielectric function is influenced by almost any change in the surrounding material, additional components are needed to provide selectivity.

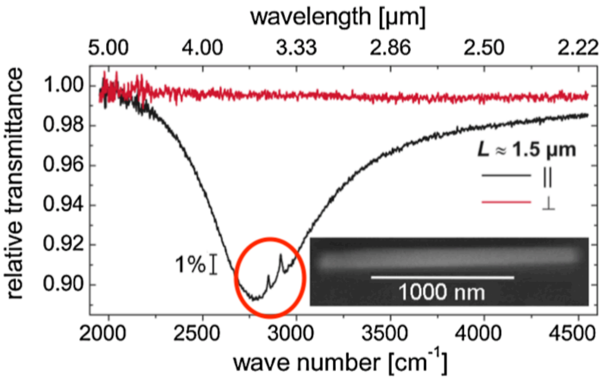

Figure 1.7 Relative IR transmittance in the spectral region of the fundamental resonance of a gold nanowire with an octadecanethiol monolayer for parallel and perpendicular polarization. Adapted with permission from: Neubrech, F.; Pucci, A.; Cornelius, T. W.; Karim, S.; García-Etxarri, A.; Aizpurua, J. Resonant Plasmonic and Vibrational Coupling in a Tailored Nanoantenna for Infrared Detection. *Phys. Rev. Lett.* **2008**, *101*, 157403. Copyright 2015 American Physical Society.

1.4 References

1. Jenkins, A. D.; Kratochvil, P.; Stepto, R. F. T.; Suter, U. W. Glossary of Basic Terms in Polymer Science. *Pure & Appl. Chem.* **1996**, *68 (12)*, 2287-2311.
2. Sheu, W.-S. Molecular Weight Averages and Polydispersity of Polymers. *J. Chem. Educ.* **2001**, *78 (4)*, 554- 555.
3. Technical Overview, Polymer Molecular Weight Distribution and Definitions of MW Averages, Agilent Technologies Inc., April-2015, 5990–7890EN.
4. Qiu, L. Y.; Bae, Y. H. Polymer Architecture and Drug Delivery. *Pharm. Res.* **2006**, *23 (1)*, 1-30.
5. Hiemenz P. C.; Lodge T. P. *Polymer Chemistry, 2nd Ed.*; CRC Press: Boca Raton, 2007.
6. Advincula, R. C.; Brittain, W. J.; Caster, K. C.; Rühe, J. *Polymer Brushes*; WILEY-VCH: Weinheim, 2004.
7. Discher, D. E.; Eisenberg, A. Polymer Vesicles. *Science* **2002**, 279 (*5583)*, 967-973.
8. Volt, B. I.; Lederer, A. Hyperbranched and Highly Branched Polymer Architectures—Synthetic Strategies and Major Characterization Aspects. *Chem. Rev.* **2009**, *109 (11)*, 5924-5973.

9. Richtering, W.; Saunders, B. R. Gel architectures and their complexity. *Soft Matter*, **2014**, *10 (21)*, 3695-3702.
10. Braun, D.; Cherdron, H.; Rehahn, M.; Ritter, H.; Voit, B. *Polymer Synthesis: Theory and Practice*, 5th Ed.; Springer: New York, 2013.
11. Wei, M.; Gao, Y.; Li, X.; Serpe, M. J. Stimuli-responsive polymers and their applications. *Polym. Chem.* **2017**, *8 (1)*, 127-143.
12. Meng, H.; Hu, J.; A Brief Review of Stimulus-active Polymers Responsive to Thermal, Light, Magnetic, Electric, and Water/Solvent Stimuli. J. Intell. Mater. Syst. Struct. **2010**, 21 (9), 859-885.
13. Theato, P.; Sumerlin, B. S.; O'Reilly, R. K.; Epps, T. H. Stimuli responsive materials. *Chem. Soc. Rev.* **2013**, *42 (17)*, 7055-7056.
14. Ward, M. A.; Georgiou, T. K. Thermoresponsive Polymers for Biomedical Applications. *Polymers* **2011**, *3 (3)*, 1215-1242.
15. de Vicente, J.; Klingenberg, D. J.; Hidalgo-Alvarez, R. Magnetorheological fluids: a review. *Soft Matter* **2011**, *7 (8)*, 3701-2710.
16. Yan, X.; Wang, F.; Zheng, B.; Huang, F. Stimuli-responsive supramolecular polymeric materials. *Chem. Soc. Rev.* **2012**, *41 (18)*, 6042-6065.
17. Stuart, M. A. C.; Huck, W. T. S.; Genzer, J.; Müller, M.; Ober, C.; Stamm, M.; Sukhorukov, G. B.; Szleifer, I.; Tsukruk, V. V.; Urban, M.; Winnik, F.; Zauscher, S.; Luzinov, I.; Minko, S. Emerging applications of stimuli-responsive polymer materials. *Nat. Mater.* **2010**, *9 (2)*, 101-113.
18. Hu, J.; Meng, H.; Li, G.; Ibekwe, S. I. A review of stimuli-responsive polymers for smart textile applications. *Smart Mater. Struct.* **2012**, *21 (5)*, 053001.
19. Chen, J.-K.; Chang, C.-J. Fabrications and Applications of Stimulus-Responsive Polymer Films and Patterns on Surfaces: A Review. *Materials* **2014**, *7 (2)*, 805-875.
20. Kulkarni, R. V.; Biswananth, S. A. Electrically Responsive Smart Hydrogels in Drug Delivery: A Review. *Appl. Biomater. Funct. Mater.* **2007**, *5 (3)*, 125-139.
21. Simpson, J. T.; Hunter, S. R.; Aytug, T. Superhydrophobic materials and coatings: a review. *Rep. Prog. Phys.* **2015**, *78 (8)*, 1-14.
22. Zhang, L.; Zhao, N. Xu, J. Fabrication and application of superhydrophilic surfaces: a review. *J. Adhes. Sci. Technol.* **2012**, *28 (8-9)*, 751-768.

23. Li, Y.; Xu, Y.; Fleischer, C. C.; Huang, J.; Lin, R.; Yang, L.; Mao, H. Impact of anti-biofouling surface coatings on the properties of nanomaterials and their biomedical applications. *J. Mater. Chem. B* **2018**, *6 (1)*, 9-24.
24. Yebra, D. M.; Kiil, S.; Dam-Johansen, K. Antifouling technology—past, present and future steps towards efficient and environmentally friendly antifouling coatings. *Prog. Org. Coat.* **2004**, *50 (2)*, 75-104.
25. Sorensen, P. A.; Kiil, S.; Dam-Johansen, K.; Weinell, C. E. Anticorrosive coatings: a review. *J. Coat. Technol. Res.* **2009**, *6 (2)*, 135-176.
26. Ulbricht, M. Advanced functional polymer membranes. *Polymer* **2006**, *47 (7)*, 2217-2262.
27. Jaiswal, M.; Menon, R. Polymer electronic materials: a review of charge transport. *Polym. Int.* **2006**, *55 (12)*, 1371-1384l.
28. Sheehan, P. E.; Whitman, L. J. Detection Limits for Nanoscale Biosensors. *Nano Lett.* **2005**, *5 (4)*, 803-807.
29. Kim, K.; Tsay, O. G.; Atwood, D. A.; Churchill, D. G. Destruction and Detection of Chemical Warfare Agents. *Chem. Rev.* **2011**, *111* (9), 5345-5403.
30. Chaudhury, M. K.; Whitesides, G. M. How to make water run uphill. *Science* **1992**, *256 (5063)*, 1539-1541.
31. Katira, P.; Hess, H. Two-Stage Capture Employing Active Transport Enables Sensitive and Fast Biosensors. *Nano Lett.* **2010**, *10 (2)*, 567-572.
32. Fang, J.; Park, S.; Schlag, L.; Stauden, T.; Pezoldt, J.; Jacobs, H. O. Localized Collection of Airborne Analytes: A Transport Driven Approach to Improve the Response Time of Existing Gas Sensor Designs. *Adv. Funct. Mater.* **2014**, *24 (24)*, 3706-3714.
33. Zhang, C.; Sitt, A.; Koo, H.-J.; Waynant, K. V.; Hess, H.; Pate, B. D.; Braun, P. V. Autonomic Molecular Transport by Polymer Films Containing Programmed Chemical Potential Gradients. *J. Am. Chem. Soc.* **2015**, *137* (15), 5066-5073.
34. Koo, H.-J.; Waynant, K. V.; Zhang, C.; Braun, P. V. Polymer Brushes Patterned with Micrometer-Scale Chemical Gradients Using Laminar Co-Flow. *ACS Appl. Mater. Interfaces* **2014**, *6 (16)*, 14320-14326.
35. Koo, H.-J.; Waynant, K. V.; Zhang, C.; Haasch, R. T.; Braun, P. V. General Method for Forming Micrometer-Scale Lateral Chemical Gradients in Polymer Brushes. *Chem. Mater.* **2014**, *26 (8)*, 2678-2683.

36. Strathmann, H. *Introduction to Membrane Science and Technology*; Wiley-VCH: Weinheim, 2011.
37. Baker, R. W. *Membrane Technology and Applications, 3rd ed.*; Wiley: West Sussex, 2012.
38. Mulder, M. *Basic Principles of Membrane Technology, 2nd ed.*; Kluwer Academic Publishers: Dordrecht, 1997.
39. Bell C.L., Peppas N.A. Biomedical membranes from hydrogels and interpolymer complexes. In *Biopolymers II. Advances in Polymer Science, vol. 122.* Peppas N.A., Langer R.S.; Springer: Heidelberg, 1995.
40. Kamoun, E. A.; Kenawy, E.-R. S.; Chen, X. A review on polymeric hydrogel membranes for wound dressing applications: PVA-based hydrogel dressings. *J. Adv. Res.* **2017**, *8 (3)*, 217-233.
41. Tokarev, I.; Minko, S. Stimuli-Responsive Porous Hydrogels at Interfaces for Molecular Filtration, Separation, Controlled Release, and Gating in Capsules and Membranes. *Adv. Mater.* **2010**, *22(31)*, 3446-3462.
42. Tracton, A. A. *Coatings Technology Handbook, 3rd ed.*; CRC Press: Boca Raton, 2005.
43. Goldschmidt, A.; Streitberger, H.-J. *Basics of Coating Technology*. BASF Coatings AG: Hannover, 2007.
44. Streitberger, H. J.; Dössel, K.-F. *Automotive Paints and Coatings*. Wiley-VCH: Weinheim, 2008.
45. Ebnesajjad, S.; *Fluorinated Coatings and Finishes Handbook, 2nd ed.;* Elsevier: Waltham, 2016.
46. Krishnan, S.; Weinman, C. J.; Ober, C. K. Advances in polymers for anti-biofouling surfaces. *J. Mater. Chem.* **2008**, *18 (29)*, 3405−3413.
47. Keating, J. J., IV; Imbrogno, J.; Belfort, G. Polymer Brushes for Membrane Separations: A Review. *ACS Appl. Mater. Interfaces* **2016**, *8* (42), 28383−28399.
48. Kim, M.; Schmitt, S. K.; Choi, J. W.; Krutty, J. D.; Gopalan, P. From Self-Assembled Monolayers to Coatings: Advances in the Synthesis and Nanobio Applications of Polymer Brushes. *Polymers* **2015**, *7 (7)*, 1346-1378.
49. Thérien-Aubin, H.; Chen, L.; Ober, C. K. Fouling-resistant polymer brush coatings. *Polymer* **2011**, *52 (24)*, 5419-5425.

50. Yang, W. J.; Neoh, K.-G.; Kang, E.T.; Teo, S. L.-M.; Rittschof, D. Polymer brush coatings for combating marine biofouling. *Prog. Polym. Sci.* **2014**, *39 (5)*, 1017−1042.
51. Gunkel, G.; Weinhart, M.; Becherer, T.; Haag, R.; Huck, W. T. S. Effect of Polymer Brush Architecture on Antibiofouling Properties. *Biomacromolecules* **2011**, *12 (11)*, 4169−4172.
52. Hawkins, W. L. *Polymer Degradation and Stabilization*. Springer: Heidelberg, 1984.
53. Kulkarni, A.; Dasari, H. Current Status of Methods Used In Degradation of Polymers: A Review. *MATEC Web Conf.* **2018**, *144*, 02023.
54. Göpferich, A. Mechanisms of polymer degradation and erosion. *Biomaterials* **1996**, *17 (2)*, 103-114.
55. Banerjee, A.; Catterjee, K.; Madras, G. Enzamatic degradation of polymers: a brief review. *Mater. Sci. Technol.* **2014**, *30 (5)*, 567-573.
56. Pathak, V. M.; Navneet. Review on the current status of polymer degradation: a microbial approach. *Bioresour. Bioprocess.* **2017**, *4 (15)*.
57. Cheneler, D.; Bowen, J. Degradation of Polymer Films. *Soft Matter* **2013**, *9*, 344-358.
58. Yousif, E.; Haddad, R. Photodegradation and photostabilization of polymers, especially polystyrene: review. *Springerplus* **2013**, *2 (398)*.
59. Guo, Y.; He, S.; Yang, K.; Xue, Y.; Zuo, X.; Yu, Y.; Liu, Y.; Chang, C.-C.; Rafailovich, M. H. Enhancing the Mechanical Properties of Biodegradable Polymer Blends Using Tubular Nanoparticle Stitching of the Interfaces. *ACS Appl. Mater. Interfaces* **2016**, *8 (27)*, 17565-17573.
60. Siepmann, J.; Siegel, R. A.; Rathbone, M. J. *Fundamentals and Applications of Controlled Release Drug Delivery*. Springer: New York, 2012.
61. Rosoff, M. *Controlled Release of Drugs: Polymers and Aggregate Systems*. Wiley-VCH: Weinheim, 1989.
62. Kamaly, N.; Yarmeen, B.; Wu, J.; Farokhzad, O. C. Degradable Controlled-Release Polymers and Polymeric Nanoparticles: Mechanisms of Controlling Drug Release. *Chem Rev* **2016**, *116 (4)*, 2602-2663.
63. Miller, K. A.; Morado, E. G.; Samanta, S. R.; Walker, B. A.; Nelson, A. Z.; Sen, S.; Tran, D. T.; Whitaker, D. J.; Ewoldt, R. H.; Braun, P. V.; Zimmerman, S. C. Acid-Triggered, Acid-Generating, and Self-Amplifying Degradable Polymers. *J. Am. Chem. Soc.* **2019**, *141 (7)*, 2838-2842.

64. An, J.; Teoh, J. E. M.; Suntornnond, R.; Chua, C. K. Design and 3D Printing of Scaffolds and Tissues. *Engineering* **2015**, *1 (2)*, 261-268.
65. Kisley, L.; Serrano, K. A.; Kong, X.; Gruebele, M.; Leckband, D. E. Direct Imaging of Protein Stability and Folding Kinetics in Hydrogels. *ACS Appl. Mater. Interfaces* **2017**, *9 (26)*, 21606-21607.
66. Nadarassan, D. Biomolecule Adsorption and Release from Porous Silicon. In *Handbook of Porous Silicon*; Canham, L; Springer: New York, 2016.
67. Emami, F. S.; Puddu, V.; Berry, R. J.; Varshney, V.; Patwardhan, S. V.; Perry, C. C.; Heinz, H. Prediction of Specific Biomolecule Adsorption on Silica Surfaces as a Function of pH and Particle Size. *Chem. Mater.* **2014**, *26 (19)*, 5725-5734.
68. Brückner, S. I.; Donets, S.; Dianat, A.; Bobeth, M.; Gutiérrez, R.; Gianaurelio, C.; Brunner, E. Probing Silica–Biomolecule Interactions by Solid-State NMR and Molecular Dynamics Simulations. *Langmuir* **2016**, *32 (44)*, 11698-11705.
69. Iqbal, M.; Gleeson, M. A.; Spaugh, B.; Taybor, F.; Gunn, W. G.; Hochberg, M.; Baehr-Jones, T.; Bailey, R. C.; Gunn, L. C. Label-Free Biosensor Arrays Based on Silicon Ring Resonators and High-Speed Optical Scanning Instrumentation. *IEEE J. Sel. Top. Quantum Electron. 16 (3)*, 654-661.
70. Duan, X.; Li, Y.; Rajan, N. K.; Routenberg, D. A.; Modis, Y.; Reed, M. A. Quantification of the affinities and kinetics of protein interactions using silicon nanowire biosensors. *Nat. Nanotechnol.* **2012**, *7 (6)*, 401-407.
71. Limo, M. J.; Sola-Rabada, A.; Bolx, E.; Thota, V.; Westcott, Z.; Puddu, V.; Perry, C. C. Interactions between Metal Oxides and Biomolecules: from Fundamental Understanding to Applications. *Chem. Rev.* **2018**, *118 (22)*, 11118-11193.
72. Patwardhan, S. V.; Patwardhan, G.; Perry, C. C. Interactions of biomolecules with inorganic materials: principles, applications and future prospects. *J. Mater. Chem.* **2007**, *17 (28)*, 2875-2884.
73. Kisley, L.; Serrano, K. A.; Davis, C. M.; Murphy, E. A.; Gruebele, M.; Leckband, D. E. Soluble Zwitterionic Poly(sulfobetaine) Destabilizes Proteins. *Biomacromolecules* **2019**, 1*9 (9)*, 3894-3901.
74. Spicer, C. D.; Davis, B. G. Selective chemical protein modification. *Nat. Comm.* **2014**, *5 (5)*, 4740.

75. Keefe, A. J.; Jiang, S. Poly(zwitterionic)protein conjugates offer increased stability without sacrificing binding affinity or bioactivity. *Nat. Chem.* **2012**, *4 (1)*, 59-63.
76. Leng, C.; Hung, H.-C.; Sun, S.; Wang, D.; Li, Y.; Jiang, S.; Chen, Z. Probing the Surface Hydration of Nonfouling Zwitterionic and PEG Materials in Contact with Proteins. *ACS Appl. Mater. Interfaces* **2015**, *7 (30)*, 16881-16888.
77. Jin, Q.; Chen, Y.; Wang, Y.; Ji, J. Zwitterionic drug nanocarriers: A biomimetic strategy for drug delivery. *Colloids Surf. B Biointerfaces* **2014**, *124*, 80-86
78. Veronese, F. M. Peptide and protein PEGylation: a review of problems and solutions. *Biomaterials* **2001**, *22 (5)*, 405-417.
79. Falde, E. J.; Yohe, S. T.; Colson, Y. L.; Grinstaff, M. W. Superhydrophobic Materials for Biomedical Applications. *Biomaterials* **2016**, *104 ()*, 87-103.
80. Novick, S. J.; Dordick, J. S. Protein-containing hydrophobic coatings and films. *Biomaterials* **2002**, *23 (2)*, 441-448.
81. Cox, J. D.; Curry, M. S.; Skirboll, S. K.; Gourley, P. L.; Sasaki, D. Y. Surface passivation of a microfluidic device to glial cell adhesion: a comparison of hydrophobic and hydrophilic SAM coatings. *Biomaterials* **2002**, *23 (3)*, 929-935.
82. Lumsdmon, S. O.; Green, J.; Stieglitz, B. Adsorption of hydrophobin proteins at hydrophobic and hydrophilic interfaces. *Colloids Surf. B* **2005**, *44 (4)*, 172-178.
83. Baker, J. S.; Dudley, L. Y. Biofouling in membrane systems — A review. *Desalination*, **1998**, *118 (1-3)*, 81-89.
84. Vermonden, T.; Censi, R.; Hennink, W. E. Hydrogels for Protein Delivery. *Chem. Rev.* **2012**, *112 (5)*, 2853-2888.
85. Kopeček, J. Hydrogel biomaterials: A smart future? *Biomaterials* **2007**, *28 (34)*, 5185-5192.
86. Censi, R.; Martino, P. D.; Vermonden, T.; Hennink, W. E. Hydrogels for protein delivery in tissue engineering. *J. Control Release* **2012**, *161 (2)*, 680-692.
87. Jonker, A. M.; Löwik, D. W. P. M.; van Hest, J. C. M. Peptide- and Protein-Based Hydrogels. *Chem. Mater.* **2012**, *24 (5)*, 759-773.
88. Wade, J. H.; Bailey, R. C. Applications of Optical Microcavity Resonators in Analytical Chemistry. *Annu. Rev. Anal. Chem.* **2016**, *9 (1)*, 1-25.
89. Luchansky, M. S.; Washburn, A. L.; Martin, T. a.; Iqbal, M.; Gunn, L. C.; Bailey, R. C. Characterization of the Evanescent Field Profile and Bound Mass Sensitivity of a Label- Free

Silicon Photonic Microring Resonator Biosensing Platform. *Biosens. Bioelectron.* **2010**, *26 (4)*, 1283-1291.

90. Qavi, A. J.; Mysz, T. M.; Bailey, R. C. Isothermal Discrimination of Single-Nucleotide Polymorphisms via Real-Time Kinetic Desorption and Label-Free Detection of DNA Using Silicon Photonic Microring Resonator Arrays. *Anal. Chem.* **2011**, *83 (17)*, 6827-6833.
91. Washburn, A. L.; Gunn, L. C.; Bailey, R. C. Label-Free Quantitation of a Cancer Biomarker in Complex Media Using Silicon Photonic Microring Resonators. *Anal. Chem.* **2009**, *81 (22)*, 9499-9506.
92. Qavi, A. J.; Bailey, R. C. Multiplexed Detection and Label-Free Quantitation of MicroRNAs Using Arrays of Silicon Photonic Microring Resonators. *Angew. Chemie Int. Ed.* **2010**, *49 (27)*, 4608-4611.
93. McClellan, M. S.; Domier, L. L.; Bailey, R. C. Label-Free Virus Detection Using Arrays of Silicon Photonic Microring Resonators. *Biosens. Bioelectron.* **2012**, *31 (1)*, 388-392.
94. Vallance, C. *An Introduction to Chemical Kinetics*. Morgan & Claypool: San Rafael, 2017.
95. Mataperez, F.; Perezbenito, J. F. The Kinetic Rate Law for Autocatalytic Reactions. *J Chem Educ* **1987,** *64* (11), 925-927.
96. Lee, O. P.; Hernandez, H. L.; Moore, J. S. Tunable Thermal Degradation of Poly(vinyl butyl carbonate sulfone)s via Side-Chain Branching. *Acs Macro Lett* **2015,** *4* (7), 665-668.
97. Flory, P. J.; Rehner, J. Statistical mechanics of cross-linked polymer networks I Rubberlike elasticity. *J. Chem. Phys.* **1943,** *11* (11), 512-520.
98. James, H. M.; Guth, E. Theory of the elastic properties of rubber. *J. Chem. Phys.* **1943,** *11* (10), 455-481.
99. Chompff, A. J.; Duiser, J. A. Viscoelasticity of Networks Consisting of Crosslinked or Entangled Macromolecules .I. Normal Modes and Mechanical Spectra. *J. Chem. Phys.* **1966,** *45* (5), 1505-1514.
100. Graessley, W. W. Statistical-Mechanics of Random Coil Networks. *Macromolecules* **1975,** *8* (2), 186-190.
101. Graessley, W. W. *Polymeric liquids and networks: structure and properties*. Garland Science: New York, 2004.
102. Rubinstein, M.; Colby, R. H. *Polymer Physics.* Oxford University Press: Oxford; New York, 2003.

103. Jameson, D. M. *Introduction to Fluorescence*. CRC Press: Boca Raton, 2014.
104. Kubitscheck, U. *Fluorescence Microscopy: From Principles to Biological Applications, 2nd ed.* Wiley-VCH: Weinheim, 2017.
105. Kang, M.; Day, C. A.; Kenworthy, A. K.; DiBenedetto, E. Simplified Equation to Extract Diffusion Coefficients From Confocal FRAP Data. *Traffic* **2012**, *13* (12), 1589-1600.
106. Heitzman, C. E.; Tu, H. L.; Braun, P. V. Two-Dimensional Diffusion of Prodan on Self-Assembled Monolayers Studied by Fluorescence Recovery After Photobleaching. *J Phys Chem B* **2004**, *108* (36), 13764-13770.
107. Lorén, N.; Hagman, J.; Jonasson, J. K.; Deschout, H.; Bernin, D.; Cella-Zanacchi, F.; Diaspro, A.; McNally, J. G.; Ameloot, M.; Smisdom, N.Fluorescence Recovery after Photobleaching in Material and Life Sciences: Putting Theory into Practice *Q. Rev. Biophys.* **2015**, 48, 323-387.
108. Gelman, H.; Platkov, M.; Gruebele, M. Rapid Perturbation of Free-Energy Landscapes: From In Vitro to In Vivo *Chem. - Eur. J.* **2012**, 18, 6420-6427.
109. Ebbinghaus, S.; Gruebele, M. Protein Folding Landscapes in the Living Cell *J. Phys. Chem. Lett.* **2011**, 2, 314-319.
110. Guzman, I.; Gruebele, M. Protein Folding Dynamics in the Cell *J. Phys. Chem. B* **2014**, 118, 8459-8470.
111. Maluf, N. *An Introduction to Microelectromechanical Systems Engineering*. Artech House: Boston, 2000.
112. Allen, J. J. *Micro Electro Mechanical System Design*. CRC Press: Boca Raton, 2005.
113. Lee, K. B. *Principles of Microelectromechanical Systems*. Wiley: New Jersey, 2011.
114. Nan, K.; Want, H.; Ning, X.; Miller, K. A.; Wei, C.; Liu, Y.; Li, H.; Xue, Y.; Xie, Z.; Luan, H.; Zhang, Y.; Huang, Y.; Rogers, J. A.; Braun, P. V. Soft Three-Dimensional Microscale Vibratory Platforms for Characterization of Nano-Thin Polymer Films. *ACS Nano* **2019**, *13 (1)*, 449-457.
115. Brand, O.; Dufour, I.; Heinrich, S.; Josse, F.; Fedder, G. K.; Hierold, C.; Korvink, J. G.; Tabata, O. *Resonant MEMS: Fundamentals, Implementation, and Application.* Wiley-VCH: Weinheim, 2015.
116. Adato, R.; Aksu, S.; Altug, H. Engineering Mid-Infrared Nanoantennas for Surface Enhanced Infrared Absorption Spectroscopy. *Materials Today* **2015**, *18* (8), 436–446.

117. Dregely, D.; Neubrech, F.; Duan, H.; Vogelgesang, R.; Giessen, H. Vibrational Near-Field Mapping of Planar and Buried Three-Dimensional Plasmonic Nanostructures. *Nat Comms* **2013**, *4*, 2237.
118. Bochterle, J.; Neubrech, F.; Nagao, T.; Pucci, A. Angstrom-Scale Distance Dependence of Antenna-Enhanced Vibrational Signals. *ACS Nano* **2012**, *6* (12), 10917–10923.
119. Mesch, M.; Zhang, C.; Braun, P. V.; Giessen, H. Functionalized Hydrogel on Plasmonic Nanoantennas for Noninvasive Glucose Sensing. ACS Photonics 2015, 2 (4), 1–3.
120. Neubrech, F.; Pucci, A.; Cornelius, T. W.; Karim, S.; García-Etxarri, A.; Aizpurua, J. Resonant Plasmonic and Vibrational Coupling in a Tailored Nanoantenna for Infrared Detection. *Phys. Rev. Lett.* **2008**, *101* (15), 157403–157404.
121. Dregely, D.; Neubrech, F.; Duan, H.; Vogelgesang, R.; Giessen, H. Vibrational near-field mapping of planar and buried three-dimensional plasmonic nanostructures. *Nat. Commun.* **2013**, *4*, 2237.
122. Neubrech, F.; Pucci, A.; Cornelius, T. W.; Karim, S.; García-Etxarri, A.; Aizpurua, J. Resonant Plasmonic and Vibrational Coupling in a Tailored Nanoantenna for Infrared Detection. *Phys. Rev. Lett.* **2008**, *101*, 157403.

CHAPTER 2: POLYMER BRUSH-MODIFIED MICRORING RESONATORS FOR PARTITION-ENHANCED SMALL MOLECULE CHEMICAL DETECTION[1]

2.1 Introduction

The sensitive, selective, and quantitative real-time measurement of non-chromophoric, non-fluorogenic species remains a challenge for a range of analytical applications, including environmental analysis, and chemical warfare agent detection. For example, the detection of small molecules such as bisphenol A, diethyl phthalate, melamine, triclosan, and organophosphates is crucial for applications ranging from consumer safety to chemical warfare defense. However, these analyses are complicated by the fact that these targets do not contain convenient spectroscopic signatures amenable to simple measures, thus often requiring more sophisticated (and complicated) spectroscopic approaches. Physical property detectors are an attractive solution to these detection problems as they do not rely on analyte chromophoric properties, lending them high versatility but at a cost of reduced specificity and sensitivity. Refractive index-based optical sensors, such as photonic crystals, surface plasmon resonance detectors, microcavity resonators, and interferometric techniques, have shown particular promise for chemical detection, yet suffer from temperature-induced drift, insufficient sensitivity, poor selectivity, and often a low dynamic range, excluding their use in detection of many analytes. Silicon photonic microcavity-based sensors, owing in particular to their high sensitivity and large dynamic range, are therefore attractive for these detection applications. Furthermore, the intrinsic scalability of silicon microfabrication might allow for widely deployed sensor array networks.

Silicon photonic microring sensor array technology has previously been utilized for the surface-sensitive, refractive index-based detection of biomolecular targets, including proteins,[1] miRNA,[2] and DNA.[3] This technology has also been applied to monitor layer-by-layer assembly[4] and chemical reactions occurring at the sensor surface.[5] Unfortunately, when there are no specific binding motif/recognition elements (i.e. antibodies or DNA compliments), detection capabilities significantly decrease, as there is no interaction to localize the analyte within the surface-confined sensing region. Previously microring resonator arrays were modified using surface-initiated atom-

---

[1] Reproduced with permission from: Stanton, A. L. D.; Serrano, K. A.; Braun, P. V.; Bailey, R. C. Polymer Brush-Modified Microring Resonators for Partition-Enhanced Small Molecule Chemical Detection. *ChemistrySelect* **2017**, *2 (4)*, 1521-1524. Copyright 2017 Wiley-VCH Verlag GmbH & Co. KGaA, Weinheim.

transfer radical polymerization (ATRP) to grow polymer brushes directly from the ring surface (Figure 2.1), and brush growth could be tracked in real time directly from the resulting shift in resonance wavelength.[6] ATRP is a living radical polymerization technique which effectively grows relatively monodisperse and structurally controlled polymers.[7] Polymer brushes grown using surface-initiated (SI) ATRP can possess low polydispersity, and there is generally control over composition, grafting density, and chain length.[8]

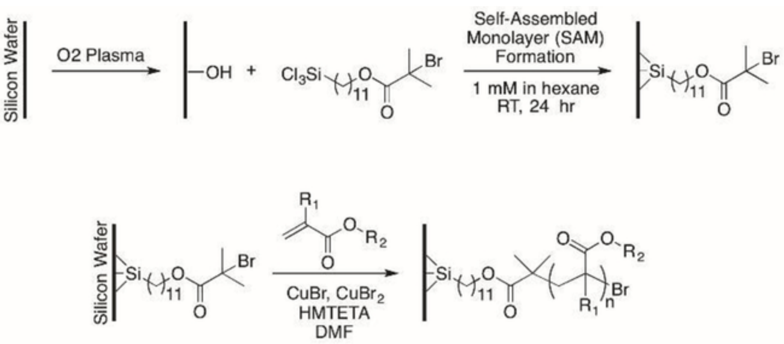

Figure 2.1 Sensor functionalization process. Bare chips are activated with oxygen plasma followed by chemical grafting of the initiator monolayer. Surface-bound polymer brushes are then grown from the sensor surface by ATRP.

This led to consideration of using ATRP-based organic modifications to change the sensor surface chemistry in hopes of enhancing the sensitivity and molecular selectivity through non-covalent molecular interactions. Light is confined within the microring waveguide via total internal reflection and the evanescent field that extends from the sensor surface has an exponential decay length (1/e) of 63 nm,[4] putting the majority of the active sensing volume within 100 nm of the ring surface. ATRP-grown polymer brushes are particularly attractive as a general approach to organic surface modification, as they can conveniently be grown to thicknesses of ~100 nm with amenability to a diverse set of functional group chemistries. Notably, thicker polymer layers deposited via drop casting or spin coating would be limited by slow response times and relatively poorer sensitivity. The polymer brushes serve to localize molecular species within the evanescent field of the sensors, significantly increasing the sensor response by 1-2 orders of magnitude for given concentrations of analyte, and providing a pathway towards greater sensor selectivity.

2.2 Results and discussion

2.2.1 Enhanced detection of pharmaceutical standards

This concept was first investigated using the common pharmaceutical standards caffeine and acetaminophen. Hydrophilic PNIPAM (43 nm dry thickness), and hydrophobic PMMA, (24 nm dry thickness) polymer brushes were grown off the microring resonator arrays using literature SI-ATRP procedures. Brush thicknesses were determined by ellipsometry, using bulk wafers derivatized in the same reaction flask. The resulting modified arrays were then exposed to water-based solutions of each standard using integrated microfluidics as described previously.[9]

Initial observations reveal enhanced response of the analytes on the modified rings compared to bare, unmodified rings, due to localization of the organic molecules within the organic brush on microring surface. In order to just focus on the amount of analyte partitioned into the polymer brush, and not bulk refractive index changes in solution, the response from unmodified sensors was subtracted from the polymer brush-modified microrings, as shown in Figure 2.2 (Non-subtracted resonance shift data, as well as percentage enhancement compare to unmodified sensors, can be found in Figure 2.5). Analyte enhancement is observed within both polymer brushes; however, acetaminophen shows a significantly greater response when interacting with the PNIPAM brush, with a 10-fold larger resonance shift compared to the response of PMMA-modified microrings, and 400% enhancement over unmodified sensors.

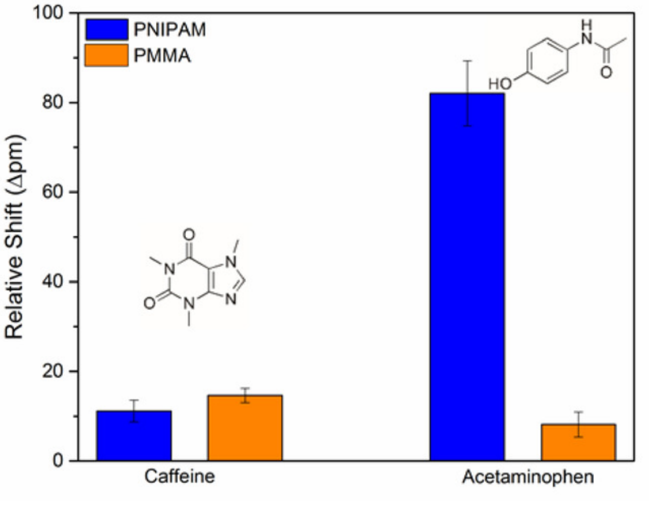

Figure 2.2 Resonance wavelength shifts measured for PNIPAM- and PMMA-modified microring resonators upon exposure to 10 mM aqueous solutions of caffeine and acetaminophen. The responses from bare microrings (20 pm for caffeine and 27 pm for acetaminophen) was subtracted to remove bulk refractive index effects. Partition-based signal enhancement was observed for both polymer brushes; however, the greatest selective enhancement was observed for acetaminophen interacting with PNIPAM-modified microrings. Error bars represent the standard deviations from four individual microring responses from a single detection experiment.

The enhancement is almost certainly due to partitioning of the small molecule analyte into the organic layer. While there are many factors which can drive partitioning, the effect of solvent and brush swelling is likely important. PMMA is hydrophobic, and swells only 2% in water,[10] in contrast to the much more hydrophilic PNIPAM brush, which likely extends further into solution, providing a more accessible construct for chemically-selective analyte partitioning.

2.2.2 Example enhanced detection of a toxic industrial chemical

Further exploring the role of brush extension and response, the partitioning of bisphenol A (BPA), a toxic industrial chemical, into PNIPAM (230 nm thick) and PMMA (250 nm thick) polymer brushes was probed in both aqueous and 90:10 water:acetonitrile solutions. For both brushes, the response to a 10 mM solution of BPA was increased in the acetonitrile-containing solvent, as shown in Figure 2.3. Again, the more hydrophilic PNIPAM brush showed a larger response, but the addition of a small amount of organic solvent, which presumably swelled both polymer brushes, led to a substantial increase in observed resonance wavelength shift for both brushes. Interestingly, the relative percent enhancement between PNIPAM and PMMA remained constant (~9-fold larger for PNIPAM) in both solvent systems (see Figure 2.6).

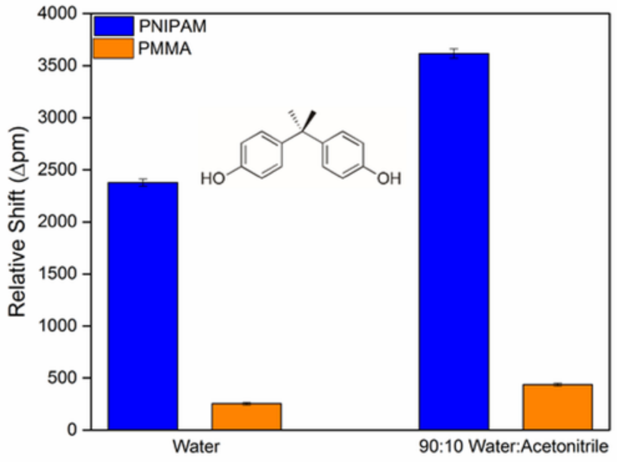

Figure 2.3 Resonance wavelength shifts measured for PNIPAM- and PMMA-modified microring resonators upon exposure to 10 mM solutions of bisphenol A prepared in both water and a 90:10 water:acetonitrile mixture. The responses from bare microrings (25 pm and 152 pm for water and water:acetonitrile,respectively) was subtracted to remove bulk refractive index effects. Greater overall response was observed for the relatively more hydrophilic PNIPAM brush in both solvent systems, but both brushes showed signal enhancement as the addition of the organic solvent likely increased brush swelling and partitioning of BPA within both polymer brushes. Error bars represent the standard deviations from four individual microring responses from a single detection experiment.

2.2.3 Effects of alcohol partitioning into various polymer brushes

To further investigate the interactions of solution-phase analytes with different polymer brush chemistries, we studied the partitioning of aqueous solutions of methanol, ethanol, and octanol with microring sensors presenting hydrophobic PMMA and hydrophilic PDMAEMA polymer brushes. These polymer brushes had dry thicknesses of 65 and 40 nm, respectively, as determined on blank silicon wafers grown in the same ATRP reaction flask via spectroscopic ellipsometry. This set of experiments focused on a single class of small molecule targets—alcohols—and was designed to examine the role of hydrophobicity and polymer solubility in a systematic way. The real-time resonance shifts accompanying exposure to these solutions, as well as the resonance shifts measured with a blank microring sensor (no polymer brush) are shown in Figure 2.4.

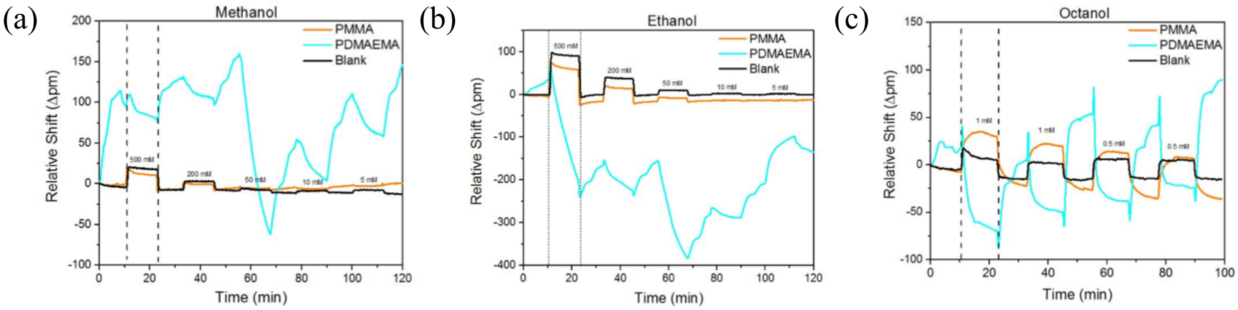

Figure 2.4 Real-time resonance shifts of PMMA and PDMAEMA-modified microring resonators to aqueous solutions of methanol, ethanol, and octanol. (a) Exposure to methanolic solutions show large magnitude shifts for PDMAEMA-modified rings due to strong solubility of methanol in the polymer brush. The response of PMMA-modified rings is equivalent to bare microring indicating no partitioning. (b) Exposure to ethanolic solutions shows similar behavior; strong interactions with PDMAEMA and nothing for PMMA. (c) Exposure to octanolic solutions elicits responses from both PMMA and PDMAEMA-modified microrings on account of octanol being an interacting solvent for both polymer brushes. Both responses are distinctly different from that of bare microrings.

For methanol and ethanol, both of which are highly water-miscible, the hydrophilic PDMAEMA showed large negative resonance shifts, whereas hydrophobic PMMA showed a response similar to the blank microring, indicating no analyte partitioning. For octanol, which is significantly more hydrophobic (much less miscible with water), highly differential responses were observed, with PMMA-modified sensors showing a positive shift in resonance wavelength larger than the blank ring, while PDMAEMA brushes showed a negative shift. The opposite signs of these shifts suggest that the resonance shifts are reflective of partitioning according to intermolecular forces. In this case, this is a combination of solubility and hydrophobicity differences between the analytes and two different polymer brush chemistries.

To help explain these responses it is important to consider the solubility parameters, δ, of the compounds involved in this interaction, which are listed in Table 2.1. Equivalent solubility parameters suggest that compounds are miscible, or are a good solvent combination. First considering the responses of PMMA, we found that there was no difference in response from PMMA-modified microrings compared with bare microring sensors, and this is consistent with the fact that methanol and ethanol do not interact with PMMA. However, when exposed to octanol, which has a solubility parameter similar to PMMA, we see a positive resonance wavelength shift, consistent with the notion that octanol can partition into the polymer brush.

Table 2.1 Solubility parameters of various alcohols and polymers.

Compound	δ [(MPa)$^{0.5}$]
Water	48.1[11]
Methanol	29.7[12]
Ethanol	26.1[12]
Octanol	21.0[11]
PMMA	20.0[12]
PDMAEMA	unknown

The interactions of the alcohols with PDMAEMA is somewhat more complex, and the solubility parameter for this polymer is unknown. However, the hydrophilic nature of PDMAEMA and literature reports suggest that both methanol[13] and ethanol[14] are good solvents for this polymer. By contrast, one would not expect octanol to be as good of a solvent considering it more hydrophobic nature. PDMAEMA is also soluble in water and upon flowing water across these initially dry polymer brushes, brush hydration is observed as a positive shift in resonance wavelength. The addition of both ethanol and methanol leads to a large negative shift in the resonance wavelength. The magnitude of the shift is understandable on account of the high solubility of these alcohols in the polymer brush.

The negative direction of the shift for PDMAEMA exposed to ethanol and octanol is explained by the fact that the polymer brush is likely swelling as to extend beyond the evanescent field of the sensor, replacing higher refractive index polymer ($n \approx 1.42$) with much lower index water (n = 1.33) and methanol (n = 1.33) or ethanol (n = 1.36). The original PDMAEMA brush was 40 nm thick when fully dried, and is expected to be ~60 nm when hydrated. This is already nearly equivalent to the 1/e decay length of the microrings evanescent field sensitivity profile. While the resonators are still sensitive to refractive index at and beyond this distance from the surface, the relative sensitivity to changes in this region are less than the same RI changes nearer the surface. Moreover, it was previously determined that "ethanol is a more effective solvent for PDMAEMA than water."[14] Therefore additional partitioning of ethanol into the polymer brush would likely lead to additional polymer swelling. Moreover, as mentioned above, as the polymer brush swells beyond into this less sensitive distance from the surface, the extended PDMAEMA is replaced by lower refractive index water and alcohol, effectively lowering the n_{eff} sampled by the optical mode and leading to a negative resonance wavelength shift. When exposed to octanol, negative resonance shifts are again observed for PDMAEMA; however, their magnitude is reduced because octanol is a poorer solvent for this polymer.

It is worthwhile to point out that the responses from PDMAEMA upon cycling from water to methanol and ethanol appear somewhat irregular, but the negative shift in the alcohol solution followed by positive shift in water is consistent. The irregularity of the "shape" of the response is something that will require additional studies to fully understand; however, it is perhaps not surprising given the complexities of these solubility/hydration interactions. Also, it is important to note the difference between simple swelling and brush strand dissolution. Many compounds will penetrate a chemical film, simply diffusing in at a rate dictated by penetrant size and brush matrix, but the localized relaxation of the brush in the presence of a penetrant is classified as dissolution. Dissolution of the brush structure is likely concentration-dependent and defined by non-Fickian transport. Our measurement is likely sensitive to brush extension and dissolution as that changes the relative occupancy of the evanescent field by higher RI polymer and lower RI water/alcohols, and the partition kinetics are complex and warrant future studies. By comparison, PMMA, which only shows partitioning of octanol, is a glassy polymer., in contrast to PDMAEMA. Dissolution is be more likely to occur in a "Case II" manner where a sharp front distinguishes swollen and unswollen regions, while a front of solvent penetrates at a constant rate.[15] This more well-defined and more limited partitioning may explain the more well- behaved shifts in resonance wavelength. Also, the refractive index of octanol (n = 1.43) is closer to that of the polymer brush so that any volume replaced by this solvent might still support a positive resonance shift.

In summary, these experiments revealed that sensors showed large responses only when the solubilities of the alcohol and polymer brush were well matched, supporting the proposed partition-driven sensing mechanism. PMMA sensors only responded to octanol and hydrophilic PDMAEMA brushes showed large responses when exposed to methanol and ethanol, which are known to be good solvents for the polymer.

2.2.4 Enhancement and array-based methods for chemical warfare agent detection

These initial experiments indicate the possibility of using polymer brush-modified microring resonators for small molecule, organic compound detection, and the potential to tune analyte sensitivity and selectivity by altering brush:analyte:solvent interactions. One particularly interesting application for which rapid, highly sensitive analyses of non-chromophoric species would be important is the detection of chemical warfare agents and chemically similar pesticides. Nerve-based chemical warfare agents (CWAs) are a particular concern, given that many organophosphate CWAs have IC_{50} values on the order of parts per billion,[16,17] yet lack chromophoric or fluorogenic signatures. This excludes their detection using standard instrumentation such as UV-Vis and fluorescence spectroscopy. More advanced trace analytical techniques, such as mass spectrometric methods, are difficult to deploy into the field, thus limiting real time monitoring, as would be important for detection of CWAs. By contrast, robust silicon microfabrication could allow for wide-scale deployment of microring resonators when appropriately-modified to meet these analytical detection challenges.

As a preliminary test of the applicability of polymer brush-modified microring resonators, the detection of 4-methylumbelliferyl phosphate, a CWA simulant, was investigated. Three different types of polymer brushes were grown on microring resonator array substrates: PNIPAM (43 nm thick), PMMA (24 nm thick), and PDMAEMA (26 nm thick). First, four different concentrations of 4-methylumbelliferyl phosphate were separately flowed across the differentially-modified sensors, with the resonance wavelength shifts (with bare microring response subtracted) shown in Figure 2.5a. In all cases, a concentration-dependent response is observed, with the PDMAEMA brush showing the largest degree of enhancement—at least 20-fold for greater signals compared to other brush chemistries, and 5000+% response enhancement compared to non-functionalized sensors (see Figure 2.8).

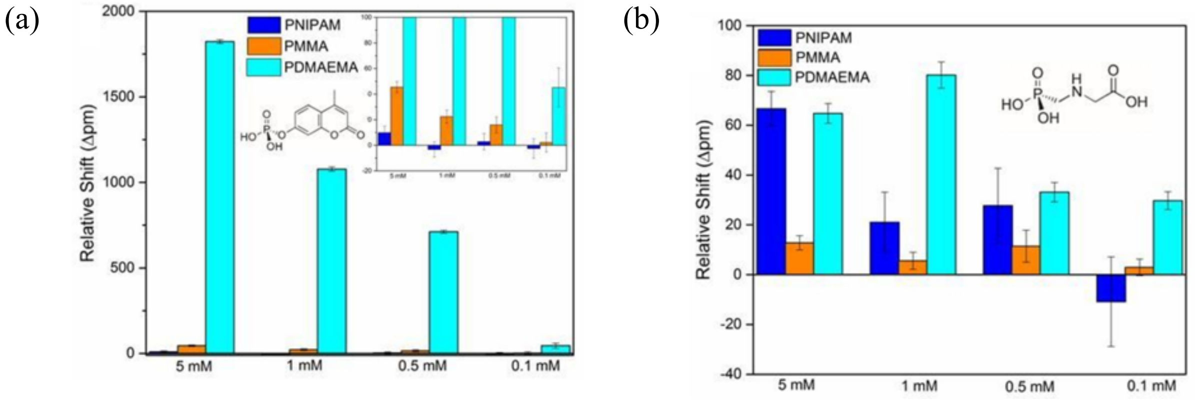

Figure 2.5 Resonance wavelength shifts measured for PNIPAM-, PMMA-, and PDMAEMA-modified microring resonators upon exposure to various concentrations of aqueous solutions of phosph(on)ate analytes. In all cases, responses from bare microrings were subtracted to remove bulk refractive index effects, and error bars represent the standard deviations from four individual microring responses from a single detection experiment. A) Solutions of 4-methylumbelliferyl phosphate showed largest enhancements for PDAEMA brushes, but also significant enahncements for PMMA-modified sensors (see inset). B) Glyphoshate solutions elicited enhanced responses from the hydrophilic PDAEMA- and PNIPAM-modified sensors, compared to PMMA. Interestingly, the differential responses between the three different brush modifications suggests that arrays of uniquely brush-modified sensors might be able to provide an analyte-specific response that would have utility in target identification. Non-subtracted resonance shifts and percent enhancement values can be found in Figures S3 and S4, respectively.

We also investigated the detection of glyphosate, and found that enhanced responses are also observed for this herbicide (Figure 2.5a). Notably, the overall resonance wavelength shifts are much smaller for this analyte, as the refractive index of glyphosphate is lower than the aromatic 4-methylumbelliferyl phosphate analyte; however, the effects of bulk refractive index change have been corrected by again subtracting the bare resonator signal. This reinforces the observation that molecular partitioning plays a substantial role in dictating sensor response as higher refractive index analytes partitioned within polymer brush-modified microrings show enhanced sensor response.

Importantly, the differential signal measured by the different brush-modified microrings suggests the potential for array-based target identification. Specifically, arrays of differentially-functionalized microrings could potentially, in a single detection experiment, provide both quantitative concentration determination, as well as a target-specific signature that would facilitate agent identification. This could be analogous to the highly successful optoelectronic “nose” arrays, which respond to the subtly different chemical reactivities of volatile organic compounds.[18] The origin of specific intermolecular forces that lead to this differential response are beyond the scope of this manuscript; however, we speculate that a combination of brush and analyte solubilities in the solvent system play an important role in sensor response that could be optimized for particular target agents of interest.

2.3 Conclusions

Polymer brush-modified silicon photonic microring resonators were found to exhibit differential chemical interactions with small molecule analytes, enhancing the sensor response in excess of 1000% for some brush-analyte combination, compared to unmodified sensors. Presumably, this enhancement is due to intermolecular interactions that could be optimized to be highly specific and sensitive for particular classes of target analytes. At this early stage, the results are encouraging as the brushes and small molecules selected represent several different, generally-relevant classes of analytes. Future work will focus on optimizing polymeric constructs for specific analytical targets and applications. For example, one could presumably select a polymer brush, such as poly(methacryoyloxyethyl trimethylammonium fluoride) (polyMETAF) that would have optimized partitioning or even specific reactions with a CWA such as malathion. These types of highly specific interactions would lead to even lower LODs, making this chip-integrated measurement approach useful in detecting low-abundant analytes such as CWAs.

2.4 Experimental section

2.4.1 Data correction methods and percent enhancement results

In order to focus on the amount of analyte partitioned into the polymer brush and not bulk refractive index changes in solution, the response from unmodified sensors was subtracted from the polymer brush-modified microrings. The non-corrected resonance shift data can be found in Figure 2.6a for caffeine and acetaminophen detection, including bare and brush-modified microring sensors. Additionally, percent detection enhancement values can be found in Figure 2.6b and were determined by dividing brush-modified responses by bare microring sensor response.

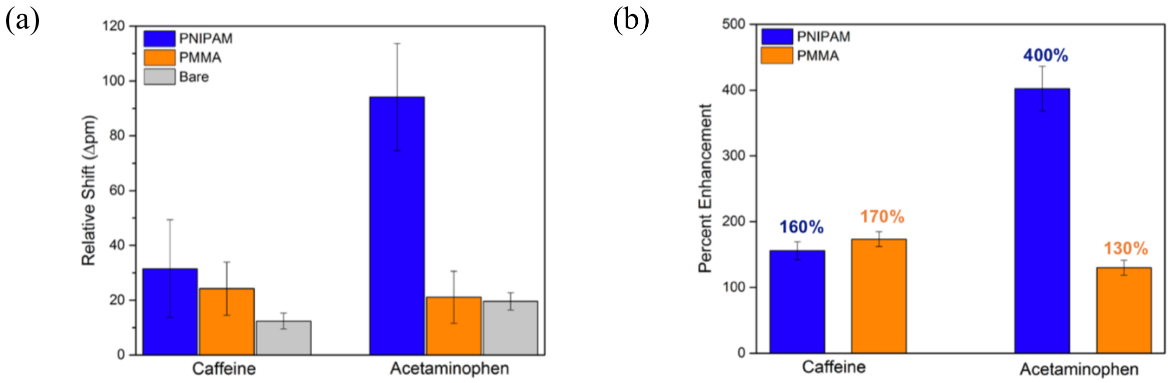

Figure 2.6 (a) Non-corrected resonance wavelength shifts and (b) percent detection enhancement for 10 mM aqueous acetaminophen and caffeine detection by using PNIPAM and PMMA polymer brushes.

Additionally, the non-corrected resonance data and percent enhancement values for Bisphenol A (BPA) detection in can be found in Figure 2.7. These experiments investigated the effect of water and 9:1 water/acetonitrile mixtures on a 10 mM solution of BPA. The non-corrected resonance wavelength data was collected for bare and brush-modified sensors. Percent enhancement was found again by dividing brush-modified responses by bare microring response.

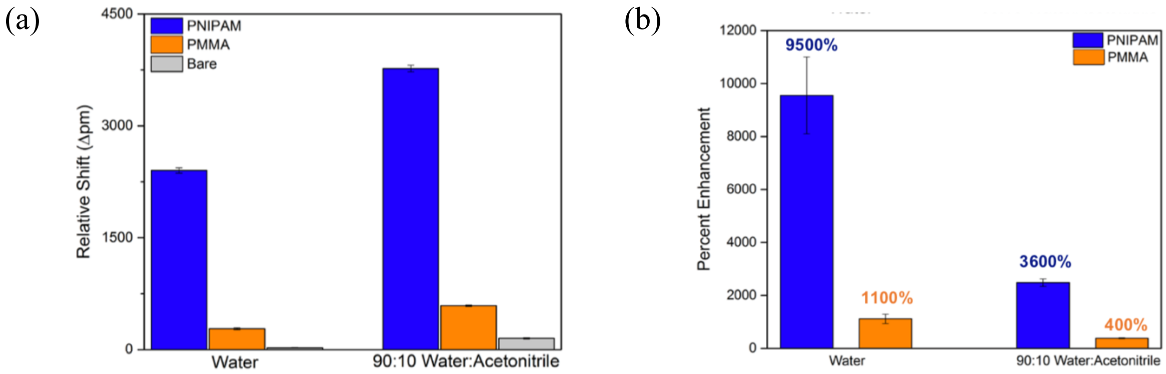

Figure 2.7 (a) Non-corrected resonance wavelength shifts and (b) percent detection enhancement for 10 mM bisphenol A by using PNIPAM and PMMA polymer brushes and water/acetonitrile mixtures.

Finally, this method was used as well for the enhancement of 4-methylumbelliferyl phosphate and glyphoshpate. The non-corrected resonance data and percent enhancement values for Bisphenol A (BPA) and glyphosphate detection in can be found in Figure 2.8 and Figure 2.9, respectively. These experiments investigated the effect of concentration on the successful detection of nerve agent simulants. The non-corrected resonance wavelength data was collected for bare and brush-modified sensors. Percent enhancement was found again by dividing brush-modified responses by bare microring response.

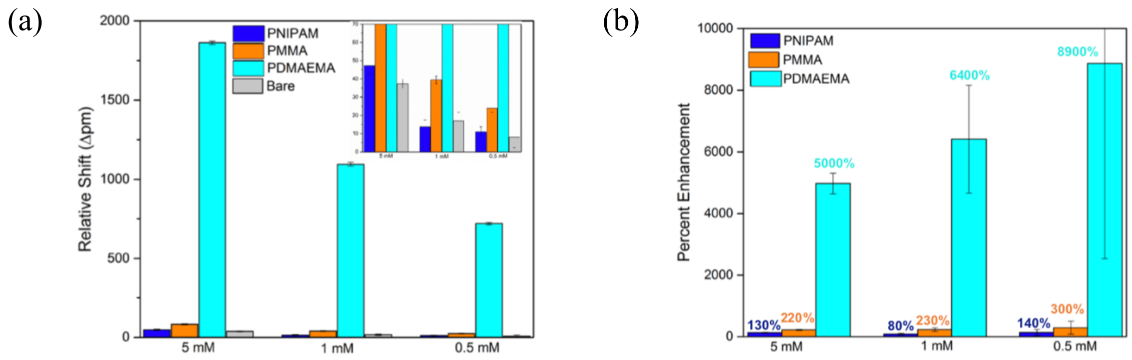

Figure 2.8 (a) Non-corrected resonance wavelength shifts and (b) percent detection enhancement for 0.5, 1, and 5 mM 4-methylumbelliferyl phosphate by using PNIPAM, PMMA, and PDMAEMA polymer brushes.

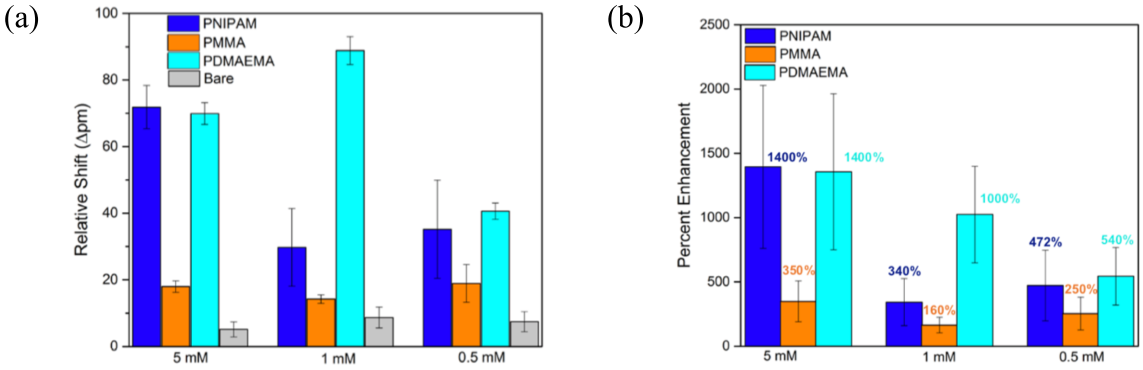

Figure 2.9 (a) Non-corrected resonance wavelength shifts and (b) percent detection enhancement for 0.5, 1, and 5 mM glyphosphate by using PNIPAM, PMMA, and PDMAEMA polymer brushes.

2.4.2 Polymer brush synthesis and characterization

Hydrophilic poly(N-Isopropylacrylamide) (PNIPAM),[19] hydrophilic poly(2-dimethylamino- ethylmethacrylate) (PDMAEMA),[20] and hydrophobic poly(methyl methacrylate) (PMMA)[21] polymer brushes were grown off the microring resonator substrates using adapted literature surface-initiated, atom-transfer radical polymerization (SI-ATRP) procedures. First, the silicon microring resonator chips were cleaned using oxygen plasma. Then, self-assembled monolayers of the initiator 11-(2-bromo-2-methyl)-propionyl undecyl tricholorosilane were formed on the substrates by immersion in a 1 mM hexane solution for 24 hours. After being rinsed in fresh hexane and dried under a nitrogen stream, the microchips were placed in a reaction vessel. 1,1,4,7,10,10-hexamethyltriethylene tetramine (HMTETA) was used for the ligand[22] and standard

Schlenk techniques were used to transfer appropriate ratios of [monomer]:[Cu(I)]:[Cu(I)]:[ligand] into the reaction vessel. The polymeric substrates were rinsed with THF, IPA, and H2O and then dried under a stream of nitrogen. Dry polymer thicknesses were measured using single wavelength ellipsometry (Gaertner L116C).

The modified chips were exposed to the analytes via integrated microfluidics within the Genalyte Maverick M1 optical scanning instrumentation, whose operation has been described previously.[23] In brief, four microring resonators were monitored to determine both either bare- or polymer brush-modified sensor response, while four occluded rings were used for real-time temperature correction. The sensor responses are measured in real-time and extracted resonance wavelength shifts averaged over a suitable time period are plotted for exposure to different small molecule analytes.

2.5 References

1. Washburn, A. L.; Gunn, L. C.; Bailey, R. C.; Label-Free Quantitation of a Cancer Biomarker in Complex Media Using Silicon Photonic Microring Resonators. *Anal. Chem.* **2009**, *81 (22)*, 9499-9506.
2. Qavi, A. J.; Bailey, R. C. Multiplexed Detection and Label-Free Quantitation of MicroRNAs Using Arrays of Silicon Photonic Microring Resonators. *Angew. Chemie Int. Ed.* **2010**, *49 (27)*, 4608-4611.
3. Qavi, A. J.; Mysz, T. M.; Bailey, R. C. Isothermal Discrimination of Single-Nucleotide Polymorphisms via Real-Time Kinetic Desorption and Label-Free Detection of DNA Using Silicon Photonic Microring Resonator Arrays. *Anal. Chem.* **2011**, *83* (17), 6827-6833.
4. Luchansky, M. S.; Washburn, A. L.; Martin, T. A.; Iqbal, M.; Gunn, L. C.; Bailey, R. C. Characterization of the evanescent field profile and bound mass sensitivity of a label-free silicon photonic microring resonator biosensing platform. *Biosens. Bioelectron.* **2010**, *26 (4)*, 1283-1291.
5. Byeon, J.; Limpoco, F. T.; Bailey, R. C. Efficient Bioconjugation of Protein Capture Agents to Biosensor Surfaces Using Aniline-Catalyzed Hydrazone Ligation. *Langmuir* **2010**, *26 (19)*, 15430-15435.
6. Limpoco, F. T.; Bailey, R. C. Real-Time Monitoring of Surface-Initiated Atom Transfer Radical Polymerization Using Silicon Photonic Microring Resonators: Implications for

Combinatorial Screening of Polymer Brush Growth Conditions. *J. Am. Chem. Soc.* **2011**, *133 (38)*, 14864-14867.

7. Matyjaszewski, K. Atom Transfer Radical Polymerization (ATRP): Current Status and Future Perspectives. *Macromolecules* **2012**, *45 (10)*, 4015-4039.
8. Hui, C. M.; Pietrasik, J.; Schmitt, M.; Mahoney, C.; Choi, J.; Bockstaller, M. R.; Matyjaszewski, K. Surface-Initiated Polymerization as an Enabling Tool for Multifunctional (Nano-)Engineered Hybrid Materials. *Chem. Mater.* **2014**, *26 (1)*, 745-762.
9. Iqbal, M.; Gleeson, M. A.; Spaugh, B.; Tybor, F.; Gunn, W. G.; Hochberg, M.; Baehr-Jones, T.; Bailey, R. C.; Gunn, L. C. Label-Free Biosensor Arrays Based on Silicon Ring Resonators and High-Speed Optical Scanning Instrumentation. *IEEE J. Sel. Top. Quantum Electron.* **2010**, *16 (3)*, 654-661.
10. N'Diaye, M.; Pascaretti-Grizon, F.; Massin, P.; Baslé, M.; Chappard, D. Water Absorption of Poly(methyl methacrylate) Measured by Vertical Interference Microscopy. *Langmuir* **2012**, *28 (31)*, 11609-11614.
11. Xu, H.; Song, J.; Tian, T.; Feng, R. Estimation of Organogel Formation and Influence of Solvent Viscosity and Molecular Size on Gel Properties and Aggregate Structures. *Soft Matter* **2012**, *8 (12)*, 34780-3486
12. Groele, R. J.; Krasicky, P. D.; Chun, S.-W.; Sullivan, J.; Rodriguez, F. Dissolution Rates of Poly (Methyl Methacrylate) in Mixtures of Nonsolvents. *J. Appl. Polym. Sci.* **1991**, *42 (1)*, 3-8.
13. Mao, B. W.; Gan, L. H.; Gan, Y. Y. Ultra High Molar Mass poly[2-(Dimethylamino)ethyl Methacrylate] via Atom Transfer Radical Polymerization. *Polymer* **2006**, *47 (9)*, 3017-3020.
14. Samal, S.; Dubruel, P. *Cationic Polymers in Regenerative Medicine*; RSC Polymer Chemistry Series; The Royal Society of Chemistry, 2014.
15. Papanu, J. S.; Hess, D. W.; Soong, D. S. S.; Bell, A. T. Swelling of Poly (Methyl Methacrylate) Thin Films in Low Molecular Weight Alcohols. *J. Appl. Polym. Sci.* **1990**, *39 (4)*, 803-823.
16. Pohanka, M.; Binder, J.; Kuca, K. Sarin Assay using Acetylcholinesterases and Electrochemical Sensor Strip. *Def. Sci. J.* **2009**, *59 (3)*, 300-304.
17. Jenkins, A. L.; Yin, R.; Jensen, J. L. Molecularly imprinted polymer sensors for pesticide and insecticide detection in water. *Analyst* **2001**, *126 (6)*, 798-802.

18. Askim, J. R.; Mahmoudi, M.; Suslick, K. S. Optical sensor arrays for chemical sensing: the optoelectronic nose. *Chem. Soc. Rev.* **2013**, *42 (22)*, 8575-8800.
19. Xue, C.; Yonet-Tanyeri, N.; Brouette, N.; Sferrazza, M.; Braun, P. V.; Leckband, D. E. Protein Adsorption on poly(N-Isopropylacrylamide) Brushes: Dependence on Grafting Density and Chain Collapse. *Langmuir* **2011**, *27 (14)*, 8810-8818.
20. Koo, H. J.; Waynant, K. V.; Zhang, C.; Braun, P. V. Polymer Brushes Patterned with Micrometer-Scale Chemical Gradients Using Laminar Co-Flow. *ACS Appl. Mater. Interfaces* **2014**, *6 (16)*, 14320-14326.
21. Ramakrishnan, A.; Dhamodharan, R.; Rühe, J. Controlled Growth of PMMA Brushes on Silicon Surfaces at Room Temperature. *Macromol. Rapid Commun.* **2002**, *23 (10-11)*, 612-616.
22. Millard, P.-E.; Mougin, N. C.; Böker, A.; Müller, A. H. E. Fast ATRP of N-Isopropylacrylamide in Water and Its Application to Bioconjugates. *Polym. Prepr. (Am. Chem. Soc. Div. Polym. Chem.)* **2008**, *49 (2)*, 121-122.
23. Washburn, A. L.; Gunn, L. C.; Bailey, R. C. Label-Free Quantitation of a Cancer Biomarker in Complex Media Using Silicon Photonic Microring Resonators. *Anal. Chem.* **2009**, *81 (22)*, 9499-9506.

CHAPTER 3: POLYMER BRUSH-MODIFIED MICRORING RESONATORS FOR MONITORING ANALYTE PARTITIONING AND CONFORMATION CHANGE

3.1 Introduction

Polymer brush functionalization has become a powerful approach to modify interfaces, often creating properties and behaviors that are vastly different from those accessible using analogous bulk materials.[1] Brush-modified surfaces have led to great advances in surface and interface science, with their most well-known applications in the biomedical field,[2] protective and antibiofouling coatings,[3] membranes,[4] functional nanomaterials,[5] wettability,[6] and colloidal stabilization.[7] However, direct measurement of analyte-brush interactions, a key aspect of protective coating and membrane development, remains a challenge. Analyte-brush interactions govern not only the speed of diffusion of an analyte into the brush, and thus the lifetime of a coating,[8] but also the partitioning ability of the analyte into the brush which determines the ultimate analyte equilibrium concentration. Understanding analyte-brush interactions are thus crucial for creating optimal membrane or coating systems, such as proton exchange membrane fuel cells, where partitioning and diffusion would directly control the speed and amount of fuel stored.[9]

There is a need to develop technologies which can rapidly characterize analyte-brush interactions for a variety of systems. While analysis could occur quickly on one analyte-brush system at a time, multiplexing capabilities would be ideal for speeding up and normalizing the measurement process. Complicating analyte-brush interaction analysis is the potential for the polymer brush to either swell or collapse as a result of analyte partitioning,[10] resulting in temporally changing analyte-brush interactions. The need for temporal resolution suggests the optimal measurement method should also allow for real-time measurement.

A majority of techniques currently used to analyze analyte-brush interactions focus on the brush response to analyte introduction. The most commonly studied analyte system has been one causing a pH change in the brush, thus relaying a brush conformational change. Atomic force microscopy (AFM) is a common brush conformational analysis techniques,[11] but does not provide vertical resolution in the brush, making AFM a more limited technique for analyzing brush-analyte interactions. X-ray photoelectron spectroscopy (XPS),[12] neutron reflectivity (NR),[13] and, most common of all, *in situ* spectral ellipsometry (SE)[14] have all been used as analysis techniques for pH changes impact on brushes, as well as for observing differential rates of brush modification depending on brush thickness, as they offer vertical spatial resolution allowing a fuller picture of brush dynamics to be developed. However, these techniques typically require equilibration times close to one hour per system and do not offer the ability to test multiple analyte-brush systems at one time. Fourier transform infrared spectroscopy (FTIR) has also been used to analyze the changes in brush protonation states upon analyte introduction,[15] providing an indirect means of measuring analyte diffusion but also is limited in the number of analyte-brush systems which can be analyzed at once. Additionally, FTIR relies on a chemical change as a result of analyte partitioning, which are limited cases at best. Surface plasmon resonance (SPR) and quartz crystal microbalance (QCM),[37,16,17] take a more wholesome approach, with the potential to analyze not only the brush conformation but also environmental changes. SPR and QCM offer excellent surface sensitivity and good vertical resolution, as well as providing real-time measurements on a particular system. But again, the potential for multiplexability in these systems is limited.

A new method for monitoring analyte-brush interactions has been recently developed in our group where environmental changes, including compositional and volumetric differences, are observed from polymer brush-modified silicon photonic microring resonators. The silicon-on-insulator chips each have 30 µm diameter active sensor microrings in 32 individual addressable groups of four and four temperature controls.[18] Light travels down the waveguide by total internal reflection and is coupled onto the microrings according to the interferometric-based condition:

$$m\lambda = 2\pi r n_{eff} \tag{3.1}$$

where m is an integer, λ is the resonant wavelength, r is the radius of the microring and n_{eff} is the local effective refractive index (Equation 3.1).

Each silicon microring can be selectively functionalized as the rest of the surface is covered by a protective polymer cladding (Figure 3.1a). As various analyte solutions are flowed over the microring, the effective refractive index difference can be observed by a shift in the resonant wavelength (Figure 3.1b). In previous work, brush-functionalized silicon photonic microring resonator array technology has been suggested for liquid chromatography detection,[19] combinatorial screening[20] and partition-enhanced small molecule detection.[21] However, using this technology for analyte-brush interaction observation is largely unexplored[22] and has the potential to not only further define analyte partitioning and diffusion into polymer brushes, but also rapidly optimize conditions so as to minimize or maximize partitioning (depending on the application). The high sensitivity of the platform within 100 nm from the surface[23] and the ability to measure refractive index changes in real-time also provides forms of both vertical spatial and temporal resolution, informing full analyte-brush interaction analysis. Real-time analysis results in rapid determination of the equilibrium state of the analyte-brush system, which can be reached within minutes after analyte introduction. Additionally, as more methods develop that could selectively functionalize the sensor surface,[24] the microring resonator system has the potential to multiplex brush types or brush heights across the microring resonator chip surface. Finally, the microring resonator system offers a means of monitoring both brush conformational changes and analyte presence using one platform, a more universal detection method than common techniques like SE. This allows for determination of more aspects of brush-analyte interaction properties, such as impact on brush and diffusion, in one measurement.

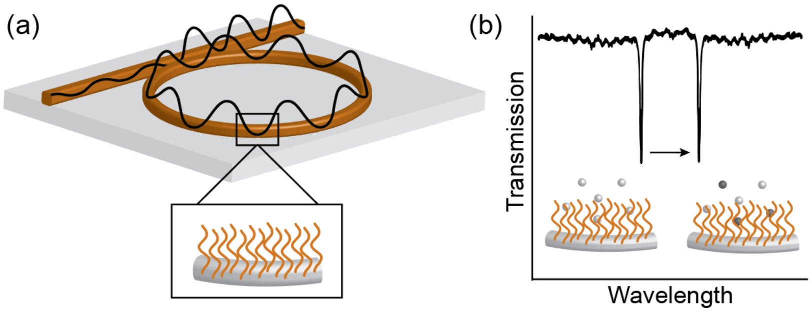

Figure 3.1 (a) Polymer-functionalized silicon photonic microring resonators couple light from the waveguide. (b) Resonant optical modes are visualized by a dip in transmission intensity. Shifts in this wavelength are observed in real-time as changing analyte solutions are passed over the microring surface.

In this work, we demonstrate the utility of silicon photonic microring resonators as a platform for the *in-situ* characterization of polymer brush analyte interactions. Microring surfaces were modified using SI-ATRP, enabling the construction of well-defined polymer brushes of hydrophilic and hydrophobic natures. Diffusion and partitioning of small molecules into the polymer brush can be observed in real-time and conformation changes can be quantified by measuring and fitting shifts in the resonance wavelength. This allows for straightforward extraction of various constants, such as pKa, diffusion coefficient and partitioning coefficient, as a function of complex variables, such as: polymer brush functionality, length, and analyte. Knowing various constants about a polymer brush-analyte system allows for rapid determination of optimal polymer brush-analyte combinations for a variety of applications, including antifouling coatings and analyte release mechanisms.

3.2 Results and discussion

3.2.1 Surface functionalization

Microring resonator arrays were modified by growing polymer brushes directly from the silicon surface. In this method, an initiator monolayer was first formed by self-assembly of BPOTS (Scheme 1). The monolayer was on average 17 ± 2 Å, which compares well to prior studies.[26] Then, the polymer brush was subsequently synthesized by SI-ATRP using MMA, HEMA, and DMAEMA monomers. The reaction was stopped at various times to obtain desired thicknesses.

Scheme 3.1 Preparation of polymer-functionalized silicon photonic microring resonators.

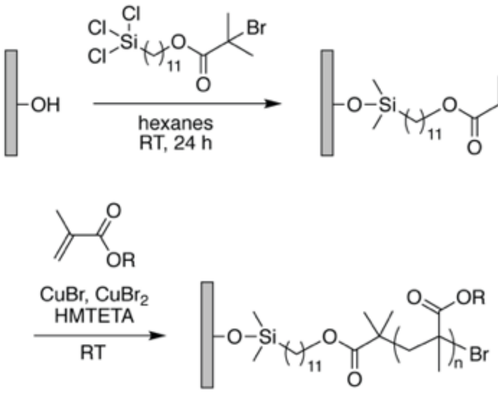

3.2.2 Polymer brush swell and collapse behavior

It is well known that the pKa of thin polymer brush films can be highly dependent on the polymer brush length and solution conditions.[27] These variations can cause challenges not only in quickly determining pKa for brushes, and thus their potential for swelling or collapse in different conditions, but also suggest that both brush thickness and the location of the primary brush/analyte interface will be important for determining pH-based swelling or collapse behavior in polymer brush systems.The pKa of a brush has also been shown previously to have a dependence on the point of measurement, where pKas measured close to the brush initiator for acidic brushes are higher than pKas measured at the top of the brush.[35]

To explore this effect, shifts in the resonance wavelength can be used to quantify characteristic values for the brush system. For example, PDMAEMA is pH responsive with a pKa of about 7.3 in water.[28] The brush undergoes a transition from swollen to collapsed conformation as the pH of the buffer solution is increased and the side chains are deprotonated (Figure 2a). By monitoring the relative shift in real-time upon exposing the PDMAEMA brush surface to increasingly basic buffer solution cycles, we can observe a sigmoidal pattern to the signal maxima (Figure 2b). This pattern is characteristic of titrations, with the pKa defined as the midpoint of the curve. The change in resonant wavelength as a function of pH can be fitted to the logistic curve:

$$Shift = \frac{Shift_{Min} - Shift_{Max}}{1 + \left(\frac{pH - pH_i}{x_0}\right)^p} \tag{3.2}$$

where Shift is the change in resonant wavelength between a pH 9 carbonate buffer and various other buffer solutions, $\text{Shift}_{\text{Min}}$ is the minimum shift observed, $\text{Shift}_{\text{Max}}$ is the maximum shift observed, p is the power parameter (the steepness of the slope of the linear region of the curve), and x_0 is the midpoint of the curve (i.e. the pKa of the polymer brush near the ring surface).

Shift values from each cycle were chosen from time points three-quarters of the way through each step. By keeping time intervals consistent, the difference in permeability of the differing brush thicknesses can be highlighted (Figure 3.2c and 3.2d). Not only this, speed of the assay was greatly increased, requiring only one and a half hours of analysis compared to the six hours needed when fully letting the brush come to equilibrium.

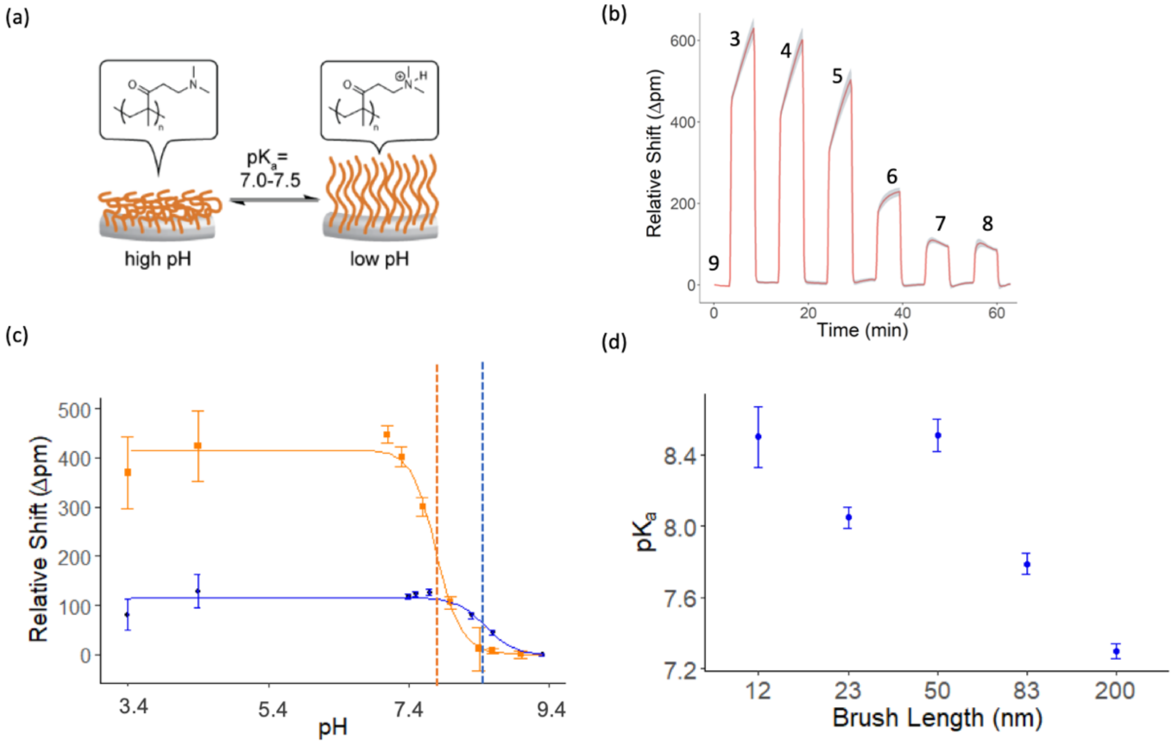

Figure 3.2 (a) Schematic of PDMAEMA polymer brush swelling and collapse. (b) Response of a sample PDMAEMA-coated microrings to carbonate (pH 9), phosphate (pH 6-8), and acetate buffers (pH 3-5).(c) Relative shift of 50 nm (orange), and 12 nm (blue) PDMAEMA-coated microrings in response to changing pH conditions. Sigmoidal curve is a fit of the data to Equation 2. Dashed vertical lines are shown to mark the extracted pKa values. (d) Dependence of pKa on polymer brush thickness shows pKa decreases with increasing brush length.

We used this method to calculate the pKa of four polymer brush thicknesses by fitting the relative wavelength shift to Equation 3.2 (Figure 3.2c). Upon plotting the pKa as a function of brush length, our results demonstrate that as brush thickness increases the pKa of the brush more closely approaches that of the bulk free polymer (Figure 3.2d). As brush thicknesses increases, more and more of the measurement region will be filled with brush interacting with the solid substrate, compared to those free ends at the polymer/liquid interface. The approaching bulk behavior of the brush polymer PDMAEMA is similar to the results found by Dong, Lindau and Ober who determined that measuring close to the substrate/brush interface gave pKas resembling the free bulk pKa for thick brushes.[35] However, Dong, Lindau and Ober did not explore the impact this had on different brush thicknesses, using brush thicknesses on the order of 60 nm and also only explored acidic brushes, which swell upon being deprotonated. We see a similar pattern being demonstrated for our basic PDMAEMA brush, and can also clearly see from our data that brush thickness does have an effect on the apparent pKa bulk value as predicted, where thinner brushes have a higher pKa than thicker brushes.[35] The difference in surface pKa compared to bulk pKa suggests that brushes could cause a spatial charge gradient in certain pH conditions, which could be extremely important for drug delivery applications relying on nanoparticle charge for targeting and drug release.

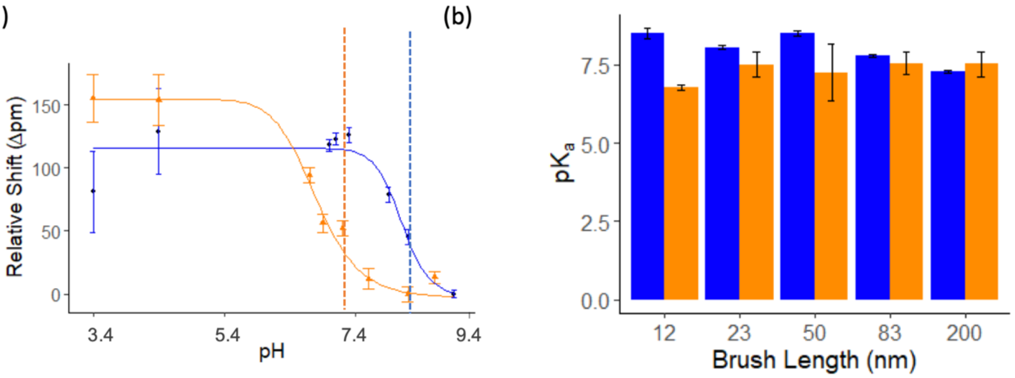

Figure 3.3 (a) Relative shift of thin (12 nm, orange lines) and thick (200 nm, blue lines) PDMAEMA-coated microrings in response to changing pH in low (0.3 M, circle) and high (1.3 M, triangle) salt conditions. Sigmoidal curve is a fit of the data to Equation 2. (b) Thin brushes are observed to have a large pKa sensitivity to salt concentration while thick brushes show less dependence. Low salt concentration (0.3 M) is blue while high salt concentration (1.3 M) is in orange.

Likewise, this method can be used to scan the impact of different analyte conditions on swelling and collapse behaviors. By measuring relative shift of collapse in different salt concentrations, we observed that there is a large difference in both the maximum shift and pKa for thin brushes. However, there seems to be no sensitivity to salt concentration in thicker brushes (Figure 3.3a). Upon extracting pKa values, we observe that this trend holds upon screening five different brush thicknesses (Figure 3.3b). This is likely because the thicker brushes are more similar to bulk materials and block the surface from the changing conditions, causing less of the salt to be able to reach the most sensitive part of the chip's sensing region. In thinner brushes, the salt is more able to penetrate to the surface, meaning it has more impact on the determined pK_a. Additionally, a thicker brush has the potential for more areas of water isolated from the bulk solvent, meaning less NaCl transfer.[29] However, in low salt conditions, there is also the possibility of cooperative action between thicker brushes, leading to faster diffusion of the analyte into the brush, which could be an alternative explanation for why the thicker brushes resemble more bulk conditions (Figure 3.3b).[30] The impact of salt content on polymer brush pKa, and thus polymer brush swelling/collapse, only reinforces the importance of ionic strength controlled experiments when relying on pH-based performance.

Microring resonators quickly provide a platform for determining optimum ionic strength content for an application of interest, either to maximize or minimize swelling in a certain pH range. This could be particularly important for nanoparticle drug delivery development, as the microring resonators allow rapid determination of characteristic swelling of polymer brushes. Not only this, but the spatially arrayed possibility of the microring resonators could allow multiple conditions, such as brush thickness or co-polymer brush composition, to be tested simultaneously and rapidly for optimal conditions in whatever analyte solvents are being used in a particular application, like serum, sea water or organic solvents.

3.2.3 Analyte partitioning between solvent and polymer brush

Additionally, several constants can be extracted from the resonant frequency shift as an analyte partitions into the polymer brush from the bulk solvent. Previously, partitioning of analytes into polymer brushes was observed and taken advantage of to enhance the concentration-dependent signal of small organic molecules on silicon photonic microring resonators.[21] In this work, determining the partition coefficient (the ratio of the analyte concentration between the brush and bulk solvent) would allow for more quantifiable comparisons between brush-analyte systems and thus a better understanding of coating capabilities. For example, a comparison could be made between the affinity of various plasticizers to different coatings which would influence the coating effectiveness. Or, if using a protective coating for long-term functionality, such as anti-oxidation, the ability to determine which brush would have minimal partitioning of an undesired compound would allow prediction of coating lifetimes. Partitioning coefficient determination would also be useful for the development of non-protective coatings, like PEM membranes, to promote best fuel storage capabilities. Alternatively, knowledge about analyte partitioning is useful for the characterization of membrane technologies as solubility (and thus partitioning) of an analyte into the membrane will cause faster transport through the membrane.

To demonstrate this concept in our system, the responses of hydrophobic (PMMA), hydrophilic (PHEMA), and pH-responsive brushes (PDMAEMA) were monitored in real-time upon exposure to two common plasticizers (NB and THF). The resonant signal of the brush-coated microring was observed in water and then the signal was tracked until equilibrium was reached with the desired analyte/water system (Figure 3.4a). Upon monitoring the partitioning of analyte into the brush, the resonant wavelength shift as a function of time was fit to a Langmuir binding isotherm derived by Sothivelr et al. for analyzing molecular partitioning into a thin film:[31]

$$Shift = B - Ae^{\frac{-t}{T}} \tag{3.3}$$

with

$$B = PC_{amb}(t) \tag{3.4}$$

where shift is the given shift at any time point t, $\text{Shift}_{\text{Max}}$ is the maximum observed shift, observed at equilibrium, T is the response time for a given analyte-coating combination, $C_{amb}(t)$ is the ambient concentration of the analyte, A is a constant and P is the brush-solvent partitioning coefficient. Note that in using this equation, it is not only assumed that there is a constant value for the analyte concentration in the bulk, due to replenishing flow, but also that the only cause of the change being measured is due to single analyte partitioning, rather than due to conformational changes or partitioning of multiple analytes. The value of the partitioning coefficient can be found by fitting relative shift as a function of time to the above equation, leaving P and T as variable parameters (Figure 3.4b).

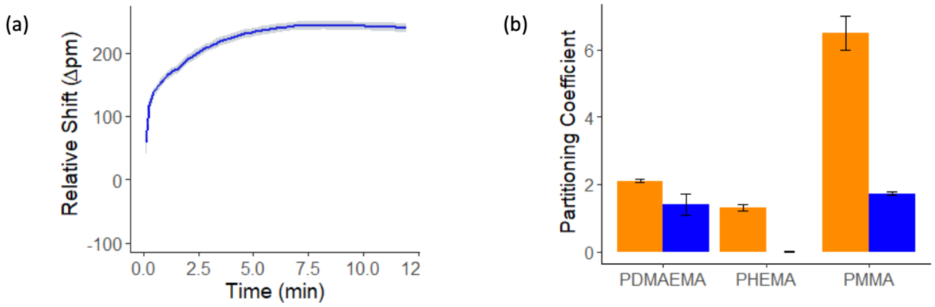

Figure 3.4 (a) The relative shift of a 40 nm PMMA-coated microring as the analyte is changed from water to 1 mM THF in water is fit to Equation 3 (a langmuir binding isotherm) to extract partitioning coefficients. (b) A summary of the partitioning coefficient from various 40 nm polymer brush/analyte combinations, where the analyte is diluted to 1 mM concentration in water. Orange is nitrobenzene and blue is THF.

Recall that the higher the partitioning coefficient, the more likely an analyte is to partition into the polymer brush compared to remaining in the external aqueous environment. All calculated partitioning coefficients were greater than zero, as organic molecules, even if polar, have more favorable energetics in the semi-organic polymer brush than in the aqueous phase due to various factors such as the unfavorable interactions between water and organic molecules. First, the partitioning coefficient of nitrobenzene into PMMA is much higher than into PDMAEMA and PHEMA. This is logical because nitrobenzene, which though a polar analyte overall, has a large aromatic moiety, and thus would preferentially partition into a more nonpolar matrix, compared to the more polar PDMAEMA and PHEMA matrices. Comparatively, THF is a more polar analyte than nitrobenzene, resulting in its lower partitioning coefficient into nonpolar PMMA. It is notable that the partitioning coefficient for THF into PMMA and PDMAEMA are about equal, while the coefficient for THF into PHEMA is approximately zero. This tracks well with a decreasing solubility of PMMA, PDMAEMA, and PHEMA in THF (SI Table 1). Although these values are not directly reported in the literature, this trend could potentially be due to the capability of PHEMA to only form only one hydrogen bond. When compared to the 3.5 formed by water, THF is likely to remain solubilized in the solvent phase rather than the brush. Comparatively, PDMAEMA offers the ability to form multiple hydrogen bonds, and PMMA provides a more hydrophobic environment than water which would encourage THF solubility.[33]

3.2.4 Diffusion coefficient dependence on brush length

Diffusion coefficients are the established method to compare mobility between various brush-analyte systems as they describe the speed in which an analyte moves through a polymer brush. Traditionally, fluorescence techniques are used to calculate diffusion coefficients of a desired type of molecule in polymer brush films. For example, fluorescence recovery after photobleaching (FRAP) analyzes the recovery curve of a photobleached fluorescent probe, fluorescence correlation spectroscopy (FCS) examines the correlations of fluctuating fluorescent probes as they move in and out of a specified area, and single particle tracking (SPT) calculates trajectories from the visualization of individual fluorescent molecules.[34] Basic equations derived from Fick's law can additionally be used to quantify diffusion in thin films upon making fundamental assumptions about the system, such as a plane sheet confinement or membrane behavior (where diffusion coefficients are a function of concentration or mass ratios), and the reaction conditions, including diffusion and the presence of convection.[35] Although these well-established methods provide an accurate means of measuring diffusion coefficients, our platform can determine multiple constants from one sample measurement, thus greatly increasing the information that can be gained from one experiment. Additionally, brush-modified microring resonators do not require fluorescent probes or chemical modifications, allowing for the most direct analysis of the system of interest.

In our system, we monitored the relative shift of 10, 50, and 200 nm PDMAEMA brushes in real-time upon exposure to a pH 8 phosphate buffer (Figure 5a). This data was first normalized in order to correctly compare systems which have differential partitioning (and thus different relative shift values at equilibrium). Then, it can be observed that thin brushes equilibrate quickly (≈1 min) while thicker brushes take much longer (>5 min). The normalized shift was fit to the exponential decay expression, based off of a Langmuir binding isotherm:[36]

$$\frac{Shift}{Shift_0} = 1 - e^{-\Gamma t} \qquad 3.5$$

which allowed the real-time data to be fit to find the decay rate Γ. A diffusivity equation commonly used in evanescent wave light scattering studies was adapted to allow the determination of the diffusivity from the decay rate:[37]

$$\langle D \rangle = \frac{\Gamma}{q^2 + \Xi^{-2}} \qquad 3.6$$

where <D> is the average molecular diffusivity (diffusion coefficient), Γ is the decay rate from Equation 5, q is a constant dependent on the difference in angle between the incident light and measured light and Ξ is the penetration of the evanescent field. Both q and Ξ are constant for the microring resonator system (see Section 3.4 for more information) as both the detector and laser are immobilized.

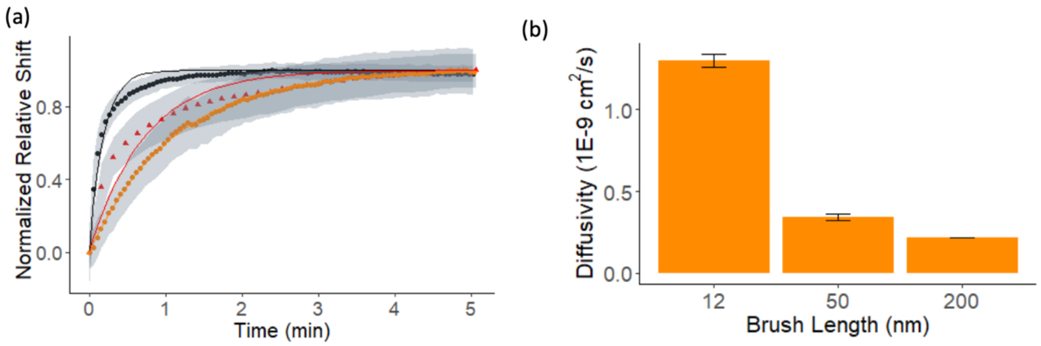

Figure 3.5 (a) The relative shift of PDMAEMA-coated microrings at 12 (black), 50 (red), and 200 nm (orange) thicknesses as the analyte is changed from 0.1 M carbonate buffer (pH 9) to 0.1 M phosphate buffer (pH 8). Data is represented as points, fitting is represented in solid lines with error as shading. (b) A summary of the extracted diffusion coefficients showing that diffusion becomes slower with increasing polymer brush thickness.

From the decay rate, diffusion coefficients of phosphate into PDMAEMA are calculated to vary between 1.3x10^{-9}, 2.2x10^{-10} cm^2/s, and 0.13-0.022 μm^2/s depending on the brush thickness (Figure 6.5b). This finding shows a clear dependence on polymer brush length: the longer the polymer brush, the smaller the coefficient. The observed trends are consistent with a variety of fluorescence correlation spectroscopy studies, as well as single molecule tracking experiments. Thicker brushes are more likely to hinder the motion of the phosphate buffer due to entanglement, which could block particle motion. Additionally, longer polymer brushes are likely to have more heterogeneity, leading to differential interactions throughout the brush and slower overall ensemble diffusion measurements.[38] These values are in good agreement with single molecule studies of ionic probes in polyelectrolyte systems, such as the dye rhodamine 66G through PSS polymer brushes as performed by Landes and co-workers which found diffusivities varying between 0.05-1 um^2/s in 50 nm brushes.[39] Other studies of polar dyes, such as sulforhodamine B, on PSSNa brushes have found similar diffusivities.[40]

It is particularly interesting that there is such good agreement between results considering the difference in size between the probes of interest. While phosphate is an ionic buffer and PDMAEMA does have the potential to be a polyelectrolyte polymer brush, phosphate is significantly smaller than rhodamine 6G and sulforhodamine B. However, phosphate is more highly charged than either dye, which suggests that the diffusivity of a molecule depends strongly on both hydrophobic interactions and charge state, contrary to what has been suggested by Zhang et al.[35] Perhaps the impact of charge state for phosphate could be particularly strong because of its polyionic nature, making charge state more important than when looking at shielding of a monoionic dye by salt. It is also important to note that, like the previously listed measurements, the measurements presented in this manuscript are ensemble diffusivity measurements. Individual diffusivity measurements in polymer brushes have been shown to cluster around a slow or a fast diffusion, which would not be observable on a microring resonator system.[41]

3.2.5 Effect of brush thickness on permeability.

Permeability refers to the ability of an analyte to diffuse through a material. Quantifying and comparing permeability is important for developing polymer systems that are commercially relevant for a wide range of applications including coatings, controlled drug release, plastics packaging, membranes, and composite materials.[42] However, unlike polymers in bulk, the confined nature of high grafting density surface-initiated films often leads to differences in polymer properties such as refractive index,[43] glass transition temperature,[44] and hydrophobicity,[45] which can change between thicknesses or even as a function of depth within a single thickness. Although many works acknowledge or even take advantage of the limited penetration of small molecules or oligomers through dense films,[46] those that characterize these effects focus on brush conformation rather than permeability.[47] Thus, there remains a need for development of accessible platforms to quantify transport abilities of an analyte through dense polymer brush films.

To probe differences in permeability through dense brushes, we are considering transport from the brush/solvent interface down to the microring sensor surface as a function of the thickness of separate samples. When PMMA is exposed to an analyte from baseline solvent, we observe that the relative shift approaches zero as the thickness of a polymer brush increases (Figure 3.6a). This suggests that there is a certain thickness at which the analyte can no longer reach the sensing region as the resonant wavelength before and after introducing the analyte are the same. Thus, we define the brush thickness at which the analyte is no longer permeable to the sensor surface as critical thickness.[48] An equation[49] used to define the penetration of the evanescent field in the microring resonator was adapted to determine the critical thickness from the decreasing exponential curve:

$$Shift = Shift_{max} e^{-\frac{x}{d} ln(r)} - Shift_{min} \tag{3.7}$$

where shift is the shift caused by an analyte for a given brush, $Shift_{Max}$ is the maximum shift observed to be caused by the analyte, $Shift_{Min}$ is the minimum shift observed to be caused by the analyte, x is the dry brush thickness, r is the ratio of the minimum and maximum shifts, and d is the critical thickness. It can be assumed that these effects are not due to evanescent decay because the analyte signal enhancement is first large and then decreases rather than increasing and plateauing as a function of distance away from the sensor.

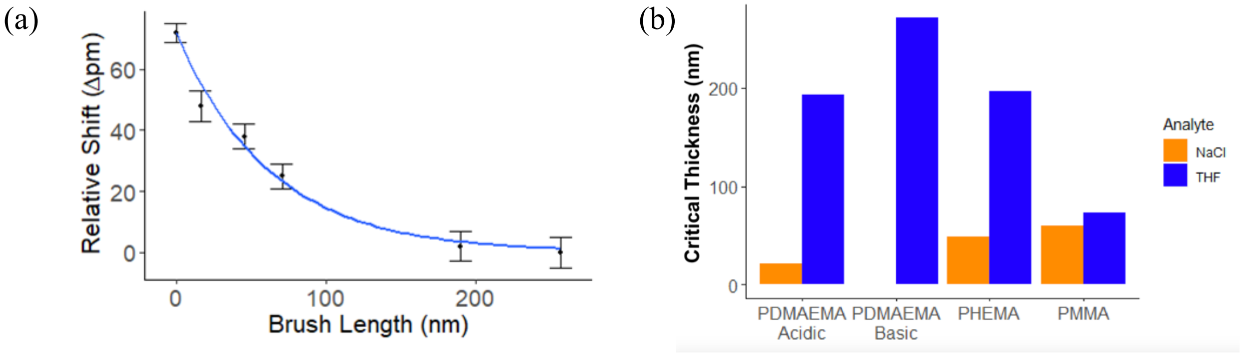

Figure 3.6 (a) Relative shift of a PDMAEMA-coated microring from 5% THF in water to 5% d8-THF in water in response to changing dry polymer brush thickness fit to Equation 7 (b) A summary of the critical thicknesses from various polymer/analyte combinations. THF permeability was calculated from difference in the shift between 5% THF and 5% d8-THF in water, whereas NaCl permeability was calculated from a difference in the shift between water/buffer and 100 mM NaCl. pH 9 is a carbonate buffer, pH 3 is an acetate buffer.

To verify this effect, PDMAEMA, PHEMA and PMMA polymer brushes were tested in combination with THF or NaCl analytes. THF measurements were defined by the shift between 5% THF in water and 5% d8-THF in water. Deuteration was used in order to change the refractive index of the analyte of interest, without changing any crucial intermolecular forces such as hydrogen bonding. For NaCl, measurements were defined by the shift between water and 100 mM NaCl, as the only pertinent force would be ionic strength. PDMAEMA was tested with the analytes in pH 9 or 3 buffer such that the brush will only be measured in either completely collapsed or swollen form. All measurements were found to follow this same trend and critical thicknesses were calculated based on Equation 3.7 (Figure 3.6b). We see that acidic PDMAEMA brushes have a lower critical thickness when compared to basic PDMAEMA, meaning that THF transport is restricted at thinner brush lengths. This can be explained by the unfavorability of the organic THF molecule interactions with the charged state of acidic PDMAEMA. Conversely, acidic PDMAEMA has a much larger critical thickness for NaCl than basic PDMAEMA by similar reasoning. However, it is interesting to observe that PMMA has a smaller critical thickness when exposed to THF compared to PDMAEMA and PHEMA, despite its solubility in bulk polymer and our results when calculating partitioning coefficients. Additionally, the relative permeability of NaCl in PDMAEMA, even in its swollen form, is lower than the relative permeability of NaCl in PMMA and PHEMA despite its charged state. It is likely that these inconsistencies result from differences in the behavior and properties as dense films when compared to their bulk polymer counterparts. For example, the confined nature of PMMA brushes near the sensor surface could due to the formation of forced crystalline morphologies that restrict analyte permeability in ways that do not occur with the other brushes.[50] The interplay of these competing factors of intra- and inter-brush interactions are hard to predict, thus demonstrating the importance of techniques that directly measure the performance of brush systems as they interact with specific analytes.

3.2.6 Probing changes in polymer brush properties

Our previous systems all showed exponential fall-off of signal with increasing brush length. For example, when PMMA is tested with three different pH buffer solutions, these curves still show consistent behaviors (Figure 3.7a). Here, the exponent and amplitude of the fit change slightly but the extracted critical thicknesses values remain similar. This can be rationalized by considering how the hydrophobic nature of this brush does not change in response to pH while the extent of relative attraction between the brush and individual buffer components (and thus partitioning behavior and diffusion speed) may differ slightly for each case. Interestingly, we did observe that not all systems behave in this way.

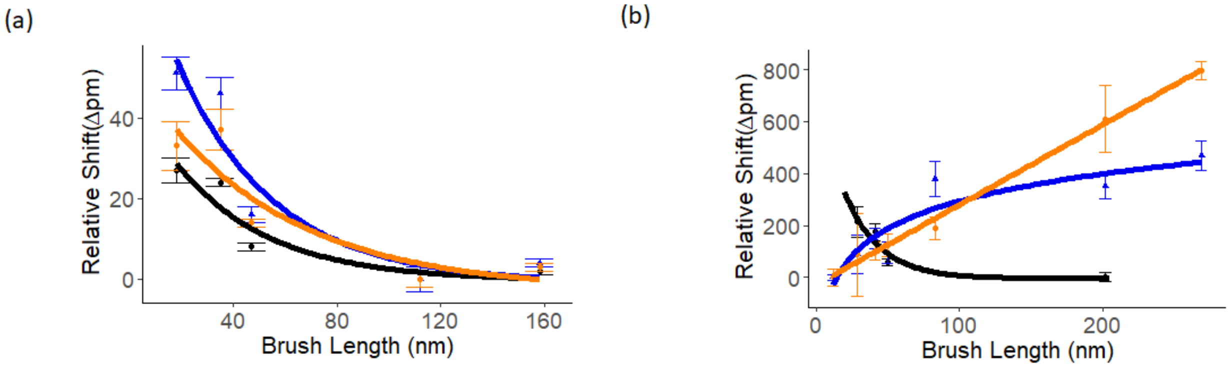

Figure 3.7 Relationship of brush length to relative shift when transitioning from pH9 to pH8 (black), pH7 (blue), and pH 3 (orange). (a) PMMA brushes show similar shifts to each other regardless of pH. (b) PDMAEMA brushes show differing shift relationships as the pH changes.

In our previous testing, acidic and basic PDMAEMA was found to be behave consistently when interacting with NaCl and THF analytes. However, when we expose this same brush to acidic, neutral, and basic buffers, we find that the curve shape changes significantly (Figure 7b). The response to pH 8 decreases exponentially and thus shows critical thickness behavior. However, the response to pH 7 increases logarithmically and response to pH 3 is linear. Because acidic PDMAEMA is known to be swollen and hydrophilic while basic PDMAEMA is collapsed and hydrophobic, it is likely that there are multiple competing factors influencing these response profiles. Changes in brush conformation from swollen to collapsed form can lead to increasing refractive index as the polymer matrix becomes denser. Additionally, the change in hydrophobicity and density will influence the partitioning coefficient of the analyte in the brush as well of the amount of solvent dissolved at a given time.

3.3 Conclusions

We have demonstrated the utility of silicon photonic microring resonators as a platform for the in-situ characterization of polymer brush surfaces. Well-defined hydrophilic, hydrophobic, and stimuli-responsive polymer brushes were grown from the resonator surface. This allowed for the direct observation and quantification of the characteristics of specific brush-solvent-analyte systems, such as: diffusion and partitioning coefficients, critical thickness, hydrophobicity, and pK_a. Many of these constants can be extracted from the same set of data, greatly increasing the amount of information gained during each experiment. Additionally, the surface sensitive nature of our detection platform provides a good complement to brush-liquid interface sensitive techniques, such as goniometry. Microring resonators spatial independence allows for spatial multiplexing of brush types, and in future work, should allow for fast combinatorial screening of analyte-brush systems in a multiplexed fashion.

3.4 Experimental section

3.4.1 Materials

2-hydroxethyl methacrylate (HEMA), 2-(dimethylamino)ethyl methacrylate (DMAEMA), methyl methacrylate (MMA), copper (II) bromide, copper (I) bromide, 1,1,4,7,10,10-hexamethyltriethylenetetramine (HMTETA), nitrobenzene (NB), tetrahydrofuran (THF), and inhibitor removers were purchased from Sigma-Aldrich. Inhibitor was removed from each monomer by passing it through a column of inhibitor removers. The initiator [11-(2-bromo-2-methyl)propionyloxy]undecyltrichlorosilane (BPOTS) was purchased from Gelest. pH 10 buffer solution was made from sodium phosphate and sodium phosphate monobasic. pH 9 buffer solution was made from sodium bicarbonate and sodium carbonate. pH 8 and pH 7 buffer solutions were made from sodium phosphate monobasic and sodium phosphate dibasic. pH 4 and pH 3 buffer solutions were made from acetic acid and sodium acetate. pH adjustments were made using 1 M NaOH and 1 M HCl until the pH measured of the solution was within 0.1 of the reported solution. Ionic strength of the pH 9, pH 8, pH 7, pH 4 and pH 3 solutions was adjusted to 0.18 M using sodium chloride. All other chemicals were obtained from Sigma-Aldrich and were used as received.

3.4.2 Monolayer self-assembly

A monolayer was formed using self-assembly of a free radical initiator on microring resonator chips and silicon wafers (cut in pieces of 2 cm x 1 cm) simultaneously. Substrates were cleaned using acetone and isopropanol, activated using oxygen plasma for 3 minutes (150 W, March Plasmod GCM-200) and then exposed to a 1 mM solution of BPOTS initiator in anhydrous hexanes at room temperature under argon. After 12 h, the substrates were removed from the reaction mixture and sonicated in hexanes, ethanol, and water. They were dried in a nitrogen stream and used immediately.

3.4.3 Surface-initiated atom transfer radical polymerization (SI-ATRP)

Following the procedures similar to those pioneered by the Matyjaszewski group,[25] the substrates were placed in a reaction vessel and purged with argon. Monomer (500 mmol, 300 equiv) was diluted with solvent to make a 5 M solution and degassed for 15 min in a separate Schlenk flask. HMTETA (544 µl, 2 mmol, 1.2 equiv), CuBr (240 mg, 1.67 mmol, 1 equiv), and $CuBr_2$ (75 mg, 0.33 mmol, 0.2 equiv) were added to the monomer solution under positive argon flow. The flask was then sealed and the mixture was transferred to the reaction vessel containing the substrates. After the appropriate amount of time, substrates were removed and sonicated in tetrahydrofuran, ethanol, and water, then dried in a nitrogen stream.

3.4.4 Ellipsometry

Control wafer film thickness was determined using spectroscopic ellipsometry (VASE, J.A. Wollam Co.) and analyzed by WVASE software using a three-layer model. The ellipsometric parameters (Ψ, Δ) were measured at three angles of incidence (65°, 70°, 75°) and from 400 nm to 800 nm. Software-supplied refractive indices were used for silicon (substrate) and silicon dioxide (empirically determined to be 2.3 nm). Then, data was fit to a Cauchy layer model, with fixed (A_n, B_n) values of (1.45, 00.1) and no optical absorption to determine dry polymer brush thickness.

3.4.5 Silicon photonic microring resonators

Design of the microring resonator array chips and operation of the instrumentation has been previously described.[49] Microring resonator sensor chips and the Maverick M1 optical scanning instrumentation were purchased from Genalyte, Inc. (San Diego, CA). The chip was functionalized (see above) and then covered with a Mylar gasket and Teflon lid to direct solution into two flow channels. Solutions were flown over the chip using peristaltic pumps at 20 μL/min for various lengths of time (as described below) while the chip was interrogated using a wavelength-tunable laser centered at 1550 nm, sweeping over a 12 nm spectral range. The change in resonant wavelength (Δpm) was measured in real-time. The evanescent field from the microring resonator falls-off exponentially from the microring surface, providing an active sensing range within 100 nm of the resonator surface.[45]

3.4.6 Data analysis

Data analysis was performed using R and software provided by Genalyte, Inc. Sensor traces were corrected for temperature fluctuations and response was averaged over clusters, or groups of 4 microrings. One cluster of rings, with a response similar to the average response over the 128 rings, was chosen for further analysis to minimize standard deviation potentially caused by brush defects. Shift measurements were taken at specific time points ~3/4 of the way into the analyte step, in order to provide time for equilibration. Differences in shift were determined by subtracting the analyte step and the preceding solvent step, unless otherwise noted. All curve fittings were performed in R using a non-linear least squares fitting.

3.5 References

1. For lead polymer brush reviews, see: (a) Zoppe, J. O.; Ataman, N. C.; Mocny, P.; Wang, J.; Moraes, J.; Klok, H.-A. Surface-Initiated Controlled Radical Polymerization: State-of-the-Art, Opportunities, and Challenges in Surface and Interface Engineering with Polymer Brushes. *Chem. Rev.* **2017**, *117 (3)*, 1105−1318. (b) Zhao, B.; Brittain, W. J. Polymer brushes: surface-immobilized macromolecules. *Prog. Polym. Sci.* **2000**, *25 (5)*, 677−710. (c) Azzaroni, O. Polymer brushes here, there, and everywhere: Recent advances in their practical applications and emerging opportunities in multiple research fields. *J. Polym. Sci. A* **2012**, *50 (16)*, 3225−3258. (d) Banerjee, S.; Paira, T. K.; Tarun K. Mandal, T. K. Surface confined atom transfer radical polymerization: access to custom library of polymer-based hybrid materials for speciality applications. *Polym. Chem.* **2014**, 5 (14), 4153−4167. (e) Chen, W.-L.; Cordero, R.; Tran, H.; Ober, C. K. 50th Anniversary Perspective: Polymer Brushes: Novel Surfaces for Future Materials. *Macromolecules*, **2017**, *50 (11)*, 4089−4113.
2. (a) Raynor, J. E.; Capadona, J. R.; Collard, D. M.; Petrie, T. A.; García, A. J. Polymer brushes and self-assembled monolayers: Versatile platforms to control cell adhesion to biomaterials (Review). *Biointerphases*, **2009**, *4 (2)*, FA3−FA16. (b) Ayres, N. Polymer brushes: Applications in biomaterials and nanotechnology. *Polym. Chem.* **2010**, *1 (6)*, 769−777. (c) Fristrup, C. J.; Jankova, K.; Hvilsted, S. Surface-initiated atom transfer radical polymerization—a technique to develop biofunctional coatings. *Soft Matter* **2009**, *5 (23)*, 4623−4634. (d) Krishnamoorthy, M.; Hakobyan, S.; Ramstedt, M.; Gautrot, J. E. Surface-Initiated Polymer Brushes in the Biomedical Field: Applications in Membrane Science, Biosensing, Cell Culture, Regenerative Medicine and Antibacterial Coatings. *Chem. Rev.* **2014**, *114 (21)*, 10976−11026. (e) Jiang, H.; Xu, F.-J. Biomolecule-functionalized polymer brushes. *Chem. Soc. Rev.* **2013**, *42 (8)*, 3394−3426. (f) Xuab, F. J.; Neoh, K. G.; Kang, E. T. Bioactive surfaces and biomaterials via atom transfer radical polymerization. *Prog. Polym. Sci.* **2009**, *34 (8)*, 719−761. (g) Hucknall. A.; Rangarajan, S.; Chilkoti, A. In Pursuit of Zero: Polymer Brushes that Resist the Adsorption of Proteins. *Adv. Mater.* **2009**, 21 (23), 2441−2446.
3. (a) Chen, H.; Zhao, C.; Zhang, M.; Chen, Q.; Ma, J.; Zheng, J. Molecular Understanding and Structural-Based Design of Polyacrylamides and Polyacrylates as Antifouling Materials. *Langmuir*, **2016**, *32 (14)*, 3315−3330. (b) Gunkel, G.; Weinhart, M.; Becherer, T.; Haag, R.;

Huck, W. T. S. Effect of Polymer Brush Architecture on Antibiofouling Properties. *Biomacromolecules* **2011**, *12 (11)*, 4169−4172. (c) Krishnan, S.; Weinman, C. J.; Ober, C. K. Advances in polymers for anti-biofouling surfaces. *J. Mater. Chem.* **2008**, *18 (29)*, 3405−3413. (d) Stuart, M. A. C.; Huck, W. T. S.; Genzer, J.; Müller, M.; Ober, C.; Stamm, M.; Sukhorukov, G. B.; Szleifer, I.; Tsukruk, V. V.; Urban, M.; Winnik, F.; Zauscher, S.; Luzinov, I.; Minko, S. Emerging applications of stimuli-responsive polymer materials. *Nat. Mater.* **2010**, *9 (2)*, 101−113. (e) Yang, W. J.; Neoh, K.-G.; Kang, E.T.; Teo, S. L.-M.; Rittschof, D. Polymer brush coatings for combating marine biofouling. *Prog. Polym. Sci.* **2014**, *39 (5)*, 1017−1042.

4. Keating, J. J., IV; Imbrogno, J.; Belfort, G. Polymer Brushes for Membrane Separations: A Review. *ACS Appl. Mater. Interfaces* **2016**, *8* (42), 28383−28399.
5. (a) Hui, C. M.; Pietrasik, J.; Schmitt, M.; Mahoney, C.; Choi, J.; Bockstaller, M. R.; Matyjaszewski, K. Surface-Initiated Polymerization as an Enabling Tool for Multifunctional (Nano-)Engineered Hybrid Materials. *Chem. Mater.* **2014**, *26 (1)*, 745–762. (b) Lin, X.; He, Q.; Li. J. Complex polymer brush gradients based on nanolithography and surface-initiated polymerization. *Chem. Soc. Rev.* **2012**, *41(9)*, 3584−3593.
6. (a) Sun, W.; Zhou, S.; You, B.; Wu, L. Polymer Brush-Functionalized Surfaces with Reversible, Precisely Controllable Two-Way Responsive Wettability. *Macromolecules* **2013**, *46(17)*, 7018−7026. (b) Kobayashi, M.; Terayama, Y.; Yamaguchi, H.; Terada, M.; Murakami, D.; Ishihara, K.; Takahara, A. Wettability and Antifouling Behavior on the Surfaces of Superhydrophilic Polymer Brushes. *Langmuir* **2012**, *28(18)*, 7212−7222.
7. (a) Harrak, A. E.; Carrot, G.; Oberdisse, J.; Eychenne-Baron, C.; Boué, F. Surface−Atom Transfer Radical Polymerization from Silica Nanoparticles with Controlled Colloidal Stability. *Macromolecules* **2004**, *37(17)*, 6376−6384. (b) Ohno, K.; Morinaga, T.; Koh, K.; Tsujii, Y.; Fukuda, T. Synthesis of Monodisperse Silica Particles Coated with Well-Defined, High-Density Polymer Brushes by Surface-Initiated Atom Transfer Radical Polymerization. *Macromolecules* **2005**, *38(6)*, 2137−2142.
8. (a) Skale, S.; Doleček, V.; Slemnik, M. Substitution of the constant phase element by Warburg impedance for protective coatings. *Corros. Sci.* **2007**, 49(3), 1045−1055. (b) Paul, D. R.; Kemp, D. R. The diffusion time lag in polymer membranes containing adsorptive fillers. *Polym. Sci.: Polym. Symp.* **1973**, *41(1)*, 79−93. (c) Xu, Q.; Zhang, K.; Jiang, J. Molecular

Simulation and Analysis of Sorption Process toward Theoretical Prediction for Liquid Permeation through Membranes. *J. Phys. Chem. B* **2018**, *122(50)*, 12211−12218.

9. Wang, S.; Jing, B.;Zhu,Y. Molecule Motion at Polymer Brush Interfaces from Single-Molecule Experimental Perspectives. *Journal of Polymer Science, Part B: Polymer Physics*. **2014**, 52, 85-103.
10. Barbey, R.; Lavanant, L.; Paripovic, D.; Schüwer, N.; Sugnaux, C.; Tugulu, S.; Klok, H.-A. Polymer Brushes via Surface-Initiated Controlled Radical Polymerization: Synthesis, Characterization, Properties, and Applications. Chem. Rev., 2009, 109 (11), pp 5437−5527.
11. (a) Lego, B.; Skene, W. G.; Giasson, S. Swelling Study of Responsive Polyelectrolyte Brushes Grafted from Mica Substrates: Effect of pH, Salt, and Grafting Density. *Macromolecules* **2010**, *43 (9)*, 4384−4393. (b) Parnell, A. J.; Martin, S. J.; Jones, R. A. L.; Vasilev, C.; Crook, C. J.; Ryan, A. J. Direct visualization of the real time swelling and collapse of a poly(methacrylic acid) brush using atomic force microscopy. *Soft Matter* **2009**, *5 (2)*, 296−299. (c) Valiaev, A.; Abu-Lail, N. I.; Lim, D. W.; Chilkoti, A.; Zauscher, S. Microcantilever Sensing and Actuation with End-Grafted Stimulus-Responsive Elastin-Like Polypeptides. *Langmuir* **2007**, *23 (1)*, 339−344.
12. Barbey, R.; Laporte, V.; Alnabulsi, S.; Klok, H.-A. Postpolymerization Modification of Poly(glycidyl methacrylate) Brushes: An XPS Depth-Profiling Study. *Macromolecules* **2013**, *46 (15)*, 6151−6158.
13. (a) Schüwer, N.; Geue, T.; Hinestrosa, J. P.; Klok, H.-A. Neutron Reflectivity Study on the Postpolymerization Modification of Poly(2-hydroxyethyl methacrylate) Brushes. *Macromolecules* **2011**, *44 (17)*, 6868−6874. (b) Sanjuan, S.; Perrin, P.; Pantoustier, N.; Tran, Y. Synthesis and Swelling Behavior of pH-Responsive Polybase Brushes. *Langmuir* **2007**, *23 (10)*, 5769−5778.
14. (a) Fielding, L. A.; Edmondson, S.; Armesa, S. P. Synthesis of pH-responsive tertiary amine methacrylate polymer brushes and their response to acidic vapour. *J. Mater. Chem.* **2011**, *21 (32)*, 11773−11780. (b) Willott, J. D.; Murdoch, T. J.; Humphreys, B. A.; Edmondson, S.; Webber, G. B.; Wanless, E. J. Critical Salt Effects in the Swelling Behavior of a Weak Polybasic Brush. *Langmuir* **2014**, *30 (7)*, pp 1827−1836. (c) Zhang, H.; Rühe, J. Swelling of Poly(methacrylic acid) Brushes: Influence of Monovalent Salts in the Environment. *Macromolecules* **2005**, *38 (11)*, 4855−4860.

15. (a) Dong, R.; Lindau, M.; Ober, C. K. Dissociation Behavior of Weak Polyelectrolyte Brushes on a Planar Surface. *Langmuir* **2009**, *25 (8)*, 4774−4779. (b) Schuh, C.; Rühe, J. Penetration of Polymer Brushes by Chemical Nonidentical Free Polymers. *Macromolecules* **2011**, *44 (9)*, pp 3502−3510.
16. He, J.; Wu, Y.; Wu, J.; Mao, X.; Fu, L.; Qian, T.; Fang, J.; Xiong, C.; Xie, J.; Ma, H. Study and Application of a Linear Frequency−Thickness Relation for Surface-Initiated Atom Transfer Radical Polymerization in a Quartz Crystal Microbalance. *Macromolecules* **2007**, *40 (9)*, 3090−3096.
17. Du, Y.; Gao, J.; Chen, T.; Zhang, C.; Ji, J.; Xu, Z.-K. Understanding the Oxidative Stability of Antifouling Polymer Brushes. *Langmuir* **2017**, *33 (29)*, 7298−7304.
18. Iqbal, M.; Gleeson, M. A.; Spaugh, B.; Tybor, F.; Gunn, W. G.; Hochberg, M.; Baehr-Jones, T.; Bailey, R. C.; Gunn, L. C. Label-Free Biosensor Arrays Based on Silicon Ring Resonators and High-Speed Optical Scanning Instrumentation. *IEEE J. Sel. Top. Quantum Electron*. **2010**, *10 (3)*, 654−661.
19. Wade, J. H.; Bailey, R. C. Refractive Index-Based Detection of Gradient Elution Liquid Chromatography using Chip-Integrated Microring Resonator Arrays. *Anal. Chem.* **2014**, *86 (1)*, 913−919.
20. Limpoco, F. T.; Bailey, R. C. Real-Time Monitoring of Surface-Initiated Atom Transfer Radical Polymerization Using Silicon Photonic Microring Resonators: Implications for Combinatorial Screening of Polymer Brush Growth Conditions. *J. Am. Chem. Soc.* **2011**, *133 (38)*, 14864−14867.
21. Stanton, A. L. D.; Serrano, K. A.; Braun, P. V.; Bailey, R. C. Polymer Brush-Modified Microring Resonators for Partition-Enhanced Small Molecule Chemical Detection. *Chemistry Select* **2017**, *2 (4)*, 1521−1524.
22. Wade, J. H.; Bailey, R. C. Applications of Optical Microcavity Resonators in Analytical Chemistry. *Annu. Rev. Anal. Chem.* **2016**, 9 (1), 1−25.
23. Luchansky, M. S.; Washburn, A. L.; Martin, T. A.; Iqbal, M.; Gunn, L. C.; Bailey, R. C. Characterization of the evanescent field profile and bound mass sensitivity of a label-free silicon photonic microring resonator biosensing platform. *Biosens. Bioelectron.* **2010**, *26 (4)*, 1283−1291.

24. Narupai, B.; Page, Z. A.; Treat, N. J.; McGrath, A. J.; Pester, C. W.; Discekici, E. H.; Dolinski, N. D.; Meyers, G. F.; de Alaniz, J. R.; Hawker, C. J. Simultaneous Preparation of Multiple Polymer Brushes under Ambient Conditions using Microliter Volumes. *Angew. Chem.* **2018**, *57 (41)*, 13433−13438.
25. Matyjaszewski, K.; Atom Transfer Radical Polymerization (ATRP): Current Status and Future Perspectives. *Macromolecules* **2012**, *45 (10)*, 4015−4039.
26. Xue, C.; Yonet-Tanyeri, N.; Brouette, N.; Sferrazza, M.; Braun, P. V.; Leckband, D. E. Protein Adsorption on Poly(N-isopropylacrylamide) Brushes: Dependence on Grafting Density and Chain Collapse. *Langmuir* **2011**, *27 (14)*, 8810−8818.
27. (a) Xu, Q.; Zhang, K.; Jiang, J. Molecular Simulation and Analysis of Sorption Process toward Theoretical Prediction for Liquid Permeation through Membranes. *J. Phys. Chem. B* **2018**, *122(50)*, 12211−12218. (b) Barbey, R.; Lavanant, L.; Paripovic, D.; Schüwer, N.; Sugnaux, C.; Tugulu, S.; Klok, H.-A. Polymer Brushes via Surface-Initiated Controlled Radical Polymerization: Synthesis, Characterization, Properties, and Applications. Chem. Rev., 2009, 109 (11), pp 5437−5527. (c) Lego, B.; Skene, W. G.; Giasson, S. Swelling Study of Responsive Polyelectrolyte Brushes Grafted from Mica Substrates: Effect of pH, Salt, and Grafting Density. *Macromolecules* **2010**, *43 (9)*, 4384−4393. (d) Parnell, A. J.; Martin, S. J.; Jones, R. A. L.; Vasilev, C.; Crook, C. J.; Ryan, A. J. Direct visualization of the real time swelling and collapse of a poly(methacrylic acid) brush using atomic force microscopy. *Soft Matter* **2009**, *5 (2)*, 296−299. (e) Valiaev, A.; Abu-Lail, N. I.; Lim, D. W.; Chilkoti, A.; Zauscher, S. Microcantilever Sensing and Actuation with End-Grafted Stimulus-Responsive Elastin-Like Polypeptides. *Langmuir* **2007**, *23 (1)*, 339−344. (f) Barbey, R.; Laporte, V.; Alnabulsi, S.; Klok, H.-A. Postpolymerization Modification of Poly(glycidyl methacrylate) Brushes: An XPS Depth-Profiling Study. *Macromolecules* **2013**, *46 (15)*, 6151−6158. (g) Schüwer, N.; Geue, T.; Hinestrosa, J. P.; Klok, H.-A. Neutron Reflectivity Study on the Postpolymerization Modification of Poly(2-hydroxyethyl methacrylate) Brushes. *Macromolecules* **2011**, *44 (17)*, 6868−6874. (h) Sanjuan, S.; Perrin, P.; Pantoustier, N.; Tran, Y. Synthesis and Swelling Behavior of pH-Responsive Polybase Brushes. *Langmuir* **2007**, *23 (10)*, 5769−5778. (i) Fielding, L. A.; Edmondson, S.; Armesa, S. P. Synthesis of pH-responsive tertiary amine methacrylate polymer brushes and their response to acidic vapour. *J. Mater. Chem.* **2011**, *21 (32)*, 11773−11780. (b) Willott, J. D.; Murdoch, T. J.; Humphreys, B. A.; Edmondson, S.;

Webber, G. B.; Wanless, E. J. Critical Salt Effects in the Swelling Behavior of a Weak Polybasic Brush. *Langmuir* **2014**, *30*

28. (a) Zhang, C.; Maric, M. Synthesis of Stimuli-responsive, Water-soluble Poly[2-(dimethylamino)ethyl methacrylate/styrene] Statistical Copolymers by Nitroxide Mediated Polymerization. *Polymers* **2011**, *3 (3)*, 1398−1422. (b) Bütün, V.; Armesa, S. P.; Billingham, N. C. Synthesis and aqueous solution properties of near-monodisperse tertiary amine methacrylate homopolymers and diblock copolymers. *Polymer* **2001**, *42 (14)*, 5993−6008.
29. Nagai, K. et al. Solubility and diffusivity of sodium chloride in phase-separated block copolymers of poly(2-dimethylaminoethyl methacrylate), poly(1,1'-dihydroperfluorooctyl methacrylate) and poly(1,1,2,2-tetrahydroperfluorooctyl acrylate). *Polymer*. **2001**, *42*, 9941-9948.
30. Semenov, A. N.; Anastasiadis, S. H. Collective Dynamics of Polymer Brushes. *Macromolecules* **2000**, *33 (2)*, 613−623.
31. Sothivelr, K.; Bender, F.; Josse, F.; Yaz, E. E.; Ricco, A. J. Obtaining Chemical Selectivity from a Single, Nonselective Sensing Film: Two-Stage Adaptive Estimation Scheme with Multiparameter Measurement to Quantify Mixture Components and Interferents. ACS Sens., 2018, 3 (9), pp 1656−1665.
32. (a) Yazici, D.T., Askin, A., Bütün, V.: J. Chem. Thermodyn.40(2008) 353; (b) van Dyk, J.W.; Frisch, H.L.; Wu, D.T. Solubility, Solvency and Solubility Parameters. *Ind. Eng. Chem. Prod. Res. Dev*. **1985**, *24*, 473-478. (c) Lindvig, T.; Michelsen, M.L.; Kontogeorgis, G.M. A Flory-Huggins model based on the Hansen solubility parameter. *Fluid Phase Equilibra*. **2002**, *203*, 247-260. (d) Padmanabhan, P.; Chavis, M.; Ober, C.K.; Escobedo, F.A. Phase behavior of PMMA-b-PHEMA with solvents methanol and THF: modelling and comparison to the experiment. *Soft Matter*. **2014**, *10*, 6172-6181.
33. Xu, Q.; Zhang, K.; Jiang, J. Molecular Simulation and Analysis of Sorption Process toward Theoretical Prediction for Liquid Permeation through Membranes. *J. Phys. Chem. B* **2018**, *122 (50)*, 12211−12218.
34. For representative work, see: (a) Braeckmans K., Deschout H., Demeester J., De Smedt S.C. (2011) Measuring Molecular Dynamics by FRAP, FCS, and SPT. In: Diaspro A. (eds) Optical Fluorescence Microscopy. Springer, Berlin, Heidelberg. (b) Heitzman, C. E.; Tu, H.; Braun, P. V. Two-Dimensional Diffusion of Prodan on Self-Assembled Monolayers Studied by

Fluorescence Recovery after Photobleaching. *J. Phys. Chem. B* **2004**, *108 (36)*, 13764−13770. (c) Reznik, C.; Darugar, Q.; Wheat, A.; Fulghum, T.; Advincula, R. C.; Landes, C. F. (d) Reznik, C.; Estillore, N.; Advincula, R. C.; Landes, C. F. Single Molecule Spectroscopy Reveals Heterogeneous Transport Mechanisms for Molecular Ions in a Polyelectrolyte Polymer Brush. *J. Phys. Chem. B* **2009**, *113 (44)*, 14611−14618.

35. For representative work, see: (a) Crank, J. Mathematics of Diffusion, 2nd Edn, Oxford University Press, Oxford, 1975. (b) Tsai, T.-H.; Ali, M. A.; Jiang, Z.; Braun, P. V. Dynamic Gradient Directed Molecular Transport and Concentration in Hydrogel Films. *Angew. Chem. Int. Ed.* **2017**, *56 (18)*, 5001-5006. (c) Ali, M. A.; Tsai, T.-H.; Braun, P. V. Amplified Detection of Chemical Warfare Agents Using Two-Dimensional Chemical Potential Gradients. *ACS Omega* **2018**, *3 (11)*, 14665-14670. (d) Xu, Q.; Zhang, K.; Jiang, J. Molecular Simulation and Analysis of Sorption Process toward Theoretical Prediction for Liquid Permeation through Membranes. *J. Phys. Chem. B* **2018**, *122 (50)*, 12211–12218.
36. Filippidi, E.; Michailidou, V.; Loppinet, B.; Rühe, J.; Fytas, G. Brownian Diffusion Close to a Polymer Brush. *Langmuir* **2007**, *23 (9)*, 5139−5142.
37. Filippidi, E.; Michailidou, V.; Loppinet, B.; Rühe, J.; Fytas, G. Brownian Diffusion Close to a Polymer Brush. *Langmuir* **2007**, *23 (9)*, 5139−5142.
38. Wang, S.Q.; Zhu, Y.X. Molecular diffusion on surface tethered polymer layers: coupling of molecular thermal fluctuation and polymer chain dynamics. *Soft Matter.* **2010,** *6,* 4661-4665.
39. Reznik, C.; Estillore, N.; Advincula, R.C.; Landes, C.F. Single Molecule Spectroscopy Reveals Heteogeneous Transport Mechanisms for Molecular Ions in a Polyelectrolyte Polymer Brush. *J. Phys. Chem. B*. **2009**, 113, 14611-14618.
40. Zhang, C.F.; Chu, X.; Zheng, Z.L.; Jia, P.X.; Zhao, J.Diffusion of Ionic Fluorescent Probes atop Polyelectrolyte Brushes. *J. Phys. Chem. B.* **2011**, 115, 15167-15173.
41. Elliott, L.C.C.; Barhoum, M.; Harris, J.M.; Bohn, P.W. Trajectory analysis of single molecules exhibiting non-Brownian motion. *Phys. Chem. Chem. Phys*. **2011**, 13, 4326-4334.
42. Comyn, J. *Introduction to Polymer Permeability and the Mathematics of Diffusion.* Chapman & Hall: Dordrecht, 1985.
43. Xue, C.; Yonet-Tanyeri, N.; Brouette, N.; Sferrazzza, M.; Braun, P. V.; Leckband, D. E. Protein Adsorption on Poly(N-isopropylacrylamide) Brushes: dependence on grafting density and chain collapse. *Langmuir* **2011**, *27 (14)*, 8810-8818.

44. (a) Tate, R. S.; Fryer, D. S.; Pasqualini, S.; Montague, M. F.; de Pablo, J. J.; Nealey, P. F. Extraordinary elevation of the glass transition temperature of thin polymer films grafted to silicon oxide substrates. *J. Chem. Phys.* **2001**, *115*, 9982. (b) Keddie, J. L; Jones, R. A. L.; Corey, R. A. Interface and surface effects on the glass-transition temperature in thin polymer films. *Faraday Discussions*, **1994**, *98*, 219-230. (c) Yamamoto, S.; Tsujii, Y.; Fukuda, T. Glass Transition Temperatures of High-Density Poly(methyl methacrylate) Brushes. *Macromolecules* **2002**, *35 (16)*, 6077-6079.
45. Cheng, N.; Brown, A. A.; Azzaroni, O.; Huck, W. T. S. Thickness-Dependent Properties of Polyzwitterionic Brushes. *Macromolecules* **2008**, *41 (17)*, 6317-6321.
46. (a) de Groot, G. W.; Santonicola, M. G.; Sugihara, K.; Zambelli, T.; Reimhult, E.; Vörös, J.; Vancso, G. J. Switching Transport through Nanopores with pH-Responsive Polymer Brushes for Controlled Ion Permeability. *ACS Appl. Mater. Interfaces* **2013**, *5 (4)*, 1400-1407. (b) Adiga, S. P.; Brenner, D. W. Stimuli-Responsive Polymer Brushes for Flow Control through Nanopores. *J. Funct. Biomater.* **2012**, *3 (2)*, 239-256. (c) Fortin, N.; Klock, H.-A. Glucose Monitoring Using a Polymer Brush Modified Polypropylene Hollow Fiber-based Hydraulic Flow Sensor. *ACS Appl. Mater. Interfaces* **2015**, *7 (8)*, 4631-4640. (d) Park, Y. S.; Ito, Y.; Imanishi, Y. Permeation Control through Porous Membranes Immobilized with Thermosensitive Polymer. *Langmuir*, **1998**, *14 (4)*, 910-914. (e) Lanotte, L.; Guido, S.; Misbah, C.; Peyla, P.; Bureau, L. Flow Reduction in Microchannels Coated with a Polymer Brush. *Langmuir*, **2012**, *28 (38)*, 13758-13764. (e) Castro, R. P.; Cohen, Y.; Monbouquette, H. G. The permeability behavior of polyvinylpyrrolidone-modified porous silica membranes. *J. Membrane Sci.* **1993**, *84 (1-2)*, 151-160. (r) Dhinojwala, A.; Graick, S. Surface Forces in the Tapping Mode: Solvent Permeability and Hydrodynamic Thickness of Adsorbed Polymer Brushes. *Macromolecules*, **1997**, *30 (4)*, 1079-1085. (g) Yang, T.; Li, Z.; Lyu, H.; Zheng, J.; Liu, J.; Liu, F.; Zhang, Z.; Rao, H. A graphene oxide polymer brush based cross-linked nanocomposite proton exchange membrane for direct methanol fuel cells. *RSC Adv.* **2018**, *8*, 15740. (h) Ivkov, R.; Butler, P. D.; Satija, S. K. Effect of Solvent Flow on a Polymer Brush: A Neutron Reflectivity Study of the Brush Height and Chain Density Profile. *Langmuir* **2001**, *17 (10)*, 2999-3005. (i) Binder, K.; Kreer, T.; Milchey, A. Polymer brushes under flow and in other out-of-equilibrium conditions. *Soft Matter* **2011**, *7 (16)*, 7159-7172. (j) Schuh, C.; Ruhe,

J. Penetration of Polymer Brushes by Chemical Nonidentical Free Polymers. *Macromolecules*, **2011**, *44*, 3502-3510.

47. (a) Yim, H.; Kent, M. S.; Satija, S.; Mendez, S.; Balamurugan, S. S.; Balamurugan, S.; Lopez, G. P. Evidence for vertical phase separation in densely grafted, high-molecular-weight poly(N-isopropylacrylamide) brushes in water. *Phys. Rev.* **2005**, *72*, 051801. (b) Baulin, V. A.; Zhulina, E. B.; Halperin, A. Self-consistent field theory of brushes of neutral water-soluble polymers. *J. Phys. Chem.* **2003**, *119*, 10977. (c) Mahalik, J. P.; Sumpter, B. G.; Kumar, R. Vertical Phase Segregation Induced by Dipolar Interactions in Planar Polymer Brushes. *Macromolecules* **2016**, *49 (18)*, 7096-7107.
48. Hwang, S.-T.; Kammermeyer, K. Effect of Thickness on Permeability. In: Hopfenberg, H. B. *Permeability of Plastic Films and Coatings.* Springer: Boston, 1974.
49. M.S. Luchansky, A.L. Washburn, T.A. Martin, M. Iqbal, L.C. Gunn, and R.C. Bailey. Characterization of the Evanescent Field Profile and Bound Mass Sensitivity of a Label-Free Silicon Photonic Microring Resonator Biosensing Platform. *Biosensors & Bioelectronics*, **2010**, *26*, 1283-1291.
50. Zhou, X. D.; Zhang, S. C.; Huebner, W.; Ownby, P. D. Effect of the solvent on the particle morphology of spray dried PMMA. *J. Mater. Sci.* **2001**, *36 (15)*, 3759-3768.

CHAPTER 4: ACID-TRIGGERED, ACID-GENERATING, AND SELF-AMPLIFYING DEGRADABLE POLYMERS[1]

4.1 Introduction

The simultaneous growth in waste plastics, 3D-printing, and implantable biomaterials has challenged chemists to develop new polymers able to meet the demands of real-world applications. In particular, there is increasing demand for smart polymers that change their shape or properties or degrade in response to environmental stimuli.[1] Indeed, a renewed interest in degradable polymers, especially for biomedical and engineering applications has led to an extensive search for new mechanisms to breakdown polymers.[2] Most degradable polymers contain functional groups along their main chain that cleave independently by chemical or photochemical reaction, in which case, the degradation rate remains more or less constant until the trigger or cleavable functionality is consumed (Figure 4.1a). The discovery of self-immolative polymers was particularly exciting because one triggering event is sufficient to activate an entire polymer chain to degrade.(3,4) These systems are stable under ambient conditions until a reactive unit at the polymer end is cleaved, triggering a cascade of fragmentation reactions that proceed sequentially along the polymer chain (Figure 4.1b).

More recently, the development of chain-shattering polymers allows materials to spontaneously degrade along the main chain with a triggering event occurring at each monomer unit (Figure 4.1c).[5] Both the self-immolative and chain-shattering approaches do have limitations in degradation rate and require a stoichiometric amount of the triggering agent. We were interested in a less studied approach that can be referred to as an amplified chain-shattering degradation. In this mechanism, a catalytic species accelerates chain cleavage, which in turn generates a full equivalent of the same agent, leading to an exponential degradation cascade (Figure 4.1d).[6] For example, polyesters such as PLGA show mild autocatalysis because the liberated carboxylic acids accelerate the hydrolysis.[7]

---

[1] Reproduced with permission from: Miller, K. A.; Morado, E. G.; Samanta, S. R.; Walker, B. A.; Nelson, A. Z.; Sen, S.; Tran, D. T.; Whitaker, D. J.; Ewoldt, R. H.; Braun, P. V.; Zimmerman, S. C. Acid-Triggered, Acid-Generating, and Self-Amplifying Degradable Polymers. *J. Am. Chem. Soc.* **2019**, *141 (7)*, 2838-2842. Copyright 2019 American Chemical Society.

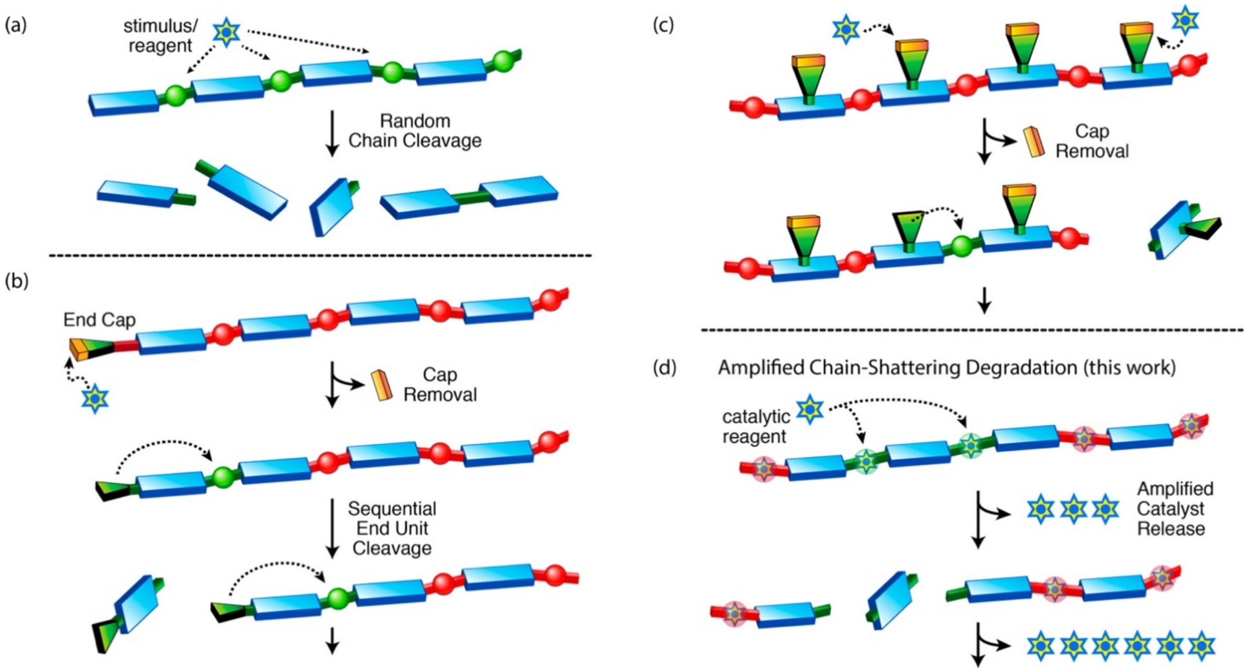

Figure 4.1 Schematic representation of polymer degradation mechanisms: (a) Traditional cleavage of polymer chain, (b) self-immolative polymer degradation. Loss of end-cap is followed by sequential loss of end units, (c) trigger-responsive chain-shattering polymer degradation mechanism, and (d) amplified chain-shattering mechanism developed in the current work. Green linkages are labile under reaction conditions, whereas red are stable.

Herein, we describe a simple, yet powerful acetal unit derived from 3-iodopropanal that undergoes acid catalyzed, self-amplified cleavage and demonstrate how it can be readily integrated into both degradable polymers and hydrogels. Unlike polyesters, our designed system shows strong autocatalysis and is more suitable to applications where exponential rates are needed. The acetal unit and acid trigger were chosen because pH gradients are ubiquitous in the environment and within biological systems. Furthermore, polymeric acetals (polyacetals) are well studied, with tunable reactivities and properties.[8] The simplest, polyoxymethylene (POM) is a widely used engineering thermoplastic, whereas more complex polyacetals are used in a range of applications from controlled release to drug delivery.

4.2 Results and discussion

The acetal design was based on small molecules reported by Ichimura and co-workers[9] that produce *p*-toluenesulfonic acid ($pK_a \approx -2.8$) in an amplified manner. With this starting point, various monomeric units were prepared and tested, ultimately leading to the 3-iodo-1,1-dialkoxy moiety as having the most suitable properties. In particular, this unit is easily prepared and has good stability, but undergoes acid amplified degradation under mildly acidic conditions. In this mechanism, the acetal likely hydrolyzes to the hemiacetal and then further to the aldehyde, which subsequently undergoes β-elimination to generate stoichiometric amounts of hydroiodic acid with pK_a ≈ −10 and acrolein (Scheme 4.1). Each of the three steps is catalyzed by acid.

Scheme 4.1 Mechanism of 3-Iodopropyl acetal hydrolysis with stoichiometric formation of HI and amplified cleavage.

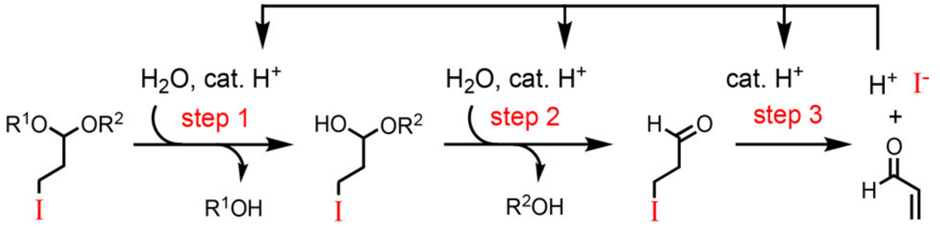

The key 3-iodopropyl acetals **1**–**3** used in this study are shown in Scheme 4.2. The synthesis of iodo-acetal monomer **1** was achieved by treatment of acrolein with TMSBr and acetalization with alcohol **4** to afford **5**.[10] Conversion of bromo acetal **5** to the iodo acetal **1** proceeded in good yield under standard Finkelstein conditions. Iodo acetals **2** and **3** were prepared in analogous fashion or by using HCl in place of TMSBr, the diol units in **2** obtained by dihydroxylation (see Section SX).

Scheme 4.2 Key 3-iodopropyl acetals **1-3** used in this study.

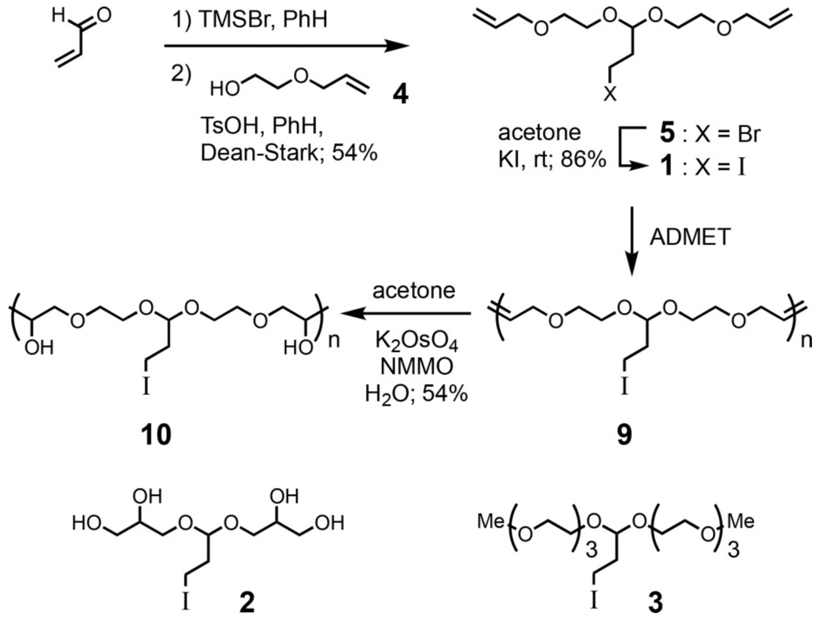

The ability of the 3-iodopropyl acetal unit to undergo acid amplified cleavage was examined by monitoring the hydrolysis of **3** using ^{1}H NMR under different conditions. A solution of **3** in D_2O at pD = 5.5 at 70 °C showed an induction period of about 15–20 min at which time the acetal underwent a rapidly accelerating degradation (Figure 4.2a). The reaction was largely complete after about 45 min. Consecutive ^{1}H NMR spectra taken over 1 h were consistent with the formation of hemiacetal **7**, further hydrolysis to aldehyde **8**, which subsequently undergoes β-elimination to generate hydroiodic acid (Figure 4.2b and Figure 4.5). The stoichiometric generation of the strong acid HI can accelerate each of the previous steps and produce the nonlinearity observed for the process. Consistent with these observations, performing the same hydrolysis reaction in the presence of 0.1 M acetate buffer dramatically suppressed the hydrolysis rate as shown in Figure 4.2a.

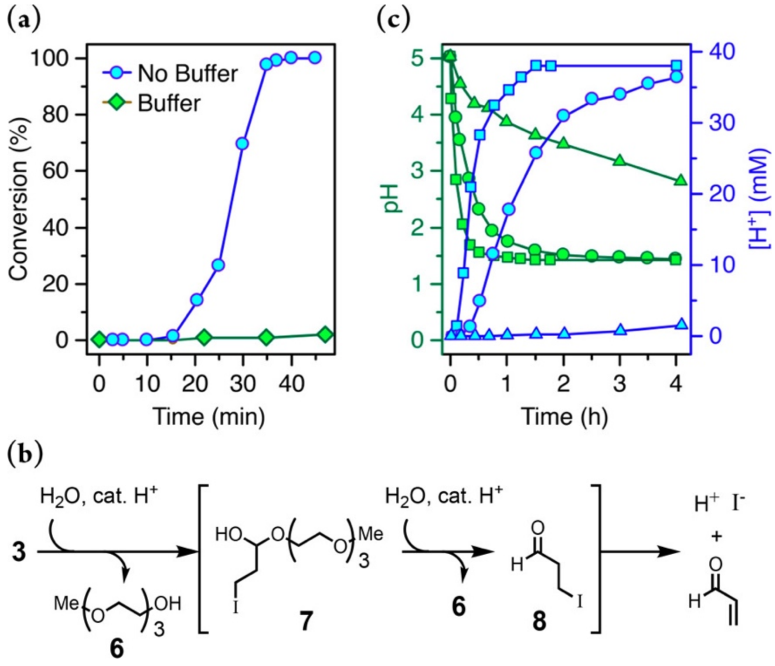

Figure 4.2 (a) Percent conversion of **3** in D_2O at initial pD = 5.5, with [**3**] = 48 mM at 70 °C in presence (green diamonds) and absence (blue circles) of 0.1 M acetate buffer. (b) Proposed mechanism of acetal hydrolysis with stoichiometric formation of HI and amplified cleavage. (c) Change in solution pH over time of a solution, [**3**] = 48 mM in nanopure water. Blue points, [H^+]; green points pH. Triangle, 50 °C, circle, 70 °C, square, 90 °C. Connected lines are added to guide the eye.

The acid amplified degradation of **3** was further characterized by measuring the pH over time. Thus, 48 mM aqueous solutions of **3** in nanopure water, which was slightly acidic (pH = 5.5) due to dissolved atmospheric CO_2, were heated at three temperatures (50, 70, and 90 °C) and the pH was measured at regular intervals (Figure 4.2c). The proliferation of acid was almost instantaneous at 90 °C, whereas an induction period of ca. 2 h and 5 min was observed at 50 and 70 °C, respectively. The release of acid at 50 °C could be made instantaneous by starting the reaction in a pH 3 solution by adding *p*-toluenesulfonic acid monohydrate. Both of the higher temperature reactions rapidly leveled off at pH ≈ 1.5, with the final [H^+] value being consistent with near quantitative conversion of **3** to HI.

Final support for the autocatalytic, acid amplification mechanism comes from successfully fitting the degradation data of **3** at 70 °C to an autocatalytic kinetic model (Equation 1.2).[11] In this model, rate constants k_1 and k_2 describe the nonautocatalytic hydrolysis step and autocatalytic HI-accelerated steps, respectively. As expected for an autocatalytic reaction, k_1 (1.9×10^{-4} min^{-1}) $\ll k_2c_0$ (3.0×10^{-2} min^{-1}) (Table 4.1). Additional support for this model involves a linear fit of the data over time using Equation 1.4 and shown in Figure 4.11.

Table 4.1 Calculated Rate Constants for the Nonautocatalytic and Autocatalytic Pathways of the Degradation of 3, 10, and 13 at Various Temperatures. Average and standard deviation values are listed from three measurements.

	temp (°C)	**k_1 (10^3 min^{-1})**	**k_2 (M^{-1} min^{-1})**
3	70	0.19 ± 0.26	6.2 ± 1.2
10	70	0.16 ± 0.19	2.9 ± 0.6
13	90	37 ± 6	7250 ± 3810

Using Grubb's first generation catalyst, monomer **1** underwent successful acyclic diene metathesis (ADMET) polymerization providing polymer **9** with $M_n \approx$ 10,000. Upjohn-dihydroxylation was subsequently used to convert **9** to **10** which significantly increased its water solubility (Scheme 2). However, polymer **10** exhibits thermoresponsiveness in pure aqueous solution with an LCST above room temperature. Therefore, a 40% (v/v) CD_3CN in D_2O (pD_0 = 5.5) mixture was used for degradation studies, which were monitored by ^{1}H NMR spectroscopy and gel permeation chromatography (GPC).

The hydrolysis of **10** was observed in NMR by watching the disappearance of the acetal proton. A plot of normalized acetal conversion vs time showed a distinctive sigmoidal shape that can be linearized (Figure 4.3a, Figure 4.12). This data fits well to our autocatalytic model and the extracted values for **10** agree with those observed for the degradation of **3** (Table 4.1). An autocatalytic, acid-amplified polymer degradation process should also be accompanied by a sigmoidal decrease in molar mass of **10**. As shown in Figure 4.3b, a solution of **10** heated to 70 °C was monitored at regular time intervals using GPC. Due to self-amplified degradation, there are only small changes in the GPC traces at first, followed by a rapid increase in retention time, and then much smaller changes.

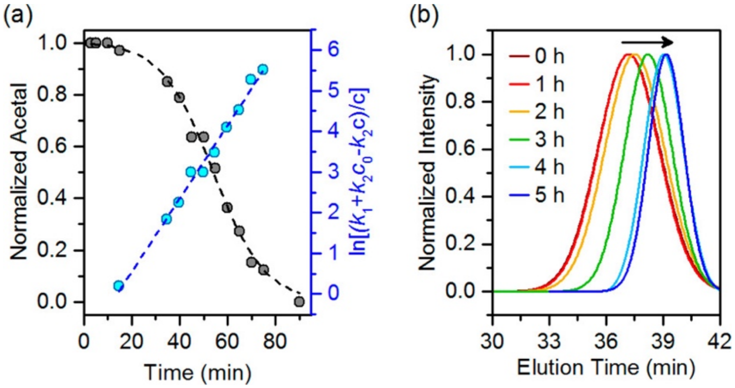

Figure 4.3 (a) Monitoring the disappearance of acetal functionality of **10** by ^{1}H NMR as a 3 mM solution in D_2O/CD_3CN at 70 °C. Black dashed line is fit of the data to Equation 1.5 and blue dashed line is provided as a guide for the eye. (b) GPC traces of the degradation of **10** in a 0.3 M solution in H_2O/CH_3CN over time at 70 °C.

Upon successful demonstration of the acid triggered self-amplified degradation behavior of the small molecule and linear polymer, we were interested in developing a degradable hydrogel containing the 3-iodopropyl acetal moiety. Treatment of **1** with HCl and acetalization with TMS-protected *N*-hydroxyethyl acrylamide gave **11**, which was converted to acrylamide cross-linker **12**containing a central 3-iodopropyl acetal unit. Finally, degradable hydrogel **13** was synthesized by free radical polymerization using 3 mol % of **12** as the cross-linker and the monomer acrylamide (AAm) with diethoxyacetophenone (DEAP) as the photoinitiator (Scheme 4.3 and 4.X). An additional example of polyol hydrogel synthesis and visual observation of its degradation can be found in Section 4.5.3.

Scheme 4.3 Synthesis of degradable hydrogel **13**.

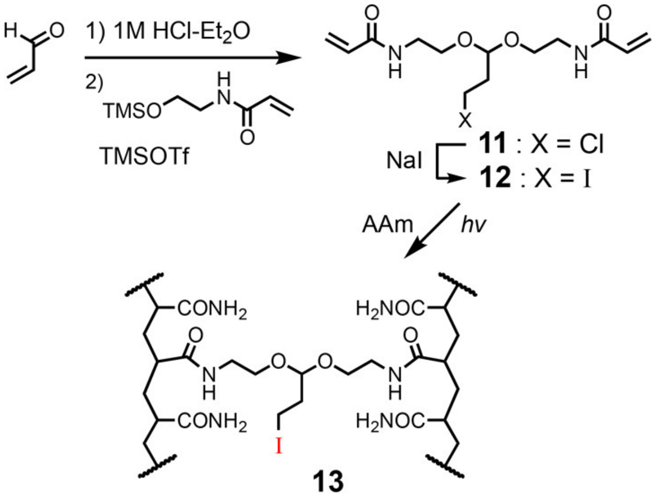

Hydrogel **13** was studied and compared to gels prepared with a nondegradable cross-linker (*N*,*N′*-methylenebis(acrylamide)) in the same mole ratio (Scheme 4.X). Visual observation of hydrogel degradation over time shows that **13** has a delay period of ~30 min and then degrades rapidly to give a solution, whereas the polyacrylamide control did not show any sign of degradation (Figure 4.4a). The degradation process was also characterized using rheology. The storage modulus was measured, and minimal degradation was seen from the polyacrylamide control (PAAm) at 90 °C, **13** at 70 °C, and **13** at 90 °C in 0.1 M acetate buffer. However, upon heating to 90 °C, **13**undergoes the rapid degradation that is characteristic of autocatalytic reactions (Figure 4.4b). This degradation profile was quantified using the autocatalytic rate equations described above and in Section 4.X, including an interrelation between elastic modulus and concentration to compare the apparent chemical rate constants (Figure 4.13). The increase of k_1 and k_2 for **13** can be attributed to increased hydrolysis and amplification rates at higher temperatures (Table 4.1).

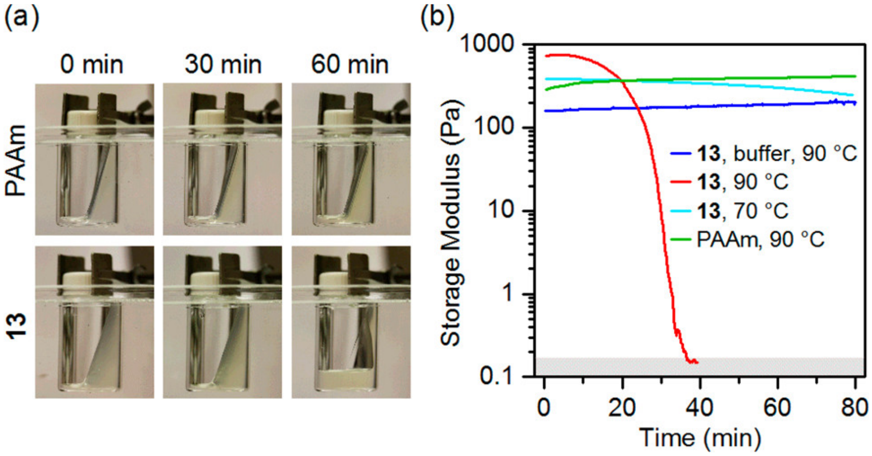

Figure 4.4 (a) Visual observation of the degradation of **13** compared to polyacrylamide control at 90 °C. Pictures are of the gel in a scintillation vial submerged in an oil bath. (b) Storage modulus of **13** at 70 °C, **13** with and without 0.1 M acetate buffer at 90 °C, and the polyacrylamide hydrogel at 90 °C.

4.3 Conclusions

We demonstrated a novel class of trigger-responsive self-amplified-degradable materials. The specific moiety developed here, the 3-iodopropyl acetal group, produces two products stoichiometrically: (1) hydroiodic acid, a very strong acid that accelerates further degradation, and (2) acrolein, a potent biocide and mercaptan scavenger. We anticipate that this acid amplifying motif could serve as a unique method for the controlled delivery of protic acid for various biological and chemical applications. These materials may also serve as benign carriers that undergo amplified release of biocidal acrolein in acidic solution. Investigations in these directions are currently in progress in our laboratory. We are further developing polymers for the self-amplified release of other reagents as well as other architectures with different rates and byproducts to expand the toolbox for potential applications.

4.4 Experimental section

4.4.1 Materials and methods

Unless otherwise noted, all solvents were ACS reagent grade and purchased from Acros Organics, Fisher Scientific, or Sigma-Aldrich, and used without further purification. HPLC grade acetonitrile (J.T. Baker) was stored over activated 4 Å molecular sieves for at least 1 day prior to use. HPLC grade acetone (Fisher Scientific) preserved under N_2 was used without purification. Acrolein, acrylamide, allyloxy ethanol, allyl alcohol, 2,2-diethoxyacetophenone, NaI, *N*-hydroxyethyl acrylamide, *N*,*N*’-methylenebis(acrylamide), *N*-methylmorpholine-*N*-oxide, p-toluenesulfonic acid, potassium osmate(VI) dihydrate, triethylene glycol monomethyl ether, trimethylsilyl trifluoromethanesulfonate, and 1st generation Grubbs Catalyst were purchased from Aldrich and used as received. TMS bromide (Oakwood Chemicals), and compressed HCl (Airgas) were used as received. 1,2-Dichlorobenzene (Aldrich) was passed through a basic alumina column and stored over activated 3 Å molecular sieves under N_2. SiliaMetS dimercaptotriazine (DMT) was purchased from SiliCycle. Silica and basic alumina chromatography were performed using 230-400 mesh (40-63 μm) silica gel and activated, basic, Brockmann I, 58 Å, respectively. D_2O was purchased from Aldrich and all other deuterated solvents were purchased from Cambridge Isotope Laboratory.

^1H and ^{13}C NMR spectra were recorded on a 400 or 500 MHz Varian Unity Inova spectrometer at ambient temperature. NMR spectra were processed using MestReNova software and chemical shifts were in parts per million (ppm). All ^1H and ^{13}C spectra were referenced to the residual solvent peak. Integration is provided and coupling constants (*J*) are reported in Hertz (Hz). Electrospray ionization mass spectra (ESI-MS) were obtained by using ESI on a Waters Micromass Q-Tof spectrometer, FD on a Waters 70-VSE spectrometer. Gel permeation chromatography (GPC) experiments were carried out on a Waters system equipped with a Waters 1515 isocratic pump, a Waters 2414 refractive index detector, and a miniDAWN TREOS 3-angle laser light scattering detector (MALLS, Wyatt Technology, CA) with the detection wavelength set at 658 nm. The MALLS detector was calibrated using pure toluene and used for the determination of the absolute molecular weights. DMF containing 0.1 M LiBr was used as the mobile phase with the flow rate = 1.0 mL/min at 50 °C using a set of four Styragel columns (5 μm): two HR 2, one HR 3 and one HR 4. Absolute molecular weights of the polymers were determined based on the dn/dc value of each sample using the ASTRA software (version 6.1, Wyatt Technology CA) assuming 100% mass recovery.

All pH values were measured on a Mettler Toledo FE20 FiveEasy Benchtop pH Meter using pH Electrode LE409. Characterization of linear viscoelastic properties was performed on a combined motor/transducer DHR-3 rotational rheometer from TA Instruments using a parallel-plate geometry with a diameter of 20 millimeters and Peltier temperature control. For rheological characterization, all gels were prepared at a nominal thickness of 1 mm for loading. During measurements, the gap was continuously varied to maintain a normal force of 0.5 ± 0.1 N to avoid edge fracture and maintain contact across the geometry. A low viscosity mineral oil was applied to the exposed surface of the gel to prevent evaporation. All data was plotted and fitted using OriginPro 8. Some plots were imported into Adobe Illustrator for annotation and coloring of lines and symbols. *Caution: Acrolein is toxic to humans following inhalation, oral or dermal exposure. All reactions using acrolein and all polymer degradation experiments that produce acrolein should be performed in a fume hood with appropriate personal protective equipment.*

4.4.2 Synthesis and characterization

Scheme 4.4 Synthesis of compound **1.**

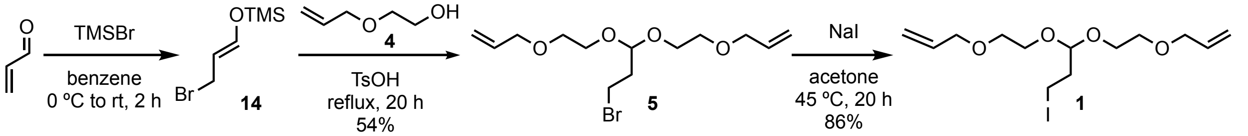

Compound 14. The preparation of **14** was carried out by following reported procedures.[12] Briefly, acrolein (7 g, 100 mmol, 1 equiv) was added dropwise into a solution of bromotrimethylsilane (15.8 mL, 120 mmol, 1.2 equiv) in benzene (120 mL) at 0 ºC. The resulting mixture was stirred for 30 min and warmed to room temperature for 60 min. The crude mixture was used directly in the next step. *Caution: Acrolein is toxic to humans following inhalation, oral or dermal exposure.*

Compound 5. The crude mixture containing **14** was treated with p-toluenesulfonic acid, monohydrate (500 mg) and **4** (14.3 g, 140 mmol, 1.4 equiv). The mixture was refluxed in a Dean-Stark apparatus for 20 h. The product was diluted with benzene (50 mL), washed with an aqueous 5% (w/w) solution of $NaHCO_3$ (2 × 250 mL) and water (250 mL), dried over $MgSO_4$, concentrated, and purified by column chromatography (SiO_2, EtOAc:hexanes, 10:90) resulting in 17.45 g of product (54% yield). ^{1}H NMR (400 MHz, $CDCl_3$) δ 5.86 (m, 2H), 5.30 – 5.07 (m, 4H), 4.77 (t, *J* = 5.7, 1H), 3.97 (d, *J* = 5.7, 4H), 3.77 – 3.59 (m, 4H), 3.55 (t, *J* = 5.0, 4H), 3.41 (t, *J* = 6.7, 2H), 2.15 (td, *J* = 6.8, 5.6, 2H). ^{13}C NMR (101 MHz, $CDCl_3$) δ 134.85, 117.23, 101.80, 72.36, 69.56, 65.53, 36.70, 28.87. *m/z* LRMS (ESI) calculated for $[M+Na]^+$: 346.08; found: 346.08. *Caution: Acrolein is toxic to humans following inhalation, oral or dermal exposure.*

Compound 1. Compound **5** (5.3 g, 0.023 mol, 1 equiv) was dissolved in acetone (30 mL) and treated with NaI (4.2 g, 0.028 mol, 1.25 equiv) at room temperature for 20 h. The reaction was diluted with diethyl ether (60 mL) and cooled to -20 ºC to precipitate NaI and NaCl. This cold solution was quickly filtered through a sintered glass funnel. The filtrate was concentrated, re-dissolved in hexanes (100 mL), washed with an aqueous 10% (w/w) $Na_2S_2O_3$ (2 × 50 mL) and brine (50 mL), dried with Na_2SO_4, concentrated, and purified by column chromatography (SiO_2, EtOAc:hexanes, 20:80). The slightly-yellow product was further purified by passing through another column (basic alumina, EtOAc:hexanes, 15:85) to afford 7.32 g of product in 86% yield. ^{1}H NMR (400 MHz, $CDCl_3$) δ 5.91 (m, 2H), 5.36 – 5.13 (m, 4H), 4.73 (t, *J* = 5.6 Hz, 1H), 4.02 (d, *J* = 5.7, 4H), 3.77 (dt, *J* = 10.7, 4.8 Hz, 2H), 3.72 – 3.64 (m, 2H), 3.59 (t, *J* = 4.8 Hz, 4H), 3.20 (t, *J* = 7.1 Hz, 2H), 2.18 (td, *J* = 7.1, 5.6 Hz, 2H). ^{13}C NMR (101 MHz, $CDCl_3$) δ 134.85, 117.23, 117.21, 103.29, 72.35, 69.57, 65.46, 37.35, 0.42. *m/z* LRMS (ESI) calculated for $[M+Na]^+$: 393.06; found: 393.05. *Caution: Acrolein is toxic to humans following inhalation, oral or dermal exposure.*

Scheme 4.5 Synthesis of compound **2**.

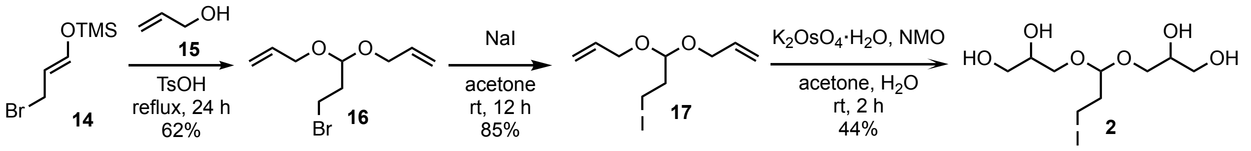

Compound 16. The crude mixture of **14** was prepared as previously mentioned and used directly to synthesize **16**. Briefly, acrolein (7 g, 100 mmol, 1 equiv) was added dropwise into a solution of bromotrimethylsilane (15.8 mL, 120 mmol, 1.2 equiv) in benzene (120 mL) at 0 ºC. The resulting mixture was stirred for 30 min and warmed to room temperature for 60 min. Then, the crude mixture was treated with p-toluenesulfonic acid, monohydrate (500 mg) and **15** (20 mL, 17 g, 294 mmol, 2.9 equiv). The mixture was refluxed using a Dean-Stark apparatus for 24 h. The product washed with an aqueous 5% (w/w) solution of $NaHCO_3$ (2 × 250 mL) and water (250 mL), dried over $MgSO_4$, concentrated, and purified by column chromatography (SiO_2, EtOAc:hexanes, 10:90) resulting in 14.5 g of product (62% yield). ^{1}H NMR (400 MHz, $CDCl_3$) δ 5.92 (m, 2H), 5.30 (m, 2H), 5.19 (m, 2H), 4.79 (t, J = 5.5 Hz, 1H), 4.19 – 4.01 (m, 4H), 3.45 (t, J = 6.7 Hz, 2H), 2.20 (td, J = 6.7, 5.5 Hz, 2H). *Caution: Acrolein is toxic to humans following inhalation, oral or dermal exposure.*

Compound 17. Compound **16** (5.3 g, 22.5 mmol, 1 equiv) was dissolved in acetone (30 mL) and treated with NaI (4.2 mg, 28.2 mmol, 1.25 equiv) at room temperature for 12 h. The reaction was diluted with diethyl ether (60 mL) and cooled to -20 °C for 2.5 h. This cold solution was quickly filtered through a sintered glass funnel. The filtrate was concentrated, re-dissolved in hexanes (100 mL), washed with an aqueous 10% (w/w) $Na_2S_2O_3$ (100 mL) and brine (100 mL), dried with Na_2SO_4, and concentrated. The product was purified by column chromatography (SiO_2, EtOAc:hexanes, 7:93) and then passed through basic alumina to afford 5.4 g (85% yield). ^{1}H NMR (400 MHz, $CDCl_3$) δ 5.92 (m, 2H), 5.30 (m, 2H), 5.19 (m, 2H), 4.70 (t, J = 5.5 Hz, 1H), 4.15 – 4.02 (m, 4H), 3.19 (t, J = 7.1 Hz, 2H), 2.18 (td, J = 7.1, 5.5 Hz, 2H).

Compound 2. The dihydroxylation of **17** was carried out by following reported procedures.[13] Briefly, **17** (1.41 g, 5 mmol, 1 equiv) was dissolved in a mixture of water (18 mL) and acetone (60 mL). N-methyl morpholine *N*-oxide (NMO, 1.76 g, 15 mmol, 3 equiv) and $K_2OsO_4 \cdot H_2O$ (0.073 g, 0.2 mmol, 0.04 equiv) were added and the reaction was stirred at room temperature for 2 h. The product was washed with diethyl ether (3 x 25 mL), saturated with NaCl, extracted with chloroform/isopropanol (1:1, 3 x 25 mL), concentrated, and purified by column chromatography (SiO_2, DCM:MeOH, 9:1) resulting in 0.77 g of product (44% yield). ^{1}H NMR (400 MHz, D_2O) δ 4.65 (t, J = 5.8 Hz, 1H), 3.83 (p, J = 5.9, 5.5 Hz, 2H), 3.76 – 3.40 (m, 8H), 1.70 – 1.52 (m, 2H), 1.33 (h, J = 7.5 Hz, 2H), 0.87 (t, J = 7.4 Hz, 2H). *Caution: Acrolein is toxic to humans following inhalation, oral or dermal exposure.*

Scheme 4.6 Synthesis of compound **3**.

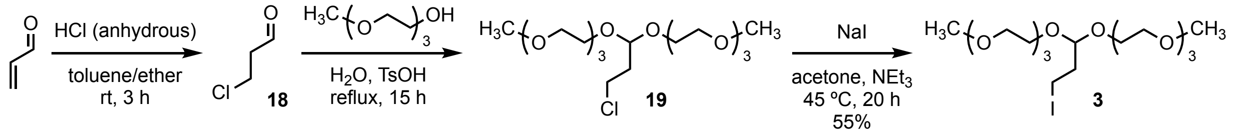

Compound 18. Acrolein (6.64 mL, 0.1 mol) was added to toluene (200 mL) and diethyl ether (60 mL). Dicinnamalacetone (5 mg) was added to the mixture as an indicator. Gaseous HCl was bubbled through the mixture for 2 h as the light-yellow solution turned bright orange. A ^{1}H NMR of the crude reaction mixture indicated ~97% conversion of acrolein to **18**. The mixture was concentrated under reduced pressure to remove the ether and used directly in the next reaction. *Caution: Acrolein is toxic to humans following inhalation, oral or dermal exposure.*

Compound 19. Triethylene glycol monomethyl ether (40 mL, 0.25 mol) and p-toluenesulfonic acid, monohydrate (230 mg, 1.2 mmol) were added to the crude mixture containing **18**. The solution was refluxed for 20 h using a Dean-Stark trap. The solvent was removed under reduced pressure. The residue was re-dissolved in ethyl acetate (100 mL), washed with hexanes

(100 mL), and an aqueous solution containing 5% (w/w) K_2CO_3 and 10% (w/w) NaCl (300 mL). The product was extracted with ethyl acetate (2 × 100 mL) and the organic layers washed with brine and dried over Na_2SO_4. The solution was concentrated under reduced pressure to provide 45 g of crude **2**, which was used directly in the next reaction without purification. *Caution: Acrolein is toxic to humans following inhalation, oral or dermal exposure.*

Compound 3. The crude **19** (24 g, 0.06 mol) was dissolved in acetone (200 mL). NaI (39 g, 0.26 mol) and NEt_3 (0.83 mL, 0.006 mol) were added and the solution was stirred at 45 °C for 20 h. Diethyl ether (200 mL) was added and the reaction was cooled to -20 °C to precipitate NaI and NaCl. This cold solution was quickly filtered through a sintered glass funnel. The filtrate was concentrated under reduced pressure, re-dissolved in hexanes (200 mL), and washed with an aqueous 10% (w/w) $Na_2S_2O_3$ solution (2 × 100 mL). The product was back extracted, washed with brine, dried over Na_2SO_4, concentrated to get a light brown viscous oil, and purified by column chromatography (SiO_2, EtOAc:hexanes, 50:50). Further purification was accomplished by a second column (basic alumina, EtOAc:hexanes, 50:50) to provide 16.4 g of product in 55% yield. ^{1}H NMR (400 MHz, $CDCl_3$) δ 4.73 (td, *J* = 5.6, 1.1 Hz, 1H), 3.84 – 3.76 (m, 2H), 3.76 – 3.63 (m, 20H), 3.59 (ddd, *J* = 5.7, 3.8, 1.2 Hz, 4H), 3.42 (d, *J* = 1.1 Hz, 5H), 3.33 – 3.18 (m, 2H), 2.26 – 2.16 (m, 2H). ^{13}C NMR (101 MHz, $CDCl_3$) δ 134.88, 117.25, 103.27, 72.36, 69.57, 65.46, 37.35, 0.48. *m/z* LRMS (ESI) calculated for $[M+H_2O+H]^+$: 517.14; found: 517.13. *Caution: Acrolein is toxic to humans following inhalation, oral or dermal exposure.*

Scheme 4.7 Synthesis of polymer **10**.

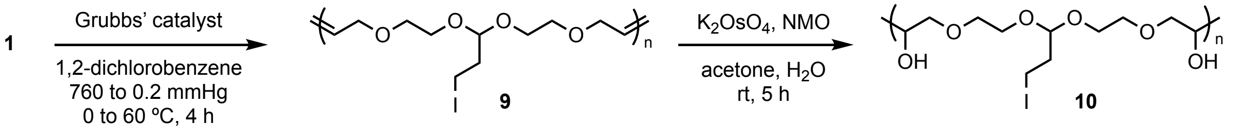

Polymer 9. A dry two-neck round-bottom flask (25 mL) was equipped with a condenser and connected to a vacuum pump (0.2 mmHg) and N_2 via Schlenk line. The flask was charged with a small stir bar, dry 1,2 dichlorobenzene (2 mL), and **5** (500 mg, 1.35 mmol) under positive N_2 flow. The other neck was closed with a rubber septum and copper wire. The reaction mixture was degassed by applying vacuum for 20 min at 0 °C. The flask was brought to room temperature, refilled with N_2 and first-generation Grubbs Catalyst (28.5 mg, 0.035 mmol, 2.5 mol%) was added under positive N_2 flow. The polymerization was carried out under gradient of vacuum and

temperature. The reaction mixture was stirred at 30 ºC for 30 min with partial opening to the vacuum line to minimize spluttering. Under this condition, the solvent evaporates gradually along with ethylene gas to result in a condensed reaction mixture. This was further heated under maximum opening of the vacuum line at 50 ºC for 1 h followed by 60 ºC for 2.5 h. The reaction mixture was cooled to room temperature, dissolved in chloroform (5 mL), and ethyl vinyl ether (5 mL) was added to quench the catalyst. The mixture was stirred for 30 min at room temperature followed by precipitation in 10 mL of hexane. Upon centrifugation and drying under reduced pressure, the product (405 mg) was obtained as a highly viscous dark brown product with $M_n \approx$ 13,000 and $M_w/M_n \approx 1.2$. *Caution: Acrolein is toxic to humans following inhalation, oral or dermal exposure.*

Polymer 10. In a 50 mL round-bottom flask charged with a magnetic stirring bar, **9** (405 mg, 1.14 mmol, 1 equiv) was dissolved in a mixture of acetone (10 mL) and *tert*-butanol (6 mL). Separately, $K_2OsO_4{\bullet}H_2O$ (24 mg, 0.065 mmol, 0.57 equiv) was dissolved in DI water (2 mL) and added to the flask. N-methyl morpholine *N*-oxide (NMO, 335 mg, 2.86 mmol, 2.5 equiv) was added and the mixture stirred at room temperature for 5 h. A saturated aqueous solution of Na_2SO_3 (0.6 mL) was addesd and the mixture stirred for 2 h. The organic layer was placed in a 50 mL round-bottom flask and stirred for 1 h with SiliaMetS (1 g) to remove residual heavy metals. The mixture was filtered, concentrated, and dried over Na_2SO_4. The crude polymer was dispersed in chloroform (2 mL), precipitated into acetone to remove residual NMO, re-dissolved in methanol (2 mL), precipitated into diethyl ether, filtered, and dried to give the product (270 mg) as a golden brown solid. *Caution: Acrolein is toxic to humans following inhalation, oral or dermal exposure.*

Scheme 4.8 Synthesis of compound **20**.

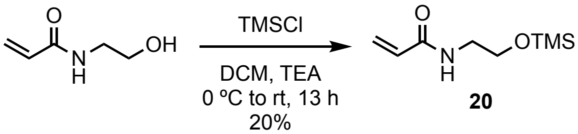

Compound 20. *N*-hydroxyethyl acrylamide (31.0 mL, 269 mmol), triethylamine (100 mL, 716 mmol), and DCM (250 mL) were added to a round-bottom flask. The reaction was stirred for 30 min under N_2. The mixture was cooled to 0 ºC and trimethylsilyl chloride (105 mL, 827 mmol) was cannulated into an addition funnel and added dropwise to the mixture over 45 min. The reaction was warmed to room temperature and stirred for 12 h. The mixture was poured into ice

water (500 mL) and extracted with DCM (3 × 150 mL). The organic layer was collected, dried over Na_2SO_4, filtered, and the solvent removed via rotary evaporation. Column chromatography was used to purify the crude compound (SiO_2, 100% DCM to 1:2 EtOAc:hexanes). A clear yellow oil was obtained in 68% yield (34.3 g). ^{1}H NMR (400 MHz, $CDCl_3$) δ 6.27 (dd, *J* = 16.9, 1.5 Hz, 1H), 6.11 (dd, *J* = 16.9, 10.3 Hz, 1H), 5.63 (dd, *J* = 10.3, 1.5 Hz, 1H), 3.67 (t, *J* = 5.3 Hz, 1H), 3.46 (q, *J* = 5.2 Hz, 1H). ^{13}C NMR (125 MHz, $CDCl_3$) δ 166.1, 131.5,126.9, 61.8, 42.2, 0.0. *m/z* LRMS (ESI) calculated for $[M+H]^+$: 187.31; found: 188.11.

Scheme 4.9 Synthesis of Gel **13**.

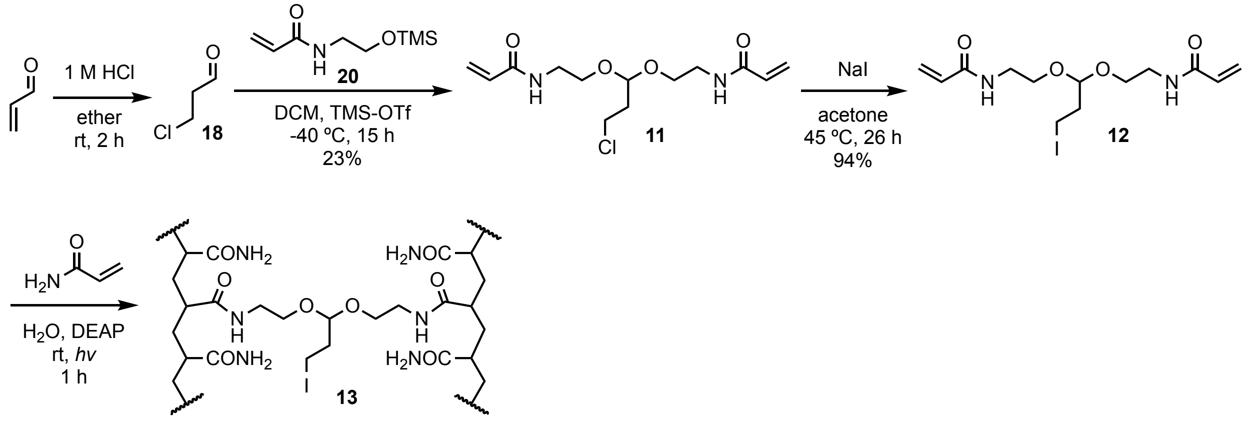

Compound 18. Acrolein (1 mL, 15 mmol, 1 equiv) and 1 M HCl in diethyl ether (30 mL) were added to a round-bottom flask and stirred for 2 h under N_2. The mixture was placed in dry ice/acetonitrile bath and used directly in the next step without purification. *Caution: Acrolein is toxic to humans following inhalation, oral or dermal exposure.*

Compound 11. The crude reaction mixture containing **18** was treated with trimethylsilyl trifluoromethane sulfonate (92 mL) via syringe followed by dropwise addition of a solution of **20** (5 g, 27 mmol, 1.8 equiv) dissolved in DCM (10 mL). The reaction was stirred for 3 h and quenched with triethylamine (3 mL). The mixture was washed with a saturated aqueous solution of $NaHCO_3$ (100 mL) and extracted with DCM (4 × 250 mL). The organic layer was collected, dried over sodium sulfate, filtered, and dried using rotary evaporation. The product was purified using column chromatography (SiO_2, EtOAc:DCM 80:20 to MeOH:DCM 3:97) resulting in the product as a partially impure clear yellow oil (1.1 g) that was used directly in the next step. *Caution: Acrolein is toxic to humans following inhalation, oral or dermal exposure.*

Compound 12. Sodium iodide (5.4 g, 36 mmol, 10 equiv), **11** (1.1 g, 3.6 mmol, 1 equiv), and acetone (35 mL) were combined in a flask and stirred under N_2. Using a condenser, the reaction mixture was heated to 45 ºC for 26 h and then quenched by pouring directly into a saturated $NaHCO_3$ solution (100 mL). The product was extracted using DCM (5 × 250 mL). The organic layer was collected, dried over sodium sulfate, and the solvent removed by rotary evaporation. The product was purified using column chromatography (SiO_2, MeOH:DCM 3:97). An orange viscous oil was collected as the product in 94% yield (0.940 mg). ^{1}H NMR (500 MHz, $CDCl_3$) δ 6.31 (dd, *J* = 17.0, 1.5 Hz, 2H), 6.15 (dd, *J* = 17.0, 10.2 Hz, 4H), 5.66 (dd, *J* = 10.2, 1.6 Hz, 2H), 4.63 (t, *J* = 5.5 Hz, 1H), 3.85 – 3.44 (m, 8H), 3.16 (t, *J* = 6.9 Hz, 2H), 2.12 (td, *J* = 6.9, 5.4 Hz, 2H). ^{13}C NMR (125 MHz, $CDCl_3$) δ 166.4, 131.2, 127.4, 104.1, 77.8, 65.7, 40.2, 37.3. *m/z* LRMS (EI) calculated for $[M+Na]^+$: 419.22; found: 419.04. *Caution: Acrolein is toxic to humans following inhalation, oral or dermal exposure.*

Gel 13. Gel preparation was carried out similar to a reported procedure.[14] Briefly, crosslinker **12** (40.4 mg, 0.1 mmol, 3 equiv) was dissolved in 0.3 mL of a 2,2-diethoxyacetophenone (DEAP) photoinitiator solution (0.3 mL of DEAP dissolved in 10 mL DMSO) and diluted with Millipore water (5 mL) in a buffer-washed scintillation vial. Acrylamide (241.5 mg, 3.4 mmol, 100 equiv) and KCl (5 mg) were added, the mixture was vortexed, and polymerized under a mercury UV lamp (Blak-Ray longwave lamp B-100AP, 365 nm, 100 W) for 1 h. *Caution: Acrolein is toxic to humans following inhalation, oral or dermal exposure.*

Scheme 4.10 Synthesis of polyacrylamide hydrogel.

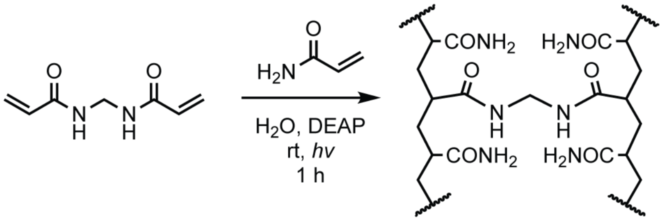

Polyacrylamide hydrogel. The polyacrylamide hydrogel (PAAm) was prepared using reported procedures.[5] Briefly, *N*,*N'*-methylenebisacrylamide (15.7 mg, 0.1 mmol, 3 equiv) was dissolved in 0.3 mL of a 2,2-diethoxyacetophenone (DEAP) photoinitiator solution (0.3 mL of DEAP dissolved in 10 mL DMSO) and diluted with Millipore water (5 mL) in a buffer-washed scintillation vial. Acrylamide (241.5 mg, 3.4 mmol, 100 equiv) and KCl (5 mg) were added, the mixture was vortexed, and then polymerized under a mercury UV lamp (Blak-Ray longwave lamp B-100AP, 365 nm, 100 W) for 1 h. *Caution: Acrolein is toxic to humans following inhalation, oral or dermal exposure.*

Scheme 4.11 Synthesis of **21**.

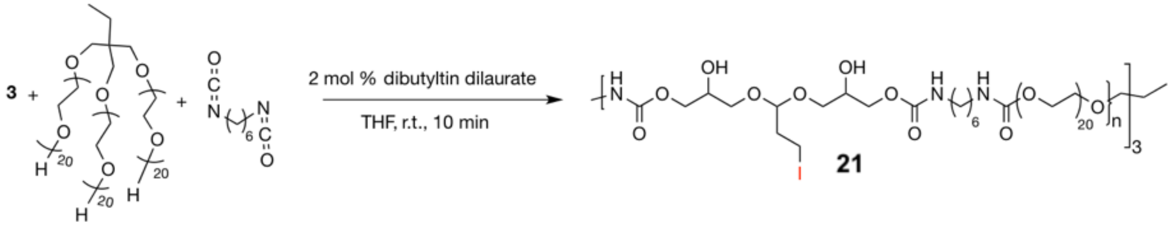

Compound 21. To a nitrogen purged 4 mL glass screw-cap vial containing 0.25 g (0.714 mmol) of 3 was added to 0.48 g (0.476 mmol) anhydrous 3-ARM PEG (MW: 1,014), 8.5 µL dibutyltin dilaurate, 1 mL anhydrous THF, and 0.23 mL (1.43 mmol) of hexamethylene diisocyanate while using vortexing and nitrogen to mix and purge the reaction vial between additions. The mixture was allow to stand at room temperature for ~10 min until the transparent yellow liquid solution turned to a yellow opaque gel. The reaction was left for an additional 3 h at room temperature to ensure complete gelation. The gel was cut in half and dialyzed against nanopure water for 2 d (MWCO: 12-14 kD). The resulting translucent gels were lyophilized until constant weight and stored covered at 0 °C. ATR IR (1/cm): 3320, 2930, 2860, 1690, 1530, and 1250. *Caution: Acrolein is toxic to humans following inhalation, oral or dermal exposure.*

4.4.3 Degradation experiments

Degradation of 3 Monitored by ^{1}H NMR. To monitor the degradation by NMR, two sets of solutions of **3** (48 mM) were prepared in D_2O at pD 5.5. For the acid amplification study, D_2O of pD 5.5 was prepared by adding p-toluenesulfonic acid to D_2O. For the control experiment, 0.1 M acetate buffer of pD 5.5 in D_2O was prepared. The pD value of a solution made in D_2O was obtained by adding a constant of ca. 0.4 to pH*,[15] which was measured from the direct reading in a H_2O-calibrated pH-meter. This adjustment between pD and pH* is based on the measurements of acids and/or bases dissolved at the same concentrations in H_2O and D_2O. For each set of NMR experiments, several NMR tubes containing 0.7 mL of the solution were capped and sealed with parafilm and heated to 70 °C. One NMR tube was taken out at each time point and the reaction was quenched by immediately immersing the NMR tube in an ice bath. The conversions were calculated by integrating the signal at 1.9 ppm (2 proton at 0 min) with respect to the signal at 3.2 ppm (6 protons, constant throughout).

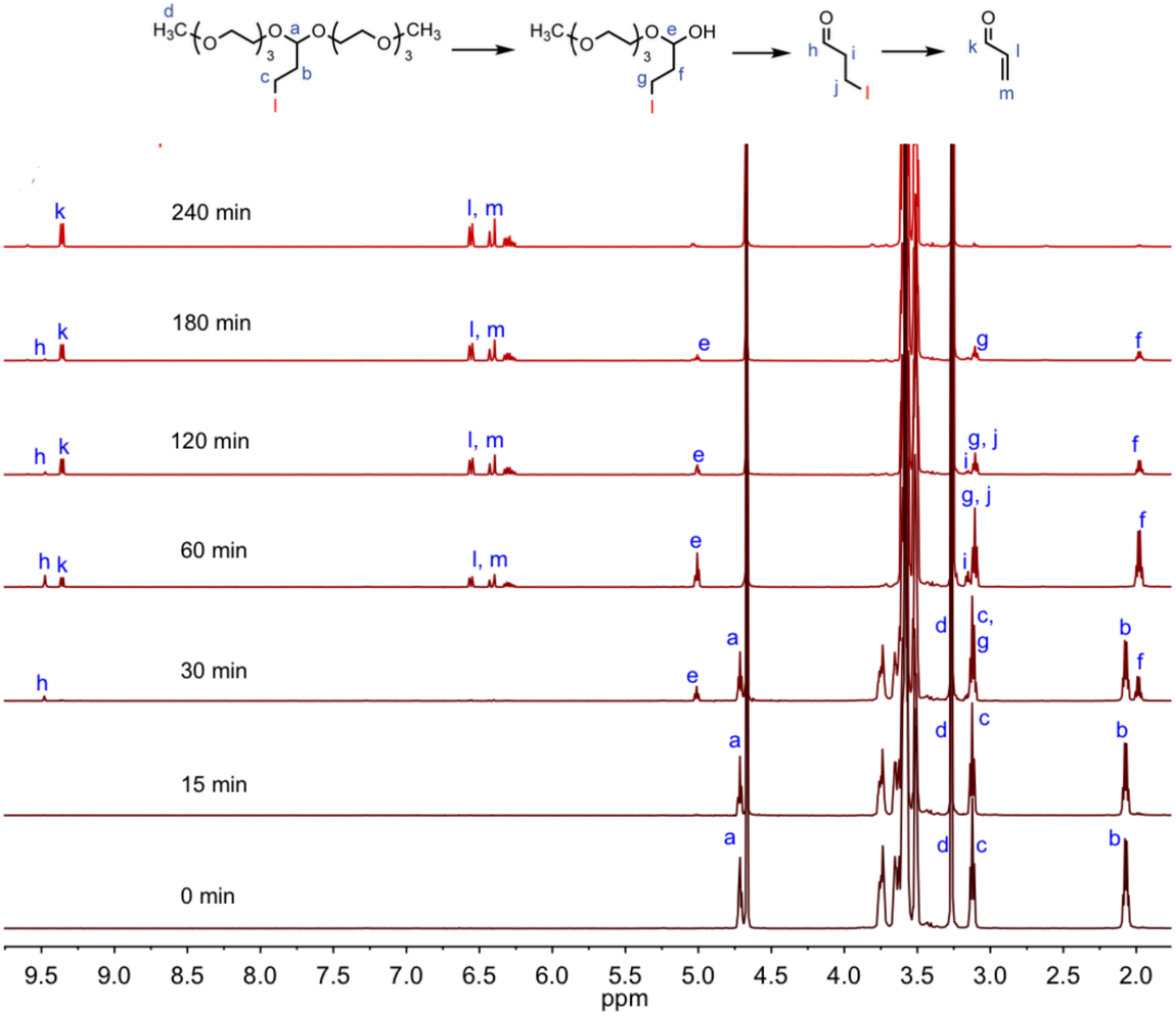

Figure 4.5 ^{1}H NMR analysis of the degradation kinetics of **3** in a 48 mM solution in D_2O.

Degradation of 3 Monitored by pH. To monitor degradation by pH, **3** (0.27 mL) was added to a conical screw cap vial and dissolved in Millipore water (15 mL) to make a 48 mM aqueous solution. The solution was sonicated briefly and heated at the desired temperature. 1 mL aliquots were taken out via syringe at each time point and quenched by immediate cooling in an ice bath. The pH values of the aliquots were measured at room temperature by the pH meter calibrated for pH 4 and 7. KCl (1 mg/ml) was added to each aliquot to increase their ionic strength to improve the precision and response time of the measurement. Starting pH of 3 was obtained by adding external p-toluenesulfonic acid.

Degradation of 10 Monitored by ^{1}H NMR. A solution of **10** (0.35 M) was prepared in a solvent mixture containing 40% CD_3CN in D_2O of pD 5.5 with DMSO (8 mM) as an internal standard (see arrow). This slightly acidic D_2O solution was prepared by adding toluene sulfonic acid into D_2O. The pD value of a solution made in D_2O was obtained by adding a constant of ca. 0.4 to pH*,[6] which is obtained from the direct reading in a H_2O-calibrated pH-meter. NMR tubes containing the solution (0.2 mL) were capped, sealed with parafilm, and heated to 70 °C. One NMR tube was taken out at each time point and the reaction was quenched by immediately immersing the NMR tube in an ice bath. The solutions were diluted with 0.5 mL of 40% CD_3CN in D_2O and ^{1}H NMR were recorded. The conversions of acetal were calculated by integrating the signal at 5.05-5.28 ppm (acetal signal, 1 proton at 0 min) with respect to the signal at 3.25 ppm (DMSO internal standard, constant throughout).

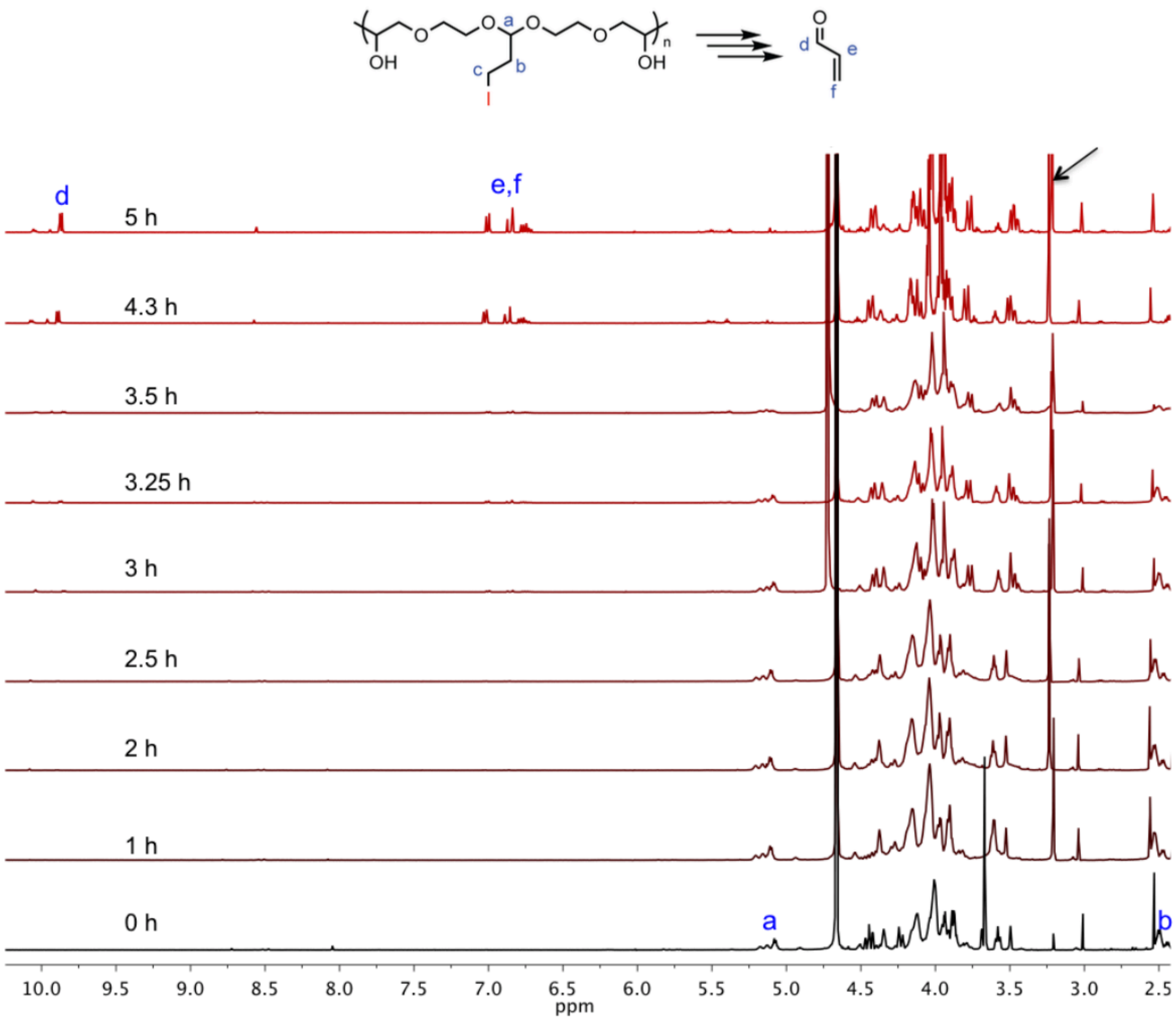

Figure 4.6 ^{1}H NMR analysis of the degradation kinetics of **10** in a 48 mM solution in D_2O.

Degradation of 10 Monitored by GPC. After running NMR samples, solutions of **10** were transferred into a tared vial, concentrated, and dried under high vacuum. Final vial weights were recorded, and the products were dissolved in DMF containing 0.1 M LiBr to result in 30 mg/mL solution. The solutions were passed through 0.45 μm syringe filters and analyzed by GPC. Due to the small molecular weight of the degraded polymers, peak deconvolution was performed to obtain retention times.

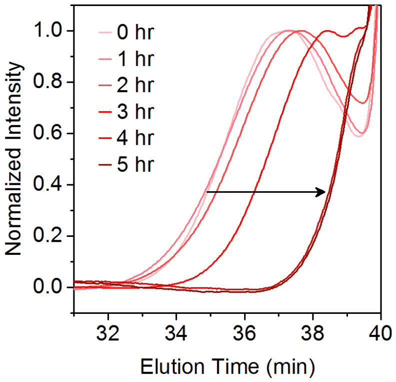

Figure 4.7 GPC traces of the degradation of **10** in a 48 mM solution in H_2O over time at 70 °C.

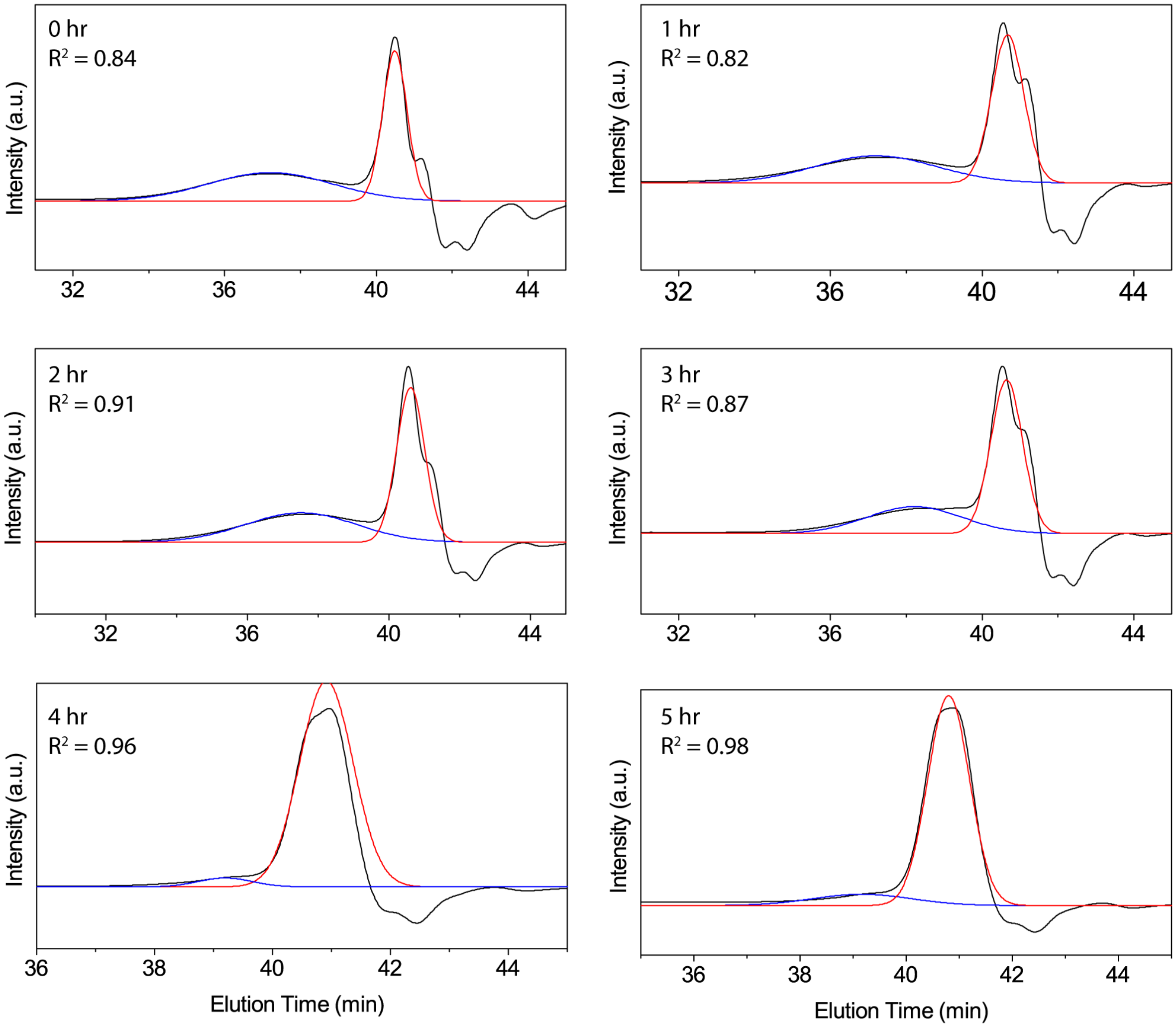

Figure 4.8 Deconvolution results for the GPC traces of the degradation of **10**.

Degradation of 13 Monitored by pH. A Canon EOS Rebel T3 Digital SLR Camera with EF-S 60 mm lens was used to take pictures of the hydrogel degradation every 5 min using an Aputure remote shutter release timer. Hydrogels were polymerized vertically on the side of a 20 mL scintillation vial for visualization of the degradation process. Pictures were taken through an oil bath that was set to 90 ºC.

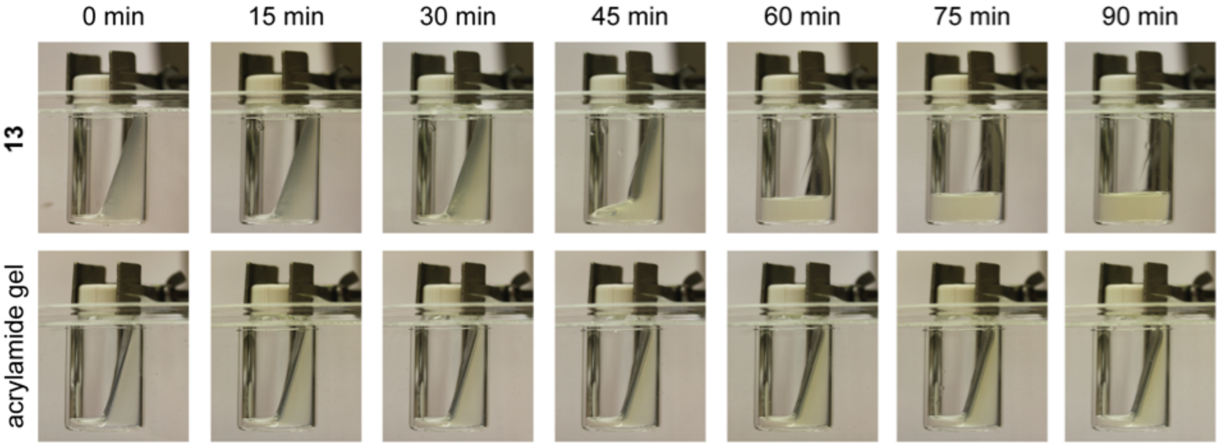

Figure 4.9 Visual observation of the degradation of **13** compared to polyacrylamide control at 90 ºC.

Measurements of solution pH were taken before polymerization and after depolymerization for each system. The pHs were measured at room temperature by the pH meter calibrated for pH 4 and 7. KCl (1 mg/ml) was added to each sample to increase their ionic strength to improve the precision and response time of the measurement. The polyacrylamide hydrogel was measured after 24 h such that sufficient hydrolysis had taken place to achieve an accurate pH measurement. All values are an average of three separate samples.

Table 4.2 Monitoring hydrogel pH before and after degradation.

	pH before	pH after
13	4.73 ± 0.04	1.83 ± 0.02
Polyacrylamide hydrogel	5.19 ± 0.05	4.53 ± 0.04

Degradation of 13 Monitored by Rheology. All samples were heated from 25 °C to the final temperature at a rate of 5 °C per minute. To obtain the viscoelastic storage and loss moduli, G' and G", samples were held at the final temperature and probed at a frequency of 1 rad/s and an oscillatory strain amplitude of 3% or below which was in the linear deformation regime. For all samples, before any significant change in the moduli of the material, the ratio of G'' to G' (i.e. tan(δ) = G''/G') was always less than 0.1. For the samples that undergo a dramatic decrease in G', during and after the decrease, tan(δ) was always less than 1. G'' and tan(δ) are omitted from plots for clarity. All rheological plots begin once the final temperature is reached by the Peltier temperature controller. At short times, slight increases in moduli are observed for all materials; we attribute this to temperature equilibration of the sample. Little frequency dependence was observed for any of the materials across the range of 0.1 to 30 rad/s.

Visual observation of the degradation of 21. Encouraged by the degradation behavior of **13**, we applied the 3-iodopropyl acetal moiety to another polyol hydrogel. When **21** was incubated in H_2O at 70 ºC in acetate buffered solutions (pH 5.35) and un-buffered solution (pH 5.5), an amplified degradation behavior of the hydrogel was observed. Thermoresponsive collapse (opacity) of the hydrophobic domains within the hydrogel structure was observed and no significant degradation was observed after 53 h of incubation. However, complete disappearance of the hydrogel occurred in the following 16 h. Comparatively, no visible degradation of the hydrogel occurred over the 69 h incubation period for the buffered system. Although, we cannot exclude the influence of the polyurethane structure or acid diffusion through the gel as it degrades, this qualitative result is in good agreement with our hypothesis that only when the acid amplifying unit is allowed to proliferate, and not be quenched by buffering conditions, will the macroscopic auto-catalytic degradation be realized.

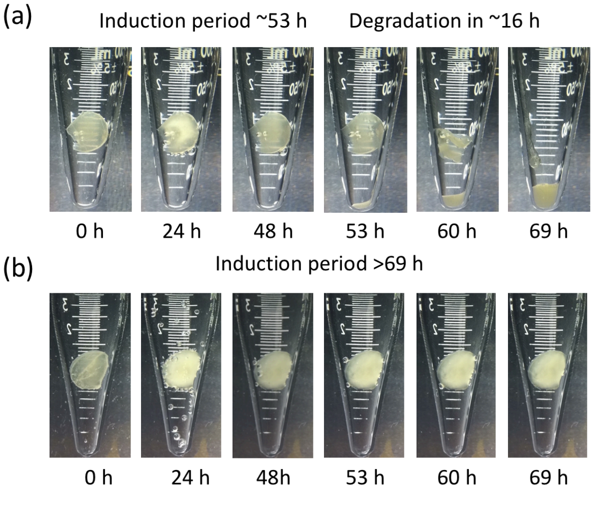

Figure 4.10. (a) Photos displaying acid triggered self-amplified degradation of **21** in pH 5.5 H_2O at 70 ˚C. (b) Photos displaying minimal acid triggered self-amplified degradation of **21** in acetate buffer at 70 ˚C.

ADMET control experiment. An attempt was made to prepare a control polymer with the same *M*n as **10** but lacking the halogen. Poly(PTPD)-hydroxyl was prepared with a significantly lower molecular weight. A preliminary comparison of its degradation by NMR is shown in Figure 4.10.

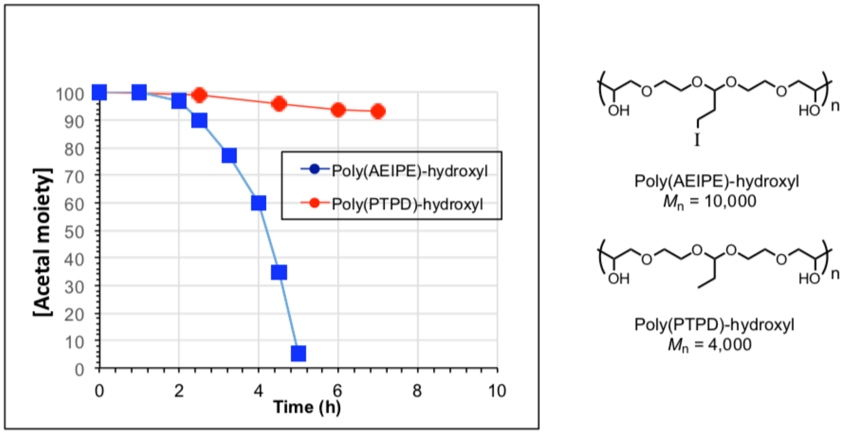

Figure 4.11 Preliminary comparison of hydrolysis rates of ADMET polymer with and without I.

4.4.4 Kinetic analysis

Full derivation of equations can be found in Chapter 1. For each degradation profile, k_1 and k_2 were found using least-squares regression of either the normalized acetal (using Equation 1.5) or normalized storage modulus (using Equation 1.7). The values from each triplicate measurement were averaged and reported in Table 4.1. A plot of $\ln[(k' + k,c5 - k,c)/c]$ versus time is shown for visual representation to give a straight line based on the relationship provided in Equation 1.4. For polymer samples, it should be noted that concentration must be calculated from the moles of total degradable agents in the solution rather than simply the moles of polymer. The c0 values used were 0.048 M for **3**, 0.045 M for **10**, and 0.050 M, 0.022 M, or 0.037 M for **13**. In addition, the hydrogel k_2 values calculated from storage modulus neglect the effects of loops and other inactive cleavage sites. These could be accounted for in the rate equation by assuming a constant ratio of elastically inactive cleavage sites $\varnothing = c^{\text{inactive}} / c^{\text{active}}$, where $c^{\text{total}} = c^{\text{inactive}} + c^{\text{active}}$. Equation 1.3 is true for c^{total} but can be rewritten to account for inactive crosslinking by substituting $c^{\text{total}} = (1 + \varnothing)\, c^{\text{active}}$. We have assumed that $\varnothing = 0$, so k_2 from our fit may be larger than the true rate constant by a factor of $1 + \varnothing$. In comparing the rates between systems, we found that the

k_1/k_2c_0 value for all systems is ≪ 1 as is characteristic of autocatalytic reactions (**3**, **10**, and **13** are 0.00064, 0.0012 and 0.00014, respectively).

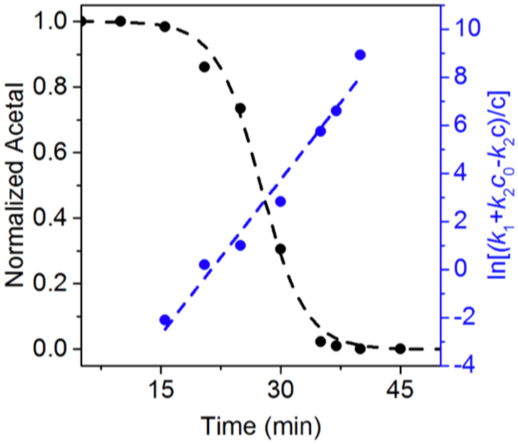

Figure 4.12 Representative data fitting for monitoring the disappearance of acetal functionality of **3** by ^{1}H NMR as a 48 mM solution in D_2O at 70 °C. Dashed lines are fits of the data to Equation 1.5 (R^2 = 0.997) and dotted lines are provided to guide the eye.

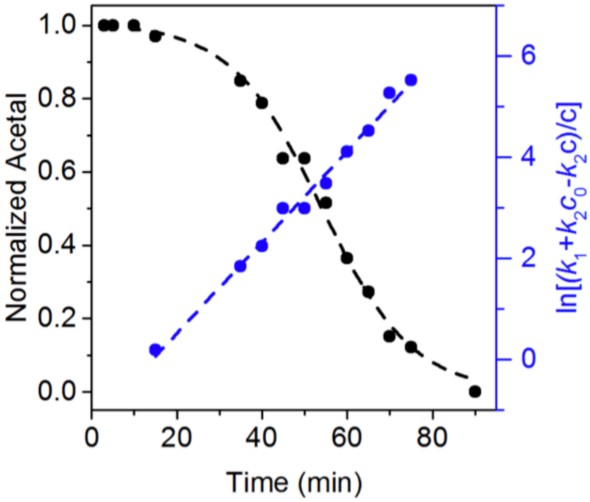

Figure 4.13 Representative data fitting for monitoring the disappearance of acetal functionality of **10** by ^{1}H NMR as a 3 mM solution in D_2O/CD_3CN at 70 °C. Dashed lines are fits of the data to Equation 1.5 (R^2 = 0.983) and dotted lines are provided to guide the eye.

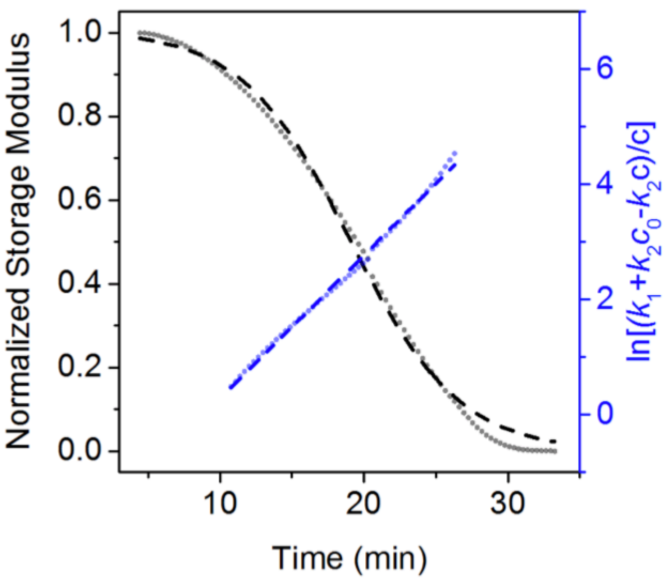

Figure 4.14 Representative data fitting for monitoring the disappearance of acetal functionality of **13** by rheology at 90 °C. Data points are shown as small faded circle symbols. Dashed lines are fits of the data to Equation 1.5 (R^2 = 0.997) and dotted lines are provided to guide the eye.

4.5 GPC traces and NMR spectra

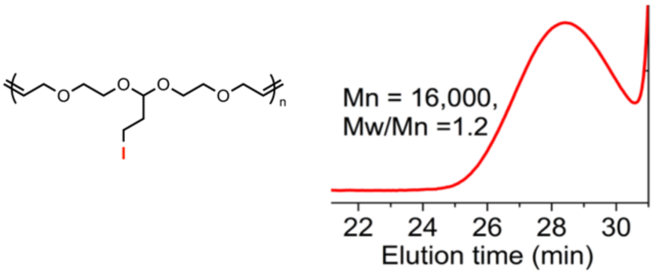

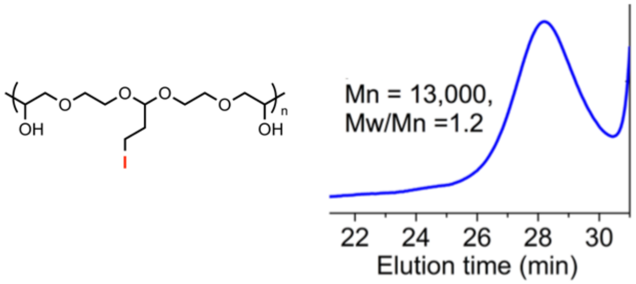

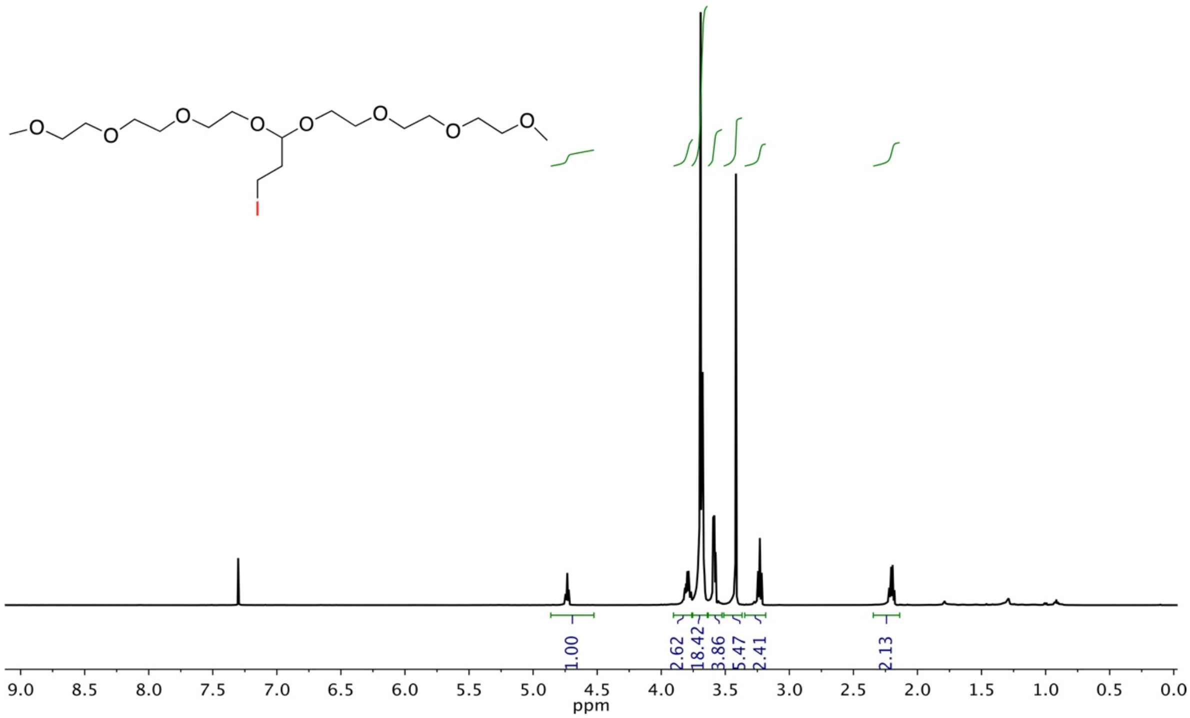
O
O
O
O
O
O
O
O
I
1.00
2.62
18.42
3.86
5.47
2.41
2.13
9.0 8.5 8.0 7.5 7.0 6.5 6.0 5.5 5.0 4.5 4.0 3.5 3.0 2.5 2.0 1.5 1.0 0.5 0.0
ppm

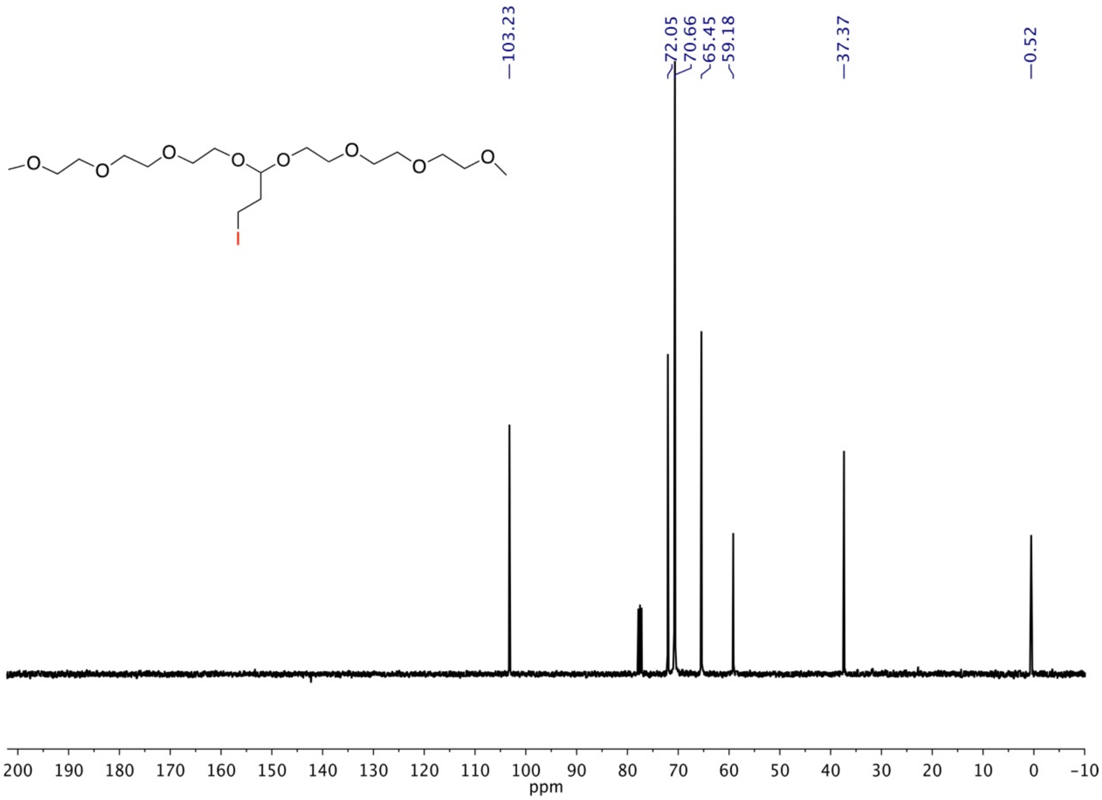
103.23
72.05
70.66
65.45
59.18
37.37
0.52
O
O
O
O
O
O
O
O
I
200 190 180 170 160 150 140 130 120 110 100 90 80 70 60 50 40 30 20 10 0 −10
ppm

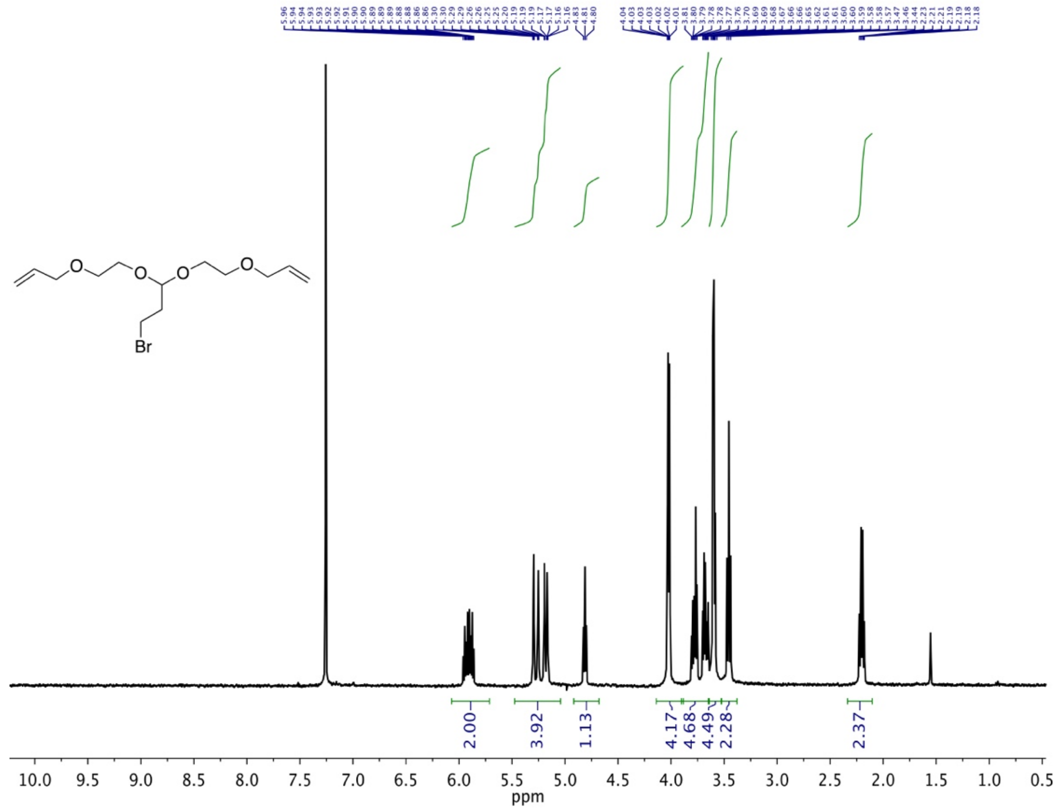

5.96
5.94
5.94
5.93
5.93
5.92
5.92
5.91
5.90
5.90
5.89
5.89
5.89
5.88
5.88
5.86
5.86
5.30
5.30
5.29
5.29
5.26
5.26
5.25
5.25
5.20
5.19
5.19
5.19
5.17
5.17
5.16
5.16
4.83
4.81
4.80
4.04
4.03
4.03
4.03
4.02
4.02
4.01
3.81
3.80
3.79
3.79
3.78
3.78
3.77
3.76
3.70
3.69
3.69
3.68
3.67
3.66
3.66
3.65
3.62
3.61
3.61
3.60
3.60
3.59
3.58
3.58
3.57
3.47
3.46
3.44
2.23
2.21
2.21
2.19
2.18
2.18
O
O
O
O
Br
2.00
3.92
1.13
4.17
4.68
4.49
2.28
2.37
10.0
9.5
9.0
8.5
8.0
7.5
7.0
6.5
6.0
5.5
5.0
4.5
4.0
3.5
3.0
2.5
2.0
1.5
1.0
0.5
ppm

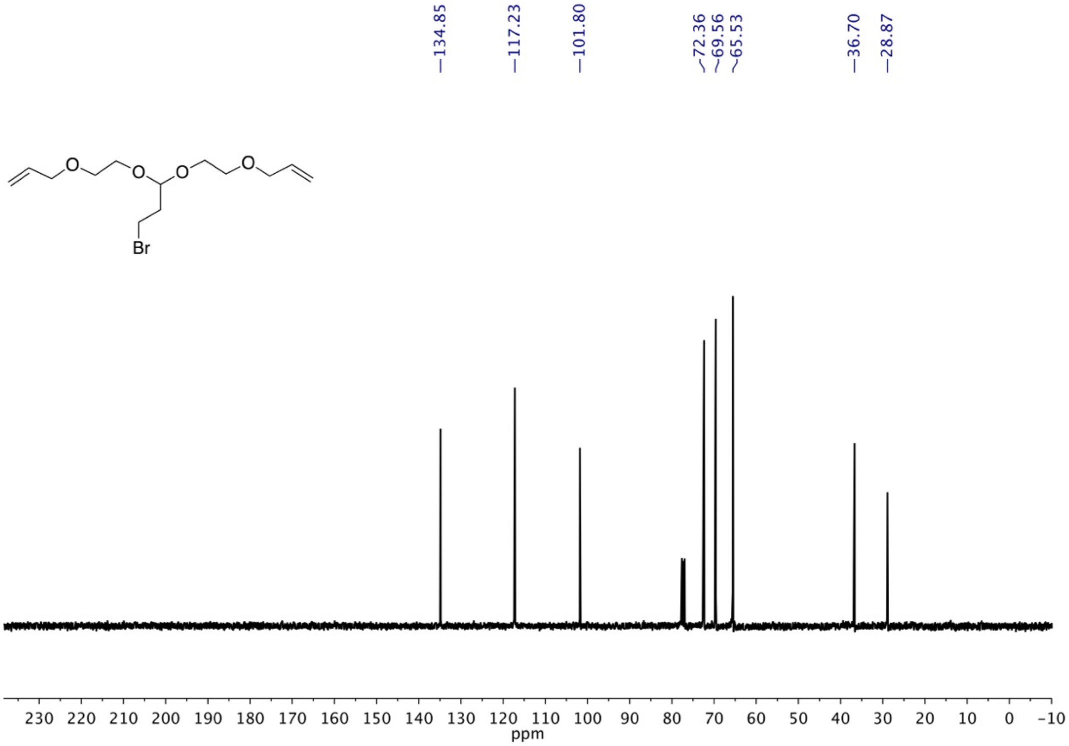

134.85
117.23
101.80
72.36
69.56
65.53
36.70
28.87
O
O
O
O
Br
230
220
210
200
190
180
170
160
150
140
130
120
110
100
90
80
70
60
50
40
30
20
10
0
−10
ppm

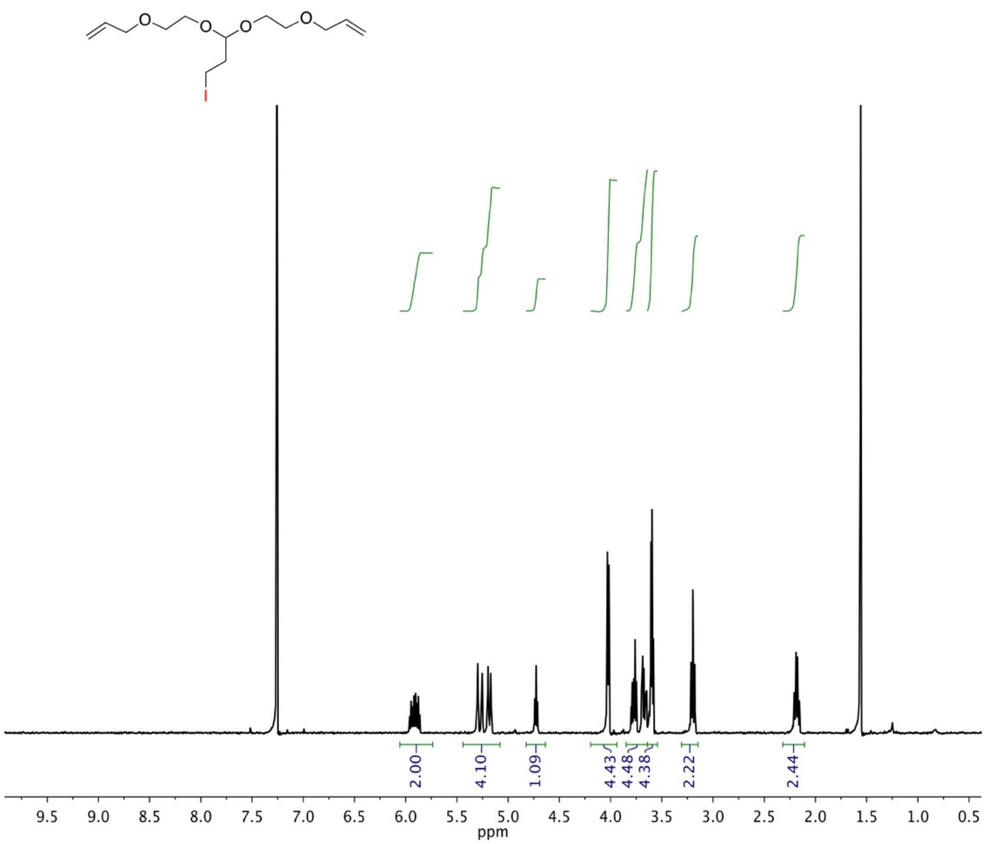
O
O
O
O
I
2.00
4.10
1.09
4.43
4.48
4.38
2.22
2.44
9.5 9.0 8.5 8.0 7.5 7.0 6.5 6.0 5.5 5.0 4.5 4.0 3.5 3.0 2.5 2.0 1.5 1.0 0.5
ppm

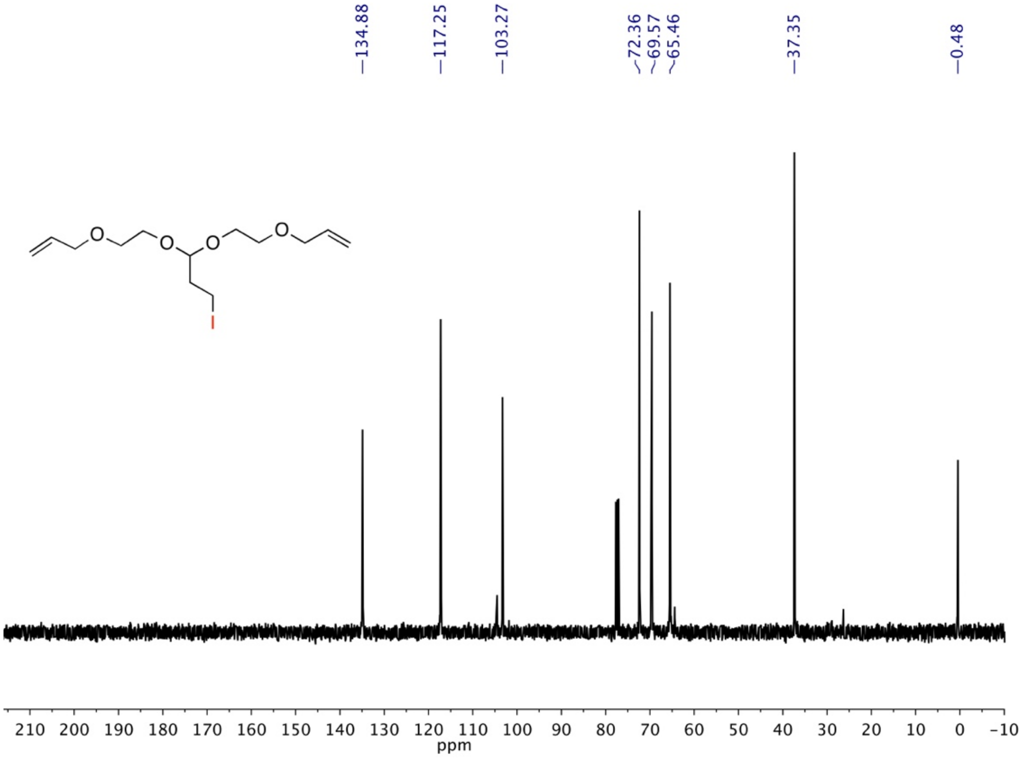
134.88
117.25
103.27
72.36
69.57
65.46
37.35
0.48
O
O
O
O
I
210 200 190 180 170 160 150 140 130 120 110 100 90 80 70 60 50 40 30 20 10 0 −10
ppm

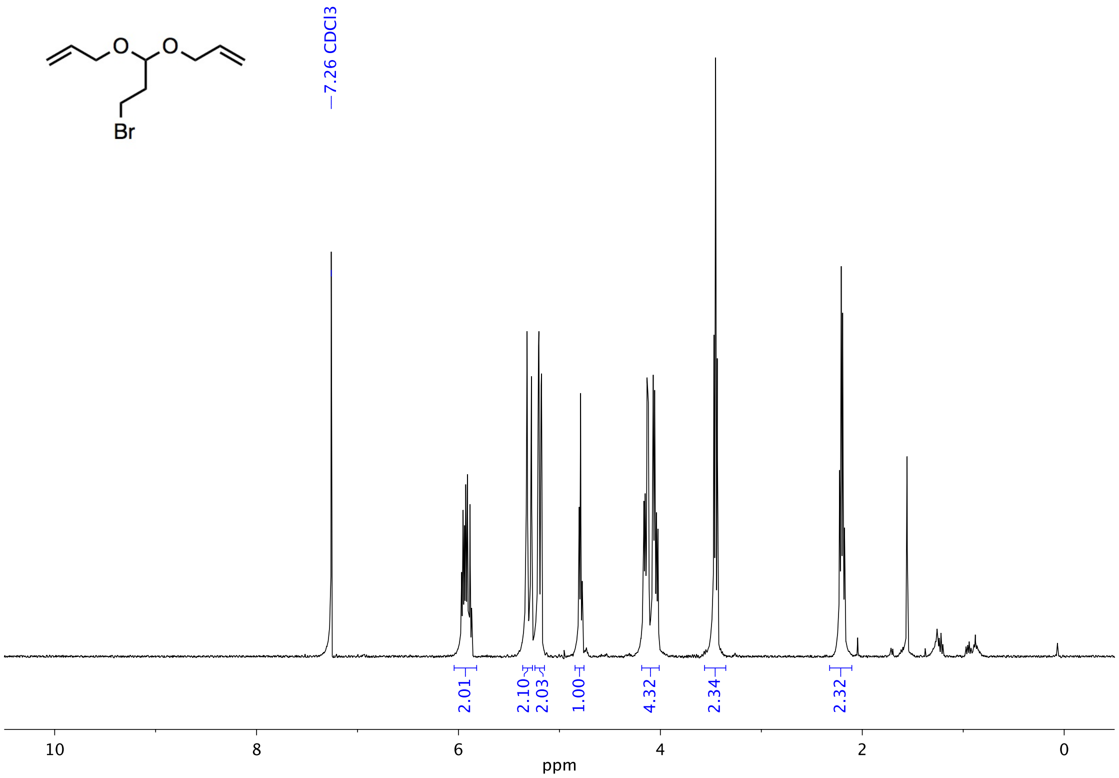
O
O
Br
7.26 CDCl3
2.01
2.10
2.03
1.00
4.32
2.34
2.32
10
8
6
4
2
0
ppm

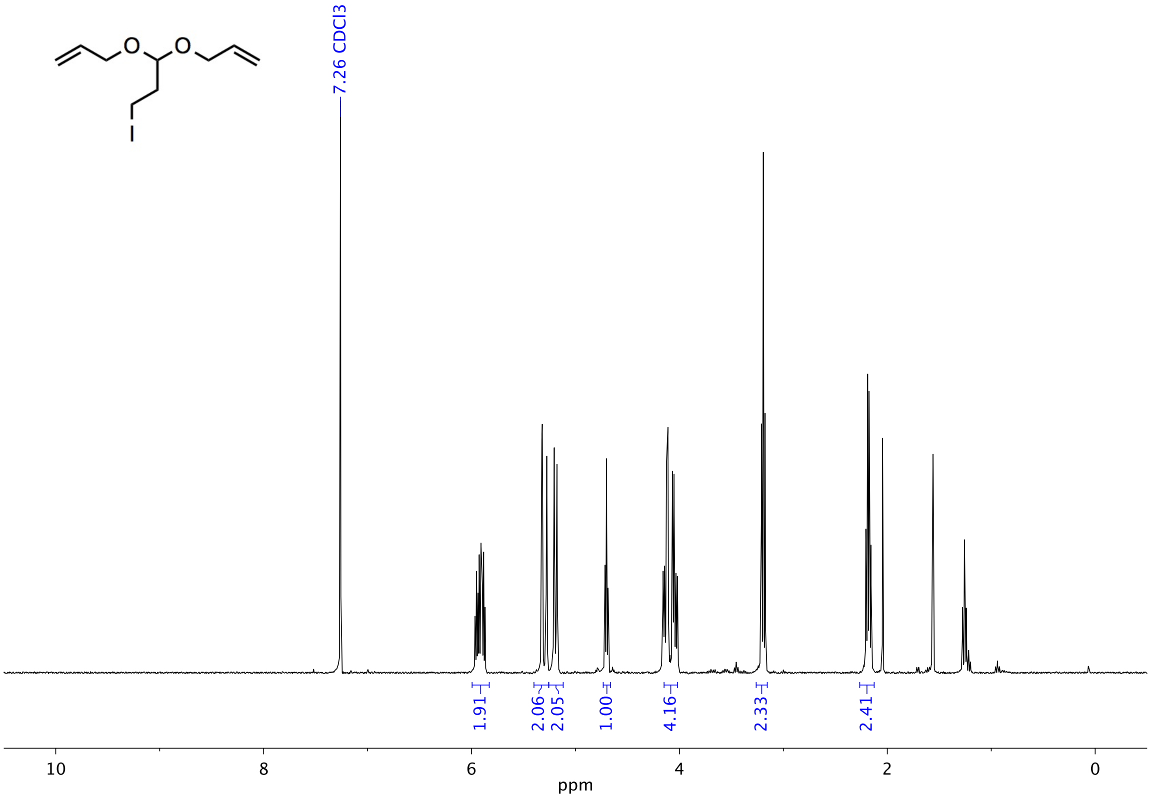
O
O
I
7.26 CDCl3
1.91
2.06
2.05
1.00
4.16
2.33
2.41
10
8
6
4
2
0
ppm

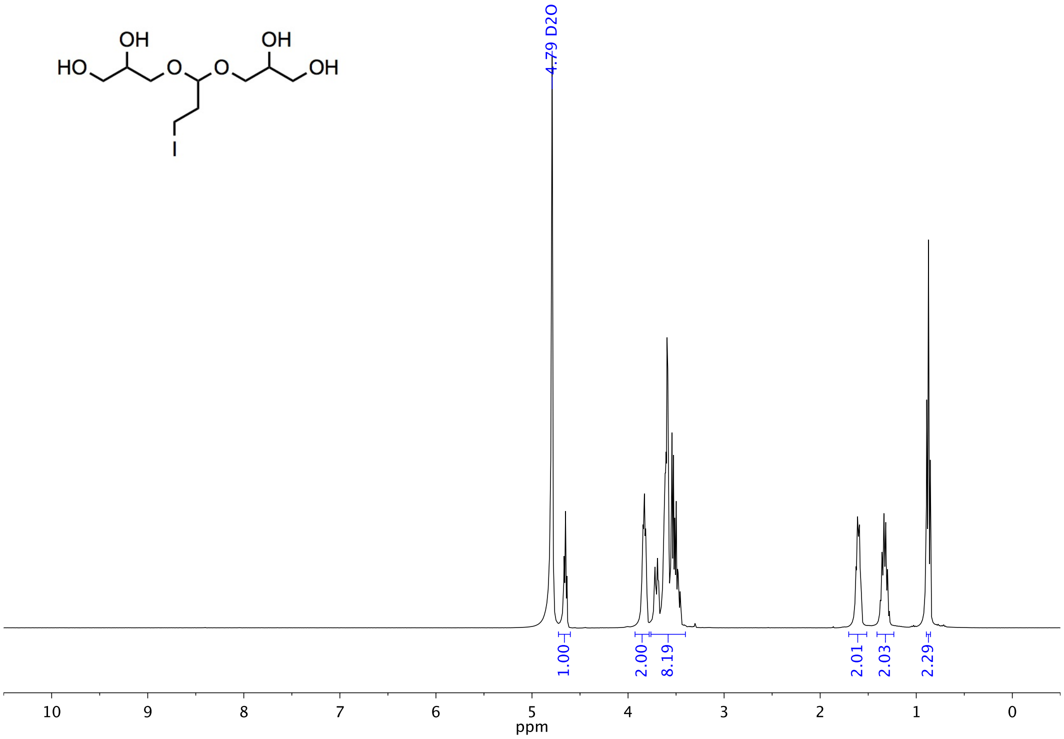
HO
OH
O
O
OH
OH
I
4.79 D2O
1.00
2.00
8.19
2.01
2.03
2.29
10
9
8
7
6
5
4
3
2
1
0
ppm

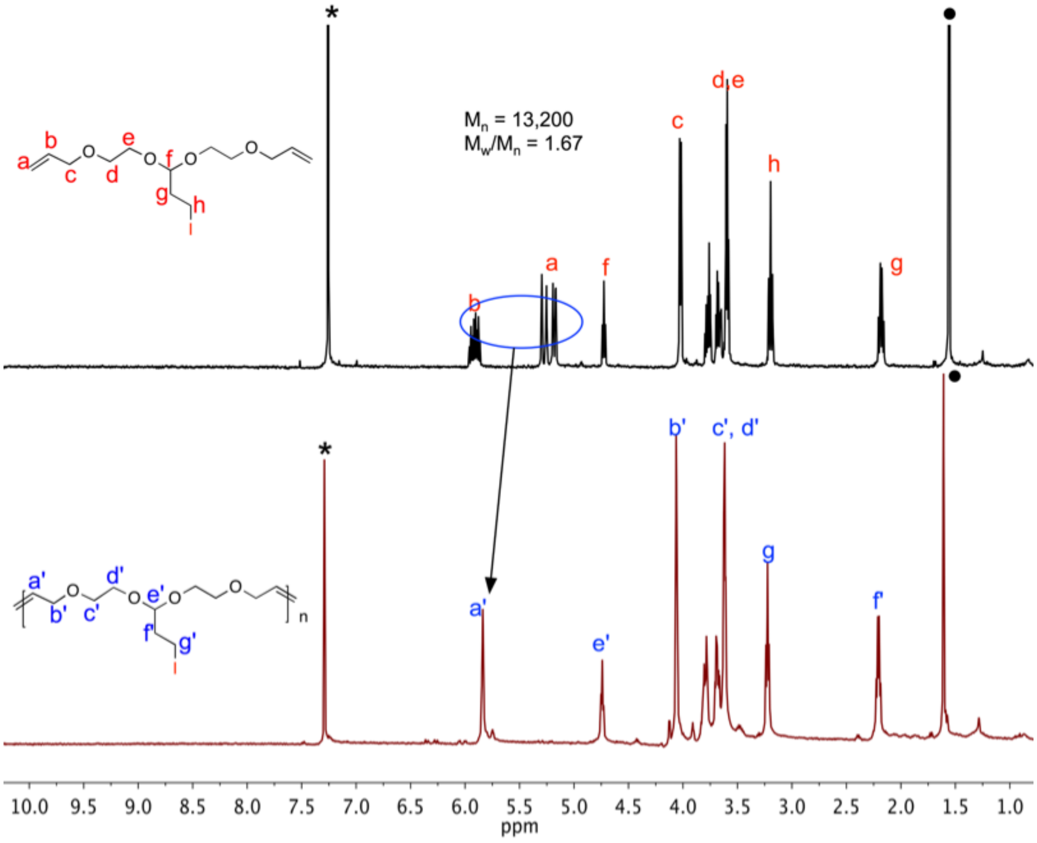
*
●
a
b
c
d
e
f
g
h
I
O
M_n = 13,200
M_w/M_n = 1.67
d,e
c
h
a
f
b
g
*
●
a'
b'
c'
d'
e'
f'
g'
I
n
b'
c', d'
g
f'
a'
e'
10.0
9.5
9.0
8.5
8.0
7.5
7.0
6.5
6.0
5.5
5.0
4.5
4.0
3.5
3.0
2.5
2.0
1.5
1.0
ppm

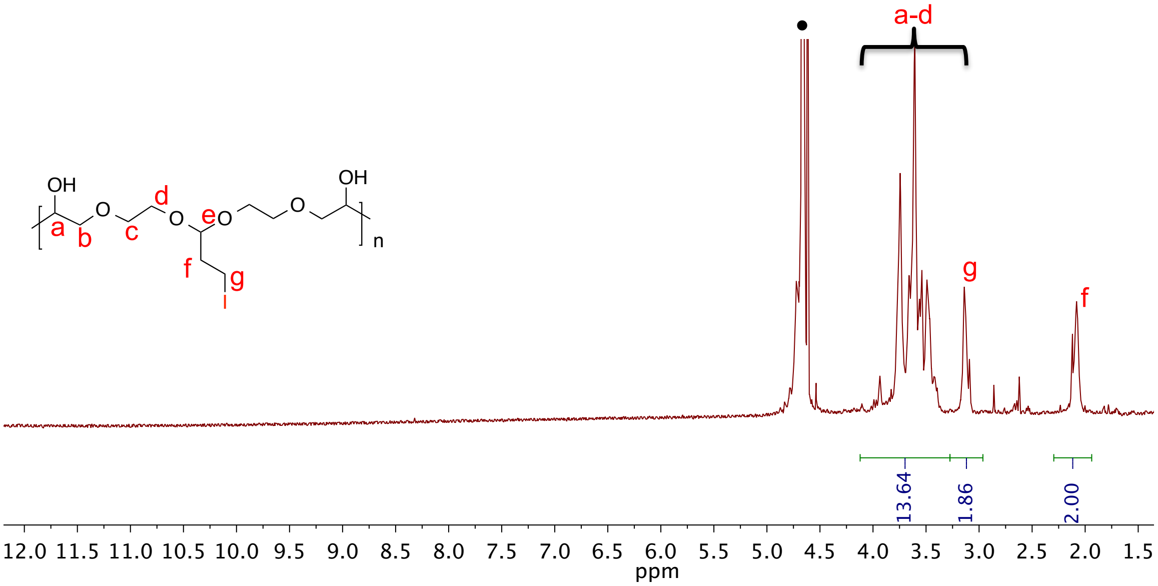
OH
OH
O
O
O
O
O
a
b
c
d
e
f
g
I
n
a-d
g
f
13.64
1.86
2.00
12.0 11.5 11.0 10.5 10.0 9.5 9.0 8.5 8.0 7.5 7.0 6.5 6.0 5.5 5.0 4.5 4.0 3.5 3.0 2.5 2.0 1.5
ppm

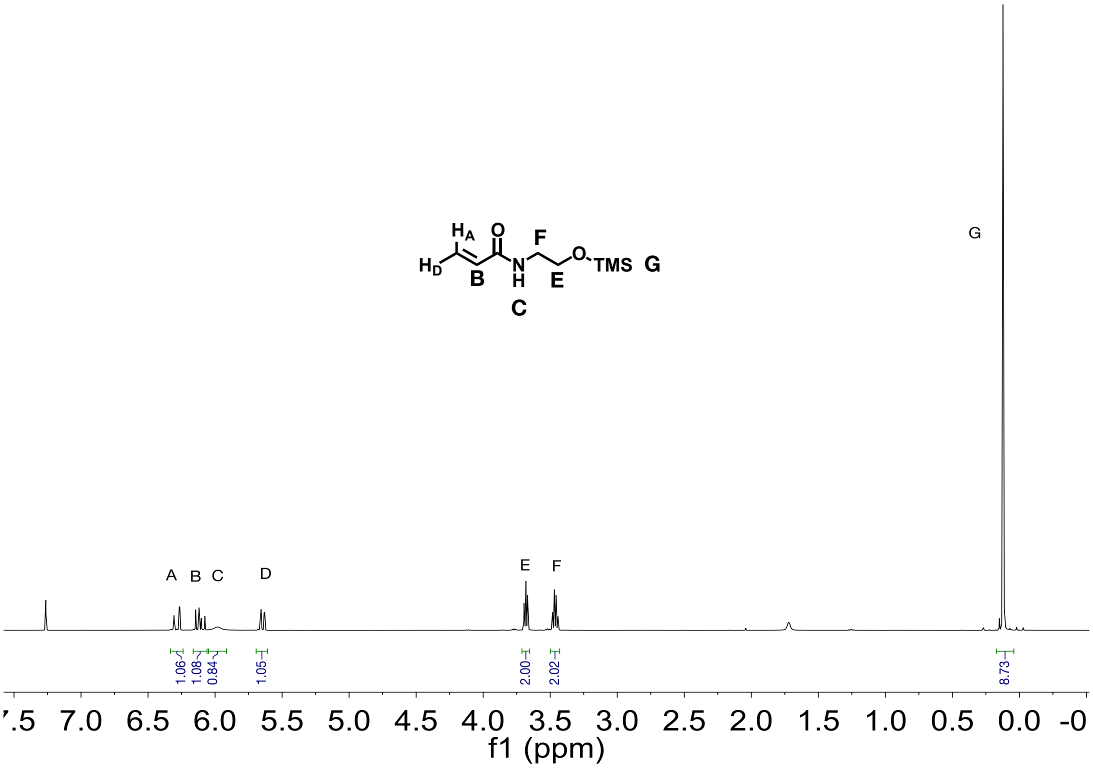
H_A
O
F
H_D
B
N
H
E
O
TMS
G
C
G
A
B
C
D
E
F
1.06
1.08
0.84
1.05
2.00
2.02
8.73
7.5 7.0 6.5 6.0 5.5 5.0 4.5 4.0 3.5 3.0 2.5 2.0 1.5 1.0 0.5 0.0 -0
f1 (ppm)

Crude ^1H NMR ($CDCl_3$, 400 MHz)

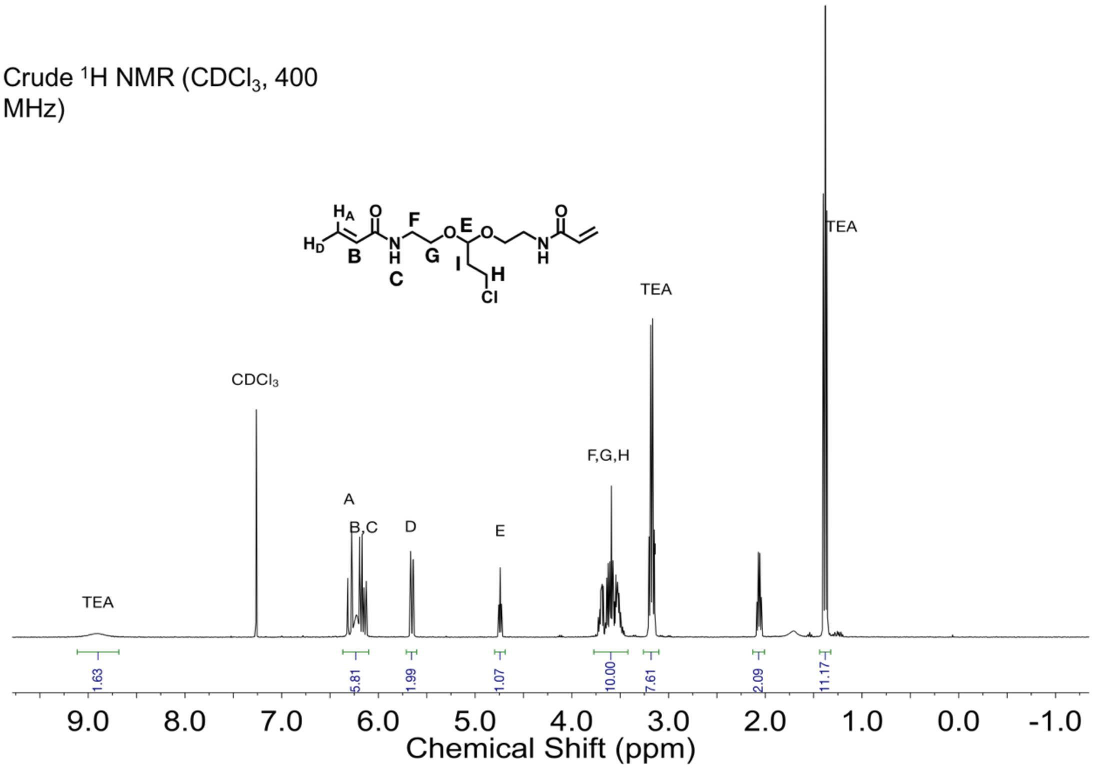

^1H NMR ($CDCl_3$, 400 MHz)

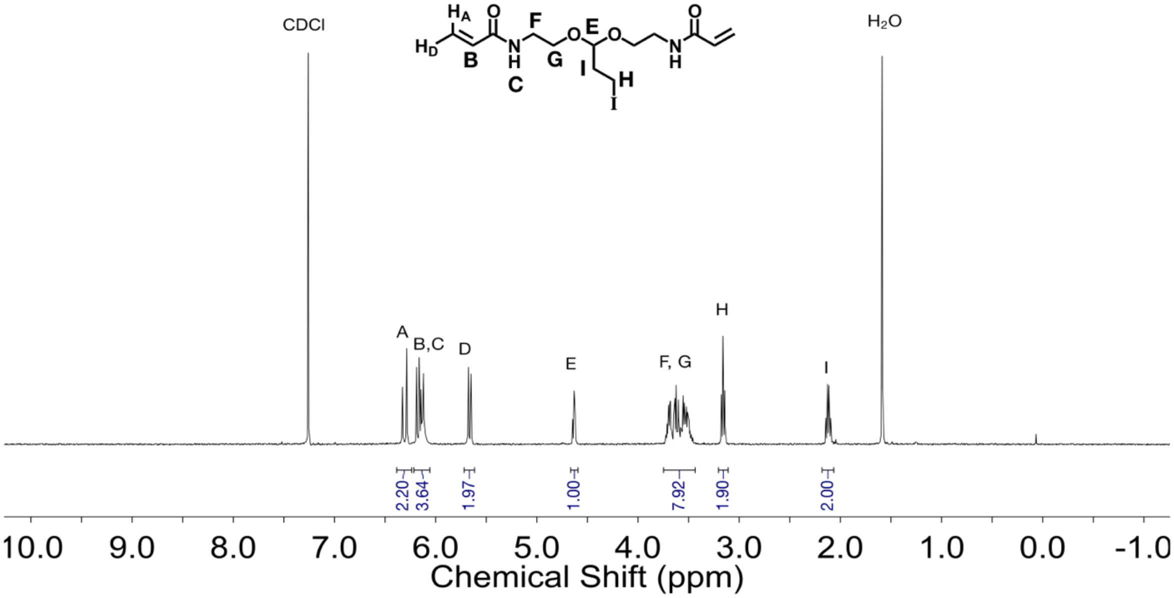

4.6 References

1. For lead reviews of stimuli responsive polymers, see: (a) Stuart, M. A. C.; Huck, W. T. S.; Genzer, J.; Muller, M.; Ober, C.; Stamm, M.; Sukhorukov, G. B.; Szleifer, I.; Tsukruk, V. V.; Urban, M.; Winnik, F.; Zauscher, S.; Luzinov, I.; Minko, S. Emerging Applications of Stimuli-Responsive Polymer Materials. *Nat. Mater.* **2010**, *9*, 101-113. (b) Fomina, N.; Sankaranarayanan, J.; Almutairi, A. Photochemical Mechanisms of Light-Triggered Release from Nanocarriers. *Adv. Drug Delivery Rev.* **2012**, *64*, 1005– 1020. (c) Yan, X. Z.; Wang, F.; Zheng, B.; Huang, F. H. Stimuli-Responsive Supramolecular Polymeric Materials. *Chem. Soc. Rev.* **2012**, *41*, 6042-6065. (d) Roy, D.; Brooks, W. L. A.; Sumerlin, B. S. New Directions in Thermoresponsive Polymers. *Chem. Soc. Rev.* **2013**, *42*, 7214-7243. (e) Schattling, P.; Jochum, F. D.; Theato, P. Multi-Stimuli Responsive Polymers–The All-in-One Talents. *Polym. Chem.* **2014**, *5*, 25-36. (f) Lehn, J. M. Perspectives in Chemistry—Aspects of Adaptive Chemistry and Materials. *Angew. Chem., Int. Ed.* **2015**, *54*, 3276– 3289. (g) Wei, M. L.; Gao, Y. F.; Li, X.; Serpe, M. J. Stimuli-Responsive Polymers and Their Applications. *Polym. Chem.* **2017**, *8*, 127-143.
2. For recent reviews of degradable polymers, see: (a) Binauld, S.; Stenzel, M. H. Acid-Degradable Polymers for Drug Delivery: A Decade of Innovation. *Chem. Commun.* **2013**, *49*, 2082-2102. (b) Delplace, V.; Nicolas, J. Degradable Vinyl Polymers for Biomedical Applications. *Nat. Chem.* **2015**, *7*, 771-784. (c) Kamaly, N.; Yameen, B.; Wu, J.; Farokhzad, O. C.Degradable Controlled-Release Polymers and Polymeric Nanoparticles: Mechanisms of Controlling Drug Release. *Chem. Rev.* **2016**, *116*, 2602-2663. (d) Albertsson, A. C.; Hakkarainen, M. Designed to Degrade. *Science* **2017**, *358*, 872-873.
3. (a) Li, S.; Szalai, M. L.; Kevwitch, R. M.; McGrath, D. V. Dendrimer Disassembly by Benzyl Ether Depolymerization. *J. Am. Chem. Soc.* **2003**, *125*, 10516-10517. (b) de Groot, F. M. H.; Albrecht, C.; Koekkoek, R.; Beusker, P. H.; Scheeren, H. W."Cascade-Release Dendrimers" Liberate All End Groups Upon a Single Triggering Event in the Dendritic Core. *Angew. Chem., Int. Ed.* **2003**, *42*, 4490-4494. (c) Amir, R. J.; Pessah, N.; Shamis, M.; Shabat, D. Self-Immolative Dendrimers. *Angew. Chem., Int. Ed.* **2003**, *42*, 4494-4499.
4. (a) Peterson, G. I.; Larsen, M. B.; Boydston, A. J. Controlled Depolymerization: Stimuli-Responsive Self-Immolative Polymers. *Macromolecules* **2012**, *45*, 7317-7328. (b) Wong, A. D.; DeWit, M. A.; Gillies, E. R. Amplified Release Through the Stimulus Triggered

Degradation of Self-Immolative Oligomers, Dendrimers, and Linear Polymers. *Adv. Drug Delivery Rev.* **2012**, *64*, 1031-1045. (c) Wang, H. C.; Zhang, Y. F.; Possanza, C. M.; Zimmerman, S. C.; Cheng, J. J.; Moore, J. S.; Harris, K.; Katz, J. S. Trigger Chemistries for Better Industrial Formulations. *ACS Appl. Mater. Interfaces* **2015**, *7*, 6369-6382.

5. (a) Zhang, Y. F.; Yin, Q.; Yin, L. C.; Ma, L.; Tang, L.; Cheng, J. J. Chain-Shattering Polymeric Therapeutics with On-Demand Drug-Release Capability. *Angew. Chem., Int. Ed.* **2013**, *52*, 6435-6439. (b) Mutlu, H.; Barner-Kowollik, C.Green Chain-Shattering Polymers Based on a Self-Immolative Azobenzene Motif. *Polym. Chem.* **2016**, *7*, 2272-2279.
6. For related self-propagating amplification reaction systems in sensing using small molecules and dendrimers, see: (a) Sella, E.; Shabat, D. Dendritic Chain Reaction. *J. Am. Chem. Soc.* **2009**, *131*, 9934-9936. (b) Mohapatra, H.; Kim, H.; Phillips, S. T. Stimuli-Responsive Polymer Film that Autonomously Translates a Molecular Detection Event into a Macroscopic Change in Its Optical Properties via a Continuous, Thiol-Mediated Self-Propagating Reaction. *J. Am. Chem. Soc.* **2015**, *137*, 12498-12501. (c) Sun, X. L.; Dahlhauser, S. D.; Anslyn, E. V. New Autoinductive Cascade for the Optical Sensing of Fluoride: Application in the Detection of Phosphoryl Fluoride Nerve Agents. *J. Am. Chem. Soc.* **2017**, *139*, 4635-4638. (d) Sun, X.; Shabat, D.; Phillips, S. T.; Anslyn, E. V. Self-Propagating Amplification Reactions for Molecular Detection and Signal Amplification: Advantages, Pitfalls, and Challenges. *J. Phys. Org. Chem.* **2018**, *31*, e3827.
7. (a) Siepmann, J.; Elkharraz, K.; Siepmann, F.; Klose, D. How Autocatalysis Accelerates Drug Release from PLGA-Based Microparticles: A Quantitative Treatment. *Biomacromolecules* **2005**, *6*, 2312-2319. (b) Ford Versypt, A. N.; Pack, D. W.; Braatz, R. D. Mathematical Modeling of Drug Delivery from Autocatalytically Degradable PLGA Microspheres — A Review. *J. Controlled Release* **2013**, *165*, 29-37.
8. (a) Masamoto, J. Modern Polyacetals. *Prog. Polym. Sci.* **1993**, *18*, 1-84. (b) Murthy, N.; Thng, Y. X.; Schuck, S.; Xu, M. C.; Frechet, J. M. J. A Novel Strategy for Encapsulation and Release of Proteins: Hydrogels and Microgels with Acid-Labile Acetal Cross-Linkers. *J. Am. Chem. Soc.* **2002**, *124*, 12398-12399. (c) Visakh, P. M.; Chandran, S. *Polyoxymethylene Handbook: Structure, Properties, Applications and Their Nanocomposites*; John Wiley & Sons, **2014**. (d) Fan, B.; Trant, J. F.; Wong, A. D.; Gillies, E. R. Polyglyoxylates: A Versatile Class of Triggerable Self-Immolative Polymers from Readily Accessible Monomers. *J. Am. Chem.*

Soc. **2014**, *136*, 10116– 10123. (e) Kaitz, J. A.; Lee, O. P.; Moore, J. S.Depolymerizable Polymers: Preparation, Applications, and Future Outlook. *MRS Commun.* **2015**, *5*, 191-204. (f) Liu, B.; Thayumanavan, S. Substituent Effects on the pH Sensitivity of Acetals and Ketals and Their Correlation with Encapsulation Stability in Polymeric Nanogels. *J. Am. Chem. Soc.* **2017**, *139*, 2306-2317.

9. (a) Arimitsu, K.; Kudo, K.; Ichimura, K. Autocatalytic Fragmentation of Acetoacetate Derivatives as Acid Amplifiers to Proliferate Acid Molecules. *J. Am. Chem. Soc.* **1998**, *120*, 37-45. (b) Ichimura, K. Nonlinear Organic Reactions to Proliferate Acidic and Basic Molecules and Their Applications. *Chem. Rec.* **2002**, *2*, 46– 55.
10. (a) Hsung, R. P. An Improved Synthesis of 2-(β-Bromoethyl)-2-methyl-1,3-dioxolane, A Useful Methyl Vinyl Ketone Equivalent. *Synth. Commun.* **1990**, *20*, 1175-1179. (b) Paquette, L. A.; Tae, J. Stereocontrolled Preparation of Spirocyclic Ethers by Intramolecular Trapping of Oxonium Ions with Allylsilanes. *J. Org. Chem.* **1996**, *61*, 7860-7866.
11. (a) Mata-Perez, F.; Perez-Benito, J. F. The Kinetic Rate Law for Autocatalytic Reactions. *J. Chem. Educ.*1987, *64*, 925-927. (b) Perez-Benito, J. F. Permanganate Oxidation of α-Amino Acids: Kinetic Correlations for the Nonautocatalytic and Autocatalytic Reaction Pathways. *J. Phys. Chem. A* **2011**, *115*, 9876-9885. (c) Lee, O. P.; Lopez Hernandez, H.; Moore, J. S. Tunable Thermal Degradation of Poly(vinyl butyl carbonate sulfone)s via Side-Chain Branching. *ACS Macro Lett.* **2015**, *4*, 665-668. (d) Ashley, B.; Vakil, P. N.; Dyer, C. M.; Tracy, J. B.; Owens, J.; Lynch, B. B.; Strouse, G. F. Microwave Enhancement of Autocatalytic Growth of Nanometals. *ACS Nano* **2017**, *11*, 9957-9967.
12. (a) Hsung, R. P. An Improved Synthesis of 2-(Beta-Bromoethyl)-2-Methyl-1,3-Dioxolane, a Useful Methyl Vinyl Ketone Equivalent. *Synthetic Commun* **1990,** *20* (8), 1175-1179. (b) Paquette, L. A.; Tae, J. S. Stereocontrolled preparation of spirocyclic ethers by intramolecular trapping of oxonium ions with allylsilanes. *J. Org. Chem.* **1996,** *61* (22), 7860-7866.
13. (a) Molander, G. A.; Figueroa, R. cis-dihydroxylation of unsaturated potassium alkyl- and aryltrifluoroborates. *Org. Lett.* **2006,** *8* (1), 75-78. (b) Bai, Y. G.; Xing, H.; Vincil, G. A.; Lee, J.; Henderson, E. J.; Lu, Y.; Lemcoff, N. G.; Zimmerman, S. C. Practical synthesis of water-soluble organic nanoparticles with a single reactive group and a functional carrier scaffold. *Chem Sci* **2014,** *5* (7), 2862-2868.

14. Zhang, C. J.; Sitt, A.; Koo, H. J.; Waynant, K. V.; Hess, H.; Pate, B. D.; Braun, P. V. Autonomic Molecular Transport by Polymer Films Containing Programmed Chemical Potential Gradients. *J Am Chem Soc* **2015,** *137* (15), 50665073.
15. Krezel, A.; Bal, W. A formula for correlating pKa values determined in D_2O and H_2O. *J Inorg Biochem* **2004,** *98* (1), 161-166.

CHAPTER 5: FLUORESCENT TECHNIQUES FOR THE DIRECT IMAGING OF PROTEIN STABILITY AND FOLDING KINETICS IN HYDROGELS[1]

5.1 Introduction

A major challenge in exploiting the unique functions of biomacromolecules in engineered devices is the inherent protein incompatibility of commonly used materials. Such materials, including silicon, metal oxides, hydrophobic coatings, or highly charged materials, destabilize protein structures and can lead to adverse effects such as aggregation, biofouling, and degradation that reduce device performance. Hydrogels—cross-linked networks of water-soluble polymers—are widely used in diverse biotechnological and clinical applications such as tissue engineering,[1] drug delivery,[2] microfluidics,[3] sensors,[4] and separation methods,[5] among others. The dielectric constants, polymer solvation, and hydrogen bonding properties in hydrogels are believed to mimic the solvation environment most conducive to protein stability. The polymer solvation shells are also believed to repel proteins and thereby prevent close interaction of the protein with the potentially destabilizing polymer matrix.[6-9]

This simple picture fails to capture the complexity of protein–hydrogel interactions. For example, poly(carboxybetaine) hydrogels and polyacrylamide brushes exhibited counterintuitive trends of reduced protein adsorption at low cross-linking and grafting densities.[10-11] Additionally, despite its reported protein resistance and biocompatibility, poly(ethylene oxide) binds proteins and appears to function like a chaperone that prevents protein aggregation.[12-15] Inhomogeneities in materials may also disproportionately affect protein stability. These observations motivate the need for in situ approaches for identifying material properties that affect protein function.

However, interrogating the influence of materials on protein stability has been a major challenge. Bulk activity measurements provide no information on the spatial distribution or state of the remaining active protein. Instruments used to interrogate the structures of interfacial protein can have limited chemical sensitivity, lack spatial or temporal information, or cannot probe proteins in situ. For example, surface plasmon resonance and quartz crystal microbalance measurements quantify interfacial protein adsorption[16] but cannot assess the folded state or activity

---

[1] Reproduced with permission from: Kisley, L.; Serrano, K. A.; Kong, X.; Gruebele, M.; Leckband, D. E. Direct Imaging of Protein Stability and Folding Kinetics in Hydrogels. *ACS Appl. Mater. Interfaces* **2017**, *9 (26)*, 21606-21607. Copyright 2017 American Chemical Society.

of the protein. Circular dichroism[17] lacks the sensitivity necessary to specifically detect protein secondary structure at surfaces or in materials that scatter light.[18] X-ray photoelectron spectroscopy can detect side chain exposure during protein adsorption and unfolding but requires ultrahigh-vacuum conditions.[19] Raman and infrared spectroscopies have limited sensitivity unless metallic substrates are used to enhance signal.[20-21] Deuterated water can be used to shift protein absorption spectra into an optimal wavelength window, but organic polymers may obscure protein bands even upon deuteration of the solvent. Infrared–visible sum frequency generation spectroscopy has been more successful at revealing in situ structural dynamics of proteins at interfaces,[22-23] but links between spectral changes, the folded state, and function are indirect. In a convincing demonstration of single-molecule fluorescence resonance energy transfer (FRET), it was observed that lysozyme diffuses in a folded state until unfolding at specific strong adsorption sites on glass surfaces, where it gets stuck.[24]

Fast relaxation imaging (FReI) can quantify the equilibrium thermodynamic and kinetic signatures of proteins via changes in FRET on a conventional epifluorescence microscope platform. Changes in protein folding and stability are imaged by monitoring differences in FRET following a temperature jump perturbation.[25] FReI has been used to study how local microenvironments influence the structure, thermal stability, and folding of model proteins in live cells.[26,27] We now extend this approach to study proteins at biomaterial interfaces. We applied FReI to study the folding dynamics of two model proteins in hydrogels with different cross-linking in situ. Our studies used polyacrylamide as the initial model hydrogel, due to its ease of preparation and widespread use in a range of biological applications.[28-30] We used the protein CrH2, with two conformationally flexible alpha-helical peptides that are sensitive to crowding, to serve as a molecular conformational "rheostat" for confinement within the hydrogel.[31,32] We then used phosphoglycerate kinase (PGK), whose cooperative folding and stability have been extensively studied and are known to be sensitive to small environmental influences.[33] Labeling CrH2 or PGK with a FRET pair (PGK-FRET) enables direct observations of structural perturbations in response to the local microenvironment in the hydrogels.

Our findings demonstrate that polyacrylamide gels are mildly stabilizing for PGK, but they also promote aggregation of PGK once the protein unfolds at higher temperature. FReI demonstrates that noncovalent protein interactions with the polymer are a stronger factor in this behavior than simple confinement: the results in the hydrogel differ from free solution, but the 4%

and 10% polyacrylamide hydrogel results resemble each other, despite the different degree of cross-linking. Results from fluorescence recovery after photobleaching (FRAP) showed the irreversible recovery of adsorbed PGK-FRET at the surface and within the hydrogel with the better recovery of CrH2 under identical hydrogel conditions. Future studies enabled by this new analytical approach will lead to a better understanding of material properties that preserve immobilized protein functions in diverse interfacial environments.

5.2 Results

5.2.1 FReI reports position-dependent protein stability and folding kinetics in hydrogels

FReI images the changes in FRET during a temperature jump perturbation in order to interrogate protein-folding stability and kinetics. See Figure 1.6 for information about the experimental FReI setup. The time-dependent infrared laser light is absorbed by the water (Figure 5.6a, black curve),[34] heating the sample and increasing the temperature (Figure 5.6a, blue curve). Each laser power spike, when convoluted with the thermal conductivity properties of the sample, leads to a step-shaped 4-6 °C increase in temperature that equilibrates within milliseconds of the initial jump. The subsequent slower ramp of the continuous wave laser power maintains a constant temperature between jumps. Thus, the temperature increases in a series of steps as a function of time. To allow for fast measurements of protein unfolding thermodynamics as a function of temperature, the computer-controlled infrared laser was programmed to generate multiple, successive temperature jumps, with 8 s dwell times for equilibration.[35] Observing the increase in the ratio of donor to acceptor fluorescent intensity (D/A) quantifies the protein unfolding under each temperature perturbation (Figure 5.6b). An increase in D/A indicates that donor and acceptor are more separated; this could, for example, be due to protein unfolding. A decrease in D/A indicates that the donor and acceptor are closer together. The latter could, for example, be due to protein aggregation or increased crowding.

Three types of measurements were performed on the samples: (1) temperature titrations to assess how the protein unfolds in the gel; (2) temperature jumps to follow folding kinetics; (3) axial *z* scans and lateral pixel-by-pixel analysis to see how the protein is distributed in the gel, how heterogeneous the stability is as a function of position within the gel, and to detect solution–gel boundaries within the sample. Prior to analyzing our FReI temperature titration measurements, controls on the confinement and diffusion behavior of CrH2 and PGK-FRET were performed to determine how unfolding, irreversible aggregation, and confinement are coupled so that we could select the appropriate thermodynamic models to fit the data.[36]

5.2.2 Crowding sensor CrH2 reveals confinement only in the 10% cross-linked hydrogel

CrH2 senses confinement within the hydrogels, and we detected substantial confinement only in the most cross-linked (10%) gel. Here, we use the term "confinement" for the polyacrylamide because it is a stable cross-linked network, as opposed to "crowding", which refers to the volume exclusion by diffusive macromolecules of similar size to the sample protein.[36-39] The CrH2 sensor is insensitive to temperature (Figure 5.8) but undergoes changes in D/A up to 50% due to the adoption of a more compact conformation in the presence of 40% Ficoll, a macromolecular crowding agent (Figure 5.1a and 5.7). When introduced into the hydrogels, CrH2 has a similar value of D/A in the 4% hydrogel as in solution, equivalent to ~4% Ficoll. CrH2 has a much reduced value of D/A only in the 10% hydrogel, equivalent to ~27% Ficoll (Figure 5.1b).

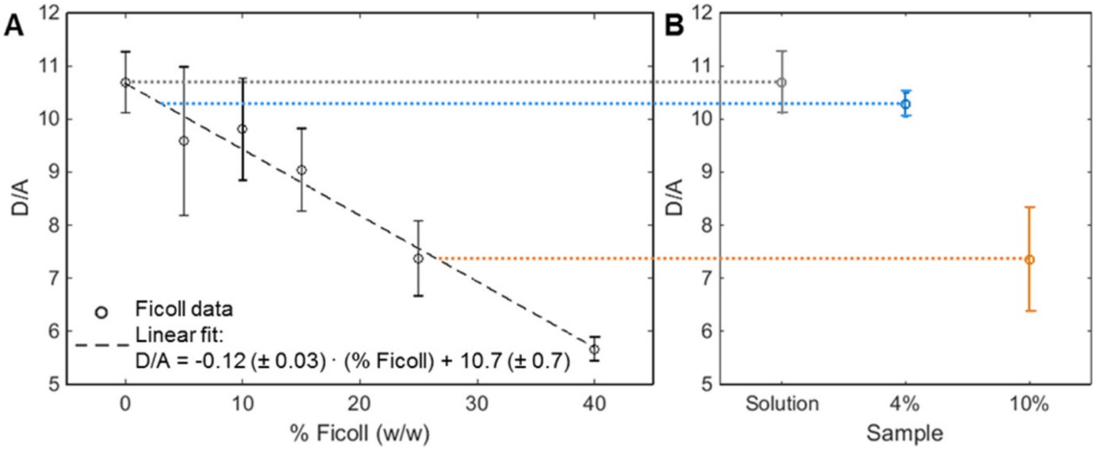

Figure 5.1 CrH2 senses differences in confinement within hydrogels. (a) Calibration of AcGFP-CrH2-mCherry on the FReI microscope with a macromolecular crowding agent, Ficoll. (b) Results of D/A for AcGFP-CrH2-mCherry in the 4% and 10% hydrogels. Dashed lines provided as a guide to the equivalent confinement in Ficoll solutions and in hydrogels.

5.2.3 CrH2 does not adsorb on the hydrogels, even at higher temperature

We quantified irreversible adsorption by FRAP. The majority of CrH2 signal both in the bulk and at the surface of the hydrogel recovered after bleaching under equilibrium (Figure 5.2a). FRAP determines the diffusion properties of fluorescently labeled proteins by selectively photobleaching a spot and monitoring the recovery as unbleached proteins exchange with bleached proteins in the spot under equilibrium (Figure 5.2a).[40] We measured FRAP both near the surface and ~20 μm into the bulk hydrogel using the confocal capabilities of the separate FRAP microscope. With Equation 1.8 we fitted the fraction of fluorescence recovered from the bleaching A, the anomalous stretching factor α (deviation from simple exponential relaxation), and the characteristic diffusion time τ_D. We then calculated the diffusion coefficient D using τ_D and Equation 1.9.

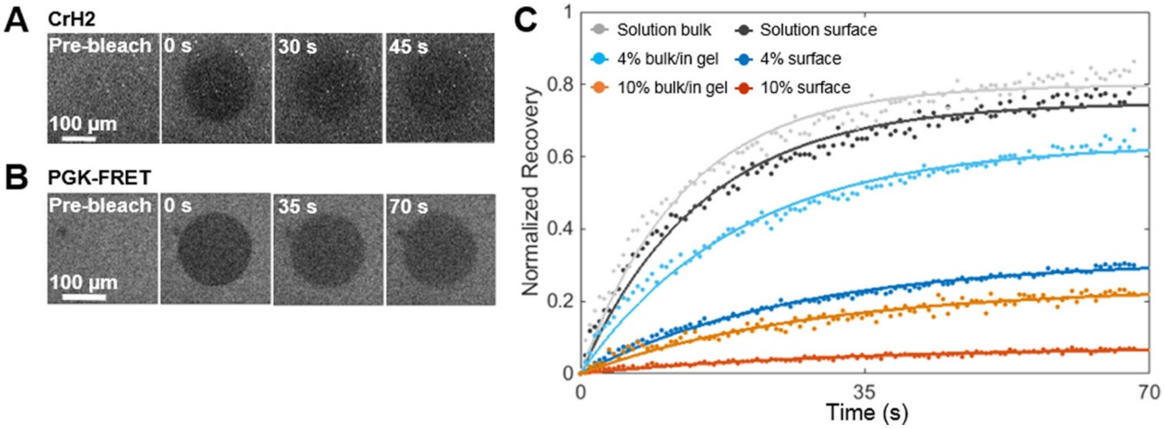

Figure 5.2 PGK-FRET aggregates and is irreversibly adsorbed to the hydrogel, while CrH2 does not interact strongly with the hydrogel. (a, b) Example FRAP images from 20 μm within the bulk of the 10% hydrogel of (a) CrH2 and (b) PGK-FRET. (c) FRAP measurements of PGK-FRET at 22 °C. Normalized fluorescence within a 80 μm radius photobleached spot at the hydrogel surface and within the bulk of the hydrogel as a function of time after photobleaching. Fluorescence is normalized to the prebleach intensity. Curves reflect fluorescence recovery at the surface or in the bulk of the 4% and 10% hydrogels and in solution. Solid lines are fits of the data to Equation 1.8, with the best-fit parameters averaged from six trials summarized in Table 5.1. FRAP curves of CrH2 provided as Figure 5.10.

Figure 5.2a shows CrH2 recovery after bleaching. Recovery is comparable to the magnitude of CrH2 recovery in solution (A = 80 ± 10%, Figure 5.10). The fraction recovered in solution is below 1, probably due to protein aggregation at the surface of the glass coverslip. Further measurements of D/A of CrH2 at different temperatures show that protein does not interact with the hydrogels, even at elevated temperature (Figure 5.11).

5.2.4 FRAP measurements show that PGK-FRET irreversibly adsorbs to the hydrogel

The results for the cooperative folder PGK-FRET are in contrast with the crowding sensor CrH2. Representative images and recovery curves with fits to Equation 1.8 are shown in Figure 5.2b and 5.2c, with the resulting fitting parameters reported in Table 5.1.

Table 5.1 FRAP Fitting Results of PGK-FRET Diffusion at Surface and within Hydrogel.

sample	**fraction recovered, *A***	**anomalous exponent, α**	***D* ($\mu m^2/s$)**
solution, bulk	0.80 ± 0.01	1	33 ± 1
4%, bulk	0.60 ± 0.1	0.99 ± 0.01	23 ± 2
10%, bulk	0.24 ± 0.05	0.88 ± 0.05	
solution, surface	0.66 ± 0.13	1	29 ± 2
4%, surface	0.4 ± 0.2	0.98 ± 0.03	21 ± 6
10%, surface	0.09 ± 0.02	0.89 ± 0.05	

In solution, PGK-FRET undergoes Brownian diffusion ($\alpha = 1$) with the homogeneous diffusion coefficient of 33 ± 1 $\mu m^2/s$ at $T = 22$ °C. This agrees with the expected value based on an approximate hydrodynamic radius (R_h) of ~8 nm for PGK-FRET based on the size of PGK and the respective fluorescent protein labels.[41,42] In the 4% hydrogel, the protein still undergoes normal diffusion ($\alpha \approx 1$) with smaller D (23 ± 2 $\mu m^2/s$ in the hydrogel bulk) due to the hindered diffusion within the 4% hydrogels. In the 10% hydrogel, the signal recovery after bleaching was small as to make it impossible to determine a reliable value of D. However, the recovery kinetics fit Equation 1.8 with a value of $\alpha < 1$, which indicates the onset of subdiffusive and more heterogeneous protein behavior that is known to occur in hydrogels.[43]

In both the 4% and the 10% hydrogels, PGK-FRET shows irreversible adsorption to the hydrogel. A decreases by 25% from the bulk solution value in the 4% hydrogel and by 70% in the 10% hydrogel. A in Equation 1.8 ranges from 66% to 80%. In solution, drops to 40–60% in the 4% hydrogel, and finally drops to 9–24% in the 10% hydrogel, depending on whether the sample surface or bulk was probed.

5.2.5 PGK-FRET is stabilized in 4% hydrogel but aggregates more easily upon unfolding

When PGK-FRET is thermally denatured in the hydrogel, the gel could stabilize the protein, shifting the denaturation curve to a higher midpoint temperature T_m or it could have the opposite effect. The gel could also increase the compactness of the protein via confinement, which leads to a smaller D/A value for the unfolded protein. Finally, the gel can facilitate irreversible protein aggregation, which yields a turnover of D/A when labels from different proteins interact.[44] Our confinement sensor and FRAP results show that confinement in the 4% hydrogel is minimal, but irreversible aggregation could occur, thus explaining the reduced diffusion and FRAP recovery. Confinement will be significant in the 10% hydrogel, competing with irreversible aggregation as the main cause for a smaller D/A ratio upon heat denaturation.[39]

To quantify PGK-FRET stability from FReI thermal unfolding data, we first determined the average equilibrated D/A fluorescence intensity ratio during the last 1 s of each temperature step and then plotted the average D/A value normalized by the room-temperature value as a function of the temperature. The resulting plot is a sigmoidal thermal denaturation curve (Figure 5.3a), from which the thermal denaturation midpoint, T_m, is extracted from fits to Equations 5.1a-5.1d[33]

$$\frac{\mathrm{D}}{\mathrm{A}} = (m_\mathrm{F}T + b_\mathrm{F})f_\mathrm{F} + (m_\mathrm{U}T + b_\mathrm{U})f_\mathrm{U} \tag{5.1a}$$

where the fraction of folded and unfolded protein is given by

$$f_\mathrm{F} = \exp\left[-\frac{\Delta G}{RT}\right] \Big/ \left(1 + \exp\left[-\frac{\Delta G}{RT}\right]\right) \tag{5.1b}$$

$$f_\mathrm{U} = 1 - f_\mathrm{F} \tag{5.1c}$$

and the dependence of free energy on temperature over our narrow temperature range is represented by a linear expansion[26]

$$\Delta G \approx \delta g_T (T - T_\mathrm{m}) \tag{5.1d}$$

Here, T_m is the temperature at which 50% of the protein is unfolded, and corresponds to the inflection point of the sigmoidal curve. At this point, the folded fraction f_F and the unfolded fraction f_U are equal. Linear baselines with slopes, *m*, and offsets, *b*, above and below T_m (i.e., folded, F, and unfolded, U) are also incorporated, in order to account for the intrinsic temperature dependence of the FRET probes via their quantum yields.[33] As shown in ref 33, the small systematic error in T_m introduced by fitting the ratio D/A to Equations 5.1a-5.1d has a negligible effect on melting point differences ΔT_m between various samples.

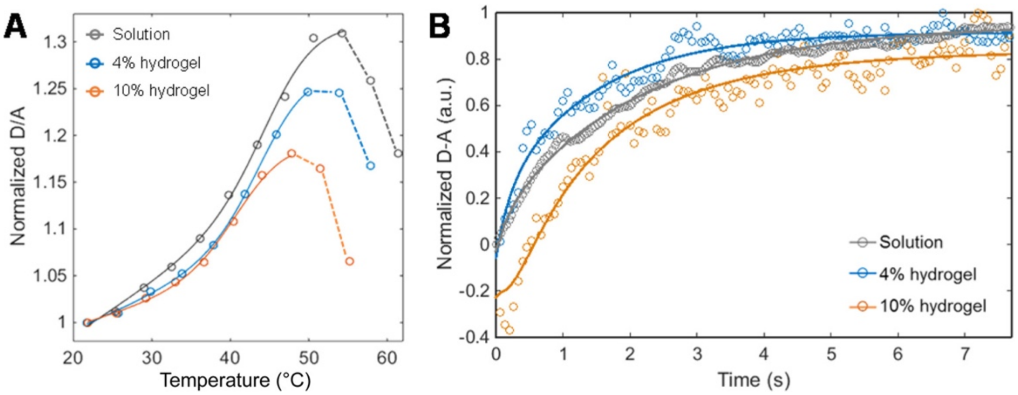

Figure 5.3 FReI measurements of equilibrium thermodynamics and folding kinetics of PGK-FRET in solution, in 4% polyacrylamide, and in 10% polyacrylamide. (a) Equilibrium thermodynamic melt of PGK-FRET normalized to the D/A value measured at room temperature. Fits to Equations 5.1a-5.1d listed in Table 5.1 are shown as solid lines, while dashed lines are provided to guide the eye where the turnover to aggregation occurs. The 4% hydrogel denaturation curve is shifted to slightly higher temperature in the hydrogel but turns over at lower temperature in the hydrogel than in solution due to aggregation. The 10% hydrogel is also shifted to higher temperature, but its turnover is affected by both aggregation and confinement (see Figure 5.1). (b) Time-dependent PGK-FRET folding near T_m (40–45 °C). Data show the normalized $D(t) - A(t)$ of PGK-FRET as a function of time after a temperature jump. Solid lines represent the fit to a stretched exponential (Equation 5.2), and the best-fit parameters are in Table 5.3. Non-normalized equilibrium thermodynamic melt and folding kinetic data are provided in Figure 5.13.

Representative thermal unfolding curves for PGK-FRET are shown in Figure 5.3a, along with fits of the data to Equations 5.1a-5.1dx. Non-normalized thermal denaturation curves are provided in Figure 5.13a. The important features of the denaturation curves are (1) a small linear slope at low temperature when the protein is in the native state (due to the temperature-dependent quantum yield of the FRET labels),[26] (2) a rapid increase in D/A as the protein unfolds at T_m, (3) leveling off due to confinement or aggregation (both lower the D/A ratio), (4) which is followed by a turnover of the D/A ratio due to irreversible aggregation.

The thermal denaturation curve in Figure 5.3a is shifted by $\Delta T_m \approx +2$ °C in 4% hydrogel relative to bulk solution. Furthermore, PGK-FRET fluorescence is reversible when using temperature jumps up to T_m, confirming that we detect reversible unfolding up to T_m (Figure 5.12). Thus, the hydrogel environment stabilizes PGK-FRET, based on visual qualitative inspection of the melting curves in Figure 5.3a.

A quantitative fit of the melting curves in Figure 5.3a to Equations 5.1a-5.1d supports the view that PGK-FRET is stabilized in the 4% hydrogel, although several assumptions have to be made (Table 5.1). On the basis in the small change of crowding sensor CrH2 response (Figure 5.1), we expect the unfolded state baseline to be very similar in solution and in the 4% hydrogel, although the baseline in Figure 5.3a is obscured by the turnover due to aggregation at >50 °C.

Thus, we fitted the aqueous solution data with the observed intercept $b_U = 1.31$ and a slope m_U ranging from 0 to m_f, yielding T_m(solution) = 44 ± 2 °C (the uncertainty includes systematic error due to unknown baseline slope). We also fitted the 4% hydrogel data with the same b_U and m_U, yielding $\Delta T_m = +1.9 \pm 0.4$ °C. Thus, ΔT_m can be determined more accurately than T_m itself. Figure 5.14 shows that fitting to alternative unfolded baselines at high temperatures yields the same $\Delta T_m \approx +2$ °C.

Table 5.2 Fitting Results of Equations 5.1a–5.1d to FReI Data in Figure 5.3a. T_m in solution is 44 ± 2 °C, and unfolded baselines were assumed to remain the same in solution and hydrogel. Fitted m_u value does not take into account the confinement effect which lowers the unfolded state D/A ratio in 10% hydrogel (Figure 5.1). Unfolded baselines for b_u were fixed with zero slope and constant intercept for the 4% hydrogel and solution fits, since the experimental unfolded baseline is obscured by protein aggregation. See Figure 5.14 for the effect of changing the value of m_u, which is significant for T_m but small for ΔT_m.

sample	ΔT_m (°C)	m_f	b_f	dg_T	m_u[c]	b_u[c]
solution	0	0.0063 ± 0.0004	0.85 ± 0.01	800 ± 300	0 to m_f	1.31
4% hydrogel	1.9 ± 0.4	0.0055 ± 0.0006	0.87 ± 0.02	800 ± 200	0 to m_f	1.31
10% hydrogel[b]	(3.9 ± 0.8)[b]	0.0049 ± 0.0009	0.89 ± 0.03	900 ± 100	0 to m_f	1.31

Once PGK has unfolded, the turnovers in Figure 5.3a occur at successively lower temperatures $T_{aggregate}$ in more cross-linked gels. Values for $T_{aggregate}$ in solution, in the 4% hydrogel, and in the 10% hydrogel are, respectively, $T_{aggregate} = 58 \pm 3$ °C, $T_{aggregate} = 53.8 \pm 0.8$ °C, and $T_{aggregate} = 51 \pm 2$ °C. The earlier onset of the turnover shows that aggregation is promoted by higher cross-linking. In 4% hydrogel, confinement does not play a role based on the CrH2 measurements, so the turnover and aggregation of PGK-FRET at high temperature is attributed to protein–polymer interaction.

We do not report a value for T_m in the 10% hydrogel because the leveling off of the thermal melting curve in the 10% hydrogel may partly be due to confinement, not just aggregation, based on the CrH2 sensor data in the 10% hydrogel (Figure 5.1). The stabilization of PGK-FRET in the 10% hydrogel may be less than in the 4% hydrogel if the lower FRET at the turnover point were in part due to confinement.

The non-normalized thermal denaturation curves (Figure 5.13a) show very similar FRET values in the 4% and 10% hydrogel samples, but both differ significantly from solution. Since the confinement effect is very different in the 4% and 10% hydrogels (Figure 5.1a), we conclude that the smaller D/A (more compact configuration of the FRET labels) in hydrogel is due to interaction of PGK-FRET with the hydrogel surface, rather than to confinement. Thus, protein–polymer surface interaction again dominates over confinement for determining protein properties in the hydrogel.

5.2.6 Folding kinetics speed up slightly in hydrogels

We quantified PGK-FRET folding/unfolding kinetics with ~200 ms time resolution after a single temperature jump of ~5 °C by monitoring the difference in donor and acceptor fluorescence, $D(t) - A(t)$, as a function of time after the initial temperature increase. Subtraction of the acceptor from the donor fluorescence is used in kinetics measurements for two reasons. First, temperature-dependent changes in quantum yields are small when measured at a single temperature and thus do not require corrections as for thermal denaturation curves. Second, $D(t) - A(t)$ is a linear function of the protein population, yielding more accurate population kinetics.[33] The resulting curves are fit to Equation 5.2.

$$D(t) - A(t) = A_1 \exp[-t/0.2\text{s}] + A_2 \exp[-(t/\tau)^{\beta}] + y_0 \tag{5.2}$$

which is a two-component exponential. The first component with a fixed decay time of 200 ms and negative amplitude accounts for the known fast dynamics of the chromophore within AcGFP1.[33]This part of the signal is unrelated to PGK folding/unfolding kinetics. The slower second component includes the relaxation time τ of PGK and a stretching factor β to account for multistate folding and spatial heterogeneity in the protein ensemble.[33,35] In the two-state approximation, $\tau = (1/\tau_f + 1/\tau_u)^{-1}$ samples both the folding and the unfolding relaxation times.[35] Given the AcGFP1 dynamics and 60 Hz frame rate, we should be able to achieve temporal resolutions of 233 ms. This could be improved in future work with synthetic fluorescent labels that have reduced temperature-dependent dynamics.

Kinetic measurements by FReI show that the relaxation time is faster in hydrogels than in solution (Figure 5.3b, Table 5.3) with relaxation times $\tau = 1.2 \pm 0.3$ and 1.3 ± 0.5 s in the 4% and 10% hydrogels, compared to $\tau = 2.2 \pm 0.2$ s in solution. This speed up occurs only in the gels but is independent of confinement: the same ~1.25 s relaxation time is observed in the 4% and 10% cross-linked hydrogels, even though the CrH2 sensor shows much stronger confinement in the 10% hydrogel (Figure 5.1). Non-normalized kinetic curves further show the similarity of the magnitude of change in $D(t) - A(t)$ within the hydrogels compared to that in aqueous solution (Figure 5.13b). The stretching factor β decreases from 1 in solution and 4% hydrogel to 0.85 ± 0.09 in the 10% hydrogel, indicative of multistate or heterogeneous folding kinetics in the highly cross-linked hydrogel.

Table 5.3 Time-Dependent PGK-FRET Folding Fitting Results.

sample	τ (s)	β
solution	2.2 ± 0.2	1
4% hydrogel	1.2 ± 0.3	0.9 ± 0.1
10% hydrogel	1.3 ± 0.5	0.85 ± 0.09

5.2.7 Vertical distribution of protein within the hydrogel

PGK-FRET was not included during the hydrogel polymerization because we found that the free radicals degrade the fluorophores and affect the measured D/A fluorescence values. Instead, PGK-FRET was introduced to the hydrogel by “soaking in” the proteins, by rehydrating the dehydrated gels with the PGK-FRET solution. PGK-FRET penetrates the polyacrylamide gel during rehydration.

We first quantified the protein distribution normal to the gel/liquid interface (see Section 5.6). Time-dependent *z* stacks show the protein distribution within the hydrogel during the 30 min equilibration with the protein solution (Figure 5.15). The distribution at a single time point is shown in Figure 5.4a. The control measurement of PGK-FRET in solution shows a uniform protein distribution throughout the sample volume, with a slight decrease in fluorescence intensity further from the interface, due to the depth of field of the objective.

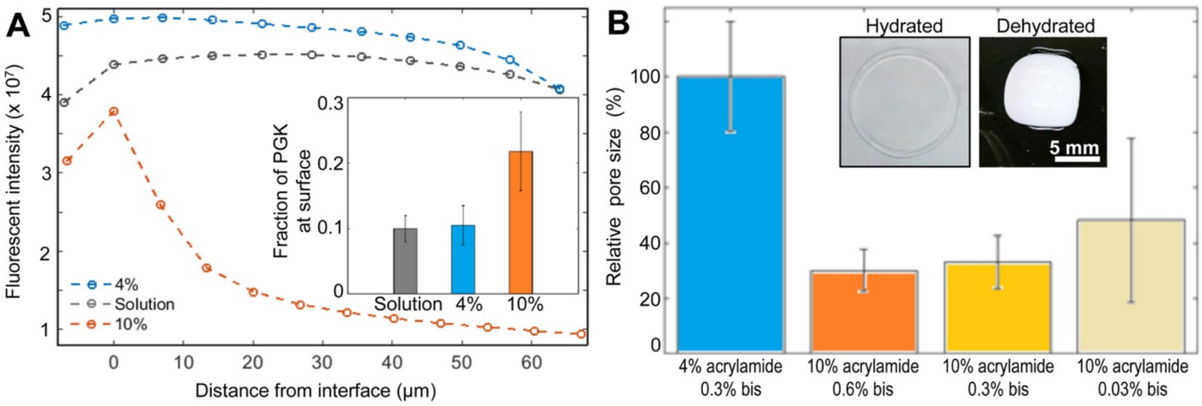

Figure 5.4 Axial distribution of PGK-FRET normal to the hydrogel interface depends on the pore size. (a) Fluorescence intensity vs the distance from the surface, constructed from z-stack confocal scans of the directly excited

acceptor intensity of PGK-FRET. Measurements were of PGK-FRET in solution (t = 5 min) and within hydrogels (t = 15 min for 4% gel; t = 60 min for 10% gel). (a, inset) Fraction of PGK-FRET at the surface for the three indicated conditions. (b) Quantified relative pore size as a percent of the largest pore size measured in 4% acrylamide gels. (b, inset) Example images of the macroscale volume change of hydrated to dehydrated 10% acrylamide/0.6% bis-acrylamide hydrogel from which the pore size was quantified.

Measurements of PGK-FRET in the 4% hydrogel reveal a uniform distribution, similar to that in aqueous solution. In contrast, the PGK-FRET distributed nonuniformly in the 10% hydrogel. There is a peak in the protein intensity at the interface followed by a decrease with increasing distance into the hydrogel from the interface. The quantified intensity at the interface as a fraction of the total protein intensity within the sample shows that ~20% of the protein was at the surface of the 10% hydrogel, in contrast to the relatively uniform protein distribution both in solution and in the 4% hydrogels (Figure 5.4a, inset). The different distributions of PGK-FRET in the 4% and 10% hydrogels further support the view that PGK-FRET is confined in the 10% hydrogel but can diffuse more freely in the 4% hydrogel. This interpretation also supports the FRAP results.

The different distributions of PGK-FRET normal to the surfaces of the 4% and 10% hydrogels are likely due to different relative pore sizes. Macroscale estimates of the pore size were calculated from the volume change of the hydrogel upon replacing the water within the hydrogel with ethanol (Figure 5.4b). Although other methods such as scanning electron microscopy or atomic force microscopy can characterize individual pore sizes, those methods perturb the sample and have led to discrepancies in reported pore sizes that ranged over 3 orders of magnitude.[45-48] Therefore, we focused on the relative, instead of the absolute, pore sizes in the hydrogels.

The volume changes of the hydrogels, $v_{2,s}$, from fully hydrated to dehydrated gel in 100% ethanol were converted to the number-average molecular weight of the polyacrylamide chain between cross-links, M_c, which is inversely proportional to pore size, according to Equation 5.3[48,49]

$$\frac{1}{M_c} = \frac{2}{M_n} - \frac{\bar{v}}{V_1} \cdot \frac{\ln(1 - v_{2,s}) + v_{2,s} + \chi v_{2,s}^2}{v_{2,s}^{1/3} - v_{2,s}/2} \qquad 5.3$$

where V_1 is the molar volume of solvent (water, 18.0 mL/mol), $\bar{v}$ is the specific volume of bulk polyacrylamide (48.8 mL/mol),[50] χ is the Flory–Huggins parameter of polyacrylamide in water (χ

= 0.499),[51] and M_n is the number-average molecular weight of polyacrylamide prepared in the absence of cross-linkers (estimated values were used for the relative size). The results in Figure 5.4b show that the average pore size in the 4% hydrogel is approximately four times that in the 10% hydrogels. As a result, we attribute the reduced penetration of PGK-FRET into the 10% hydrogel to hindered diffusion due to the smaller average pore size in the gel.

5.2.8 Lateral Distribution of the Protein in the Hydrogels and Imaging of Boundaries

The lateral resolution of the FReI instrument is illustrated in Figure 5.5. Marker beads in Figure 5.5a show submicrometer diffraction-limited resolution in the hydrogel. Figure 5.5b resolves PGK-FRET fluorescence across the hydrogel-solution boundary, and the corresponding differences in D/A distributions in solution vs the hydrogels are evident in Figure 5.5c. Images of both microscale heterogeneities that resulted from variations in the thickness of the gel near the edges and purposely patterned hydrogels are reported in Figures 5.16 and 5.17.

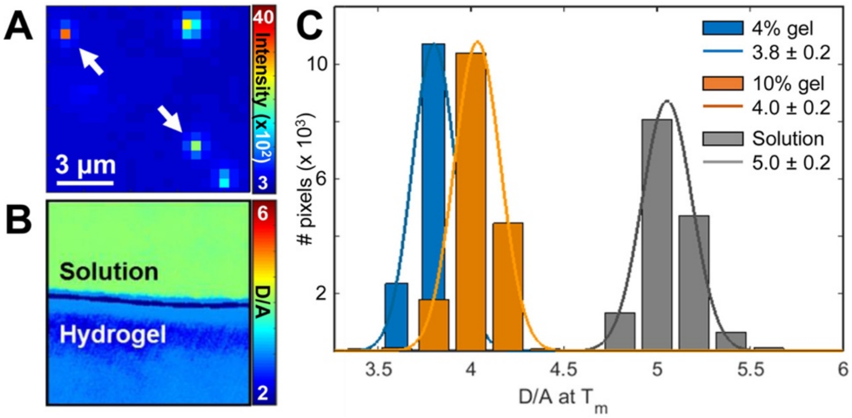

Figure 5.5 Lateral *x–y* homogeneity in the folded state of PGK-FRET is determined from D/A ratios measured at 41 °C with the imaging capabilities of FReI. (a, b) Spatial resolution capabilities of FReI. (a) Demonstration of single-pixel resolution capabilities by detecting 100 nm fluorescent beads in a 10% hydrogel (1 pixel = 500 nm × 500 nm). Beads are distributed throughout the 120 μm thick sample, but beads in focus in the axial plane have their intensity localized to a single pixel (indicated by the white arrows). (b) D/A image of PGK-FRET both within solution and a 10% hydrogel in a single sample. Quantification of 1.2 ± 0.2 μm resolution at this interface provided in Figure 5.16. (C) Histograms of D/A measured at individual pixels in aqueous solution and 4% and 10% hydrogel were fitted to a Gaussian distribution (curves). Images were collected at ~T_m (41 °C) to construct the histograms. Example D/A image of 10% gel is provided in Figure 5.18.

In contrast to the protein distributions along the *z* axis measured by confocal microscopy, in the *x–y* plane we find that the unfolding of PGK-FRET is spatially homogeneous across all of the hydrogels studied by FReI at diffraction-limited resolution. Visual inspection of the images also shows no noticeable spatial heterogeneity within the hydrogels (Figure 5.18). Thus, the hydrogels we prepared were quite homogeneous on a 500 nm length scale and provide similar microenvironments for PGK-FRET molecules embedded in or near the surface of the gel.

Using pixel-by-pixel image analysis of FReI data, we calculated the D/A in individual 500 nm × 500 nm areas in solution and in the polyacrylamide hydrogels at a temperature of 41 °C. Figure 5.5c shows histograms of the D/A values of all 500 nm × 500 nm areas within a 125 μm × 125 μm area for representative individual trials. Both the 4% and the 10% hydrogel have similar D/A distributions, with a much lower average value than in aqueous solution. Thus, we conclude again that the hydrogel surface, rather than confinement, determines protein and FRET label conformation: the 4% hydrogel has low confinement similar to aqueous solution (Figure 5.1), yet it has a D/A distribution similar to the 10% hydrogel, which shows strong confinement.

Increasing cross-linking density does not increase the apparent heterogeneity of the protein microenvironment within the hydrogels. Previous studies have shown that cross-linker content can lead to heterogeneities within polyacrylamide hydrogels due to bundling or clustering of highly cross-linked regions that span length scales from subnanometer to hundreds of nanometers.[52-54] Here, we varied the cross-linker content of the 10% acrylamide gels from 0.3% to 6% as a percent of monomer (or 0.03–0.6% bis-acrylamide in the total solution). The literature suggests that the onset of cross-linker clustering occurs around 5% bis-acrylamide as a percent of monomer.(54) As shown in Figure 5.19, the standard deviations of the distribution of D/A values for all 500 nm × 500 nm pixels within 125 μm × 125 μm areas remained the same at ±0.2 D/A, regardless of the gel composition. This standard deviation is also the same as in solution and in the hydrogels reported in Figure 5.5c.

5.3 Discussion

FReI has been used successfully to image protein folding in different environments in live cells.[26,55] Here we demonstrate the ability of FReI to determine how biomaterial properties affect protein folding. These determinations of the influence of hydrogels on protein stability in situ differ from standard approaches for assessing protein–material interactions. More common methods are based on retained immobilized protein activity, epitope exposure, or altered spectra, for example, that reflect the population averaged behavior of an entire sample. The ability of FReI to image D/A changes in situ opens the door for investigations of protein stability in more complex materials, such as biomaterials with micron-scale heterogeneities.

Although hydrated microenvironments of hydrogels such as polyacrylamide are commonly thought to preserve protein structure, the FReI results revealed that while gel pore size alters diffusion of the protein (Figures 5.2 and 5.4), only gel–protein interaction altered the folding stability and kinetics of adsorbed protein (Figuer 5.3). The FReI measurements reveal that the 4% hydrogel increases PGK-FRET stability, but once protein unfolding begins, proteins aggregate at lower temperature in the hydrogel. Thus, fouling in this matrix is not due to protein destabilization per se but to the promotion of irreversible aggregation of any unfolded protein present in the gel.

FReI measurements combined with FRAP revealed differences between embedded protein vs proteins at the hydrogel surface that would not be apparent with standard approaches. At the surface, unfolded PGK-FRET is less constrained than within the pores, yet the FRAP recovery is less than in the bulk (Figure 5.2c). The dominant influence of polymer surface–protein interactions over any confining effects is similar to the previously observed discrepancy between myoglobin stability within AOT reverse micelles and models that only considered entropic contributions due to protein confinement by (assumed) noninteracting micelle walls.[56]

Increased confinement with decreasing pore size also appears to have less influence on the PGK-FRET stability than the chemical properties of the polymer. Crowding by either macromolecules or confinement within cavities ranging in size from one to hundreds of nanometers restricts the excluded volume occupied by the unfolded protein.[38,39,56-58] Such confinement favors the more compact, folded protein over the unfolded conformational ensemble. However, there is little further increase in protein stability in Figures 5.3a and 5.Xa when going from the minimally confining 4% gel to that in the substantially confining 10% gel (confinement according to Figure 5.1). Quite the contrary, any contribution to the unfolded state D/A baseline in Figure 5.3a from confinement would lower the fitted melting temperature of PGK-FRET in the 10% hydrogel.

Because capillary forces draw the protein solution into the gel during rehydration, the PGK-FRET can diffuse freely through the pores and should not be entrapped. The smaller average pore size in the 10% hydrogel relative to the 4% hydrogel sterically hinders protein penetration into the gel (Figure 5.4a). This is a further sign that the 10% hydrogel is more confining, while causing little further change in either stability or folding relaxation kinetics relative to the 4% hydrogel.

PGK-FRET folds faster in hydrogels than in aqueous buffer, but there is no difference in the relaxation times in the 4% and 10% hydrogels, although the latter more strongly confines the crowding sensor CrH2. A factor of 2 *slower* folding relaxation in cells vs aqueous solution was previously attributed to differential weak interactions of the labels and protein with the cellular matrix and not to crowding.[59,60] With confinement ruled out as a factor because 4% and 10% hydrogels differ equally from aqueous solution, either a decrease of the activation energy or interaction of protein with the hydrogel matrix must be the cause for the slightly faster kinetics observed in hydrogels.

Diffraction-limited resolution FReI was previously able to resolve variations in protein folding stability in the cytosolic microenvironments of live cells at ~1 μm resolution.[26,61] Improved optical magnification increased our resolution to 500 nm × 500 nm regions as demonstrated with fiduciary markers smaller than both the diffraction limit and the pixel size (Figure 5.5a). Further, measuring a sample in which PGK-FRET was visible in juxtaposed solution and hydrogel environments showed a boundary of roughly 1–2 μm width (Figures 5.5b and 5.16). We also imaged micrometer-sized heterogeneities due to variations in the gel thickness near the edges of the sample (Figure 5.16). Nevertheless, the D/A value at the melting temperature T_m in polyacrylamide hydrogels was homogeneous both above and below cross-linker concentrations at which cross-linker clustering should occur (Figures 5.5c, 5.18, and 5.19).[53] Given that scattering techniques detected inhomogeneities due to such clustering on length scales ranging from 0.25 to 250 nm,[53,62] it is unlikely that our spatial resolution would image folding inhomogeneities at our 500 nm resolution. We anticipate imaging microphase-separated materials, regions of microcrystallinity in biomaterials, and chemically patterned gradients[63] on the submicrometer scale in future work with the current setup.

FRET-labeling strategies must be carefully considered when applying FReI to biomolecules. Our current demonstration of FReI with PGK-FRET uses fluorescent protein labels that were optimally positioned to detect known hinge-like motions[39] and total unfolding distance of PGK. To apply FReI to other biomolecules, selecting the appropriate labels and locations would be crucial.[64,65] Donor/acceptor pairs with Förster distance ranges of 2.2–8.5 nm are commercially available in the forms of either genetically incorporated fluorescent proteins or organic fluorophores for site-selective labeling.[66] Selected donor and acceptor locations should be positioned for optimal sensitivity to anticipated conformation changes.[67] Further, the labels should not interfere with the biomolecule function. Despite these constraints, there is a wide range of potential candidates, including apatamers,[68] protein and nucleic acid sensors,[69] and specifically designed proteins[24] that can be studied.

5.4 Conclusions

We demonstrated a new technique for the in situ analysis of proteins within biomaterials. FReI images the influence of material properties on protein stability. The approach differs from typical bulk measurements used to assess protein–material compatibility. Our studies interrogated the equilibrium thermodynamic, kinetic, and spatial details of protein unfolding in polyacrylamide hydrogels with different cross-linking density (pore size). The results somewhat surprisingly demonstrate that polyacrylamide–protein interactions are more important than confinement in controlling protein folding stability and kinetics. Future applications of FReI could identify design rules for protein-compatible drug carriers, biosensors, or functional biomaterials. The approach can also be extended to other FRET-labeled biomacromolecules, including other proteins or DNA and RNA aptamers that are used in nucleic acid-based sensors and in drug targeting.[24,68-70]

5.5 Experimental section

5.5.1 Protein expression and purification

To quantify confinement in the cross-linked hydrogel, we used the protein FRET sensor CrH2 (“crowding helix two”)[31] that is sensitive to confinement. CrH2 contains two contiguous, conformationally flexible alpha-helical peptides flanked by donor and acceptor labels, AcGFP and mCherry, at the N- and C-termini (Figure 5.7). CrH2 gives a linear, continuous response to temperature instead of a binary response typical of cooperative folding proteins so that it can serve as a conformation sensor (Figure 5.8).[32] As confinement in the gel increases, the FRET efficiency of CrH2 increases, the donor emission intensity decreases, and the acceptor intensity increases.

The model protein PGK is an ATP-producing enzyme that undergoes multistate folding, which can be approximately modeled by a two-state process on a 1 s time scale.[33] The multistate process makes it a sensitive probe for small environmental influences, as shown by comparing PGK folding in solution versus within cells.[26] PGK unfolding can be monitored by FRET when donor AcGFP1 and acceptor mCherry fluorescent proteins are engineered at the N- and C-termini of the protein to make PGK-FRET.[44] The fluorescent protein labels have high thermal stability (>70 °C) and an ideal Förster distance of ∼5 nm for the fluorophore separation in the folded (2 nm) and unfolded (>7 nm) states.[71] As PGK-FRET unfolds and energy transfer efficiency decreases, the donor emission intensity increases and the acceptor intensity decreases.

For these studies either the cDNA for PGK or CrH2, each engineered with N-terminal AcGFP1 and C-terminal mCherry with a 5X-His tag, was cloned into the pDream 2.1 vector (Genscript) that contains a T7 and CMV promoter for dual expression in bacterial and mammalian cells. The soluble protein was expressed in *E. coli* BL-21 (DE3) Codon Plus (RIPL) cells (Agilent Technologies) chemically transformed with one of the above plasmids by heat shocking at 42 °C for 20 s. The cells were grown in Lennox LB broth (tryptone 10 g/L, yeast extract 5 g/L, NaCl 10 g/L, Fisher Biosciences) at 37 °C to an optical density of 0.681 at 600 nm. The cells were then induced with 1 mM isopropyl β-d-1-thiogalactopyranoside (IPTG, Inalco) and allowed to express protein for 12 h at 18 °C. The cells were collected by centrifugation (Beckman Coulter Avanti J-E, 2,795 xg, 7 min, 4 °C) and resuspended in lysis buffer (300 mM NaCl, 50 mM Na_2PO_4, pH 8), 1 mM phenylmethylsulfonyl fluoride (PMSF, Sigma), and 20 μL of DNase (New England Biolabs). Cells were further disrupted by sonication (Qsonica, 70% intensity, 6 s pulse/min, 4 min total sonication time), and the cell lysate was clarified by centrifugation (10 062*g*, 20 min, 4 °C) and filtration (Millipore Millex, 0.45 and 0.22 μm). The protein was then affinity purified (GE Aktapure) by binding to a 5 mL HisTrap column (GE Healthcare) in 30 mM imidazole (Sigma), followed by elution with a solution containing 200 mM imidazole. The eluted protein solution was exchanged into storage buffer (20 mM Na_2PO_4, pH 7) using 10 kDa molecular weight cutoff dialysis tubing (Thermo Scientific). The purity of the final PGK-FRET or CrH2 fractions used in measurements was assessed by SDS-PAGE. The protein properties were further evaluated by UV–vis and circular dichroism spectroscopy and by spectrofluorometry as detailed in Figures 5.8 and 5.9.

5.5.2 FReI sample preparation

Glass coverslips (Fisherbrand, No. 1.5, 22 × 22 mm) and microscope slides (Fisherbrand, 22 × 75 × 1 mm, cut in half to 22 × ∼37 (±1) × 1 mm) were cleaned in a base bath (4% (v/v) H_2O_2 [Macron] and 13% (v/v) NH_4OH [Macron]) at 70 °C for 90 s, rinsed with excess Millipore-purified H_2O, dried with N_2, and then cleaned with air plasma for 2 min at high power (Harrick Plasma PDC-001, max power 30 W to the rf coil). A silicon spacer (Grace Biolabs, 20 mm circular diameter opening × 0.5 mm thickness) was placed on the microscope slide. To adhere the polyacrylamide to the glass slide, the glass slide was treated with neat (3-aminopropyl)-trimethoxysilane (APTMS, Aldrich) for 6 min at room temperature. Unreacted APTMS was rinsed off the surface with 10, 1 mL rinses with H_2O, and the treated glass slide was dried. A 200 μL aliquot of 0.5% (v/v) glutaraldehyde (Sigma-Aldrich) diluted in PBS buffer (Lonza) was added to the glass slide, incubated for 30 min at room temperature, and followed with 10, 1 mL rinses with H_2O. The silicon spacer was removed, and an adhesive secure seal imaging spacer was placed on the microscope slide (Grace Biolabs, 20 mm circular diameter opening × 0.12 mm thickness).

Polyacrylamide with 4% or 10% acrylamide (Bio-Rad) and either 0.03%, 0.1%, 0.3%, or 0.6% bis-acrylamide (Bio-Rad) was prepared by mixing appropriate amounts of acylamide, bis-acrylamide, and H_2O for a final volume of 1 mL. The solution was then polymerized by adding 5 μL of 10% (w/w) ammonium persulfate (APS, Biorad) and 0.5 μL of tetramethylethylenediamine (TEMED, Biorad). In brief, we will refer to the 10% acrylamide/0.6% bis-acrylamide gels as "10% hydrogels" and to the 4% acrylamide/0.3% bis-acrylamide gels as "4% hydrogels", whereas other combinations will be referred to explicitly.

Fiduciary marker beads (Phosphorex, 6 μm, polystyrene-carboxylate, 460/500 ex/em) were added at a dilution of 1:10 000 to either the acrylamide solution prior to polymerization for FReI measurements or to the protein solution for confocal measurements. To determine the microscope spatial resolution capabilities, 100 nm marker beads (Invitrogen, F8780, 488/605 ex/em) were added to the gelation solution instead of the 6 μm beads. An aliquot of 60 μL of the prepolymerized solution was quickly added to the region of the prepared microscope slides confined by the spacer, and a coverslip was placed on top. After chemical polymerization for >2 h, the coverslip was removed from the sample, which was then allowed to dehydrate overnight. Prior to measurements, a solution of 0.5 μM CrH2 or 3.5 μM PGK-FRET in 20 mM sodium phosphate buffer at pH 7 was then used to rehydrate the samples and absorb the protein. A glass coverslip was placed on top of the gel in order to seal the sample, which was then allowed to equilibrate for >30 min before performing FReI or FRAP measurements.

To estimate the average pore size, hydrogels were prepared on nontreated glass microscope slides, as described above. The hydrogel was dehydrated by replacing the water with ethanol in a series of submersions of the hydrogel in ∼10 mL solutions of 37% ethanol, 10 min; 67% ethanol, 10 min; 95% ethanol, 10 min; 100% ethanol, 3 × 10 min on an orbital shaker table at 100 rpm. The volume of the hydrogel was measured at the initial hydrated and final dehydrated (100% ethanol) conditions. The diameter and thickness to ±0.025 mm were measured using a caliper at three locations on each individual hydrogel, and two replicates were performed for each condition. The thicknesses of the hydrated gels were assumed to be 120 μm based on the spacer used to prepare them.

5.5.3 FReI microscopy setup

A schematic of the FReI microscope is shown in Figure 1.6. FReI measurements were performed on a modified Carl Zeiss Axio Observer.A1 microscope body. A white LED (Prizmatix, UHP-T2-LED-White) was used for excitation of AcGFP1 and FRET by passing the light through a Chroma ET470/40x bandpass filter and reflecting the light to the sample through a Chroma T495lpxt dichroic. The excitation was focused onto the sample with a Carl Zeiss, 40×/0.75 NA EC Plan Neo Fluar or Carl Zeiss 63×/0.85 NA N-Achroplan objective with an approximate power density of 525 ± 50 μW/cm^2. Alternatively, for direct excitation of the mCherry used to determine the amplitude of the temperature jump based on the temperature-dependent quantum yield changes,[33] a Chroma ET580/25× bandpass filter and T600lpxr dichroic were used. The FRET emission was collected in epifluorescent mode, passed through a Chroma ET500lp filter, and split into two channels with a Chroma T600lpxr dichroic onto a Lumenera LT225 NIR/SCI CMOS detector. Images were taken at 15–60 Hz frame rates and 16–66 ms integration times.

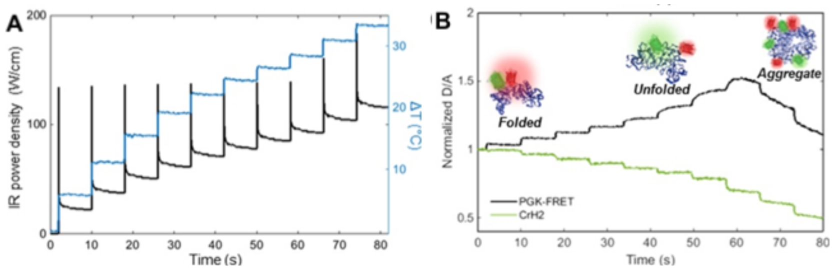

Figure 5.6 FReI of protein state, unfolding, and aggregation in biomaterials. (a) Profile of the infrared laser power (black) and actual temperature jump profile at the sample (blue), monitored by the change in the mCherry quantum yield. (b) D/A (donor to acceptor emission) of the two proteins during a rapid sequence of temperature jumps such as those shown in B. (Black) D/A ratio increases in PGK-FRET due to cooperative unfolding as the labels separate (up to 50 °C) then decreases due to aggregation (after 60 °C). (Green) D/A ratio decreases smoothly in CrH2, reflecting quantum yield-dependent changes of the fluorescent protein labels; no folding or aggregation transitions are observed.

Temperature jumps were achieved using a 2 μm continuous wave fiber laser (AdValue Photonics) aligned 45° to the normal of the sample. The laser was focused to a full width at half-maximum spot size of 400 μm and a maximum power density of 165 W/cm^2. The power density at the sample was controlled by a TTL voltage input provided by LabView (myRIO 2013, shown as "V input" in Figure 1.6).

Data collected with the CMOS detector were converted to a MATLAB-compatible format and analyzed in MATLAB R2014b. The channels were separated and aligned using the 6 μm marker beads and the built-in MATLAB control point selection, correlation, and affine transformation functions. Corrections for bleaching of the AcGFP1 and mCherry that occurred during image acquisition were incorporated into the analysis described in Section 5.5.

5.5.4 Confocal z-scan and FRAP measurements

To complement FReI measurements, confocal microscopy was performed on a separate Carl Zeiss LSM 710 instrument. To assess the equilibration of the protein penetration into the hydrogel, *z*-stack scans were measured with an EC Plan-Neofluar 10×/0.3 NA objective immediately after adding the PGK-FRET solution to the hydrogels. The fluorescence of the mCherry was monitored with 561 nm excitation and 590–690 nm detection. Three ~500 μm × 500 μm areas of the sample were imaged in 18 stacks, with an axial step size of 7.1 μm from the interface indicated by the marker beads to within the bulk of the hydrogel. This was repeated every 10 min for 2 h.

FRAP measurements of PGK-FRET were performed by monitoring the fluorescence of the mCherry with 561 nm excitation and 575–690 nm detection. After collecting initial measurements of the fluorescent intensity prior to bleaching, the mCherry was bleached using 405, 458, 488, 514, and 561 nm light at a spot radius of 80 μm. The recovery was then monitored for 70 s at a frame rate of 1.67 Hz. FRAP measurements were taken either at the gel/liquid interface or 20 μm into the hydrogel, as indicated by the marker beads. FRAP measurements of CrH2 were performed on a similar setup as detailed in Section 5.6. In the FRAP measurements, the time-dependent intensity change in the region of interest was normalized to the prebleach intensity ($I(t)/I_0$), and the bleaching recovery was analyzed with the analytical expression listed in Section 1.3.3.[40]

5.5.5 Details and characterization of AcGFP-CrH2-mCherry

Characterization of AcGFP-CrH2-mCherry (Figure 5.7) by circular dichroism, spectrofluorometry, and UV-vis was performed at a protein concentration of 1 μM (Figure 5.8) and use of the same conditions described in Section 5.6.6. The AcGFP-CrH2-mCherry structure was relatively insensitive to temperature changes and no unfolding transition was observed. There was a slight decrease in D/A measured by spectrofluorometry due to the quantum yield changes of the AcGFP and mCherry with temperature (Figure 5.8a) and to a slight decrease in the alpha helical character of the peptide linkers (Figure 5.8b).

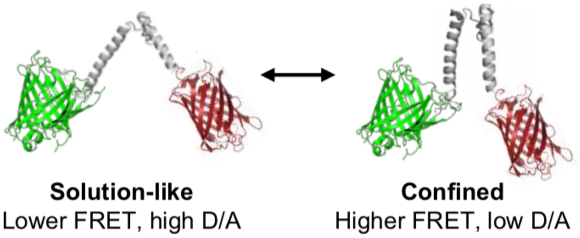

Figure 5.7 Cartoon representation of AcGFP-CrH2-mCherry showing changes in conformation, FRET, and D/A based on environment: either (left) non-confined in solution or in a solution-like environment like in the 4% hydrogel or (right) confined like in the 10% hydrogel or crowded in a high percent Ficoll solution. Adapted from Boersma, *et al.*[72]

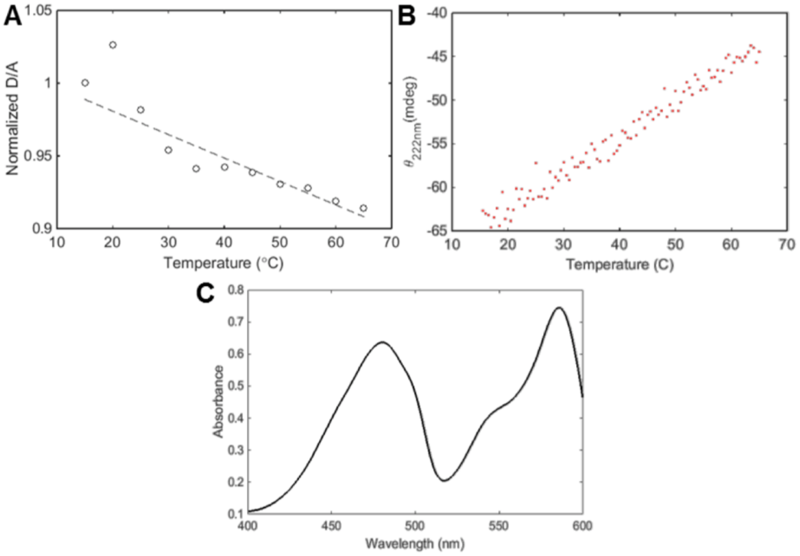

Figure 5.8 Characterization of bacterially-expressed, recombinant AcGFP-CrH2-mCherry CrH2 using (a) spectrofluorometry (dashed line provided to guide the eye), (b) circular dichroism spectroscopy, and (c) UV-visible spectroscopy.

5.5.6 Characterization of PGK-FRET

The purified, recombinant PGK-FRET (see Section 5.6.1) was characterized by circular dichroism, spectrofluorometry, and UV-visible spectroscopy (Figure 5.9). A Jasco J-715 spectropolarimeter was used to monitor the thermal denaturation of PGK-FRET, based on the measured ellipticity at 222 nm. The protein was diluted to 1 μM in 20 mM sodium phosphate buffer, pH 7 and the ellipticity was measured in a quartz cuvette with a 1 cm path length. Mineral oil was placed on top of the protein solution to prevent evaporation. The temperature was varied from 15-65 °C with a 120 °C/hr slope by using a Jasco PFD-350S Peltier thermostat. The resulting denaturation curve had the expected sigmoidal shape. The solid line is the data fit to a simplified Boltzmann equation in Origin, and the best fit melting temperature *Tm* was 46.0 ± 0.5 °C (Figure 5.9a).

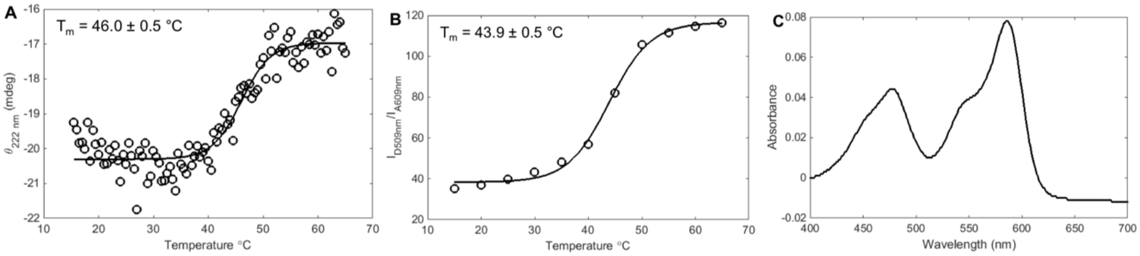

Figure 5.9 Characterization of bacterially-expressed, recombinant PGK-FRET using (a) circular dichroism spectroscopy, (b) spectrofluorometry, and (c) UV-visible spectroscopy.

The thermal denaturation of PGK-FRET was further characterized with a Jasco spectrofluorometer FP-8300, at temperatures from 15-65 °C in 5 °C intervals at a heating rate of 120 °C hr-1 with 300 s equilibration times. The protein was diluted to 1 μM in 20 mM sodium phosphate buffer, pH 7 and measured in a 1 cm path length quartz cuvette. Mineral oil was placed on top of the protein solution to prevent evaporation. The donor was excited with 475 nm light and the emission from 480-700 nm was monitored at a scan speed of 200 nm/min and with data intervals of 1 nm. The resulting denaturation was quantified from the change in the ratio of donor fluorescence at 509 nm and acceptor fluorescence at 609 nm (D/A), and a Boltzmann fit of the data resulted in a melting temperature *Tm* of 43.9 ± 0.5 °C (Figure 5.9b).

Finally, UV-vis spectra measured with a Shimadzu UV-1800 show the expected absorbance bands from the donor AcGFP and acceptor mCherry labels that are used to calculate the respective concentration of protein using Beer's Law (Figure 5.9c).

The discrepancy between the *Tm* values obtained by fast relaxation imaging, circular dichroism, and spectrofluorometry for PGK-FRET in solution is likely due to the different temperature monitoring systems used on each instrument. The differences for *Tm* for PGK-FRET in solution (Figure 5.9) are also different from the changes in *Tm* reported in the main text that compare gels and solution. We were unable to determine the *Tm* in gel environments by using either circular dichroism or spectrofluorometry due to scattering by the gel and the inability to polymerize the hydrogel in the presence of PGK-FRET, as discussed in the introduction and results sections of the main text. Further, the lack of observed aggregation in spectrofluorometry and CD cuvette measurements compared to the turnover in the upper baseline at temperatures >*Tm* observed in FReI measurements is due to differences in pathlength (120 µm for FReI and 1 cm for fluorometery) and, hence, fraction of protein in contact with glass.

5.5.7 CrH2 does not adsorb or interact strongly with the hydrogels

FRAP measurements of CrH2 were performed on a Carl Zeiss LSM 880 confocal microscope by monitoring the fluorescence of the mCherry label with 561 nm excitation and 575-690 nm detection. After collecting control images prior to bleaching, the mCherry was bleached using 514 and 561 nm light at a spot radius of 80 µm. The recovery was then monitored for 45 s at a frame rate of 2.6 Hz. FRAP measurements were either taken at the gel/liquid interface or 20 µm into the hydrogel, as indicated by the marker beads.

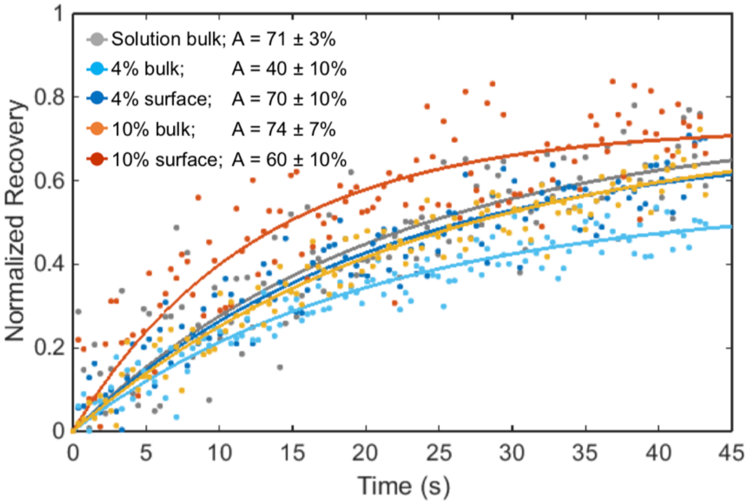

Figure 5.10 Normalized fluorescence within an 80 μm radius photobleached spot at the hydrogel surface and within the bulk of the hydrogel as a function of time after photobleaching. The fluorescence is normalized to the prebleach intensity. The FRAP measurements used CrH2 at 22 °C. The curves reflect fluorescence recovery at the surface or in the bulk of 4% and 10% hydrogels, and in the bulk of solution. The solid lines are fits of the data to Equation 1.8, where the percent recovery, *A*, for each condition are listed next to the conditions in the legend. The large amount of noise led to low confidence in *D* and *α* and we do not report these values. This lower quality of data for CrH2 compared to PGK-FRET was due to relatively low amounts of bleaching achieved with only the 514 and 561 nm laser lines.

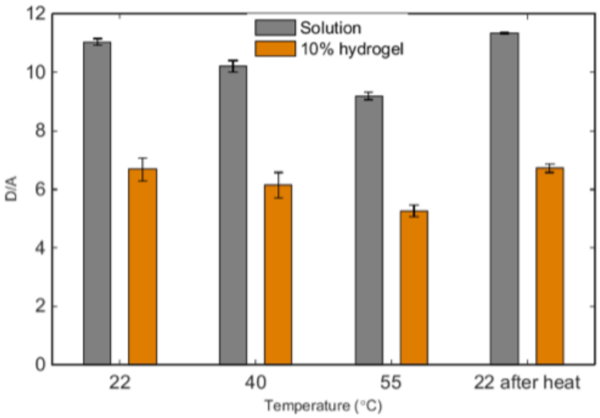

Figure 5.11 D/A of AcGFP-CrH2-mCherry on FReI microscope in solution and in 10% hydrogel as temperature is changed. As the temperature is increased, D/A decreases both in solution and in the hydrogel due to the temperature effects on the quantum yield of the fluorescent protein labels. After returning back to room temperature, both CrH2 in solution and in the hydrogel are able to obtain a D/A value statistically indistinguishable from the starting room temperature.

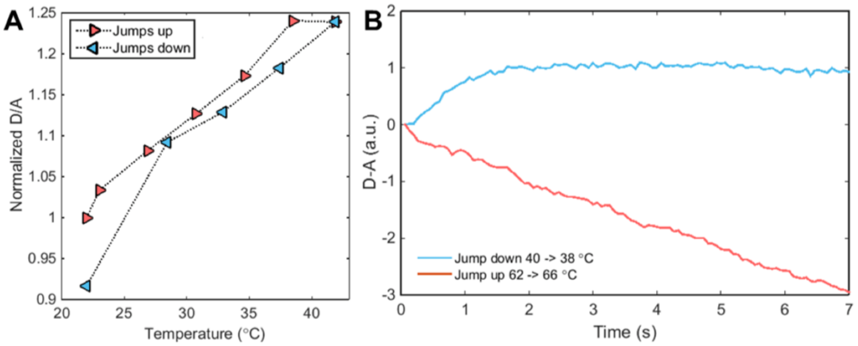

Figure 5.12 Reversibility studies of PGK-FRET in the 10% hydrogel using temperature jumps from room temperature up to T_m and back to room temperature. (a) Normalized D/A values versus temperature during temperature increases (red) and decreases (blue) at $T < T_m$. At the indicated temperature range, PGK unfolding is reversible. The small observed hysteresis is due to limitations in the ability to equilibrate the sample within the 8 s jump when cooling the sample. (b) Difference between donor and acceptor fluorescence (*D-A*) versus time after a heating jump above T_m (red) and cooling jump below T_m (blue). The kinetics further support that folding is occurring during these reverse jumps near T_m due to the exponential shape (blue line, jump from 40 °C to 38 °C), while after aggregation occurs at higher temperatures where the shape is distinctly non-exponential (red line, jump from 62 °C to 66 °C).

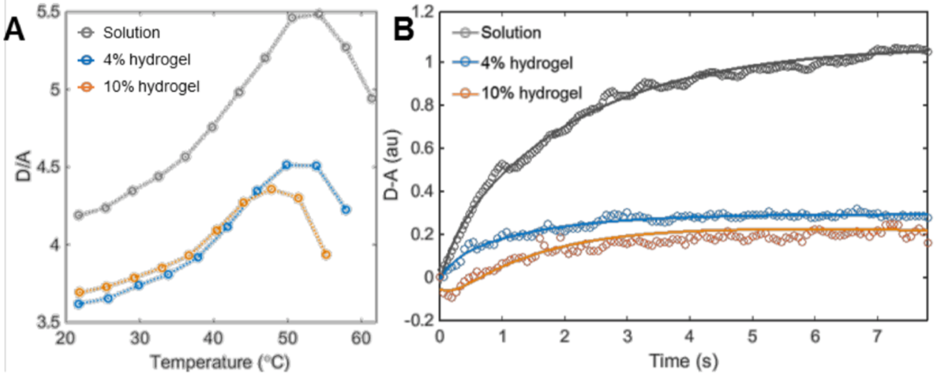

Figure 5.13 Unnormalized FReI measurements show similar stability and folding behavior of PGK-FRET within the hydrogels compared to in solution. (a) Equilibrium thermodynamic melt of PGK-FRET. The dashed lines provided to guide the eye (c) Time-dependent PGK-FRET folding near T_m (40-45 °C). The solid lines represent the fit to a stretched exponential (Equation 5.2). PGK-FRET in the 4% and 10% hydrogels have similar values of D/A and D-A compared to the values observed between the 4% hydrogel and in solution. This emphasizes that the polyacrylamide-protein interactions are more important than confinement in controlling protein stability and kinetics.

5.5.8 Alternative unfolded baselines

An alternative method for fitting the thermodynamic data assumes that confinement effects would prevent PGK-FRET in the hydrogels from reaching the same maximum D/A baseline of 1.31 in Table 5.2 and Table 5.4 observed in solution. Here, Equation 5.1 of the main text was fit to the melting curves below the onset of aggregation. Any data with aggregation signatures were discarded and values of the maximum values of D/A obtained in the hydrogel sample were used in its place (Table 5.4, last column and Figure 5.3a). With that fit, ΔT_m decreases in the hydrogel, showing that if the unfolded baselines differ, the hydrogels may not stabilize PGK-FRET. For the 4% hydrogel, this does not agree with our control measurements of CrH2, or our qualitative interpretation of the data. In the 10% hydrogel on the other hand, there may be a significant contribution of confinement, yielding a baseline < 1.31. Therefore, we do not report quantitative results of T_m for the 10% hydrogel, as discussed previously.

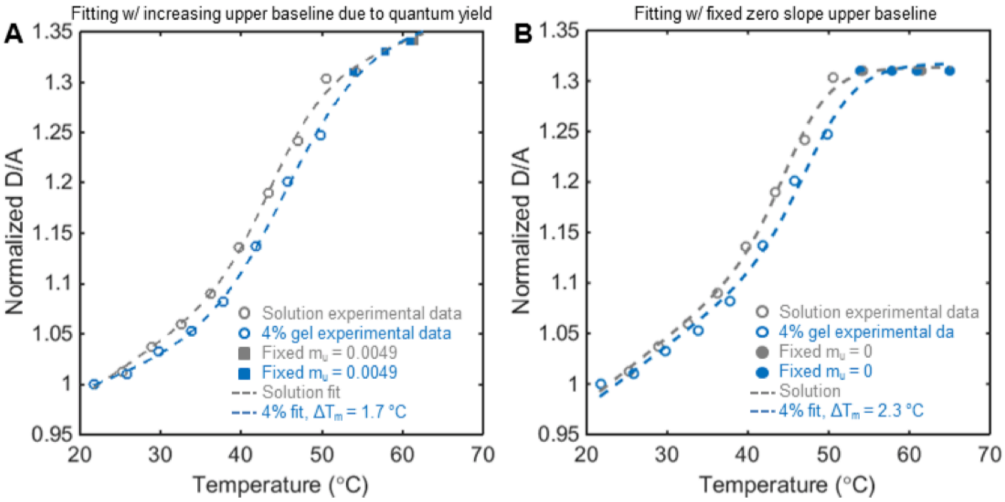

Figure 5.14 Using a range of unfolded baselines results in similar ΔTm. We used a range of slopes from $mu = 0$ to mf . For demonstration, we show unfolded baselines based on either the (a) quantum-yield dependence of the fluorescent protein labels or (b) a fixed slope. We replaced any aggregation data of D/A to start at the maximum value in aqueous solution at *Taggregate*. For (a), after *Taggregate*, we increased D/A with temperature based on the known temperature-dependent quantum yield changes of the fluorescent protein labels[73] (AcGFP quantum yield decreases less to increased temperature than mCherry, resulting in a higher D/A). For (b) after $T_{aggregate}$, we fix D/A = 1.31. We fit these curves for Tm using Equation 5.1 and observed the T_m = 42 – 46 °C in aqueous solution and T_m = 44 – 48 °C in the 4% hydrogel. But the overall ΔT_m remained similar with an increase of $\Delta T_m \sim +1.9 \pm 0.4$ °C in the 4% hydrogel compared to that in aqueous solution.

Table 5.4 Fitting results of PGK-FRET from Equation 5.1 with a confinement-based, fixed baseline.

Sample	Curve fitting with confinement-based baseline T_m (°C)	m_f	b_f	dg_T	m_u	b_u
Solution	45.7 ± 0.8	0.0063 ± 0.0004	0.85 ± 0.01	900 ± 100	~0	1.31
4% hydrogel	45.4 ± 0.4	0.0058 ± 0.0005	0.86 ± 0.02	1200 ± 300	~0	1.25
10% hydrogel	42.0 ± 0.8	0.0041 ± 0.0002	0.907 ± 0.006	1300 ± 100	~0	1.18

5.5.9 Distribution of PGK-FRET in hydrogels over time

To quantify axial diffusion into the gel, PGK-FRET is introduced to the hydrogel samples by pipetting 60 µL of the protein solution onto a dehydrated hydrogel. The samples are allowed to equilibrate for > 30 min before measuring protein stability and folding by FReI. In a control measurement, the time required for the protein to equilibrate with the gel was measured by taking a confocal z-stack scan in 7.1 µm steps over a 120 µm total axial distance every 10 min over the course of 2 hours. Using the Carl Zeiss LSM 710 instrument, the 561 nm excitation/590- 690 nm detection scheme was used to monitor the directly-excited acceptor emission, which correlates with the amount of protein present (as opposed to 488 nm excitation of the donor where the intensity is related to the folded state of the protein). As a control measurement, PGK- FRET in solution over a glass slide was measured every 2.5 min for 25 min. The results revealed a slight amount of bleaching due to repeat measurements (Figure 5.15a). In the 4% acrylamide hydrogel, the protein equilibrates throughout the hydrogel within the first 16 min after the protein is introduced (Figure 5.15b).

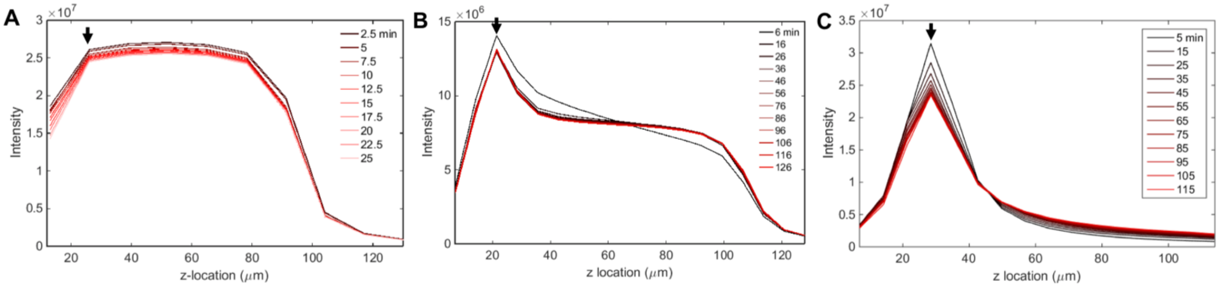

Figure 5.15 Time-dependence of the axial distance PGK-FRET diffuses into the polyacrylamide hydrogels. (a-c) Confocal z-scans of mCherry emission intensity from the PGK-FRET taken over time in (a) solution, (b) 4% acrylamide hydrogel, and (c) 10% acrylamide hydrogel. The black arrows indicate the interface of the sample where fiduciary marker beads on the sample were in focus. The increased peak intensity at the interface for (b, c) compared to Figure 5.1a is due to intensity of the fiduciary marker beads being included in the summed intensity plots here.

The 10% acrylamide hydrogel shows over the course of ~2 hr that the protein distribution varies slightly over time, as the intensity decreases slightly at the surface (the decrease also includes contributions from photobleaching) and increases within the hydrogel throughout the measurement (Figure 5.15c). Despite the 10% hydrogel not being fully equilibrated, we approximated how far the PGK-FRET penetrated the hydrogel by calculating the distance at which the intensity was equal to ½(max intensity at interface-control baseline) because this definition calculated the cutoff of the distribution of the PGK-FRET in the solution and 4% gels well. Between 5 min and 2 hr after introducing the PGK-FRET to the 10% hydrogel, the distance PGK-FRET enters the 10% hydrogel varied < 5 µm over the course of the measurement. The variation of the distance PGK-FRET enters different 10% hydrogel samples measured at different times also had low variation (< 10 µm). Therefore, we disregard the small amount of change in PGK-FRET distribution within the 10% hydrogel that may occur in our FReI measurements.

5.5.10 Imaging microscale heterogeneities in hydrogels

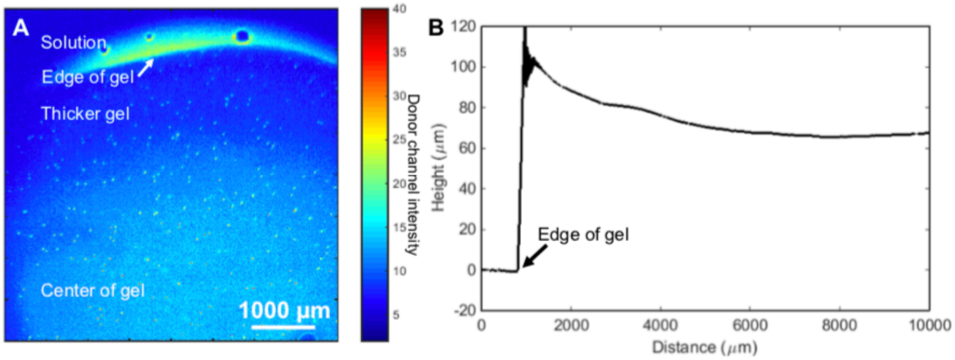

Figure 5.16 Microscale heterogeneity in PGK-FRET distribution imaged on FReI microscope. (a) Microscale spatial variations in PGK-FRET conformations near the edge of a 10% hydrogel. The variations are due to (b) differences in gel thickness measured by profilometry on a Dektak3 ST surface profiler with a 2.5 µm radius stylus, low scan speed, and 1 mg of force. There was less protein closer to the thicker edge of the gel. The small bright spots in (a) are the 6 µm fiduciary markers. The image was taken using a Carl Zeiss 2.5x N-Achroplan 0.07 NA M27 objective. All FReI measurements described in the main text were taken near the center of the hydrogels where the protein distribution was homogeneous.

5.5.11 Spatial resolution estimate obtained by FReI

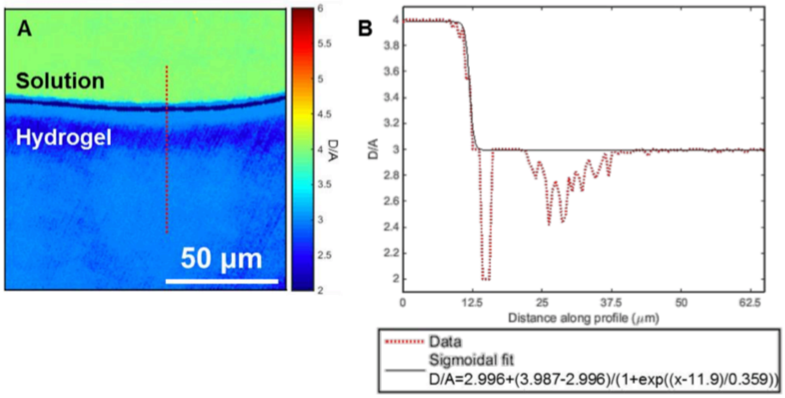

Figure 5.17 Microscale resolution of FReI from D/A ratios of PGK-FRET in an edge-defined sample. (a) D/A image of PGK-FRET both in bulk solution (above) and in the 10% hydrogel (below). This interface was created by an air bubble that formed during polymerization and then filled with solution during the gel rehydration with the PGK-FRET solution. (b) Trace of D/A values along the red dashed line in (a) that shows the change in folded state of PGK-FRET in the different environments. The black line is a sigmoidal fit to the experimental data, excluding the noisy data at D/A $\lesssim$ 3 due to scattering effects in the hydrogel. From the fit, the resolution can be estimated from 3.33 times the slope of the sigmoidal transition,[74,75] and was determined to be 1.2 ± 0.2 µm. Given that the step size at this interface is unknown, the value is an estimate and may be larger than the actual achievable resolution.

5.5.12 Lateral pixel-by-pixel analysis of PGK-FRET in hydrogels

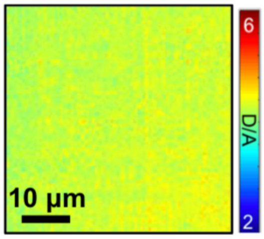

Figure 5.18 Example pixel-by-pixel analysis of D/A across the 10% acrylamide hydrogel at T = 41.6 °C. This image was used to calculate the histogram corresponding to the 10% hydrogel data reported in Figure 5.4 (orange data). (One pixel = 500 nm x 500 nm).

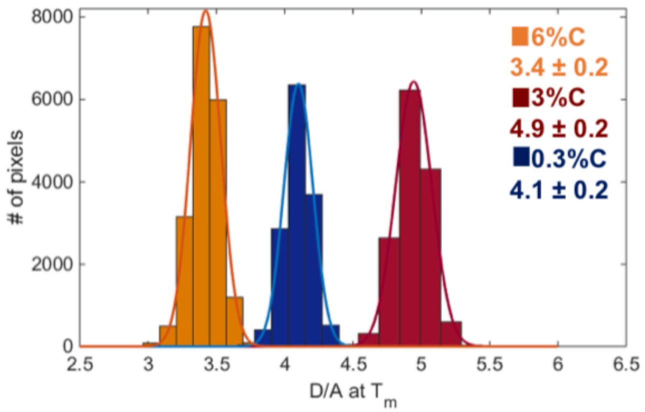

Figure 5.19 Submicron homogeneity of the folded state of PGK-FRET at T_m in 10% polyacrylamide gels made with 0.3% (blue), 3% (red), or 6% (orange) crosslinker as a percent of monomer (or 0.03 – 0.6% bisacrylamide in the total solution). The histograms of D/A ratios at individual 500 nm x 500 nm pixels for each condition were fit to a Gaussian distribution showing a standard deviation of 0.2 D/A for all samples.

5.6 References

1. Choi, B.; Kim, S.; Lin, B.; Wu, B. M.; Lee, M. Cartilaginous Extracellular Matrix-Modified Chitosan Hydrogels for Cartilage Tissue Engineering *ACS Appl. Mater. Interfaces* **2014**, 6, 20110-20121.
2. Zhang, Z.; Chen, X.; Chen, L.; Yu, S.; Cao, Y.; He, C.; Chen, X. Intracellular pH-Sensitive PEG- *Block* -Acetalated-Dextrans as Efficient Drug Delivery Platforms *ACS Appl. Mater. Interfaces* **2013**, 5, 10760-10766.
3. Dong, R.; Jensen, T. W.; Engberg, K.; Nuzzo, R. G.; Leckband, D. E. Variably Elastic Hydrogel Patterned via Capillary Action in Microchannels *Langmuir* **2007**, 23, 1483– 1488.
4. Huang, J.; Wang, L.; Xiong, C.; Yuan, F. Elastic Hydrogel as a Sensor for Detection of Mechanical Stress Generated by Single Cells Grown in Three-Dimensional Environment *Biomaterials* **2016**, 98, 103-112.
5. Kisley, L.; Landes, C. F. Molecular Approaches to Chromatography Using Single Molecule Spectroscopy*Anal. Chem.* **2015**, 87, 83-98.
6. Kjellander, R.; Florin, E. Water Structure and Changes in Thermal Stability of the System Poly(ethylene Oxide)–water *J. Chem. Soc., Faraday Trans. 1* **1981**, 77, 2053-2077.
7. He, Y.; Hower, J.; Chen, S.; Bernards, M. T.; Chang, Y.; Jiang, S. Molecular Simulation Studies of Protein Interactions with Zwitterionic Phosphorylcholine Self-Assembled Monolayers in the Presence of Water*Langmuir* **2008**, 24, 10358-10364.

8. Zheng, J.; Li, L.; Chen, S.; Jiang, S. Molecular Simulation Study of Water Interactions with Oligo (Ethylene Glycol)-Terminated Alkanethiol Self-Assembled Monolayers *Langmuir* **2004**, 20, 8931-8938.
9. Jiang, S.; Cao, Z. Ultralow-Fouling, Functionalizable, and Hydrolyzable Zwitterionic Materials and Their Derivatives for Biological Applications *Adv. Mater.* **2010**, 22, 920– 932.
10. Yang, W.; Bai, T.; Carr, L. R.; Keefe, A. J.; Xu, J.; Xue, H.; Irvin, C. A.; Chen, S.; Wang, J.; Jiang, S. The Effect of Lightly Crosslinked Poly(carboxybetaine) Hydrogel Coating on the Performance of Sensors in Whole Blood *Biomaterials* **2012**, 33, 7945-7951.
11. Hou, J.; Shi, Q.; Ye, W.; Stagnaro, P.; Yin, J. Micropatterning of Hydrophilic Polyacrylamide Brushes to Resist Cell Adhesion but Promote Protein Retention *Chem. Commun.* **2014**, 50, 14975-14978.
12. Sheth, S. R.; Leckband, D. Measurements of Attractive Forces between Proteins and End-Grafted Poly (Ethylene Glycol) Chains *Proc. Natl. Acad. Sci. U. S. A.* **1997**, 94, 8399-8404.
13. Langdon, B. B.; Kastantin, M.; Schwartz, D. K. Surface Chemistry Influences Interfacial Fibrinogen Self-Association *Biomacromolecules* **2015**, 16, 3201-3208.
14. Cleland, J. L.; Builder, S. E.; Swartz, J. R.; Winkler, M.; Chang, J. Y.; Wang, D. I. C. Polyethylene Glycol Enhanced Protein Refolding *Bio/Technology* **1992**, 10, 1013-1019.
15. Abbott, N. L.; Blankschtein, D.; Hatton, T. A. Protein Partitioning in Two-Phase Aqueous Polymer Systems. 3. A Neutron Scattering Investigation of the Polymer Solution Structure and Protein-Polymer Interactions*Macromolecules* **1992**, 25, 3932-3941.
16. Che, A.; Huang, X.; Xu, Z. Protein Adsorption on a Glycosylated Polyacrylonitrile Surface: Monitoring with QCM and SPR *Macromol. Biosci.* **2010**, 10, 955-962.
17. Pelton, J. T.; McLean, L. R. Spectroscopic Methods for Analysis of Protein Secondary Structure *Anal. Biochem.* **2000**, 277, 167-176.
18. Whitmore, L.; Wallace, B. A. DICHROWEB, an Online Server for Protein Secondary Structure Analyses from Circular Dichroism Spectroscopic Data *Nucleic Acids Res.* **2004**, 32, W668-W673.
19. Weidner, T.; Apte, J. S.; Gamble, L. J.; Castner, D. G. Probing the Orientation and Conformation of α-Helix and β-Strand Model Peptides on Self-Assembled Monolayers Using Sum Frequency Generation and NEXAFS Spectroscopy *Langmuir* **2010**, 26, 3433-3440.

20. Tuma, R. Raman Spectroscopy of Proteins: From Peptides to Large Assemblies *J. Raman Spectrosc.* **2005**, 36, 307-319.
21. Haris, P. I.; Chapman, D. The Conformational Analysis of Peptides Using Fourier Transform IR Spectroscopy *Biopolymers* **1995**, 37, 251-263.
22. Ghosh, A.; Smits, M.; Bredenbeck, J.; Dijkhuizen, N.; Bonn, M. Femtosecond Time-Resolved and Two-Dimensional Vibrational Sum Frequency Spectroscopic Instrumentation to Study Structural Dynamics at Interfaces *Rev. Sci. Instrum.* **2008**, 79, 093907.
23. Weidner, T.; Castner, D. G. SFG Analysis of Surface Bound Proteins: A Route towards Structure Determination *Phys. Chem. Chem. Phys.* **2013**, 15, 12516.
24. Weltz, J. S.; Schwartz, D. K.; Kaar, J. L. Surface-Mediated Protein Unfolding as a Search Process for Denaturing Sites *ACS Nano* **2016**, 10, 730-738.
25. Gelman, H.; Platkov, M.; Gruebele, M. Rapid Perturbation of Free-Energy Landscapes: From In Vitro to In Vivo *Chem. - Eur. J.* **2012**, 18, 6420-6427.
26. Ebbinghaus, S.; Gruebele, M. Protein Folding Landscapes in the Living Cell *J. Phys. Chem. Lett.* **2011**, 2, 314-319.
27. Guzman, I.; Gruebele, M. Protein Folding Dynamics in the Cell *J. Phys. Chem. B* **2014**, 118, 8459-8470.
28. Dan, A.; Huang, R. B.; Leckband, D. E. Dynamic Imaging Reveals Coordinate Effects of Cyclic Stretch and Substrate Stiffness on Endothelial Integrity *Ann. Biomed. Eng.* **2016**, 44, 3655-3667.
29. Mann, C.; Leckband, D. Measuring Traction Forces in Long-Term Cell Cultures *Cell. Mol. Bioeng.* **2010**, 3, 40-49.
30. Burnham, M. R.; Turner, J. N.; Szarowski, D.; Martin, D. L. Biological Functionalization and Surface Micropatterning of Polyacrylamide Hydrogels *Biomaterials* **2006**, 27, 5883-5891.
31. Boersma, A. J.; Zuhorn, I. S.; Poolman, B. A Sensor for Quantification of Macromolecular Crowding in Living Cells *Nat. Methods* **2015**, 12, 227-229.
32. Cerminara, M.; Desai, T. M.; Sadqi, M.; Muñoz, V. Downhill Protein Folding Modules as Scaffolds for Broad-Range Ultrafast Biosensors *J. Am. Chem. Soc.* **2012**, 134, 8010-8013.
33. Dhar, A.; Girdhar, K.; Singh, D.; Gelman, H.; Ebbinghaus, S.; Gruebele, M. Protein Stability and Folding Kinetics in the Nucleus and Endoplasmic Reticulum of Eucaryotic Cells *Biophys. J.* **2011**, 101, 421-430.

34. Nölting, B. *Protein Folding Kinetics: Biophysical Methods*; Springer, **2006**.

35. Guo, M.; Xu, Y.; Gruebele, M. Temperature Dependence of Protein Folding Kinetics in Living Cells *Proc. Natl. Acad. Sci. U. S. A.* **2012**, 109, 17863-17867.

36. Eggers, D. K.; Valentine, J. S. Molecular Confinement Influences Protein Structure and Enhances Thermal Protein Stability *Protein Sci.* **2001**, 10, 250-261.

37. Malik, A.; Kundu, J.; Mukherjee, S. K.; Chowdhury, P. K. Myoglobin Unfolding in Crowding and Confinement*J. Phys. Chem. B* **2012**, 116, 12895-12904.

38. Zhou, H.-X. Protein Folding in Confined and Crowded Environments *Arch. Biochem. Biophys.* **2008**, 469, 76-82.

39. Dhar, A.; Samiotakis, A.; Ebbinghaus, S.; Nienhaus, L.; Homouz, D.; Gruebele, M.; Cheung, M. S. Structure, Function, and Folding of Phosphoglycerate Kinase Are Strongly Perturbed by Macromolecular Crowding*Proc. Natl. Acad. Sci. U. S. A.* **2010**, 107, 17586-17591.

40. Lorén, N.; Hagman, J.; Jonasson, J. K.; Deschout, H.; Bernin, D.; Cella-Zanacchi, F.; Diaspro, A.; McNally, J. G.; Ameloot, M.; Smisdom, N.Fluorescence Recovery after Photobleaching in Material and Life Sciences: Putting Theory into Practice *Q. Rev. Biophys.* **2015**, 48, 323-387.

41. Terry, B. R.; Matthews, E. K.; Haseloff, J. Molecular Characterization of Recombinant Green Fluorescent Protein by Fluorescence Correlation Microscopy *Biochem. Biophys. Res. Commun.* **1995**, 217, 21-27.

42. Damaschun, G.; Damaschun, H.; Gast, K.; Misselwitz, R.; Mueller, J. J.; Pfeil, W.; Zirwer, D. Cold Denaturation-Induced Conformational Changes in Phosphoglycerate Kinase from Yeast *Biochemistry* **1993**, 32, 7739-7746.

43. Lee, C. H.; Crosby, A. J.; Emrick, T.; Hayward, R. C. Characterization of Heterogeneous Polyacrylamide Hydrogels by Tracking of Single Quantum Dots *Macromolecules* **2014**, 47, 741-749.

44. Dave, K.; Gelman, H.; Thu, C. T. H.; Guin, D.; Gruebele, M. The Effect of Fluorescent Protein Tags on Phosphoglycerate Kinase Stability Is Nonadditive *J. Phys. Chem. B* **2016**, 120, 2878-2885.

45. Kisley, L.; Brunetti, R.; Tauzin, L. J.; Shuang, B.; Yi, X.; Kirkeminde, A. W.; Higgins, D. A.; Weiss, S.; Landes, C. F. Characterization of Porous Materials by Fluorescence Correlation Spectroscopy Super-Resolution Optical Fluctuation Imaging *ACS Nano* **2015**, 9, 9158-9166.

46. Sandrin, D.; Wagner, D.; Sitta, C. E.; Thoma, R.; Felekyan, S.; Hermes, H. E.; Janiak, C.; de Sousa Amadeu, N.; Kühnemuth, R.; Löwen, H.Diffusion of Macromolecules in a Polymer Hydrogel: From Microscopic to Macroscopic Scales *Phys. Chem. Chem. Phys.* **2016**, 18, 12860-12876.

47. Wang, J.; Gonzalez, A. D.; Ugaz, V. M. Tailoring Bulk Transport in Hydrogels through Control of Polydispersity in the Nanoscale Pore Size Distribution *Adv. Mater.* **2008**, 20, 4482-4489.

48. Peppas, N. A.; Merrill, E. W. Crosslinked Poly(vinyl Alcohol) Hydrogels as Swollen Elastic Networks *J. Appl. Polym. Sci.* **1977**, 21, 1763-1770.

49. White, E. M.; Yatvin, J.; Grubbs, J. B.; Bilbrey, J. A.; Locklin, J. Advances in Smart Materials: Stimuli-Responsive Hydrogel Thin Films *J. Polym. Sci., Part B: Polym. Phys.* **2013**, 51, 1084-1099.

50. Williams, J. C.; Mark, L. A.; Eichholtz, S. Partition and Permeation of Dextran in Polyacrylamide Gel*Biophys. J.* **1998**, 75, 493-502.

51. Li, J.; Hu, Y.; Vlassak, J. J.; Suo, Z. Experimental Determination of Equations of State for Ideal Elastomeric Gels *Soft Matter* **2012**, 8, 8121-8128.

52. Mallam, S.; Horkay, F.; Hecht, A. M.; Geissler, E. Scattering and Swelling Properties of Inhomogeneous Polyacrylamide Gels *Macromolecules* **1989**, 22, 3356-3361.

53. Cohen, Y.; Ramon, O.; Kopelman, I. J.; Mizrahi, S. Characterization of Inhomogeneous Polyacrylamide Hydrogels *J. Polym. Sci., Part B: Polym. Phys.* **1992**, 30, 1055-1067.

54. Lee, C. H.; Crosby, A. J.; Emrick, T.; Hayward, R. C. Characterization of Heterogeneous Polyacrylamide Hydrogels by Tracking of Single Quantum Dots *Macromolecules* **2014**, 47, 741-749.

55. Guzman, I.; Gelman, H.; Tai, J.; Gruebele, M. The Extracellular Protein VlsE Is Destabilized inside Cells *J. Mol. Biol.* **2014**, 426, 11-20.

56. Malik, A.; Kundu, J.; Mukherjee, S. K.; Chowdhury, P. K. Myoglobin Unfolding in Crowding and Confinement*J. Phys. Chem. B* **2012**, 116, 12895-12904.

57. Bolis, D.; Politou, A. S.; Kelly, G.; Pastore, A.; Andrea Temussi, P. Protein Stability in Nanocages: A Novel Approach for Influencing Protein Stability by Molecular Confinement *J. Mol. Biol.* **2004**, 336, 203-212.

58. Eggers, D. K.; Valentine, J. S. Molecular Confinement Influences Protein Structure and Enhances Thermal Protein Stability *Protein Sci.* **2001**, 10, 250-261.
59. Gelman, H.; Wirth, A. J.; Gruebele, M. ReAsH as a Quantitative Probe of In-Cell Protein Dynamics*Biochemistry* **2016**, 55, 1968-1976.
60. Deechongkit, S.; Nguyen, H.; Powers, E. T.; Dawson, P. E.; Gruebele, M.; Kelly, J. W. Context-Dependent Contributions of Backbone Hydrogen Bonding to β-Sheet Folding Energetics *Nature* **2004**, 430, 101-105.
61. Ebbinghaus, S.; Dhar, A.; McDonald, J. D.; Gruebele, M. Protein Folding Stability and Dynamics Imaged in a Living Cell *Nat. Methods* **2010**, 7, 319-323.
62. Mallam, S.; Horkay, F.; Hecht, A. M.; Geissler, E. Scattering and Swelling Properties of Inhomogeneous Polyacrylamide Gels *Macromolecules* **1989**, 22, 3356-3361.
63. Zhang, C.; Sitt, A.; Koo, H.-J.; Waynant, K. V.; Hess, H.; Pate, B. D.; Braun, P. V. Autonomic Molecular Transport by Polymer Films Containing Programmed Chemical Potential Gradients *J. Am. Chem. Soc.***2015**, 137, 5066-5073.
64. Periasamy, A.; Mazumder, N.; Sun, Y.; Christopher, K. G.; Day, R. N. *FRET Microscopy: Basics, Issues and Advantages of FLIM-FRET Imaging*; Springer International Publishing, **2015**; pp 249-276.
65. Wu, P. G.; Brand, L. Resonance Energy Transfer: Methods and Applications *Anal. Biochem.* **1994**, 218, 1-13.
66. Periasamy, A.; Mazumder, N.; Sun, Y.; Christopher, K. G.; Day, R. N. *FRET Microscopy: Basics, Issues and Advantages of FLIM-FRET Imaging*; Springer International Publishing, **2015**; pp 249-276.
67. Roy, R.; Hohng, S.; Ha, T. A Practical Guide to Single-Molecule FRET *Nat. Methods* **2008**, 5, 507-516.
68. Taylor, J. N.; Darugar, Q.; Kourentzi, K.; Willson, R. C.; Landes, C. F. Dynamics of an Anti-VEGF DNA Aptamer: A Single-Molecule Study *Biochem. Biophys. Res. Commun.* **2008**, 373, 213-218.
69. Plaxco, K. W.; Soh, H. T. Switch-Based Biosensors: A New Approach towards Real-Time, in Vivo Molecular Detection *Trends Biotechnol.* **2011**, 29, 1-5.
70. Cho, E. J.; Lee, J.-W.; Ellington, A. D. Applications of Aptamers as Sensors *Annu. Rev. Anal. Chem.* **2009**, 2, 241-264.

71. Wirth, A. J.; Platkov, M.; Gruebele, M. Temporal Variation of a Protein Folding Energy Landscape in the Cell *J. Am. Chem. Soc.* **2013**, 135, 19215-19221.
72. Boersma, A. J.; Zuhorn, I. S.; Poolman, B. A Sensor for Quantification of Macromolecular Crowding in Living Cells. *Nat. Methods* **2015**, *12*, 227–229 .
73. Dhar, A.; Girdhar, K.; Singh, D.; Gelman, H.; Ebbinghaus, S.; Gruebele, M. Protein Stability and Folding Kinetics in the Nucleus and Endoplasmic Reticulum of Eucaryotic Cells. *Biophys. J.* **2011**, *101*, 421-430.
74. Curtin, A. E.; Skinner, R.; Sanders, A. W. A Simple Metric for Determining Resolution in Optical, Ion, and Electron Microscope Images. *Microsc. Microanal.* **2015**, *21*, 771-777.
75. Silva, W. R.; Graefe, C. T.; Frontiera, R. R. Toward Label-Free Super-Resolution Microscopy. *ACS Photonics* **2016**, *3*, 79-86.

CHAPTER 6: FLUORESCENT TECHNIQUES FOR PROBING ZWITTERIONIC POLYMER-PROTEIN INTERACTIONS[1]

6.1 Introduction

The exploitation of poly(zwitterions), polymers that contain equal numbers of cationic and anionic groups on each monomer to maintain an overall charge-neutral state, as biocompatible materials was initially inspired by the nonfouling properties of the zwitterionic headgroups of such phospholipids as phosphatidylcholine on the red blood cell membrane.[1,2] This postulate has been supported by remarkable antifouling properties of poly(zwitterionic) surface coatings in the form of hydrogels, polymer brushes, and spin-cast films that have demonstrated use in biomedical applications[3,4] such as nonadherent wound dressings,[5] biosensors,[6] and stealth nanoparticles.[7,8] Conjugating poly(zwitterions) directly to proteins also appears to protect proteins against aggregation and/or degradation in pharmaceutical applications.[9,10]

The performance of poly(zwitterions) in these diverse applications is ascribed to monomer hydration, which is proposed to generate physical and energetic barriers to protein–polymer association.[11,12] The physical chemical basis of zwitterionic monomer solvation differs from other neutral, water-soluble polymers, including the “gold standard” nonionic polymer poly(ethylene glycol) (PEG), in which water associates to the ether oxygen atoms of the polymer.[13] PEG can still weakly bind protein surfaces and can even act like a chaperone to protect against protein aggregation.[14–20] The modestly better performance of poly(zwitterions) relative to PEG in some comparisons is attributed to differences in the polymer hydration and to reduced interaction with hydrophobic protein surface patches.[21,22] Despite these postulated solvation differences, the potential influence of electrostatic interactions between proteins and zwitterionic polymers versus nonionic PEG has not been investigated. For instance, if poly(zwitterions) presumably interact less with hydrophobic surface patches on proteins, why would they not interact more with the much more prevalent charged and polar patches on the same protein surface?

Poly(zwitterions) form both inter- and intramolecular electrostatic interactions that reduce chain swelling at low ionic strength. Defined as the “anti-polyelectrolyte effect,” the solubility,

---

[1] Reproduced with permission from: Kisley, L.; Serrano, K. A.; Davis, C. M.; Murphy, E. A.; Gruebele, M.; Leckband, D. E. Soluble Zwitterionic Poly(sulfobetaine) Destabilizes Proteins. *Biomacromolecules* **2019**, 1*9 (9)*, 3894-3901. Copyright 2017 American Chemical Society.

swelling, and viscosity of poly(zwitterions) increase with increasing ionic strength[23–25] because electrolytes screen attractive electrostatic interactions between monomers.[2] By contrast, the hydrodynamic radii of classical polyelectrolytes decrease with ionic strength ("polyelectrolyte effect"), whereas nonionic polymers such as PEG are relatively insensitive to added salt.

In contrast to the neutral polymers, proteins bind electrostatically to charged polyelectrolytes.[26–30] Such complexes have been used to stabilize proteins against aggregation, denaturation, or biochemical degradation.[31–34] A limited number of studies of poly(zwitterion) interactions with proteins reported that poly(zwitterions) can inhibit antibody binding or substrate recognition, suggesting a direct protein–polymer association.[35] In other studies, the polymers reportedly repel proteins such as BSA or lysozyme.[36] Tethered zwitterionic chains also reportedly stabilize proteins.[9,10] These seemingly contradictory findings highlight the need for quantitative methods to establish the effect of poly(zwitterions) on protein stability and thermal denaturation.

Given that poly(zwitterions) form inter- and intramolecular interactions and that proteins can interact weakly with other hydrophilic polymers such as PEG, we have two questions: Do poly(zwitterions) and proteins also associate in solution? If so, what is the effect of such interactions on protein stability? Protein surfaces have both positively and negatively charged patches to which poly(zwitterions) could bind. Furthermore, since proteins are ampholytes, and zwitterionic at their isoelectric point (pI), it seems counterintuitive that poly(zwitterions) would preferentially associate with other polymer chains, but not with protein surfaces.

Here we report evidence for direct, destabilizing protein interactions with the soluble, 100 kDa zwitterionic polymer poly(sulfobetaine) (referred to as pSB hereafter). Using tryptophan fluorescence spectra, we measured the thermal denaturation of three proteins in the presence of different concentrations of pSB. Based on changes in the peak wavelength of the fluorescence emission spectrum, we quantified the protein folding thermodynamics. Specifically, studies monitored the melting temperature, which indicates the protein stability, and the protein folding cooperativity parameter, which indicates how likely unfolding of one region of the protein influences the unfolding of other regions. Results show that pSB can decrease the protein thermal stability and increase protein folding cooperativity, depending on the protein. The reduced stability combined with increased cooperativity is rather unusual in protein folding and is another sign that the protein–poly(zwitterion) system acts in concert.

6.2 Results

6.2.1 Choice of proteins

Three globular proteins with different secondary and tertiary structures, electrostatic charge distributions, and sizes were studied in the presence of different concentrations of 100 kDa pSB (Figure 6.1 and 6.7). First, two smaller proteins comprised entirely of a single type of secondary structure were used (Figure 6.1a). The primarily α-helical double mutant of the λ-repressor protein λ_{6-85} (λ_{12}) is a five-helix bundle.[37] In contrast, the R17G mutant of the hPin1 WW domain has a triple-stranded β-sheet structure.[38] The mutant was chosen due to its relatively low melting point. To study the effects of pSB on a more structurally complex protein, we also studied wild-type phosphoglycerate kinase (PGK), an ATP-producing enzyme with mixed α-helical and β-sheet structure. All three of these proteins undergo folding that can be approximated as a cooperative process,[37-40] and they contain tryptophans whose fluorescence spectra report protein folding (Figure 6.1a). Relevant properties of the three proteins are summarized in Table 6.1. The proteins cover a wide mass range and hence range of accessible surface areas. The proteins were studied at pH 7, near their respective pI, and are fairly close to being globally neutral with a near-zwitterionic charge distribution (Figure 6.1b).

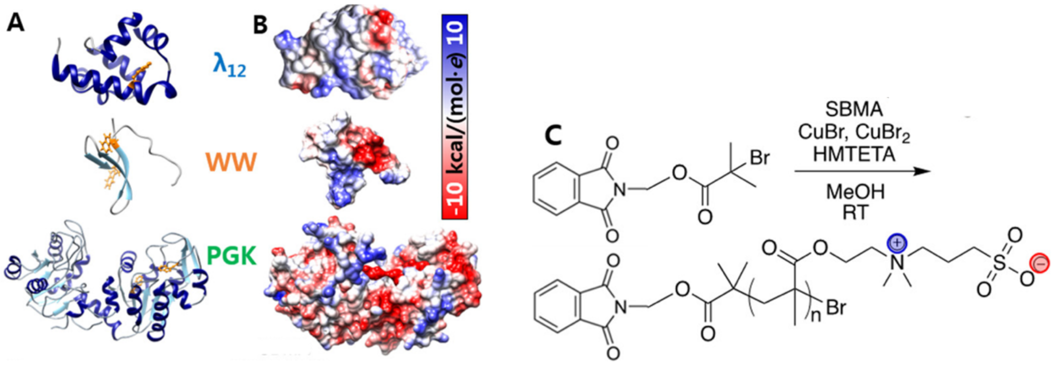

Figure 6.1 Structure and electrostatics of the proteins (λ_{12}, WW domain, and PGK) and polymer. (a) Secondary structure of the proteins (α-helices: dark blue; β-sheets: light blue) and tryptophan resides noted in orange. (b) Coulombic surface charge distribution calculated at pH 7. Protein sizes are not scaled to each other and structures are from PDB entries 3KZ3,[41] 2M8I,[42] and 3PGK.[43] Images were generated in UCSF Chimera.[44] (c) Synthesis scheme of poly(zwitterion) pSB.

Table 6.1 Properties of λ_{12}, WW, and PGK proteins.

protein	λ_{12}	WW	PGK
$\%\alpha/\%\beta$	71/0	0/34	34/11
pI	8.58	7.29	6.93
mass (kDa)	9.2	5.0	44.7

6.2.2 Poly(zwitterion) synthesis

pSB was synthesized by atom transfer radical polymerization (Figure 6.1c). ^{1}H NMR end group analysis of the initiator 1-(phthalimidomethyl) 2-bromoisobutyrate determined the molecular weight to be 100 kDa with a degree of polymerization of $n = 400$ (see Section 6.7). Further analysis by DLS established a moderate polydispersity index (PDI) of 0.25, where the PDI represents the standard deviation of the normally distributed particle size divided by the mean size (PDI = σ/μ; Table 6.5).[45] DLS further confirmed that the pSB exhibits the expected antipolyelectrolyte effect (Figure 6.9).[23,25]

6.2.3 Interaction of pSB with the proteins

Soluble pSB changes both the peak intensity and peak wavelength of protein fluorescence spectra, and indicates direct pSB interactions with the proteins. The tryptophan fluorescence emission spectra were monitored as temperature was varied (Figure 6.2). Figure 6.2a shows spectra at temperatures where the proteins are folded (30 °C) or unfolded (80 °C), in the absence and presence of 5% (w/w) pSB. The control fluorescence spectrum of soluble pSB alone (Figure 6.2a) demonstrates the negligible polymer fluorescence relative to the tryptophan fluorescence of the protein. In the absence of polymer, the spectra of all three proteins red shift as the proteins unfold and expose buried tryptophan residues to bulk solvent. The fluorescence intensity also decreases due to the decreased quantum yield upon exposure to solvent. With 5% (w/w) pSB, the spectra for all three proteins change in ways that indicate direct polymer–protein interactions, as elaborated below.

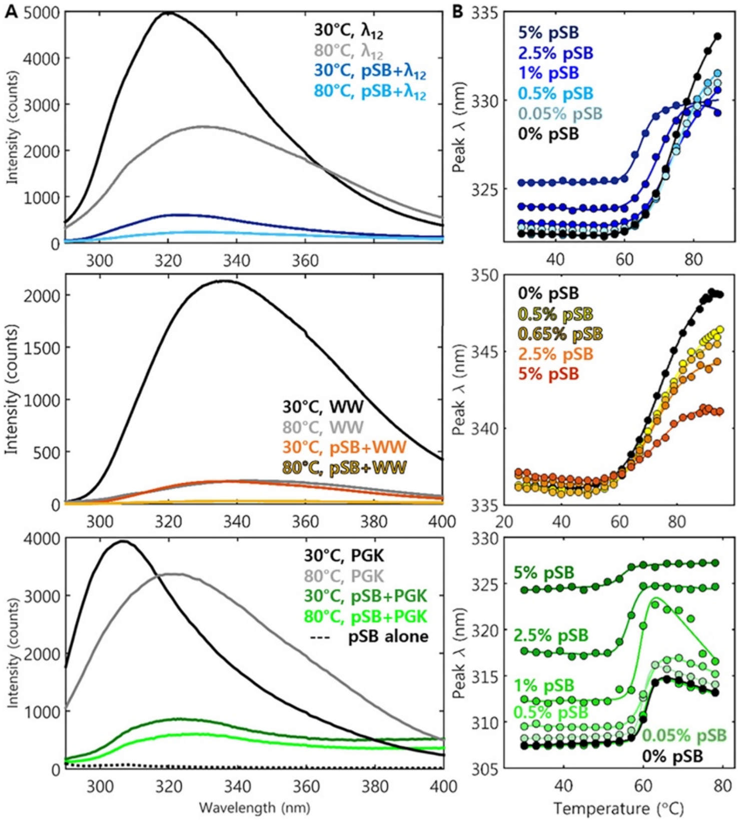

Figure 6.2 Soluble 100 kDa pSB change the stability and cooperativity of protein unfolding. The thermal denaturation of the proteins (λ_{12}, blue; WW domain, orange; PGK, green) are monitored by tryptophan fluorescence. (a) Emission spectra of proteins below (30 °C) and above (80 °C) T_m in the absence (black/gray) and presence (colored) of 5% (w/w) 100 kDa pSB. Control spectrum of 5% (w/w) 100 kDa pSB alone is also shown. (b) Peak wavelength monitors the thermal unfolding of the proteins in 100 kDa pSB ranging from 0 to 5% (w/w). Data shown are from individual trials. Curve fitting results from triplicate measurements are reported in Table 6.2.

In the presence of pSB, the peak wavelength of the fluorescence emission spectrum red-shifts. At 30 °C, the peak wavelengths of all three proteins increase by up to 15 nm depending on the protein, indicating that the tryptophan residues are in a more polar environment (Figures 6.2b and 6.10). For PGK, the red shift is larger than that seen for the unfolded protein in the absence of pSB. Given the strong electric fields around the zwitterionic monomers (bond dipole moment = 15.2 D),[46] we postulate that a local, direct interaction between the pSB and protein surface causes a large increase in the polarity of the tryptophan environment. When increasing the temperature to 80 °C in the presence of pSB, the magnitude of the red shift decreases for PGK compared to data collected without pSB, switches from red to blue for λ_{12}, and blue shifts for the WW domain (Figures 6.2band 6.10). We attribute the latter to changes in local polarity due to increased tryptophan interactions with both pSB and solvent as the protein unfolds.

The fluorescence peak intensity can decrease by an order of magnitude in pSB solutions. We attribute the fluorescence changes to a combination of static quenching by the polymer and conformational changes in the protein that increase tryptophan exposure to the solvent and quencher. Stern–Volmer analysis at three different temperatures below the T_m of PGK shows that pSB quenches the protein fluorescence through a static mechanism (Figure 6.11).[47] Quenching by the polymer could occur through the conjugated initiator group on pSB, the polymer backbone, and previously discussed increased polarity near the tryptophan side chains, which is also known to lower fluorescence intensity of tryptophan in a polar aqueous environment. Control measurements of a tryptophan analogue, *N*-acetyl-1-tryptophanamide, show a 2.5-fold decrease in fluorescent peak intensity in solutions of 5% (w/w) pSB compared to buffer (Figure 6.12). This alone does not reproduce the upward of 10-fold decrease in fluorescence peak intensity observed with the proteins. pSB could induce protein conformational fluctuations that further expose tryptophan side chains (see below for evidence that pSB can destabilize proteins) even in the native state.[48] Circular dichroism under low salt conditions where the measurement could be extended to ~210 nm (limited by sample absorption) confirms that PGK unfolds and loses secondary structure in pSB (Figure 6.8). These conformation changes would then allow for a larger decrease in fluorescent intensity by exposing the tryptophan residues to the pSB. Overall, red shifts in both the emission and the fluorescent quenching are observed for all three proteins, signifying that protein–polymer interactions do not depend strongly on the protein identity, although the effect on the protein stability does.

6.2.4 Evidence that pSB alters protein stability

Soluble pSB alters both the melting temperature and the protein folding cooperativity, but the perturbation is protein-specific. Thermodynamic parameters are extracted from fits of the average peak wavelength of the fluorescent spectra versus temperature (Figure 6.2b and Table 6.2). For λ_{12}, the introduction of 5% (w/w) pSB decreases the T_m from 74 ± 2 to 64 ± 1 °C. The protein folding cooperativity δg_1 increases from 590 ± 20 J mol^{-1} K^{-1} in buffer to 1300 ± 100 J mol^{-1} K^{-1} in the polymer solution. Similarly, the addition of 5% (w/w) pSB decreases the T_m of PGK from 60.8 ± 0.3 °C to 55 ± 1 °C, but there is no significant change in δg_1. The observed changes in T_m and δg_1depend linearly on the weight percent of pSB (Figure 6.3). In contrast, the pSB does not change WW domain folding significantly, except at the highest pSB concentration.

At 5% (w/w) pSB, the WW domain is stabilized and the T_m increases from 75 ± 1 to 84 ± 6 °C. Note that circular dichroism could not be used to confirm protein conformational changes in the presence of pSB in 1.5 M NaCl due to the high absorbance of NaCl and pSB in the far UV.

Table 6.2 Melting Temperature and Cooperativity Index from Curve Fits of Protein Folding at Different pSB Concentrations in Figure 6.2.

protein	%pSB (w/w)	T_m (°C)	δg_1 (J mol^{-1} K^{-1})
λ_{12}	0	74 ± 2	590 ± 20
	0.05	74 ± 2	630 ± 20
	0.5	75 ± 1	600 ± 20
	1	70 ± 1	680 ± 40
	2.5	71 ± 1	740 ± 80
	5	64 ± 1	1300 ± 100
WW	0	75 ± 1	400 ± 20
	0.05	74 ± 1	420 ± 10
	0.5	71 ± 1	420 ± 30
	0.65	74 ± 1	400 ± 20
	2.5	73 ± 2	420 ± 20
	5	84 ± 6	340 ± 50
PGK	0	60.8 ± 0.3	2340 ± 20
	0.05	60 ± 1	3000 ± 400
	0.25	61 ± 2	1500 ± 200
	0.5	61 ± 1	2400 ± 200
	1	60 ± 1	2200 ± 600
	2.5	56 ± 1	1900 ± 300
	5	55 ± 1	1900 ± 700

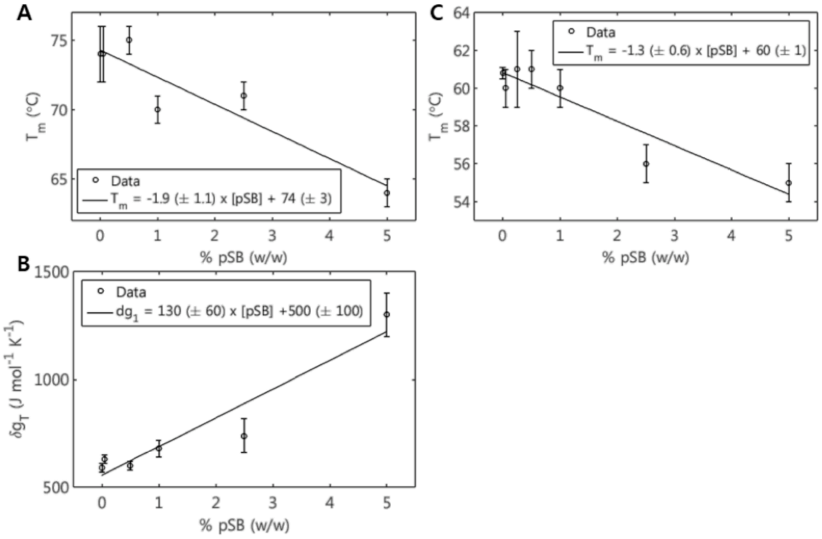

Figure 6.3 Thermodynamic protein folding parameters for (a, b) λ_{12} and (c) PGK change linearly with the concentration of pSB. Changes in (a, c) T_m and (b) δg_1 were fit to a linear equation shown as a solid line with the resulting fitted equations in the legends. Plus/minus values represent the 95% confidence intervals of the fits.

To test the possibility that the effects on the protein might be due to the hydrophobic initiator, control measurements were done with pSB synthesized with a nonhydrophobic terminal initiator group (Figure 6.13a). The results thus obtained show similar changes in protein fluorescence, stability, and folding cooperativity (Figure 6.13b), supporting our postulate that the polymer, and not the initiator, is responsible for the observed changes in protein stability and cooperativity.

6.2.5 Neither PEG nor pSB aggregates affect protein folding

In contrast to results with pSB solutions, PEG does not alter the folding stability or cooperativity of any of the proteins studied. At 10 kDa (n = 160) and 600 kDa (n = 1000), PEG has either a similar molecular weight to the pSB (600 kDa PEG and 100 kDa pSB) or a similar hydrodynamic radius (R_h = 5.36 ± 0.05 nm for 10 kDa PEG and R_h = 30 ± 3 nm for 100 kDa pSB; Table 6.5). At similar degrees of polymerization, PEG has a larger hydrodynamic radius than pSB in pure water,[9] due to the antipolyelectrolyte properties of pSB. No changes in either the T_m or δg_1 are observed for PGK in the presence of 5% (w/w) 10 kDa PEG or 5% (w/w) 600 kDa PEG compared to proteins in buffered solution without polymer (Figure 6.4 and Table 6.3). Similarly, the 10 kDa PEG has a minimal effect on the thermal denaturation of either λ_{12} or the WW domain, compared to protein in buffer without PEG (Figure 6.14 and Table 6.6).

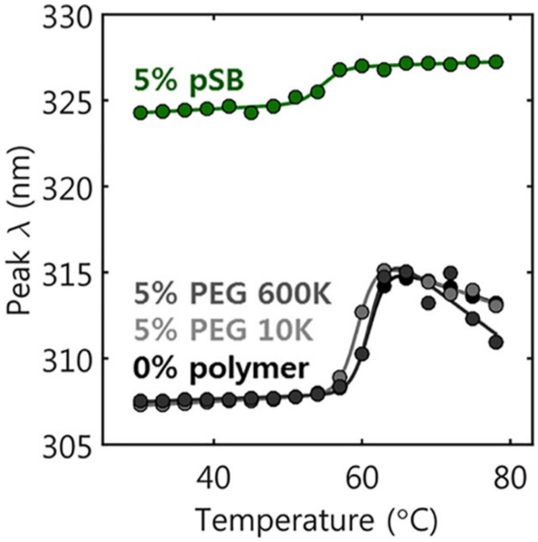

Figure 6.4 PEG does not influence PGK stability or folding cooperativity. PGK thermal denaturation curves in buffer (0%), 5% (w/w) 10 kDa PEG, 5% (w/w) 600 kDa PEG, and 5% (w/w) 100 kDa pSB. Curve fitting results are reported in Table 6.3.

Table 6.3 Melting Temperature and Folding Cooperativity from Curve Fits of PGK Folding in PEG in Figure 6.4.

protein	solution conditions	T_m (°C)	δg_1 (J mol^{-1} K^{-1})
PGK	buffer	60.8 ± 0.3	2340 ± 20
	5% PEG 10 kDa	59 ± 1	2200 ± 200
	5% PEG 600 kDa	61.3 ± 0.5	2300 ± 600
	5% pSB 100 kDa	55 ± 1	1900 ± 700

The insoluble pSB aggregates that form at low ionic strength do not influence the folding of either PGK or λ_{12}. For these studies, 100 kDa pSB was prepared at 0.5% (w/w) in 0–1500 mM NaCl (Figure 6.5a). At concentrations below 50 mM NaCl, the polymer forms heterogeneous aggregates that are visible by eye ($R_h = 8 \pm 2$ µm, Table 6.5). Higher salt concentrations disrupt interchain interactions, resulting in a more homogeneous solution of ~20 nm particles whose radii increase with salt concentration.[25] That the pSB phase state has no observable effect on either the T_m or δg_1 of PGK (Figure 6.5b and Table 6.4) suggests that protein destabilization is due to interactions with soluble pSB chains, and that proteins may be exlcuded from pSB aggregates. Similarly, there is no change in λ_{12} folding (Figure 6.15a and Table 6.7). WW domain folding varies with ionic strength in both the presence and absence of pSB. This agrees with reports that increasing ionic strength stabilizes the WW domain.[49] Here, T_m increases by 9 ± 1 °C as NaCl increases from 0 mM to 1500 mM without pSB (Figure 6.15b and Table 6.7). The T_m increases similarly by 11 ± 1 °C in 0.5% (w/w) pSB as NaCl increases from 0 mM to 1500 mM.

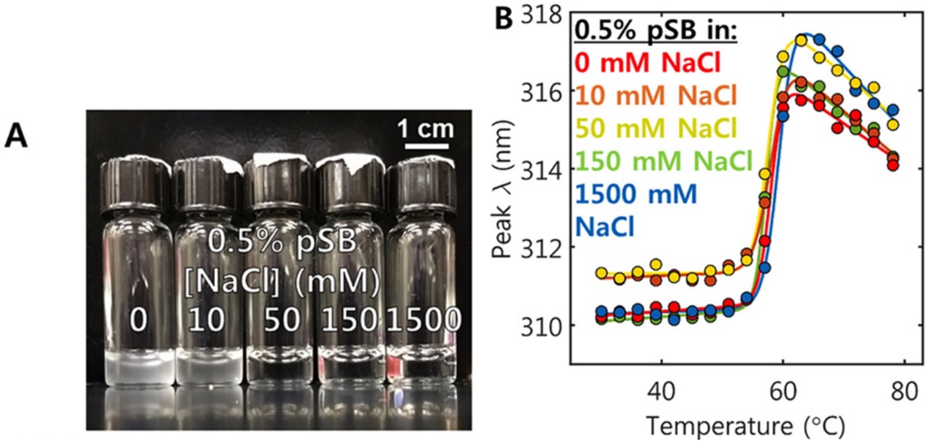

Figure 6.5 PGK destabilization does not depend on the phase or salt-dependent configuration of pSB. (a) 0.5% (w/w) 100 kDa pSB in 20 mM sodium phosphate and indicated concentration of NaCl showing two-phase pSB at NaCl < 50 mM. (b) PGK thermal denaturation curves in the presence of 0.5% (w/w) 100 kDa pSB and 0–1500 mM NaCl. Curve fitting results are reported in Table 6.4.

Table 6.4 Melting Temperature and Folding Cooperativity from Curve Fits of PGK Folding in Variable Ionic Strength and 0.5% (w/w) pSB in Figure 6.5.

protein	[NaCl] (mM)	T_m (°C)	δg_1 (J mol^{-1} K^{-1})
PGK	0	58 ± 1	2700 ± 400
	10	58 ± 1	2000 ± 200
	50	58 ± 1	2200 ± 600
	150	57 ± 1	3100 ± 500
	1500	61 ± 1	2400 ± 200

6.3 Discussion

The results outlined above might be surprising in light of the number of reports of low-fouling zwitterionic coatings, often interpreted as "zwitterion-protein avoidance." Here, reported tryptophan fluorescence intensity and wavelength shifts, the reduced protein stability, and (for λ_{12}) increased cooperativity all point toward a direct protein–pSB interaction, unlike PEG.

The following factors may account for these seeming differences relative to prior observations. First, the importance of the spacing between available unpaired monomer charges on soluble pSB is apparent when compared to small molecule zwitterionic osmolytes, such as betaine, that do not show any evidence of binding to protein surfaces.[22] For small molecules, the separation of the cationic and anionic charges are at a fixed distance of <1 nm, which is usually less than the Debye length, so that the charges do not appear discretely. For soluble pSB, more diverse charge spacing between unpaired or partially paired monomers likely exists (Figure 6.6) that can interact with the proteins, as charge spacing on the proteins can be upward of 4 nm for PGK, and still >3 nm for λ_{12}. In that context it is worth noting that the WW domain, which seems to interact least with pSB, has the smallest and fewest oppositely charged surface patches of the three proteins studied. Importantly, the pSB flexibility enables it to conformationally adapt and bind to charge distributions on the proteins, somewhat analogous to polymer adsorption driven by statistical pattern matching.[50]

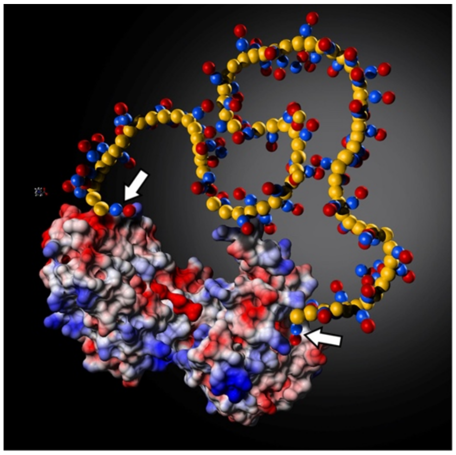

Figure 6.6 Charge spacing of soluble pSB interacts with the protein surface. Cartoon of pSB structure coarse grained to have spheres representing neutral backbone (yellow), cationic quaternary amine (blue), and anionic sulfite (red) chemical groups interacting with PGK electrostatic surface. The diverse charge spacing interacts with charge patches on protein surface, as highlighted for example monomers with arrows. A small molecule zwitterion, betaine, whose dipole spacing is too small is shown to scale as an atomic ball and stick model to the left of the polymer and protein. The length of the polymer chain is not shown to scale for clarity (R_h of pSB ~ 20 nm, while R_h of PGK ~ 8 nm).

Second, the majority of studies of protein adsorption focused on the antifouling properties of grafted poly(zwitterion) brushes in the dense, highly stretched regime where osmotic protein-brush repulsion likely overwhelms any weak protein–polymer attraction.[51] In such cases, proteins only interact with relatively sparse monomers at the outer edge of the brush. Proteins can only penetrate and interact extensively with grafted chains when weak monomer–protein attraction overcomes the osmotic penalty, and this condition depends on the protein size, as well as on the polymer grafting density and molecular weight.[1,51] Therefore, it is unlikely that the proteins are able to overcome the osmotic free energy penalty, under grafting conditions described in the many reports of nonfouling properties of grafted zwitterionic polymer brushes. In contrast, soluble pSB is not subject to the steric and osmotic constraints of a brush, allowing for proteins to interact with the chains. This scenario is somewhat similar to the observed dependence of protein adsorption on the conformation and density of grafted poly(*N*-isopropylacrylamide) chains above the lower critical solution temperature (LCST); namely, proteins were repelled from grafted chains below the LCST (good solvent), but above the LCST (poor solvent), attractive protein–polymer interactions and chain conformations enabled protein adsorption.[52,53]

The effect of soluble pSB on protein folding stability is protein-dependent due to differences in protein salt-sensitivity, surface charge, and structure. Only WW domain shows increased stability in 5% (w/w) pSB. The charge on the pSB could mimic high ionic strength solutions, which stabilize the WW domain, and thus counterbalance the destabilizing effects of the polymer observed for PGK and λ_{12} discussed in the following paragraph. The WW domain also has anionic and cationic charge patches near residues E9 and R21 with a well-defined and rather small separation of ~2.4 nm compared to the more heterogeneous charge distribution of λ_{12} and PGK. This specific distance could lead to fewer modes of interaction between the pSB and the WW domain. Finally, although we refrain from drawing overarching conclusions on the relation of protein secondary structure to pSB interactions, it is worth noting that we observe the greatest destabilization for the α-helical λ_{12}, no destabilization for the β-sheet WW domain, and that the mixed α-helical/β-sheet protein PGK falls in-between the two. Future work with additional proteins is needed to identify structural features that may predispose proteins to pSB-dependent destabilization and to identify how pSB configurations (e.g., grafted versus soluble chains) may affect technologically important proteins such as antibodies or serum proteins.

Overall, the differences in charge spacing and flexibility for soluble pSB allow for more energetically favorable interactions between the polymer and the proteins through enthalpic electrostatic attraction and the entropic release of water molecules and counterions. As the protein unfolds, the polymer can then interact with new residues, leading to the destabilization of the protein and increased cooperativity in protein folding.

6.4 Conclusions

We have shown that interaction between soluble zwitterionic pSB and proteins shifts the fluorescence of partially exposed tryptophan residues, has a destabilizing effect on two proteins, but has a stabilizing effect on a third (β-sheet) protein. This is in contrast with PEG under similar conditions for the same set of proteins. These findings open a new area of exploration in polymer physics to determine mechanisms by which biological solutes may interact differently with grafted versus soluble poly(zwitterions). This has important implications for biotechnological applications of poly(zwitterions) where the availability and spacing of charges on the polymer in relation to the protein charge spacing and the flexible polymer geometry could determine the success or failure of the material. We anticipate future studies showing that poly(zwitterion) brush grafting density and zwitterion charge spacing will influence the structure and amount of protein adsorbed. Pursuing a molecular perspective of poly(zwitterion)-protein interactions similar to PEG[14-18] will expand the understanding of molecular design rules that govern poly(zwitterions) interactions with proteins.

6.5 Experimental section

6.5.1 Protein expression

Full details of the expression of the λ-repressor protein $\lambda_{6\text{-}85}$ mutant λ_{12},[37] hPin1 WW domain,[54] and phosphoglycerate kinase (PGK)[55] by our group have been previously reported. Generally, the cDNA for the proteins with a 6X-His tag and thrombin cleavage site was cloned into the pET28b or pDream 2.1 vectors (Genscript) that contain a T7 or T7 and CMV promoter for dual expression in bacterial and mammalian cells, respectively. *E. coli* BL-21 (DE3) Codon Plus (RIPL) cells (Agilent Technologies) were transformed with the plasmid by heat-shock. Cells were grown in Lennox LB broth at 37 °C to an optical density of ~0.6 at 600 nm. To induce the cells, isopropyl β-d-1-thiogalactopyranoside (Inalco) was added to the culture solution. The cells were allowed to express protein overnight at 20 °C. The cells were then collected by centrifugation (Beckman Coulter Avanti J-E) and resuspended in a buffered solution containing phenylmethylsulfonyl fluoride (Sigma) and DNase (New England Biolabs). The cells were further disrupted by sonication (Qsonica) and the lysate was clarified by centrifugation and filtration (Millipore Millex). The protein was affinity purified (GE Aktapure) by binding to a HisTrap column (GE Healthcare) followed by elution with a solution containing imidazole (Sigma). The final protein solutions were dialyzed into 20 mM sodium phosphate buffer, pH 7. The purity and molecular weight of the final proteins used in measurements were assessed by SDS-PAGE and low-resolution matrix-assisted laser desorption ionization time-of-flight mass spectrometry, respectively.

6.5.2 Synthesis of pSB

Bulk pSB was synthesized by atom transfer radical polymerization based on the method reported by Sundaram et al.[56] The monomer solution of [2-(methacryloyloxy)ethyl]dimethyl-(3-sulfopropyl)ammonium hydroxide (Sigma) was diluted to 200 mM in methanol and degassed in a round-bottom flask with Ar using a glass frit. The ligand 1,1,4,7,10,10-hexamethyltrietylenetetramine (HMTETA, Sigma) and catalyst mixture of $CuBr_2$ (Sigma) and CuBr (Sigma) were subsequently added at concentrations of 0.147, 0.074, and 0.711 mM, respectively. The initiator in the form of 1-(phthalimidomethyl) 2-bromoisobutyrate (Sigma) was then added to the flask at a final concentration of 5 mM. The polymerization reaction proceeded at room temperature with stirring under Ar atmosphere for 24 h. We also synthesized pSB using a different initiator (Section 6.5.9).

After synthesis, the reaction was stopped by exposure to air and excess solvent was removed by rotary evaporation. The polymer precipitate was dissolved in 1.5 M NaCl. Heat was briefly applied by heat gun to assist in removal of the polymer from the sides of the flask. The salt solution was then exchanged with pure Millipore water by placing the polymer in a 3500 Da molecular weight cutoff dialysis tubing (ThermoFisher, SnakeSkin) for three rounds of 8–12 h. The final polymer was recovered by removing excess water by rotary evaporation and then dried under high vacuum (0.01–0.05 Torr).

6.5.3 Characterization of pSB molecular weight by nuclear magnetic resonance (NMR)

^{1}H NMR spectra were recorded at room temperature on a Bruker BioSpin GmbH spectrometer operating at 500 MHz. Samples were prepared using 0.5% (w/w) pSB in 100 mM NaCl in D_2O. Water suppression was used and the NMR spectra were processed using MestReNova software. Chemical shifts are referenced to the residual nuclei in the deuterated solvent. Polymer molecular weight was calculated by end group analysis.

6.5.4 Fluorometer measurements and analysis of protein thermal denaturation

pSB solutions were prepared at 0.05 to 5% (w/w) polymer and 0 to 1.5 M NaCl concentrations in 20 mM sodium phosphate buffer, pH 7. To ensure disruption of the inter- and intramolecular interactions of the pSB upon initial preparation, the pSB solutions were placed in a 70 °C water bath for ~5 min and sonicated. The final solutions were cooled to room temperature and filtered through a 0.45 μm filter (Millipore). PEG 10 kDa (Alfa Aesar B21955) and PEG 600 kDa (Acros Organics 178612500) were diluted to 5% (w/w) in 20 mM sodium phosphate buffer, pH 7, and 1.5 M NaCl. Proteins were then diluted to 1–7 μM in the respective polymer solutions.

The thermal denaturation of the proteins was measured with a Jasco spectrofluorometer FP-8300 in a 1 cm path length quartz cuvette. Mineral oil was placed on top of the protein solutions to prevent evaporation. The temperature was increased in 3 °C steps at a heating rate of 120 °C hr^{-1} with a 180 s equilibration time before each spectral measurement. The tryptophan residues were excited with 280 nm light and the emission from 290 to 400 nm was monitored at a scan speed of 200 nm/min, data intervals of 1 nm, and a 50 ms response time.

The resulting emission spectra were analyzed by calculating the peak wavelength, λ_{max}, between 290 and 400 nm. From the resulting fluorescence thermal unfolding data of λ_{max} versus temperature, T, the thermal denaturation midpoint, T_m, and thermal folding cooperativity parameter, δg_1, were obtained from fitting to Equations 6.1-6.4 in OriginPro 2015,[39]

$$\langle \lambda \rangle = (m_F T + b_F) f_F + (m_U T + b_U) f_U \tag{6.1}$$

where the fraction of folded, f_F, and unfolded, f_U, protein is given by

$$f_F = \exp\left[-\frac{\Delta G}{RT}\right] \Big/ \left(1 + \exp\left[-\frac{\Delta G}{RT}\right]\right) \tag{6.2}$$

$$f_U = 1 - f_F \tag{6.3}$$

and the dependence of free energy, ΔG, on temperature (Celsius) over a narrow temperature range is represented by the linear expansion:[57]

$$\Delta G \approx \delta g_1 (T - T_m) \tag{6.4}$$

Here, the T_m is the temperature at which f_F and f_U are equal and is located at the inflection point of the sigmoidal curve. The protein folding cooperativity, δg_1, is a measure of the slope of the transition from folded to unfolded states. Linear baselines with slopes, m, and offsets, b, above and below T_m (i.e., folded, F, and unfolded, U) are also obtained.

6.5.5 Circular dichroism to characterize the secondary structure of proteins

The purified proteins were characterized by circular dichroism (Figure 6.7). A Jasco J-715 spectropolarimeter was used to measure the far-UV spectra of the proteins diluted to a concentration range of 20-200 µM in 20 mM sodium phosphate buffer, pH 7. The mean residue ellipticity was measured from 200-250 nm in a 0.1 cm path length quartz cuvette at 25 °C. Three spectra were accumulated with standard sensitivity.

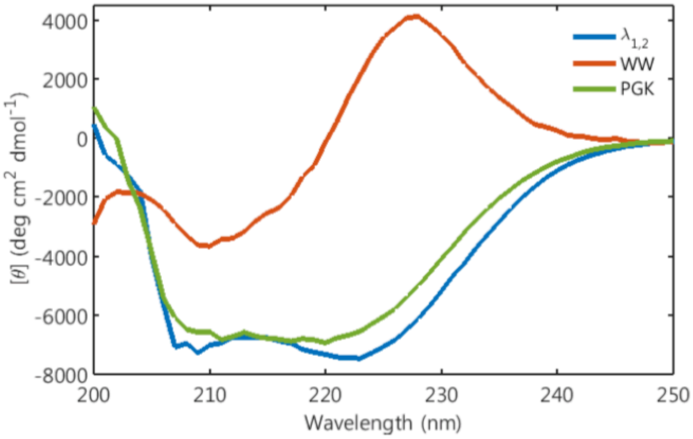

Figure 6.7 Secondary structure characterization of proteins. Circular dichroism of α-helical λ12, β-sheet WW, and mixed secondary structure PGK.

Poly(sulfobetaine) partially unfolds the protein structure below T_m (Figure 6.8). Spectra were collected from 260-210 nm and the solution contained no NaCl, as the high absorbance of NaCl and absorbance of the poly(zwitterion) itself in the far-UV obscured the CD signal. The spectra collected with pSB were further analyzed by singular value decomposition and reconstructed from the first two singular value components, as previously described.[58,59] At 45 °C the signal is lower in pSB compared to buffered solution only, showing that the polymer causes changes in the secondary structure of the protein. As temperature is increased, the protein loses more secondary structure, but does not totally denature PGK. Proteins retain residual secondary structure, even if they largely unfold.

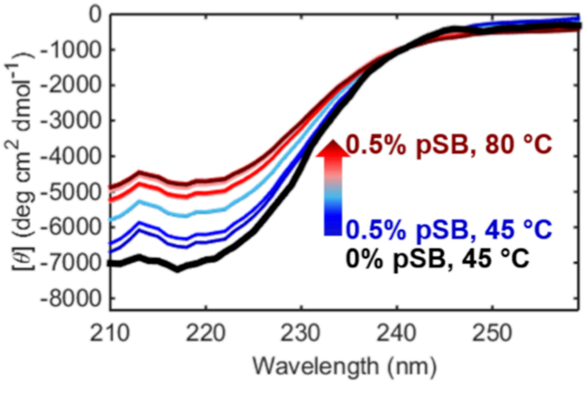

Figure 6.8 Circular dichroism spectra of 5 μM PGK in 20 mM sodium phosphate buffer (black) without pSB at 45 °C and (colored) with 0.5% (w/w) pSB from 45-80 °C.

6.5.6 Characterization of pSB hydrodynamic radius and polydispersity by DLS

In summary, Dynamic light scattering (DLS) measurements were performed using an Anton Paar Litesizer 500 running Kalliope software. A 40 mW single frequency laser diode was used at 658 nm with an avalanche photo diode detector. The scattered light was detected at an angle of 175° (back scatter) for samples containing 0 mM or 10 mM NaCl and at an angle of 90° (side scatter) for all other samples. The temperature was allowed to stabilize to 22 °C for 1 min before measurements. The particle hydrodynamic radius (R_h) and polydispersity index (PDI) were calculated using an advanced cumulant fit of the measured intensity autocorrelation function.[45] Reported values are an average of three separate measurements and all samples were measured in a 20 mM sodium phosphate buffer at pH 7. Hydrodynamic measurements of 5% (w/w) 600 kDa PEG were unable to be performed due to the high viscosity and scattering from large aggregates within the sample.

In detail, The hydrodynamic radius (R_h) and polydispersity index (PDI) were calculated using an advanced cumulant fit of the measured intensity autocorrelation function from the DLS (Table S1, Figure S3).[60-62] In detail, the raw scattering intensity fluctuations over time are autocorrelated versus a lag time, τ, to produce the autocorrelation function, $G_2(\tau)$. Using a cumulant expansion, which is an ISO-standardized procedure,[61] the correlation function is rearranged with a baseline value, B, representing the value of the $G_2(\tau)$ at large τ, and fit to a polynomial (Equation 6.5):

$$ln\left[\frac{G_2(\tau)-B}{B}\right] = ln\beta - 2\bar{\Gamma}\tau + K_2\tau^2 \qquad 6.5$$

Where $\bar{\Gamma}$ is the decay rate, K_2 is the second cumulant, which is equivalent to the second moment about the mean, or the variance, and β is an empirical factor dependent on the experimental geometry.[63] From $\bar{\Gamma}$, the diffusion coefficient, D, can be calculated by Equation 6.6:

$$D = \bar{\Gamma}/q^2 \qquad 6.6$$

where q is the magnitude of the scattering wave vector given by:

$$q = \frac{4\pi n}{\lambda} sin\left(\frac{\theta}{2}\right) \tag{6.7}$$

with n being the refractive index of the solvent, λ is the laser wavelength, and θ is the scattering angle. The R_h is then calculated using the Stokes-Einstein equation:

$$R_h = \frac{k_B T}{6\pi\eta D} \tag{6.8}$$

where k_B is the Boltzmann constant, T is the measurement temperature, and η is the dynamic viscosity. The PDI is calculated from the fitted parameters from Equation S1,

$$PDI = \frac{\sqrt{K_2}}{\overline{\Gamma}} \tag{6.9}$$

and is equivalent to the relative standard deviation in particle size. All PDI values are < 0.3, indicating that they are only moderately polydisperse.[64]

DLS confirms that pSB follows the expected anti-polyelectrolyte effect. At low salt concentrations below 50 mM, pSB aggregates to particles with µm-sized R_h due to strong inter- and intramolecular interactions. The dissolution and two-phase behavior of the pSB at low salt concentrations can even be visualized by eye (Figure 6.5a). At salt concentrations above 50 mM the intermolecular interactions are disrupted. The $R_h = 19.9 \pm 0.1$ nm in 50 mM NaCl and increases gradually as more salt is added and intramolecular interactions are disrupted. We observe a maximum $R_h = 30 \pm 3$ nm in 1500 mM NaCl, in good agreement with previous reports.[65,66]

Table 6.5 Summary of the hydrodynamic radius and polydispersity of 100 kDa pSB and 5% (w/w) 10 kDa PEG.

Polymer	% (w/w)	[NaCl] (mM)	R_h (nm)	PDI (%)
pSB	0.5	0	7000 ± 2000	20 ± 10
pSB	0.5	10	8000 ± 1000	28 ± 1
pSB	0.5	50	19.9 ± 0.1	16.3 ± 0.3
pSB	0.5	100	23.1 ± 0.2	23 ± 1
pSB	0.5	250	25.2 ± 0.9	26 ± 1
pSB	0.5	500	24.0 ± 0.3	26.7 ± 0.6
pSB	0.5	1000	28.5 ± 0.6	27 ± 1
pSB	0.5	1500	30 ± 3	25 ± 2
PEG 10 kDa	5	1500	5.36 ± 0.05	10.3 ± 0.6

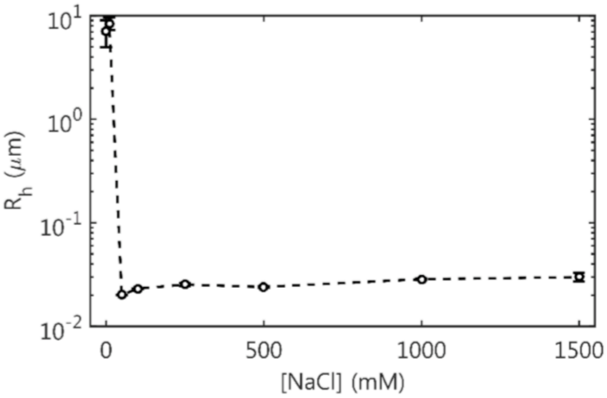

Figure 6.9 pSB exhibits the expected anti-polyelectrolyte effect. Dependence of the hydrodynamic radius of 0.5% (w/w) 100 kDa pSB in variable NaCl at 22℃ determined by DLS.

6.5.7 Tryptophan fluorescence spectra

Tryptophan fluorescence spectra found that pSB shifts the peak wavelength of the tryptophan fluorescence spectrum (Figure 6.10), linear plots indicate static quenching between pSB and PGK (Figure 6.11), and tryptophan fluorescence is quenched by pSB (6.12). The slopes of the Stern-Volmer plots decrease slightly with increasing temperature from 30 to 54 °C, which is below the melting temperature of PGK. This decreasing slope suggests that increasing temperature reduces the static quenching constant between the protein and polymer, and would result in more dissociation between the two species. This mechanism contrasts with an alternative mechanism - collisional quenching - where the quenching would increase with increasing temperature (increase the slope) due to faster diffusion and more frequent intermolecular collisions.

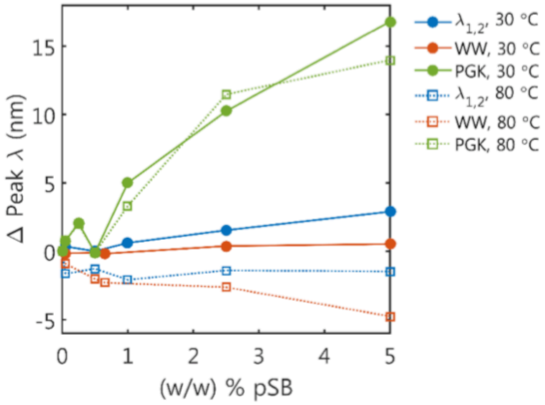

Figure 6.10 Shift in the peak wavelength of the fluorescence emission spectrum relative to 0% pSB at 30 °C (solid, •) and 80 °C (dashed, □) for λ12 (blue), WW (orange), and PGK (green).

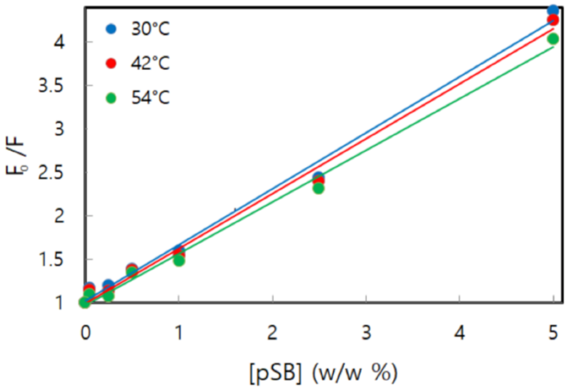

Figure 6.11 Stern-Volmer plots of the normalized peak fluorescent intensity F/F0 versus the pSB concentration measured at different temperatures.

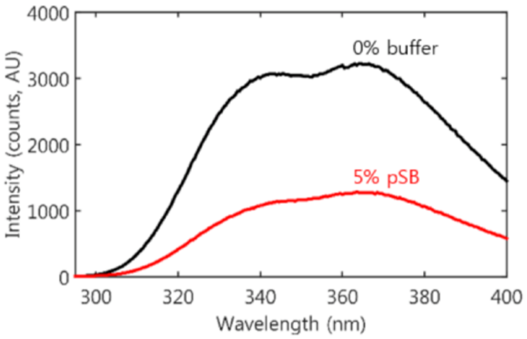

Figure 6.12 N-acetyl-1-tryptophanamide (Sigma Aldrich), a tryptophan analogue, was diluted to 0.6 mg/mL in either 1.5 M NaCl, 20 mM sodium phosphate buffer or 5% (w/w) 100 kDa pSB in 1.5 M NaCl, 20 mM sodium phosphate buffer. The N-acetyl-1-tryptophanamide fluorescence was quenched in soluble pSB (red) compared to in solution (black), with a decrease in peak fluorescence intensity by a factor of 2.5.

6.5.8 Terminal initiator group effect on protein fluorescence, stability, and folding cooperativity

We verified that the polymer backbone, and not the terminal initiator, is responsible for the changes in protein fluorescence, stability, and folding cooperativity. To demonstrate this, poly(sulfobetaine) was synthesized with a non-hydrophobic initiator, ethyl α-bromoisobutyrate (Sigma, Figure S9A). The polymer was synthesized by atom transfer radical polymerization in the same manner as the 100 kDa pSB prepared with the 1-(phthalimidomethyl) 2-bromoisobutyrate initiator described in the Methods section. We refer to this poly(sulfobetaine) with a non-hydrophobic terminal group as EBiB-pSB. The addition of 5% (w/w) EBiB-pSB to 1 μM PGK in 1.5 M NaCl, 20 mM sodium phosphate buffer at pH 7 shows the red-shifted fluorescence, decrease in Tm (57.7 ± 0.2 °C), and lack of change in δg1 (2000 ± 300 J mol-1 K-1) (Figure S9B) similar to that observed for soluble PGK in the presence of 5% (w/w) pSB (Figure 2, Table 2). The values obtained with pSB and EBiB-pSB do not match quantitatively, due to likely differences in the molecular weights of the two polymers. We are unable to characterize the molecular weight of the EBiB-pSB by NMR due to the overlap of the ^{1}H peaks on the terminal initiator group with those on poly(sulfobetaine). However, the overall changes are very similar. These results confirm that the properties of the pSB chain, and not the initiator, are responsible for the altered fluorescence and thermodynamic properties of the protein.

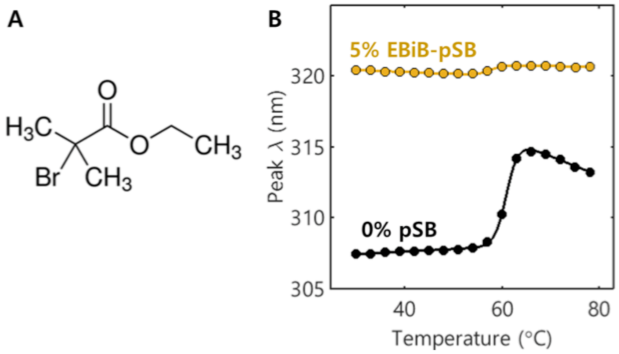

Figure 6.13 Poly(sulfobetaine) with a non-hydrophobic initiator was synthesized using (A) ethyl α-bromoisobutyrate. (B) PGK thermal denaturation curves in buffer (0%) and in 5% (w/w) EBiB-pSB.

6.5.9 Melting temperature and folding cooperativity dependence on PEG and salt conditions

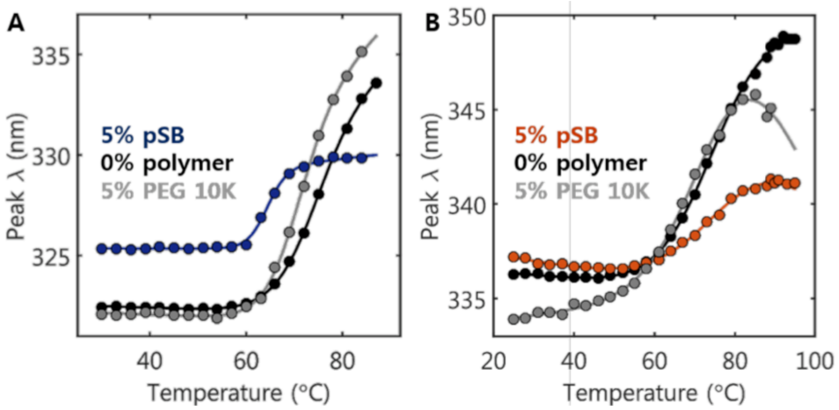

Figure 6.14 PEG minimally influences (A) λ12 or (B) WW domain stability or folding cooperativity. Protein unfolding in 1.5 M NaCl, 20 mM buffer (0%, black), 5% (w/w) 10 kDa PEG (gray), and 5% (w/w) 100 kDa pSB (colored). No or lesser changes in the Tm and δg1 were observed for PEG compared to pSB as listed in Table S2.

Table 6.6 Melting temperature and folding cooperativity from curve fits of protein folding in PEG in Figure S10**.**

Protein	Solution conditions	T_m (° C)	δg_1 (J mol^{-1} K^{-1})
λ_{12}	Buffer	74 ± 2	590 ± 20
	5% PEG 10 kDa	70 ± 1	740 ± 40
	5% pSB 100 kDa	64 ± 1	1300 ± 100
WW	Buffer	75 ± 1	400 ± 20
	5% PEG 10 kDa	71 ± 1	420 ± 40
	5% pSB 100 kDa	84 ± 6	340 ± 50

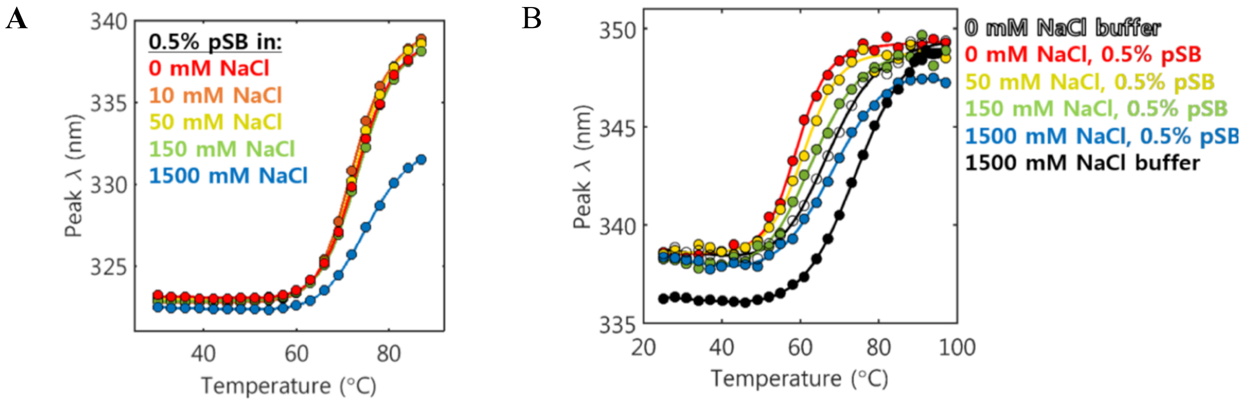

Figure 6.15 (a) The destabilization λ12 does not depend on the phase or salt-dependent configuration of pSB. λ12 thermal denaturation curves in the presence of 0.5% (w/w) 100 kDa pSB and 0-1500 mM NaCl. Extracted values of Tm and δg1 from curve fitting are reported in Table S3. (b) The destabilization WW depends on the ionic strength of the solution regardless of the presence of pSB. WW thermal denaturation curves in the presence of 0.5% (w/w) 100 kDa pSB and 0-1500 mM NaCl and 0 and 1500 mM NaCl buffered solution without pSB. Extracted values of Tm and δg1 from curve fitting are reported in Table S3.

Table 6.7 Melting temperature and folding cooperativity from curve fits of protein folding in variable ionic strength and 0.5% (w/w) pSB (unless noted otherwise) in Figures S11 and S12.

Protein	[NaCl] (mM)	T_m (° C)	δg_1 (J mol^{-1} K^{-1})
λ_{12}	0	73 ± 1	700 ± 10
	10	71.1 ± 0.8	720 ± 10
	50	73 ± 1	730 ± 10
	150	73 ± 1	710 ± 10
	1500	74 ± 2	620 ± 10
WW	0	59 ± 1	700 ± 50
	50	61 ± 1	600 ± 70
	150	63 ± 1	440 ± 70
	1500	70 ± 1	360 ± 30
WW	0, no pSB	66 ± 1	450 ± 60
	1500, no pSB	75 ± 1	400 ± 20

6.6 NMR Spectra

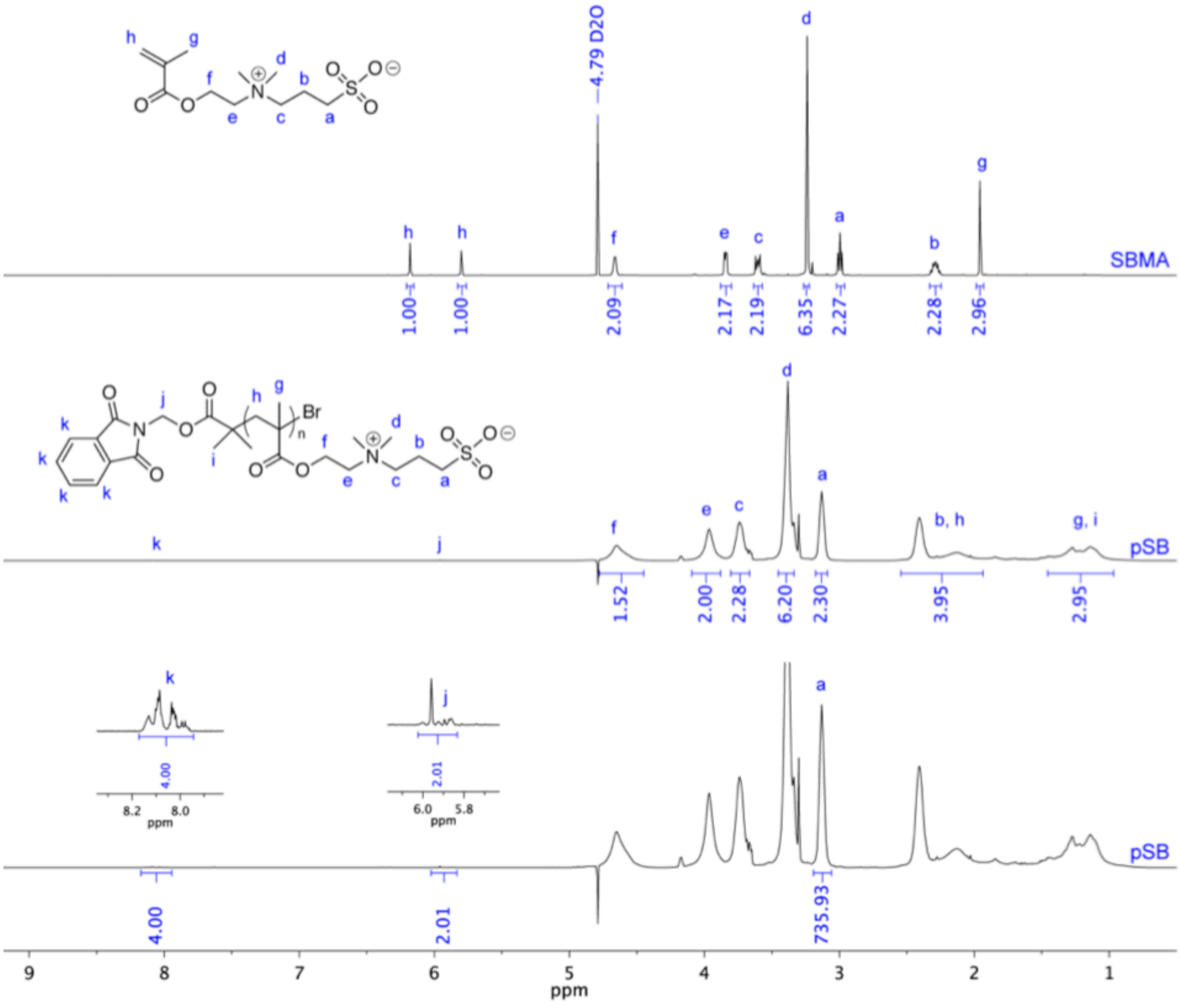

6.7 References

1. Schlenoff, J. B. Zwitteration: Coating Surfaces with Zwitterionic Functionality to Reduce Nonspecific Adsorption. *Langmuir* **2014**, *30*, 9625-9636.
2. Lowe, A. B.; McCormick, C. L. Synthesis and Solution Properties of Zwitterionic Polymers. *Chem. Rev.***2002**, *102*, 4177-4190.
3. Alswieleh, A. M.; Cheng, N.; Canton, I.; Ustbas, B.; Xue, X.; Ladmiral, V.; Xia, S.; Ducker, R. E.; El Zubir, O.; Cartron, M. L.Zwitterionic Poly(Amino Acid Methacrylate) Brushes. *J. Am. Chem. Soc.* **2014**, *136*, 9404-9413.

4. Jiang, S.; Cao, Z. Ultralow-Fouling, Functionalizable, and Hydrolyzable Zwitterionic Materials and Their Derivatives for Biological Applications. *Adv. Mater.* **2010**, *22*, 920-932.
5. Lalani, R.; Liu, L. Electrospun Zwitterionic Poly(Sulfobetaine Methacrylate) for Nonadherent, Superabsorbent, and Antimicrobial Wound Dressing Applications. *Biomacromolecules* **2012**, *13*, 1853-1863.
6. Yang, W.; Bai, T.; Carr, L. R.; Keefe, A. J.; Xu, J.; Xue, H.; Irvin, C. A.; Chen, S.; Wang, J.; Jiang, S. The Effect of Lightly Crosslinked Poly(Carboxybetaine) Hydrogel Coating on the Performance of Sensors in Whole Blood. *Biomaterials* **2012**, *33*, 7945-7951.
7. Wang, W.; Ji, X.; Kapur, A.; Zhang, C.; Mattoussi, H. A Multifunctional Polymer Combining the Imidazole and Zwitterion Motifs as a Biocompatible Compact Coating for Quantum Dots. *J. Am. Chem. Soc.* **2015**, *137*, 14158-14172.
8. Wang, B.; Blin, T.; Käkinen, A.; Ge, X.; Pilkington, E. H.; Quinn, J. F.; Whittaker, M. R.; Davis, T. P.; Ke, P. C.; Ding, F. Brushed Polyethylene Glycol and Phosphorylcholine for Grafting Nanoparticles against Protein Binding. *Polym. Chem.* **2016**, *7*, 6875-6879.
9. Keefe, A. J.; Jiang, S. Poly (Zwitterionic) Protein Conjugates Offer Increased Stability without Sacrificing Binding Affinity or Bioactivity. *Nat. Chem.* **2012**, *4*, 59-63.
10. Song, W.; Zhu, J.; Liu, L.; Liu, G. Modulation of the Binding Affinity of Polyzwitterion-Conjugated Protein by Ion-Specific Effects in Crowded Environments. *J. Phys. Chem. B* **2017**, *121*, 7366-7372.
11. Shao, Q.; Jiang, S. Influence of Charged Groups on the Properties of Zwitterionic Moieties: A Molecular Simulation Study. *J. Phys. Chem. B* **2014**, *118*, 7630-7637.
12. Leng, C.; Hung, H.-C.; Sun, S.; Wang, D.; Li, Y.; Jiang, S.; Chen, Z. Probing the Surface Hydration of Nonfouling Zwitterionic and PEG Materials in Contact with Proteins. *ACS Appl. Mater. Interfaces* **2015**, *7*, 16881-16888.
13. Zheng, J.; Li, L.; Tsao, H.-K.; Sheng, Y.-J.; Chen, S.; Jiang, S. Strong Repulsive Forces between Protein and Oligo (Ethylene Glycol) Self-Assembled Monolayers: A Molecular Simulation Study. *Biophys. J.* **2005**, *89*, 158-166.
14. Sheth, S. R.; Leckband, D. Measurements of Attractive Forces between Proteins and End-Grafted Poly (Ethylene Glycol) Chains. *Proc. Natl. Acad. Sci. U. S. A.* **1997**, *94*, 8399-8404.
15. Cleland, J. L.; Builder, S. E.; Swartz, J. R.; Winkler, M.; Chang, J. Y.; Wang, D. I. C. Polyethylene Glycol Enhanced Protein Refolding. *Nat. Biotechnol.* **1992**, *10*, 1013-1019.

16. Abbott, N. L.; Blankschtein, D.; Hatton, T. A. Protein Partitioning in Two-Phase Aqueous Polymer Systems. 3. A Neutron Scattering Investigation of the Polymer Solution Structure and Protein-Polymer Interactions. *Macromolecules* **1992**, *25*, 3932-3941.
17. Chao, S.-H.; Schäfer, J.; Gruebele, M. The Surface of Protein $\lambda_{6–85}$ Can Act as a Template for Recurring Poly(Ethylene Glycol) Structure. *Biochemistry* **2017**, *56*, 5671-5678.
18. Faulón Marruecos, D.; Kastantin, M.; Schwartz, D. K.; Kaar, J. L. Dense Poly(Ethylene Glycol) Brushes Reduce Adsorption and Stabilize the Unfolded Conformation of Fibronectin. *Biomacromolecules* **2016**, *17*, 1017-1025.
19. Leckband, D.; Sheth, S.; Halperin, a. Grafted Poly(Ethylene Oxide) Brushes as Nonfouling Surface Coatings. *J. Biomater. Sci., Polym. Ed.* **1999**, *10*, 1125-1147.
20. Ngadi, N.; Abrahamson, J.; Fee, C.; Morison, K. Are PEG Molecules a Universal Protein Repellent?. *Int. J. Chem. Mol. Eng.* **2009**, *3*, 12-16.
21. Shao, Q.; Jiang, S. Molecular Understanding and Design of Zwitterionic Materials. *Adv. Mater.* **2015**, *27*, 15-26.
22. Kane, R. S.; Deschatelets, P.; Whitesides, G. M. Kosmotropes Form the Basis of Protein-Resistant Surfaces. *Langmuir* **2003**, *19*, 2388-2391.
23. Schulz, D. N.; Peiffer, D. G.; Agarwal, P. K.; Larabee, J.; Kaladas, J. J.; Soni, L.; Handwerker, B.; Garner, R. T. Phase Behaviour and Solution Properties of Sulphobetaine Polymers. *Polymer* **1986**, *27*, 1734-1742.
24. Mary, P.; Bendejacq, D. D.; Labeau, M.-P.; Dupuis, P. Reconciling Low- and High-Salt Solution Behavior of Sulfobetaine Polyzwitterions. *J. Phys. Chem. B* **2007**, *111*, 7767-7777.
25. Delgado, J. D.; Schlenoff, J. B. Static and Dynamic Solution Behavior of a Polyzwitterion Using a Hofmeister Salt Series. *Macromolecules* **2017**, *50*, 4454-4464.
26. Kayitmazer, A. B.; Seeman, D.; Minsky, B. B.; Dubin, P. L.; Xu, Y. Protein–polyelectrolyte Interactions. *Soft Matter* **2013**, *9*, 2553-2583.
27. Karayianni, M.; Pispas, S.; Chryssikos, G. D.; Gionis, V.; Giatrellis, S.; Nounesis, G. Complexation of Lysozyme with Poly(Sodium(Sulfamate-Carboxylate) Isoprene. *Biomacromolecules* **2011**, *12*, 1697-1706.
28. Wu, B.; Liu, G.; Zhang, G.; Craig, V. S. J. Stiff Chains Inhibit and Flexible Chains Promote Protein Adsorption to Polyelectrolyte Multilayers. *Soft Matter* **2014**, *10*, 3806-3816.

29. Watanabe, J.; Shen, H.; Akashi, M. Polyelectrolyte Droplets Facilitate Versatile Layer-by-Layer Coating for Protein Loading Interface. *Acta Biomater.* **2008**, *4*, 1255-1262.
30. Woitovich Valetti, N.; Brassesco, M. E.; Picó, G. A. Polyelectrolytes-Protein Complexes: A Viable Platform in the Downstream Processes of Industrial Enzymes at Scaling up Level. *J. Chem. Technol. Biotechnol.* **2016**, *91*, 2921-2928.
31. Vander Straeten, A.; Bratek-Skicki, A.; Germain, L.; D'Haese, C.; Eloy, P.; Fustin, C.-A.; Dupont-Gillain, C.Protein-Polyelectrolyte Complexes to Improve the Biological Activity of Proteins in Layer-by-Layer Assemblies. *Nanoscale* **2017**, *9*, 17186-17192.
32. Taluja, A.; Bae, Y. H. Role of a Novel Excipient Poly(Ethylene Glycol)- *b* -Poly(l -Histidine) in Retention of Physical Stability of Insulin at Aqueous/Organic Interface. *Mol. Pharmaceutics* **2007**, *4*, 561-570.
33. Matsuda, A.; Mimura, M.; Maruyama, T.; Kurinomaru, T.; Shiuhei, M.; Shiraki, K. Liquid Droplet of Protein–Polyelectrolyte Complex for High-Concentration Formulations. *J. Pharm. Sci.* **2018**, *107 (10)*, 2713-2719.
34. Rahmani, V.; Sheardown, H. Protein-Alginate Complexes as PH-/Ion-Sensitive Carriers of Proteins. *Int. J. Pharm.* **2018**, *535*, 452-461.
35. Ivanov, I.; Tsacheva, I.; Stoyanova, V.; Nikolov, M.; Tchorbadjieva, M. I.; Petrova, S.; Christov, L.; Georgieva, V.; Georgiev, G. Chaperone-Like Effect of Polyzwitterions on the Interaction of C1q with IgG. *Z. Naturforsch., C: J. Biosci.* **2009**, *64*, 149-154.
36. Tsai, Y.-L.; Tseng, Y.-C.; Chen, Y.-M.; Wen, T.-C.; Jan, J.-S. Zwitterionic Polypeptides Bearing Carboxybetaine and Sulfobetaine: Synthesis, Self-Assembly, and Their Interactions with Proteins. *Polym. Chem.* **2018**, *9*, 1178-1189.
37. Sukenik, S.; Pogorelov, T. V.; Gruebele, M. Can Local Probes Go Global? A Joint Experiment–Simulation Analysis of $\lambda_{6\text{–}85}$ Folding. *J. Phys. Chem. Lett.* **2016**, *7*, 1960-1965.
38. Jäger, M.; Dendle, M.; Kelly, J. W. Sequence Determinants of Thermodynamic Stability in a WW Domain-An All-β-Sheet Protein. *Protein Sci.* **2009**, *18*, 1806-1813.
39. Dhar, A.; Girdhar, K.; Singh, D.; Gelman, H.; Ebbinghaus, S.; Gruebele, M. Protein Stability and Folding Kinetics in the Nucleus and Endoplasmic Reticulum of Eucaryotic Cells. *Biophys. J.* **2011**, *101*, 421-430.
40. Davis, C. M.; Dyer, R. B. The Role of Electrostatic Interactions in Folding of β-Proteins. *J. Am. Chem. Soc.***2016**, *138*, 1456-1464.

41. Liu, F.; Gao, Y. G.; Gruebele, M. A Survey of λ Repressor Fragments from Two-State to Downhill Folding. *J. Mol. Biol.* **2010**, *397*, 789-798.
42. Luh, L. M.; Hänsel, R.; Löhr, F.; Kirchner, D. K.; Krauskopf, K.; Pitzius, S.; Schäfer, B.; Tufar, P.; Corbeski, I.; Güntert, P.Molecular Crowding Drives Active Pin1 into Nonspecific Complexes with Endogenous Proteins Prior to Substrate Recognition. *J. Am. Chem. Soc.* **2013**, *135*, 13796-13803.
43. Watson, H. C.; Walker, N. P.; Shaw, P. J.; Bryant, T. N.; Wendell, P. L.; Fothergill, L. A.; Perkins, R. E.; Conroy, S. C.; Dobson, M. J.; Tuite, M. F.Sequence and Structure of Yeast Phosphoglycerate Kinase. *EMBO J.* **1982**, *1*, 1635-1640.
44. Pettersen, E. F.; Goddard, T. D.; Huang, C. C.; Couch, G. S.; Greenblatt, D. M.; Meng, E. C.; Ferrin, T. E.UCSF Chimera--A Visualization System for Exploratory Research and Analysis. *J. Comput. Chem.* **2004**, *25*, 1605-1612.
45. White Paper: Data Acquisition, Processing and Interpretation in the Litesizer Series, https://www.anton-paar.com/corp-en/services-support/document-finder/litesizertm-500/ (accessed Apr 13, **2018**).
46. Lee, H.; Puodziukynaite, E.; Zhang, Y.; Stephenson, J. C.; Richter, L. J.; Fischer, D. A.; DeLongchamp, D. M.; Emrick, T.; Briseno, A. L. Poly(Sulfobetaine Methacrylate)s as Electrode Modifiers for Inverted Organic Electronics. *J. Am. Chem. Soc.* **2015**, *137*, 540-549.
47. Lakowicz, J. R. *Principles of Fluorescence Spectroscopy*; Springer: New York, **2006**.
48. Chen, Y.; Barkley, M. D. Toward Understanding Tryptophan Fluorescence in Proteins. *Biochemistry* **1998**, *37*, 9976-9982.
49. Ibragimova, G. T. T.; Wade, R. C. C. Stability of the β-Sheet of the WW Domain: A Molecular Dynamics Simulation Study. *Biophys. J.* **1999**, *77*, 2191-2198.
50. Bratko, D.; Chakraborty, A. K.; Shakhnovich, E. I. Recognition between Random Heteropolymers and Multifunctional Disordered Surfaces. *Chem. Phys. Lett.* **1997**, *280*, 46-52.
51. Halperin, A.; Kröger, M. Collapse of Thermoresponsive Brushes and the Tuning of Protein Adsorption. *Macromolecules* **2011**, *44*, 6986-7005.
52. Choi, B.-C.; Choi, S.; Leckband, D. E. Poly(N-Isopropyl Acrylamide) Brush Topography: Dependence on Grafting Conditions and Temperature. *Langmuir* **2013**, *29*, 5841-5850.

53. Xue, C.; Yonet-Tanyeri, N.; Brouette, N.; Sferrazza, M.; Braun, P. V.; Leckband, D. E. Protein Adsorption on Poly(N-Isopropylacrylamide) Brushes: Dependence on Grafting Density and Chain Collapse. *Langmuir***2011**, *27*, 8810-8818.
54. Jäger, M.; Nguyen, H.; Crane, J. C.; Kelly, J. W.; Gruebele, M. The Folding Mechanism of a β-Sheet: The WW Domain. *J. Mol. Biol.* **2001**, *311*, 373-393.
55. Kisley, L.; Serrano, K. A.; Guin, D.; Kong, X.; Gruebele, M.; Leckband, D. E. Direct Imaging of Protein Stability and Folding Kinetics in Hydrogels. *ACS Appl. Mater. Interfaces* **2017**, *9*, 21606-21617.
56. Sundaram, H. S.; Han, X.; Nowinski, A. K.; Ella-Menye, J.-R.; Wimbish, C.; Marek, P.; Senecal, K.; Jiang, S.One-Step Dip Coating of Zwitterionic Sulfobetaine Polymers on Hydrophobic and Hydrophilic Surfaces. *ACS Appl. Mater. Interfaces* **2014**, *6*, 6664-6671.
57. Ebbinghaus, S.; Gruebele, M. Protein Folding Landscapes in the Living Cell. *J. Phys. Chem. Lett.* **2011**, *2*, 314-319.
58. Dumont, C.; Matsumura, Y.; Kim, S. J.; Li, J.; Kondrashkina, E.; Kihara, H.; Gruebele, M. Solvent-Tuning the Collapse and Helix Formation Time Scales of Lambda(6-85)*. Protein Sci. 2006, 15, 2596-2604.
59. Guin, D.; Sye, K.; Dave, K.; Gruebele, M. Dodine as a Transparent Protein Denaturant for Circular Dichroism and Infrared Studies. Protein Sci. 2016, 25, 1061-1068.
60. Min, G. K.; Bevan, M. A.; Prieve, D. C.; Patterson, G. D. Light Scattering Characterization of Polystyrene Latex with and without Adsorbed Polymer. Colloids Surfaces A Physicochem. Eng. Asp. 2002, 202, 9-21.
61. ISO 22412:2008 - Particle size analysis -- Dynamic light scattering (DLS) https://www.iso.org/standard/40942.html (accessed Apr 13, 2018).
62. White Paper: Data Acquisition, Processing and Interpretation in the LitesizerTM Series https://www.anton-paar.com/corp-en/services-support/document-finder/litesizertm-500/ (accessed Apr 13, 2018).
63. Frisken, B. J. Revisiting the Method of Cumulants for the Analysis of Dynamic Light-Scattering Data. Appl. Opt. 2001, 40, 4087.
64. Ferreira, J.; Syrett, J.; Whittaker, M.; Haddleton, D.; Davis, T. P.; Boyer, C. Optimizing the Generation of Narrow Polydispersity ‘Arm-First’ Star Polymers Made Using RAFT Polymerization. Polym. Chem. 2011, 2, 1671-1677.

65. Delgado, J. D.; Schlenoff, J. B. Static and Dynamic Solution Behavior of a Polyzwitterion Using a Hofmeister Salt Series. Macromolecules 2017, 50, 4454-4464.
66. Schulz, D. N.; Peiffer, D. G.; Agarwal, P. K.; Larabee, J.; Kaladas, J. J.; Soni, L.; Handwerker, B.; Garner, R. T. Phase Behaviour and Solution Properties of Sulphobetaine Polymers. Polymer (Guildf). 1986, 27, 1734-1742.

CHAPTER 7: SOFT 3D MICROSCALE VIBRATORY PLATFORMS FOR CHARACTERIZATION OF NANOSCALE POLYMER FILMS[1]

7.1 Introduction

Microelectromechanical systems (MEMS) with tailored mechanical vibratory resonances address a range of applications in mass detection,[1–3] microscale rheology,[4–6] energy harvesting,[7–11] wearable sensors,[12,13] and soft robotics.[14,15] Existing MEMS are largely based on two-dimensional (2D) geometries such as cantilevered beams,[16] doubly clamped bridges/wires,[17] and suspended plates,[18] which present limited numbers of accessible vibration modes and configurations of modal displacements. Consequently, the operation of most MEMS relies on a single vibration mode, thereby restricting their capability, for example, in detecting anisotropic mechanical properties in certain biological[19–21] and composite[22–26] thin-film materials. Access to multimodal resonances in 2D MEMS platforms typically requires non-idealities and asymmetries in nanomechanical resonators,[27] or advanced actuation techniques using collections of piezoelectric components[28] or patterned illumination with structured laser beams,[29] but the consequent engineering complications create challenges in scaling and adapting to complex materials systems. A potential alternative strategy relies on three-dimensional (3D) vibrational structures with multimodal and tunable resonances,[30,31] formed by microfabrication and controlled assembly.[32–39] Reported methods in actuation *via* thin-film piezoelectric elements require, however, multistep fabrication processes, and they operate over a limited range of frequencies.

In this study, we introduce a set of experimental and theoretical approaches to the design and fabrication of 3D microscale frameworks as vibratory platforms with integrated circuit elements for Lorentz-force actuation and localized heating. The assembly process exploits techniques in deterministic mechanical buckling[36–39] on elastomeric substrates. The key features of these systems are their (1) high resonant frequencies, accessible *via* a combination of Lorentz-force actuation and small characteristic dimensions, (2) diverse, multimodal motions controlled through orientation of the actuation force and design of the 3D layouts, and (3) low overall tensile stiffnesses enabled by the use of thin polymers for the structural elements. The results represent

---

[1] Reproduced with permission from: Nan, K.; Want, H.; Ning, X.; Miller, K. A.; Wei, C.; Liu, Y.; Li, H.; Xue, Y.; Xie, Z.; Luan, H.; Zhang, Y.; Huang, Y.; Rogers, J. A.; Braun, P. V. Soft Three-Dimensional Microscale Vibratory Platforms for Characterization of Nano-Thin Polymer Films. *ACS Nano* **2019**, *13 (1)*, 449-457. Copyright 2019 American Chemical Society.

promising tools for measurement of both mass and modulus in isotropic and anisotropic nano-thin polymer films. Demonstrations include extraction of modulus and density of coatings by use of multimodal resonances of a single, reusable measurement platform. Integrated thermal actuators allow for evaluation of the temperature dependence of the modulus, including those associated with phase transitions. Theoretical modeling and design suggest the potential for measurement of anisotropic mechanical properties in single or multilayer films.

7.2 Results and discussion

7.2.1 3D multimodal vibratory systems actuated by Lorentz force

Figure 7.1a is a schematic illustration of a representative 3D system assembled on an elastomeric substrate. The overall size, as measured by the distance between the two sites at which the structure bonds to the substrate, is 800 μm. The critical dimension, as defined by the width of the narrowest ribbon, is 100 μm. As shown by the exploded view in Figure 7.1b, this platform consists of a layer of patterned conductive traces (Au, thickness = 300 nm) sandwiched between two layers of polyimide (PI, thickness ~2.5 μm for each). The PI layers not only form the structural components of the system but also encapsulate and protect the traces. The 3D architecture results from mechanical buckling of a 2D precursor (see Figure 7.2) *via* controlled release of a prestretched elastomeric substrate, as described elsewhere.[36–39] The detailed fabrication process for the precursors appears in Figure 7.3 and Section 7.4. Briefly, layers of PI and gold are consecutively deposited on a silicon wafer and patterned using photolithography. Dissolution of a sacrificial layer of poly(methyl methacrylate) (PMMA) releases the precursor formed in this manner from the underlying wafer. The planar nature of the process then allows integration of nano-thin polymer films as test vehicles with a wide range of thicknesses and geometries. In this work, we demonstrate the use of a photodefinable epoxy (SU8), a cresol novolak resin (S1805), and a polymer brush (PNIPAm) as test films, patterned onto the 2D precursors *via* photopolymerization, photolithography, and selective growth, respectively (see Section 7.4 for details).

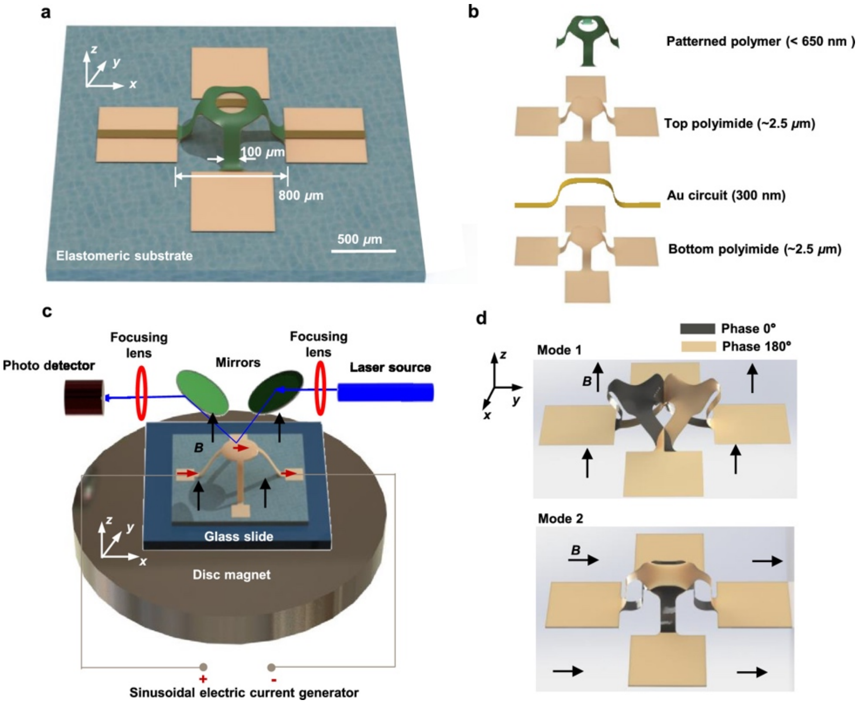

Figure 7.1 3D microstructure actuated by Lorentz force. (a) Schematic illustrations of the 3D structure, assembled on an elastomer substrate. (b) Exploded view of the layered composition with integrated conductive traces. (c) Schematic illustration of the measurement system, consisting of a magnet and current source for Lorentz-force actuation and a laser apparatus for detection of vibrational motions. (d) FEA views of the two distinct vibration modes of the vibrator, achieved by placing the permanent magnet at the bottom (top frame) and at the side (bottom frame). The amplitudes of the vibrations are exaggerated for viewing purposes.

Figure 7.1c and Figure 7.4 highlight the systems for Lorentz-force actuation and optical measurement. The Lorentz force follows from use of a sinusoidal voltage source (1.5 V, Keithley 3390) to create an alternating current (AC) through the traces, with a permanent magnet (neodymium disc) placed underneath the 3D structure to induce a static magnetic field in the *z*-direction. The result is an AC oscillatory force at the frequency of the current, imparted onto the traces at a direction perpendicular to the current and the magnetic field. The amplitude of the Lorentz force can be estimated by $F = B \times I_{\mathrm{rms}} \times L_{\mathrm{Au}} \approx 12.5$ μN (magnetic field (B) ≈ 0.5T; rms value of electric current (I_{rms}) = 25 mA; gold wire length (L_{Au}) = 1 mm). The optical measurement system uses apparatus reported in previous work[30] based on lock-in detection of laser light scattered from the 3D structure. The amplitude of such a measurement is approximately proportional to the amplitude of the vibration. Additional details are in Section 7.4. Changing the position of the magnet alters the direction of the magnetic field to allow actuation of targeted vibration modes. Figure 6.1d illustrates the lowest in-plane and out-of-plane vibration modes, obtained by 3D finite element analysis (FEA, see Section 7.4.4 for details). Experimentally, these modes are excited by placing the magnet below (denoted as mode 1, Figure 7.5a) and to the left of the 3D structure (denoted as mode 2, Figure 7.5b), respectively.

7.2.2 Characterization of modulus and density using multimodal resonances

The effects of the patterned nano-thin polymer films under test on the vibrational frequencies of these two modes allow determination of both the modulus and density of the same sample. Dimensional analysis (see Section 7.4.5 for details) and FEA suggest a linear relationship between the resonant frequency and the polymer modulus and density:

$$\frac{f}{f_0} = C_{\mathrm{E}} \frac{E_{\mathrm{P}} h_{\mathrm{P}}}{\hat{E}_{\mathrm{Base}} h_{\mathrm{Base}}} - C_{\rho} \frac{\rho_{\mathrm{P}} h_{\mathrm{P}}}{\hat{\rho}_{\mathrm{Base}} h_{\mathrm{Base}}} \tag{7.1}$$

where f and f_0 are the resonant frequencies with and without the polymer, E_{P}, ρ_{P}, and h_{P} are the polymer modulus, density, and thickness, $\hat{E}_{\mathrm{Base}}$, $\hat{\rho}_{\mathrm{Base}}$, and h_{Base} are the effective modulus, average density, and thickness of the PI/Au/PI trilayer, respectively (see Section 7.4.6 for details), and the dimensionless parameters C_{E} and C_{ρ} depend on the topology of the 3D vibratory platform, the vibration mode, and the geometries of nano-thin polymer patterns and gold circuits. For the 3D structure, vibration modes and nano-thin polymer/gold patterns in Figure 7.6, FEA gives $C_{\mathrm{E}(1)} = 0.44$, $C_{\rho(1)} = 0.30$ for mode 1 and $C_{\mathrm{E}(2)} = 0.20$, $C_{\rho(2)} = 0.30$ for mode 2, as shown in Figure 7.2a,b. The results indicate that the specific designs of the nano-thin polymer patterns and the vibration modes enable partial decoupling of the sensitivities of resonant frequencies to the polymer modulus and density. In particular, the resonant frequency of mode 1 is 2.2 ($C_{\mathrm{E}(1)} / C_{\mathrm{E}(2)}$) times more sensitive to the polymer modulus than that of mode 2, as measured by the slope of the curves in Figure 7.2 a. Meanwhile the resonant frequencies of both modes are sufficiently sensitive to the polymer density. The design of the nano-thin polymer patterns follows from use of a FEA-based algorithm that optimizes the contribution of the polymer to the strain energy and the kinetic energy of the vibrations (see Section 7.4.7 for details). The developed scaling law serves as the basis of an inverse problem to determine the polymer tensile stiffness ($E_{\mathrm{P}} h_{\mathrm{P}}$) and mass ($\rho_{\mathrm{P}} h_{\mathrm{P}}$) from the measured resonant frequencies (see Section 7.4.8 for details).

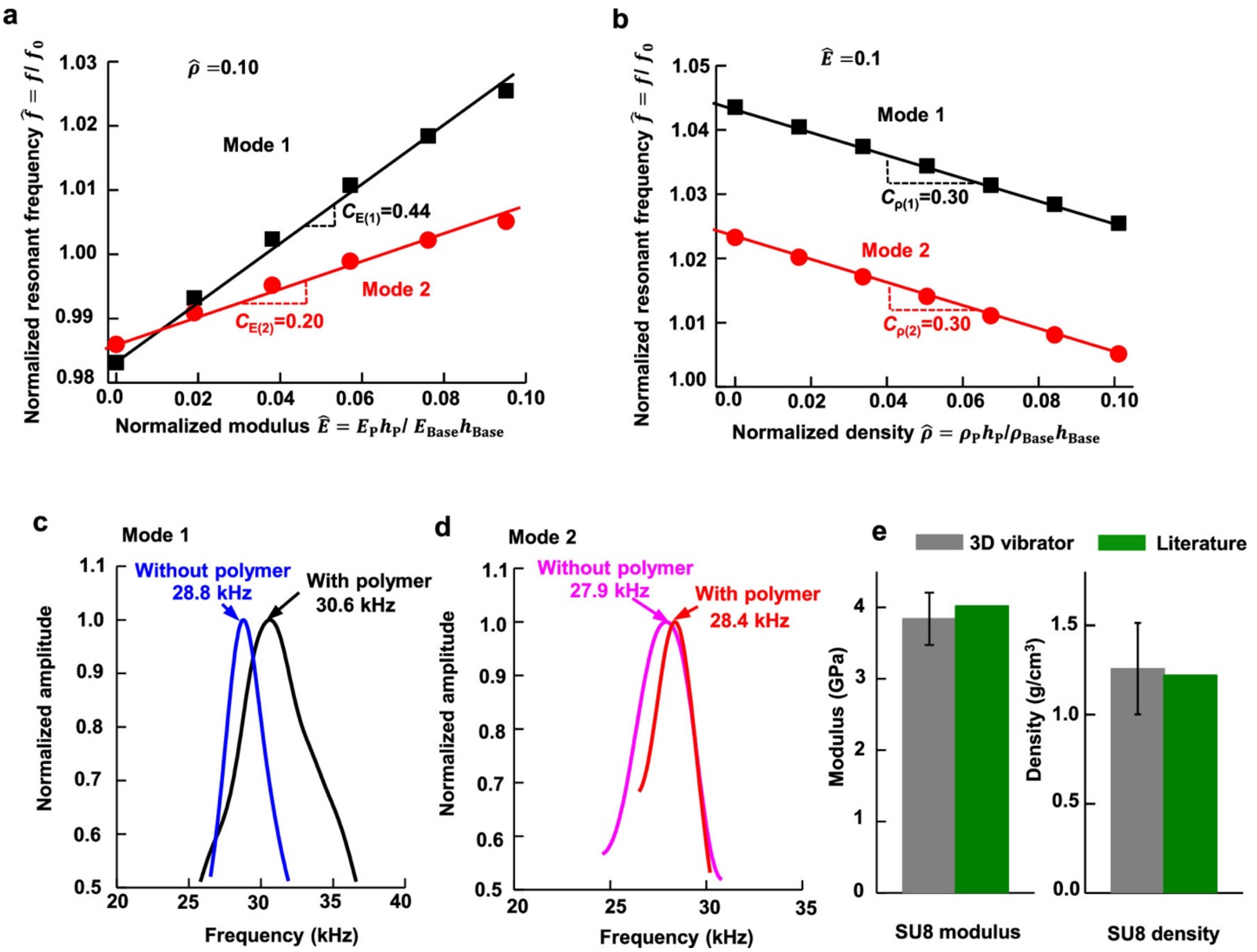

Figure 7.2 Measurement of modulus and density using a single 3D microstructure. (a, b) FEA results for variation of the normalized resonant frequency with the normalized modulus (a) and the normalized density (b), for both vibration modes 1 and 2. (c, d) Measurement results of the normalized amplitude *versus* frequency for mode 1 (c) and mode 2 (d). (e) Modulus (left frame) and density (right frame) determined by the 3D vibratory structure, compared with the literature values.

In principle, the method is applicable to evaluation of any type of material (polymers, metals, ceramics), but the tensile stiffness ($E_P h_P$) and mass ($\rho_P h_P$) of the films must be at least 1 order of magnitude smaller than those of the base layer ($\hat{E}_{\mathrm{Base}} h_{\mathrm{Base}} = 1.36 \times 10^4$N/m and $\hat{\rho}_{\mathrm{Base}} h_{\mathrm{Base}} = 0.013$ kg/m^2 for the design shown in Figure 7.2a), such that the linear relationship in Equation 7.1 applies. For all the polymers studied in this paper, $E_{\mathrm{Base}} \approx E_P$ and $\rho_{\mathrm{Base}} \approx \rho_P$, so h_P should be approximately 1 order of magnitude smaller than h_{Base}. h_{Base} in Figure 7.2a is on the order of 10 μm, which can be used to measure nano-thin films with h_P on the order of 10^2 nm or smaller. In such cases, to deduce the elastic modulus (E_P) and density (ρ_P) of the polymer from multimodal frequency measurements, the thickness (h_P) of the nano-thin polymer film must be known. Measurements of thickness are most easily performed prior to 3D assembly, in the precursor 2D geometry with techniques such as surface profilometry or spectroscopic ellipsometry (see Section 7.4 for details), with uncertainty of ∼5%.

As an example, Figure 7.2c,d shows experimental measurements of the response curves of modes 1 and 2, respectively, for the case of a patterned nano-thin layer of a photodefinable epoxy (SU8; thickness = 610 nm, Figure 7.7b). The resonant frequencies are $f_{(1)}$ = 30.6 kHz, $f_{0(1)}$ = 28.8 kHz for mode 1, and $f_{(2)}$ = 28.4 kHz, $f_{0(2)}$ = 27.9 kHz for mode 2. The repeatability of the measurement is ∼0.1%, as defined by the standard deviation of four measurements performed in sequence (Figure 7.8). The effective modulus, average density, and thickness of the base layer are $\hat{E}_{\mathrm{Base}}$ = 2.51 GPa, $\hat{\rho}_{\mathrm{Base}}$ = 2.41 g/cm^3, and h_{Base} = 5.4 μm, respectively. Inserting these values into Equation 7.1 ields the modulus E_{P} = 3.8 ± 0.4 GPa and density ρ_{P} = 1.3 ± 0.3 g/cm^3 of the epoxy, as presented in Figure 7.2 e. The combined uncertainties in thickness and frequency lead to ∼10% and ∼20% uncertainties in the extracted film modulus and density, respectively (see Section 7.4.8 for details). The ∼5% discrepancies between the modulus and density values reported here and those in the literature (SU8 modulus 4.02 GPa; SU8 density 1.22 g/cm^3) are within the uncertainties.

Based on the theoretical model (Equation 1 and Equations 7.11-7.13), both the relative uncertainties in the as determined polymer modulus ($\frac{\delta E_{\mathrm{P}}}{E_{\mathrm{P}}}$) and density ($\frac{\delta \rho_{\mathrm{P}}}{\rho_{\mathrm{P}}}$) depend linearly on the uncertainties in the measured resonant frequency (δf, see Figure 7.9 for details). Park *et al*. reports that using the laser Doppler vibrometer (MSV-300, Polytec), the uncertainty in the resonant frequency can be reduced to 1 Hz when the resonant frequency is on the order of 10–10^2 kHz,[40] that is, δf = 1 Hz. With such a level of precision, the relative uncertainties in the as determined polymer modulus and density can be reduced to 0.25% and 0.87%, respectively. The relative uncertainty in the thickness measurement, on the other hand, is also linearly related to the uncertainties in the as determined modulus and density. For example, a 1% reduction in uncertainty in the thickness measurement corresponds to a 1% reduction in uncertainty in the as determined polymer modulus and density.

7.2.3 Robustness and reusability of 3D vibrators

The elastic, reversible nature of the 3D assembly process allows repetitive use of these measurement platforms. Specifically, after measuring one nano-thin polymer sample, applying tensile strain on the underlying elastomeric substrate fully returns the 3D structure to its unbuckled, 2D form, thus allowing the removal of the nano-thin film under test and application of another material (see Figure 7.10 for the schematic illustration). Release of the tensile strain reassembles the 3D structure for frequency measurements. Cycling tests that involve 500 cycles of stretching/release reveal a resonance frequency shift of <0.3% (from 34.90 ± 0.03 kHz to 35.00 ± 0.03 kHz), despite an increase in circuit resistance of ~20% (Figure 7.11) perhaps due to some level of plastic yielding in the gold layer. Because the gold (300 nm) is much thinner than the PI (~5 µm) and because it is positioned at the neutral mechanical plane, its plastic yielding has a minor effect on the overall resonant frequency. As a demonstrating example, Figure 7.3b shows a set of experimental results on two cresol novolak resin (S1805) nano-thin films with different thicknesses (450 ± 30 nm and 650 ± 40 nm), actuated with mode 1. The scanning electron microscope images of the device before and after the novolak resin is spin coated (Figure 7.12) indicate full coverage and good uniformity of the resulted film. Note that after washing away S1805 with acetone, the response curve of the 3D vibrator matches the initial polymer-free state exceptionally well, indicating good robustness and repeatability of the system as well as effectively complete removal of S1805.

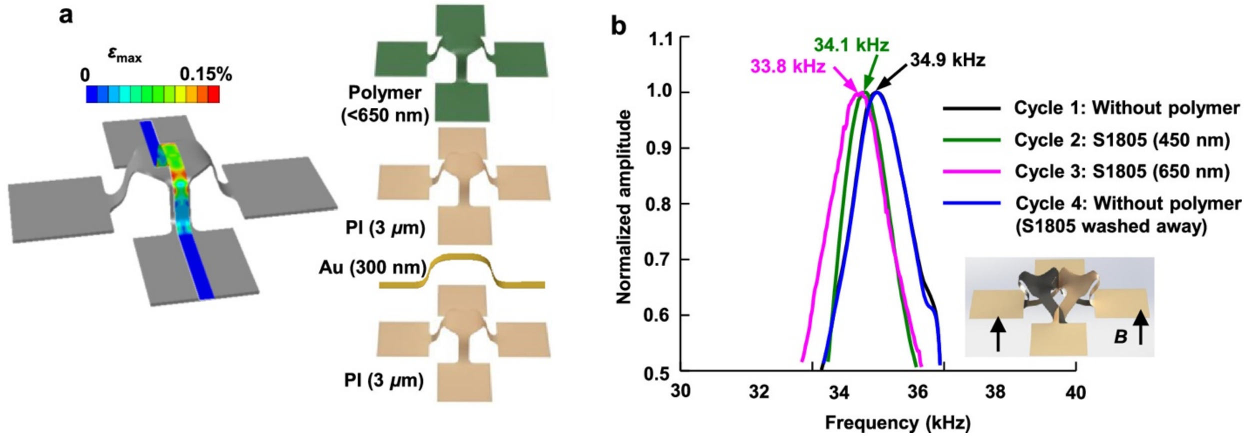

Figure 7.3 Reusability of the 3D vibratory structure. (a) Maximum strain in the gold layer obtained by FEA, which is below its yield strain (left frame). Exploded view of the layered composition of the vibratory platform (right frame). (b) FEA views of the vibration mode in this measurement (inset), and a series of measurement results on the same platform using different testing subjects. The amplitudes of the vibrations are exaggerated for viewing purposes.

7.2.4 Integration with thermal actuators for temperature-dependent measurements

The compatibility with planar fabrication technologies allows integration of additional actuating and sensing elements, *via* a few additional fabrication steps (see Section 7.4 for fabrication details). As a specific example, thermal actuators allow studies of modulus as a function of temperature. Figure 7.4a shows schematic illustrations of a modified 3D platform that includes this functionality. A bilayer of photodefinable epoxy (SU8, thickness = 40 ± 2 nm) and a poly(*N*-isopropylacrylamide) (PNIPAm) brush (thickness = 270 ± 20 nm) patterned directly on top of the thermal actuators serve as the test sample (see Section 7.4 for experimental details). Figure 7.4 b shows the FEA calibration of the temperature change *versus* direct current input for the thermal actuator (see Section 7.4.4 for details).[41] The temperature change at the nano-thin polymer region is uniform, as illustrated by the inset of Figure 7.4b. The experimental results in Figure 7.4c show as expected that the resonant frequency decreases as the temperature increases. Measurements for three cycles of heating are in Figure 7.4 c, where the peak temperature is 80 °C in the nano-thin polymer in cycle 1 (denoted by the blue solid triangles) and 300 °C in cycles 2 (red solid circles) and 3 (black solid squares). The sharp, ∼0.5 ± 0.05 kHz decrease in resonant frequency at 40–50 °C corresponds to the glass transition of PNIPAm, while the ∼0.2 ± 0.05 kHz decrease at 100–150 °C corresponds to that of SU8. The measured glass transition temperature matches well with the literature values for SU8,[42] whereas it is lower than the reported values for bulk PNIPAm,[43] as expected for this material which contains short polymer chain lengths and has a small thicknesses.[44–49] During the glass transition, the change in polymer mass ($\rho_P h_P$) is negligible because of mass conservation; the change in polymer thickness is also small (<1%) due to the small coefficient of thermal expansion[50,51] and the small change in temperature across the glass transition. The changes in the moduli of PNIPAm and SU8 nano-thin films are thus determined from the corresponding resonant frequency shifts to be ΔE_{PNIPAm} = 1.1 ± 0.2 GPa and ΔE_{SU8} = 4 ± 1 GPa, respectively (Figure 7.4d, see Section 7.4.9 for detailed calculations). The difference between the measured change in modulus of SU8 across the glass transition is consistent with the literature value (3.7 GPa),[42] to within experimental uncertainties. Finally, the further reduction in resonant frequency above 200 °C is likely attributable to the onset of softening of PI itself.[52]

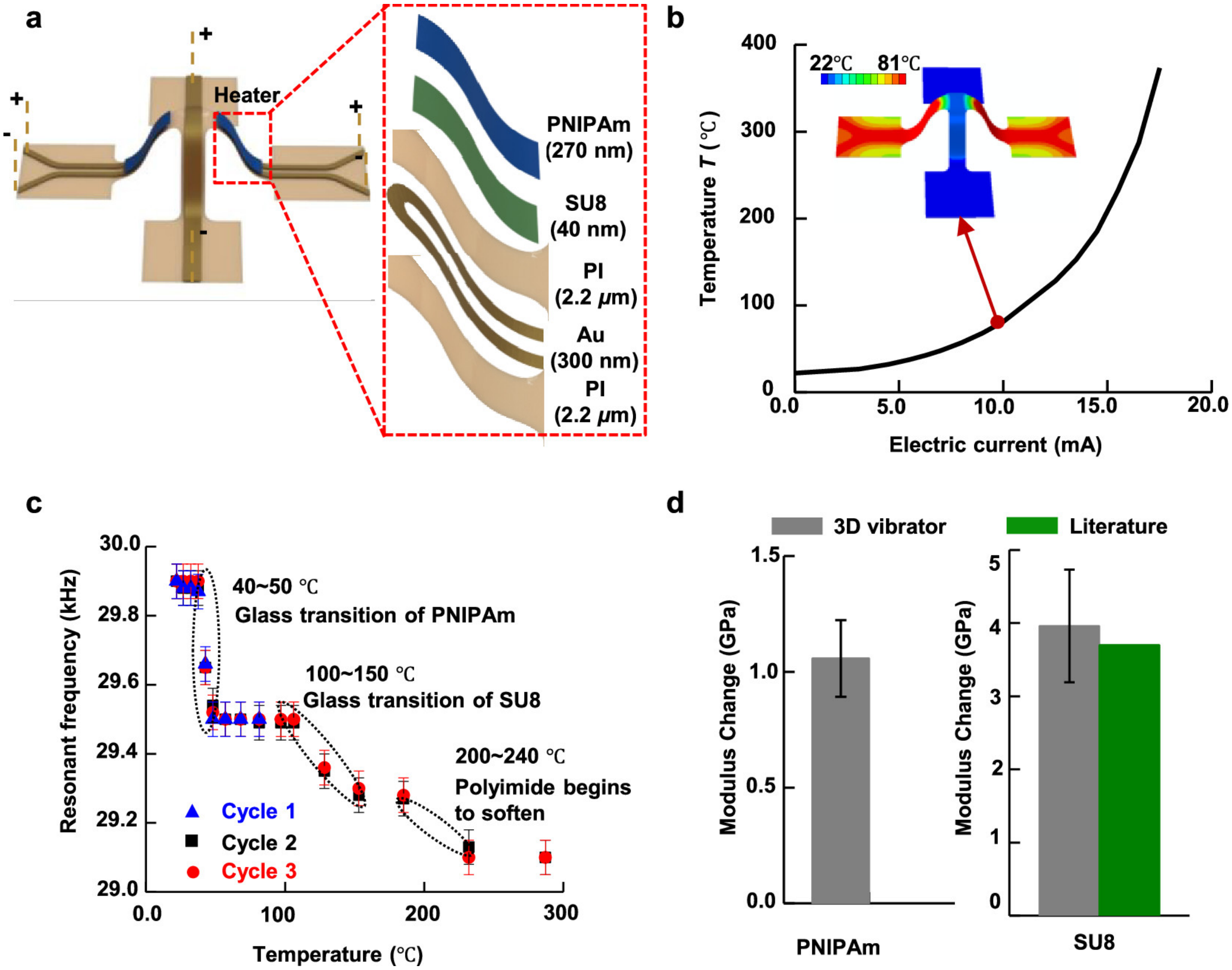

Figure 7.4 3D vibratory platform integrated with thermal actuators. (a) Schematic illustration of the 3D architecture integrated with thermal actuators, circuits for Lorentz-force actuation and patterned polymer film (left frame), and magnified, exploded view of the section containing the thermal actuators (right frame). (b) Calibration of temperature *versus* supplied electric current. (c) Experimental results for the variation of the resonant frequency with temperature. (d) Change in modulus of PNIPAm (left frame) and SU8 (right frame) determined from the results in (c).

7.2.5 Potential for characterization of anisotropic elastic moduli using multimodal resonances

The multimodal resonances of the 3D structures and the ability to pattern nano-thin polymers in a precise manner provide routes to determine the elastic moduli of anisotropic materials. Figure 7.5 presents schematic illustrations of the 3D vibratory structure with patterned test films that have transversely isotropic elastic moduli (for instance, oriented polystyrene-*block*-polydimethylsiloxane films).[53] The optimized patterns are shown in Figure 7.13, with the optimization algorithm presented in the Section 7.4.7. Briefly, the optimization algorithm uses FEA results for the distributions of strain components. To enhance the sensitivity of the resonant frequencies to the longitudinal component of the modulus, the test polymer should be patterned in locations with the largest strain along the longitudinal direction. The same consideration holds true for the transverse modulus component. Optimized patterns of typical polymers balance these two considerations (see Section 7.4.7 for details). For the current design, the resonant frequency of mode 2 is roughly 2.5 times more sensitive to the transverse modulus ($E_{P(t)}$) than the mode 1 (Figure 7.5b), while the latter is roughly 1.5 times more sensitive to the longitudinal modulus ($E_{P(l)}$, see Figure 7.5c) than the former, as measured by the slopes of the curves in Figure 7.5b,c. This decoupling allows determination of both the longitudinal and transverse moduli by measuring the frequency of modes 1 and 2 with and without the nano-thin polymer patterns, provided that the polymer density and thickness are known.

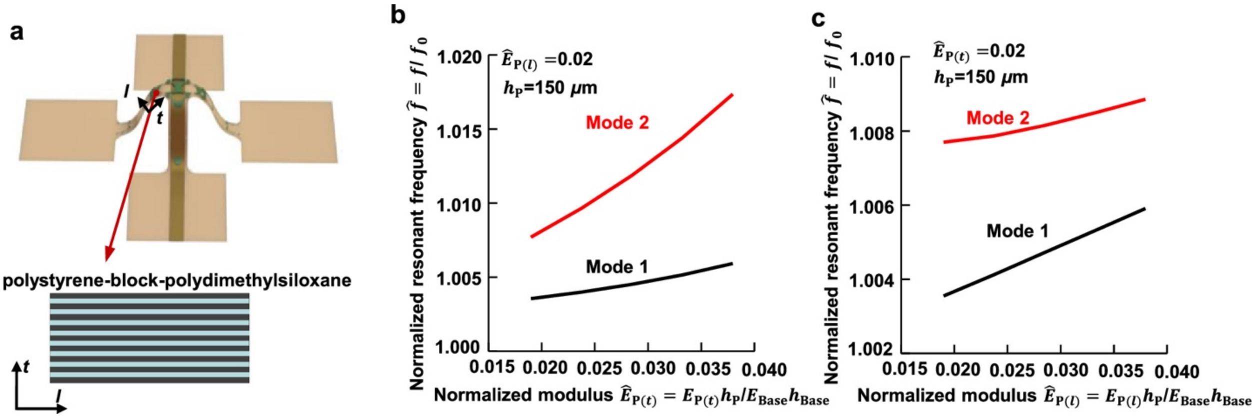

Figure 7.5 Theoretical investigation of measurement of anisotropic elastic moduli using a 3D vibratory platform. (a) Schematic illustration of the 3D vibratory platform with a thin film that has anisotropic elastic moduli. In this case, the thin film has different elastic moduli along the transverse (*t*) and longitudinal (*l*) directions. (b, c) FEA results of normalized resonant frequency for mode 1 and mode 2 with normalized modulus in transverse (*t*) (b) and longitudinal (*l*) (c) directions, respectively.

7.3 Conclusions

In summary, the results presented here demonstrate the applicability of 3D vibratory platforms to characterize the properties of nano-thin film materials, with demonstrations on three different types of polymers. With the current device parameters and optical measurement setups, modulus and density of any thin film with sufficiently small tensile stiffness and mass can be reliably and independently measured on the same sample. The robustness and reusability of these 3D systems, together with their utility in evaluating temperature-dependent film properties, create a broad range of possible uses. Theoretical modeling and design suggest opportunities for measuring anisotropic materials properties, specifically the transverse isotropic moduli of thin films. The assembly approaches can be applied to 3D structures with reduced dimensions, increased operating frequencies, and enhanced sensitivity.

7.4 Experimental Section

7.4.1 Fabrication of 3D vibratory platforms

Fabrication began with spin coating a bilayer of poly(methyl methacrylate) (950 PMMA A4, MicroChem, thickness ∼200 nm) and polyimide (PI 2545, HD MicroSystems, thickness ∼2.5 μm) on a silicon wafer. Depositing Cr (thickness ∼5 nm) and Au (thickness ∼300 nm) by electron beam evaporation followed by photolithography and wet etching defined the circuits. Spin coating another layer of PI (thickness ∼2.5 μm) followed by deposition and patterning of Cr (thickness ∼5 nm) and Au (thickness ∼50 nm) defined a hard mask in the shape of 2D devices, where the external electrodes were exposed for connections with the function generator. Oxygen plasma etching (March Jupiter III RIE) removes the unmasked PI. After removing the etching mask by wet etching, a layer of polymer was patterned on top to serve as the measurand (see below for details). The underlying PMMA layer was dissolved by immersion in acetone overnight to allow retrieval of the device onto a piece of water-soluble tape. A thin layer of silicon oxide (thickness ∼50 nm) deposited on the back side of the sample by electron beam evaporation created the necessary surface chemistry for strong adhesion to the elastomer platform at the bonding sites. The nonbonding sites were protected from SiO_2 deposition by a Kapton shadow mask created by laser cutting. A silicone elastomeric substrate (Dragon Skin 10) was stretched to a desired prestrain (30–40%) using a customized, biaxial stage. After exposing the elastomer and the 2D precursors (still on water-soluble tape) to ultraviolet (UV) induced ozone (Jelight UVO-Cleaner, Model 144AX), the two were laminated together and then baked in a convection oven at 70 °C to yield strong adhesion at the bonding sites where SiO_2 was deposited. Finally, dissolving the tape in warm water and slowly releasing the prestrain completed the assembly process. A schematic illustration of the procedures can be found in Figure 7.3.

7.4.2 Patterning and characterizing the thicknesses of the polymer films

Patterning the SU8 film used in Figure 7.2 began with spin coating the SU8 precursor (SU8 2000.5, MicroChem) onto the 2D devices at 2000 rpm for 40 s. After prebaking at 95 °C for 1 min, the film was exposed under an iron oxide photomask with 365 nm UV light at an intensity of 60 mJ/cm^2. Post-exposure baking at 95 °C for 1 min and developing in SU8 developer (MicroChem) yielded the desired patterns on the 2D precursors. The sample was then hard baked at 200 °C for 10 min. The thickness was characterized using a profilometer (Dektak 3030), while the 2D precursors were still on the silicon wafer.

Patterning of the S1805 films used in Figure 7.3 began by forming the 3D vibratory platforms, as described in the previous section, and stretching the elastomeric substrate to fully recover its 2D form. After rinsing the sample with acetone, isopropanol alcohol, and DI water, the S1805 precursor (MicroChem) was spin coated at 4000 rpm (cycle 2, Figure 7.3b) or 2000 rpm (cycle 3, Figure 7.3c), followed by baking at 110 °C for 3 min. The elastomeric substrate was then relaxed to return the sample to its 3D form. After each cycle, the sample was thoroughly rinsed with acetone to completely remove the S1805 film.

Patterning of the bilayer of SU8 and poly(*N*-isopropylacrylamide) (PNIPAm) brush used in Figure 4 began by spin coating SU8 precursor (SU8 2002, MicroChem), diluted using cyclopentanone with a 1:5 volume ratio, onto the 2D devices at 4000 rpm for 40 s. After prebaking at 95 °C for 1 min, the film was exposed under an iron oxide photomask with 365 nm UV light at an intensity of 50 mJ/cm^2. Post-exposure baking at 95 °C for 1 min and developing in SU8 developer (MicroChem) defined the desired patterns on the 2D precursors. The sample was then hard baked at 200 °C for 10 min. The PNIPAm brush was selectively grown on the SU8 patterns using surface-initiated atom-transfer radical polymerization (SI-ATRP) using previously reported procedures. Briefly, SU8 surfaces were activated using oxygen plasma for 3 min (150 W, March Plasmod GCM-200) and then functionalized with the ATRP initiator (11-(2-bromo-2-methyl)propionyloxy) undecyltrichlorosilane (BMPOUTS). Devices were placed in a 1 mM solution of BMPOUTS in anhydrous hexanes at room temperature. After 24 h, substrates were removed, sonicated in hexanes, dried using a nitrogen stream, and placed in a reaction vessel under argon. NIPAM (4.85 g, 42.9 mmol) was diluted with MeOH (15 mL) and H_2O (7 mL) and degassed in a separate Schlenk flask. Then, 1,1,4,7,10,10-hexamethyltriethylenetetramine (HMTETA, 242 µL, 0.89 mmol) and CuBr (53.8 mg, 0.38 mmol) were added to the monomer solution under positive argon flow. Once dissolved, the flask was then sealed, and the mixture was transferred to the reaction vessel containing the substrates. Substrates were removed after 10 min, sonicated in methanol, ethanol, and water to remove the film residuals in the non-SU8 regions, and then dried in a nitrogen stream.

The thickness of the PNIPAm brush was determined using spectroscopic ellipsometry (VASE, J.A. Wollam Co) on a control sample. Ellipsometric parameters (Ψ, Δ) were measured at three angles of incidence (65°, 70°, 75°) and from 400 to 800 nm. Data were analyzed by WVASE software using a three-layer model. Software-supplied refractive indices were used for silicon (substrate) and silicon dioxide (2 nm). Data were fit to a Cauchy layer model, with fixed (An, Bn) values of (1.45, 0.01) and no optical absorption. Control samples were prepared by growing the PNIPAm brush off a silicon wafer that had been patterned with SU8 using the identical conditions as the actual samples. The SU8 layer was determined to be 39.6 nm. After polymerization, the total thickness of the polymer layers (SU-8 and PNIPAM) was determined to be 312.9 nm. Thus, the NIPAM brush thickness is approximately 273.3 nm.

7.4.3 Lorentz-force actuation system and optical measurement system

A function generator (Keithley 3390) applied 1.5 V sinusoidal voltage to the 3D vibratory structure while placed in a static magnetic field induced by a permanent neodymium disc magnet. The Lorentz force, perpendicular to both the electric current and the magnetic field, oscillated at the frequency of the applied voltage to drive vibrations of the structure.

An optical measurement system was custom-built to measure the dynamics of the 3D vibratory platforms (Figure 7.4). A focusing lens and mirror delivered a focused laser beam onto the center of the 3D structure. A microscope facilitated alignment. The 3D structure was firmly mounted onto a mechanical stage capable of translation in *X*-, *Y*-, and *Z*-directions and tilt with respect to *X*- and *Y*-axes. Light scattered from the 3D structure was reflected by a second mirror, collected by a second lens and directed to a photodetector (Thorlabs, DET110) for intensity measurements. The fluctuations in the scattering intensity due to the 3D vibrations generated photocurrent in the photodetector with the same overall time dependence. The system was tuned such that the amplitude of the photocurrent responded linearly to the amplitude of the input voltage. Within the operational range of frequency, the amplitude of the fluctuating photocurrent is directly proportional to the vibration amplitude, which peaked at the resonant frequency. A lock-in amplifier (SRS 830, Stanford Research Systems) was used to record the amplitude of the photocurrent.

A Labview program was used to sweep the desired range of frequency and convert data from the lock-in amplifier. At each frequency, the measurement was repeated 64 times to ensure minimum fluctuations, and the increment of frequency was 50 Hz. The error of the system was determined to be ~50 Hz.

7.4.4 Finite element analysis (FEA)

2D to 3D transformation induced by the compressive strain: FEA was conducted by the commercial software ABAQUS (version 6.14, standard). The post-buckling analysis predicts the buckled 3D shape induced by the compressive strain. The structure was discretized by Four-node finite-strain shell element, with at least ten elements along the narrowest ribbon to guarantee convergence.

Vibration actuated by the Lorentz force: The electrical analysis imported the buckled 3D shape obtained from the post-buckling analysis and predicted the electric current ($\boldsymbol{J}$). The Lorentz force per unit volume was then calculated as $\boldsymbol{J} \times \boldsymbol{B}$ by a home-made python script and exported to the following steady-state analysis of vibration. The steady-state analysis obtained the frequency spectrum of the vibration displacement and then the resonant frequency.

Temperature change vs. direct electrical current for the micro heater: The coupled thermal-electrical analysis imported the buckled 3D shape and obtained the temperature change due to Joule heating. The power per unit volume (P) of the Joule heating is related to the electrical current by $P = \boldsymbol{J} \cdot \boldsymbol{J}$, where σ is the electrical conductivity. Eight node thermal-electric element was σ adopted.

Material properties: The Young's modulus (E), Poisson's ratio (ν) and density (ρ) of the polyimide (PI), gold (Au) and substrate are E_{PI} =2.5 GPa, ν_{PI} =0.34 and ρ_{PI} =1420 kg/m^3; E_{Au} =78 GPa, ν_{Au} =0.44, ρ_{Au} =19320 kg/m^3 ; $E_{\mathrm{Substrate}}$ =166 kPa, $\nu_{\mathrm{Substrate}}$ =0.49, $\rho_{\mathrm{Substrate}}$ =1070 kg/m^3. A stiffness proportional damping factor (10^{-7}) is introduced to account for the dissipation of PI, Au and polymers. The thermal conductivity of PI and Au is 0.12 W/(m·K) and 320 W/(m·K), respectively. The electrical conductivity of Au as a function of temperature is given in Table S1. The convection coefficient between the structure and air is 10 W/(m2·K).[55]

Table 7.1 Electrical conductivity of Au.[56]

Temperature (°C)	Electrical conductivity (S/m) ×10⁷
0	4.88
20	4.52
25	4.43
27	4.40
127	3.22
227	2.52
327	2.05
427	1.72

7.4.5 The scaling law in Eq. (1)

As a first step, a scaling law was derived *via* dimensional analysis for the resonant frequency when a thin layer of polymer is deposited homogeneously on a PI base layer (modulus-- E_{PI} , density-- ρ_{PI} and thickness h_{PI}). For a vibration mode dominated by bending deformation, the resonant frequency is[57]

$$f = \alpha \sqrt{\frac{K}{M}} \qquad 7.2$$

where the bending stiffness

$$K = \frac{E_{\mathrm{PI}}^2 h_{\mathrm{PI}}^4 + 4E_{\mathrm{PI}}E_{\mathrm{P}}h_{\mathrm{PI}}^3 h_{\mathrm{P}} + 6E_{\mathrm{PI}}E_{\mathrm{P}}h_{\mathrm{PI}}^2 h_{\mathrm{P}}^2 + 4E_{\mathrm{PI}}E_{\mathrm{P}}h_{\mathrm{PI}} h_{\mathrm{P}}^3 + E_{\mathrm{P}}^2 h_{\mathrm{P}}^4}{12\left(E_{\mathrm{PI}}h_{\mathrm{PI}} + E_{\mathrm{P}}h_{\mathrm{P}}\right)L^2} \qquad 7.3$$

the mass

$$M = \left(\rho_{\mathrm{P}}h_{\mathrm{P}} + \rho_{\mathrm{PI}}h_{\mathrm{PI}}\right)L^2 \qquad 7.4$$

and L is the in-plane size of the structure. Considering that the polymer thickness (h_P) is much smaller than the PI thickness, the ratio of the resonant frequency with/without the polymer is

$$\frac{f}{f_0} = \frac{3}{2}\frac{E_{\mathrm{P}} h_{\mathrm{P}}}{E_{\mathrm{PI}} h_{\mathrm{PI}}} - \frac{1}{2}\frac{\rho_{\mathrm{P}} h_{\mathrm{P}}}{\rho_{\mathrm{PI}} h_{\mathrm{PI}}} \tag{7.5}$$

For the 3D vibrators presented in the main text, an Au layer is sandwiched between two PI layers. Therefore, the PI modulus E_{PI} and density ρ_{PI} should be revised to the effective modulus $E\hat{}_{\mathrm{Base}}$ and average density $\rho\hat{}_{\mathrm{Base}}$ of the PI/Au/PI tri-layer (see Section 7.4.6). Equation 7.5 is for the structure with the polymer depositing on the entire surface of the base layer. When the polymer is patterned on a selected region such as the one shown in Figure 7.6a, the parameters C_{E} and C_{ρ} replace 3/2 and 1/2, respectively. These considerations lead to the scaling law Equation 7.1.

7.4.6 The scaling law in Eq. (1)

The effective modulus of an *n*-layer composite is

$$\hat{E} = \frac{12}{h^3}\left(\frac{D_3}{3} - D_2 y_{\mathrm{m}} + D_1 y_{\mathrm{m}}^2\right) \tag{7.6}$$

with

$$D_1 = \sum_{i=1}^{n} E_i h_i,\ D_2 = \sum_{i=1}^{n} E_i\left(y_i^2 - y_{i-1}^2\right),\ D_3 = \sum_{i=1}^{n} E_i\left(y_i^3 - y_{i-1}^3\right),\ y_{\mathrm{m}} = \frac{D_2}{2D_1},\ h = \sum_{i=1}^{n} h_i \tag{7.7}$$

where *Ei* and *hi* is the modulus and thickness of the *i*-th layer respectively; $y_0 = 0$ and $y_i = y_{i-1} + h$ for *i*=1, 2,..., *n*. The average density is

$$\hat{\rho} = \frac{1}{h}\sum_{i=1}^{n} \rho_i h_i \tag{7.8}$$

where ρ_i is the density of the *i*-th layer.

7.4.7 Algorithm that optimizes the polymer patterns

Polymer patterns for determining polymer modulus and density of isotropic material: An algorithm was developed to select the polymer patterns such that the resonant frequencies of the two vibration modes have decoupled sensitivities to the polymer modulus and density. FEA first predicts the distribution of the ratio $W_{Strain}/W_{Kinetic}$ without polymer for vibration mode 1 and mode 2, respectively; W_{Strain} and $W_{Kinetic}$ are the strain energy density and the kinetic energy density of vibration, respectively. For vibration mode 1, the entire region (Ω , area A) of the base layer is divided into $\Omega_{Polymer(1)}$ (area $A_{Polymer(1)}$) and $\Omega_{NoPolymer(1)}$, with $\Omega_{Polymer(1)} \cup \Omega_{NoPolymer(1)} = \Omega$, $\Omega_{Polymer(1)} \cap \Omega_{NoPolymer(1)} = \varnothing$ and $A_{Polymer(1)} = \beta_{(1)} A$. $\beta_{(1)}$ is an optimization variable. The region $\Omega_{Polymer(1)}$ is selected such that for an arbitrary point in $\Omega_{Polymer(1)}$, the ratio $W_{Strain}/W_{Kinetic}$ is larger than that of an arbitraroy point in $\Omega_{NoPolymer(1)}$. Similarly for vibration mode 2, a region $\Omega_{Polymer(2)}$ with area $A_{Polymer(2)} = \beta_2 A$ is selected such that for an arbitrary point in $\Omega_{Polymer(2)}$, the ratio $W_{Strain}/W_{Kinetic}$ is smaller than that of an arbitrary point in $\Omega_{Polymer(2)}$ ($\Omega_{Polymer(2)} \cup \Omega_{NoPolymer(2)} = \Omega$, $\Omega_{Polymer(2)} \cap \Omega_{NoPolymer(2)} = \varnothing$). $\beta_{(2)}$ is an optimization variable. The polymer patterns are the intersection of $\Omega_{Polymer(1)}$ and $\Omega_{Polymer(2)}$. With the polymer patterns obtained in this manner, FEA predicts the relationship of the resonant frequency *versus* the polymer modulus and density for the two vibration modes. A parameter study on the variables $\beta_{(1)}$ and $\beta_{(2)}$ suggests that with $\beta_{(1)} = \beta_{(2)} = 0.68$, the sensitivities of the two vibration modes to the polymer modulus and density are reasonably well decoupled (Figure 7.2a and 7.2b). The resultant polymer patterns are presented in Figure 7.6a.

Polymer patterns for determining longitudinal modulus and transverse modulus of transversely isotropic material: A similar algorithm selects the polymer patterns presented in Figure 7.12 such that the resonant frequencies of the two vibration modes have decoupled sensitivities to the longitudinal modulus and the transverse modulus. FEA first predicts the distribution of the ratio $|\varepsilon_l / \varepsilon_t|$ without polymer for vibration mode 1 and mode 2, respectively; ε_l and ε_t are the normal strain of vibration along the longitudinal direction and the transverse direction, respectively. Region $\Omega_{Polymer(1)}$ is selected such that for an arbitrary point in $\Omega_{Polymer(1)}$, the ratio $|\varepsilon_l / \varepsilon_t|$ is larger than that of an arbitrary point in region $\Omega_{NoPolymer(1)}$. Region $\Omega_{Polymer(2)}$ is selected such that for an arbitrary point in $\Omega_{Polymer(2)}$, the ratio $|\varepsilon_l / \varepsilon_t|$ is smaller than that of an arbitrary point in region $\Omega_{NoPolymer(2)}$. The polymer patterns are the intersection of $\Omega_{Polymer(1)}$ and

$\Omega_{\text{Polymer(2)}}$. $\beta_{(1)}$ and $\beta_{(2)}$ are optimization variables. A parameter study on $\beta_{(1)}$ and $\beta_{(2)}$ suggests that with $\beta_{(1)} = \beta_{(2)} = 0.62$, the sensitivities of the two vibration modes to the longitudinal modulus and the transverse modulus are reasonably well decoupled (Figure 7.5b and 7.5c). The resultant polymer patterns are presented in Figure 7.12.

7.4.8 Determination of the polymer modulus and density from the resonant frequency of two vibration modes

Equation 7.1 leads to the following formula to determine the polymer modulus and density

$$E_{\mathrm{P}} = \frac{\hat{E}_{\mathrm{Base}} h_{\mathrm{Base}}}{h_{\mathrm{P}}} \frac{C_{\rho(1)}\left(\hat{f}_{(2)} - 1\right) - C_{\rho(2)}\left(\hat{f}_{(1)} - 1\right)}{C_{\mathrm{E}(2)} C_{\rho(1)} - C_{\mathrm{E}(1)} C_{\rho(2)}} \tag{7.9}$$

$$\rho_{\mathrm{P}} = \frac{\hat{\rho}_{\mathrm{Base}} h_{\mathrm{Base}}}{h_{\mathrm{P}}} \frac{C_{\mathrm{E}(1)}\left(\hat{f}_{(2)} - 1\right) - C_{\mathrm{E}(2)}\left(\hat{f}_{(1)} - 1\right)}{C_{\mathrm{E}(2)} C_{\rho(1)} - C_{\mathrm{E}(1)} C_{\rho(2)}} \tag{7.10}$$

Where $\hat{f}_{(1)} = \frac{f_{(1)}}{f_{0(1)}}$ and $\hat{f}_{(2)} = \frac{f_{(2)}}{f_{0(2)}}$ are the ratio of the resonant frequency with/without the polymer for vibration mode 1 and 2, respectively. The uncertainties in the determined polymer modulus and density caused by the uncertainties in the experiment results of the resonant frequencies are

$$\delta E_{\mathrm{P}} = \frac{\hat{E}_{\mathrm{Base}} h_{\mathrm{Base}}}{h_{\mathrm{P}}} \frac{C_{\rho(1)} \delta \hat{f}_{(2)} - C_{\rho(2)} \delta \hat{f}_{(1)}}{C_{\mathrm{E}(2)} C_{\rho(1)} - C_{\mathrm{E}(1)} C_{\rho(2)}} - \frac{\delta h_{\mathrm{P}}}{h_{\mathrm{P}}} E_{\mathrm{P}} \tag{7.11}$$

$$\delta \rho_{\mathrm{P}} = \frac{\hat{\rho}_{\mathrm{Base}} h_{\mathrm{Base}}}{h_{\mathrm{P}}} \frac{C_{\mathrm{E}(1)} \delta \hat{f}_{(2)} - C_{\mathrm{E}(2)} \delta \hat{f}_{(1)}}{C_{\mathrm{E}(2)} C_{\rho(1)} - C_{\mathrm{E}(1)} C_{\rho(2)}} - \frac{\delta h_{\mathrm{P}}}{h_{\mathrm{P}}} \rho_{\mathrm{P}} \tag{7.12}$$

respectively, where

$$\delta \hat{f}_{(1)} = \frac{\delta f_{(1)}}{f_{(1)}} - \frac{f_{(1)}}{f_{0(1)}} \frac{\delta f_{0(1)}}{f_{0(1)}}, \quad \delta \hat{f}_{(2)} = \frac{\delta f_{(2)}}{f_{(2)}} - \frac{f_{(2)}}{f_{0(2)}} \frac{\delta f_{0(2)}}{f_{0(2)}} \tag{7.13}$$

$\delta_{f(1)}$, $\delta_{0(1)}$, $\delta_{f(2)}$, and $\delta_{0(2)}$, are the uncertainties in the resonant frequency with/without polymer of vibration mode 1 and 2, respsectifely; δh_P is the uncertainty in the polymer thickness.

7.4.9 Determination of the polymer modulus change during glass transition

The SU8 and PNIPAm are much thinner than the base layer, which simplifies the resonant frequency of the structure in Figure 4a as

$$\frac{f}{f_0} = C_{\mathrm{E}} \frac{E_{\mathrm{SU8}} h_{\mathrm{SU8}}}{\hat{E}_{\mathrm{Base}} h_{\mathrm{Base}}} + C_{\mathrm{E}} \frac{E_{\mathrm{PNIPAm}} h_{\mathrm{PNIPAm}}}{\hat{E}_{\mathrm{Base}} h_{\mathrm{Base}}} - C_{\rho} \frac{\rho_{\mathrm{SU8}} h_{\mathrm{SU8}}}{\hat{\rho}_{\mathrm{Base}} h_{\mathrm{Base}}} - C_{\rho} \frac{\rho_{\mathrm{PNIPAm}} h_{\mathrm{PNIPAm}}}{\hat{\rho}_{\mathrm{Base}} h_{\mathrm{Base}}} \tag{7.14}$$

where E_{SU8}, ρ_{SU8}, h_{SU8}, E_{PNIPAm}, ρ_{PNIPAm} and h_{PNIPAm} are the modulus, density and thickness of SU8 and PNIPAm, respectively. During the glass transition of PNIPAm, the SU8 tensile stiffness ($E_{\mathrm{SU8}}h_{\mathrm{SU8}}$) does not change because the glass transition temperature of SU8 is much higher than that of PNIPAm. Meanwhile, the change in the polymer mass and thickness are also negligible as discussed in the main text. Therefore, the PNIPAm modulus change is

$$\Delta E_{\mathrm{PNIPAm}} = \frac{\hat{E}_{\mathrm{Base}} h_{\mathrm{Base}} \Delta f_{\mathrm{PNIPAm}}}{C_{\mathrm{E}} h_{\mathrm{PNIPAm}} f_0} \tag{7.15}$$

where CE = 0.53 is determined by FEA and ΔfPNIPAm is the resonant frequency change during glass transition. Similarly, during the glass transition of SU8, the SU8 tensile stiffness change is

$$\Delta E_{\mathrm{SU8}} = \frac{\hat{E}_{\mathrm{Base}} h_{\mathrm{Base}} \Delta f_{\mathrm{SU8}}}{C_{\mathrm{E}} h_{\mathrm{SU8}} f_0} \tag{7.16}$$

where Δf_{SU8} is the resonant frequency change. The uncertainties in the determined modulus change are

$$\delta\left(\Delta E_{\text{PNIPAm}}\right)=\frac{\delta\left(\Delta f_{\text{PNIPAm}}\right)}{\Delta f_{\text{PNIPAm}}}\Delta E_{\text{PNIPAm}}-\frac{\delta h_{\text{PNIPAm}}}{h_{\text{PNIPAm}}}\Delta E_{\text{PNIPAm}} \tag{7.17}$$

$$\delta\left(\Delta E_{\text{SU8}}\right)=\frac{\delta\left(\Delta f_{\text{SU8}}\right)}{\Delta f_{\text{SU8}}}\Delta E_{\text{SU8}}-\frac{\delta h_{\text{SU8}}}{h_{\text{SU8}}}\Delta E_{\text{SU8}} \tag{7.18}$$

for PNIPAm and SU8 respectively, where $\delta(\Delta f_{\text{PNIPAm}})$, δh_{PNIPAm}, $\delta(\Delta f_{\text{SU8}})$ and δh_{SU8} are the uncertainties in the resonant frequency changes and thicknesses of PNIPAm and SU8 respectively.

7.4.10 Design and fabrication schematics

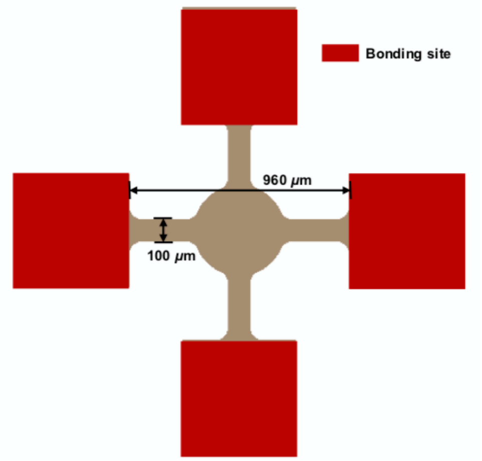

Figure 7.6 2D precursor design of the 3D vibrator in Figure 1a&b.

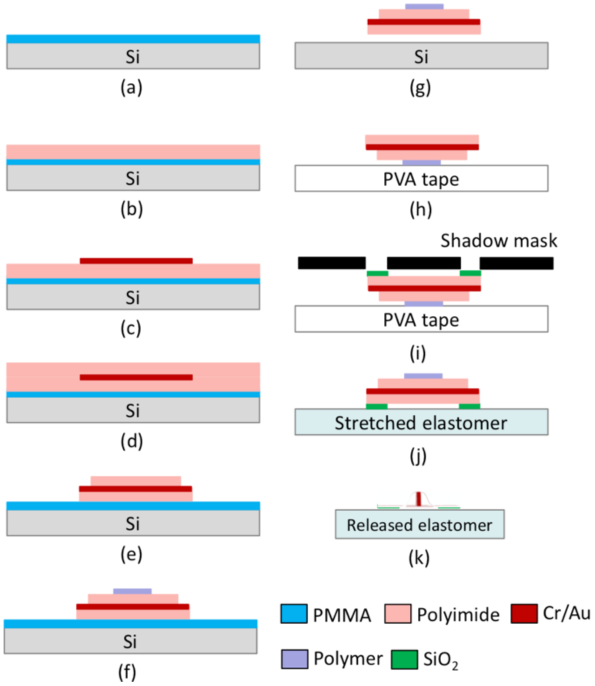

Figure 7.7 Fabrication process of the 3D vibrator.

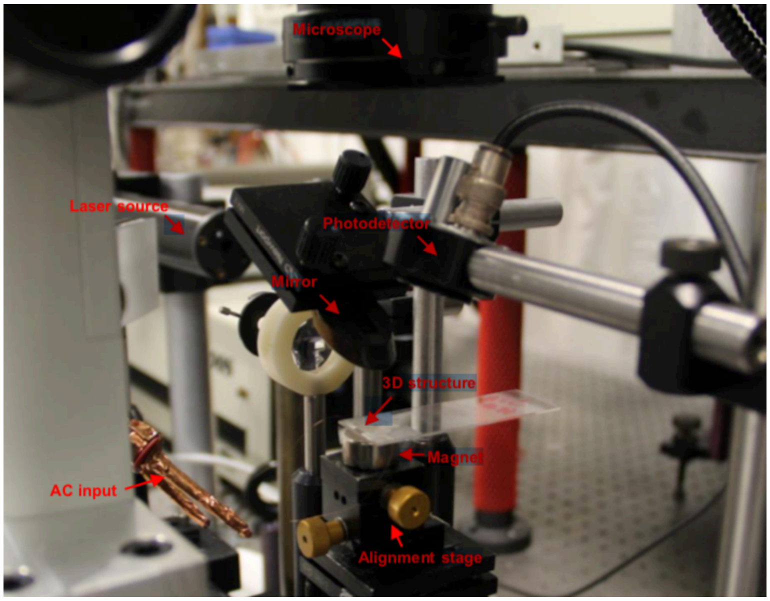

Figure 7.8 Optical image of the custom-built Lorentz-force actuation system and the optical measurement system.

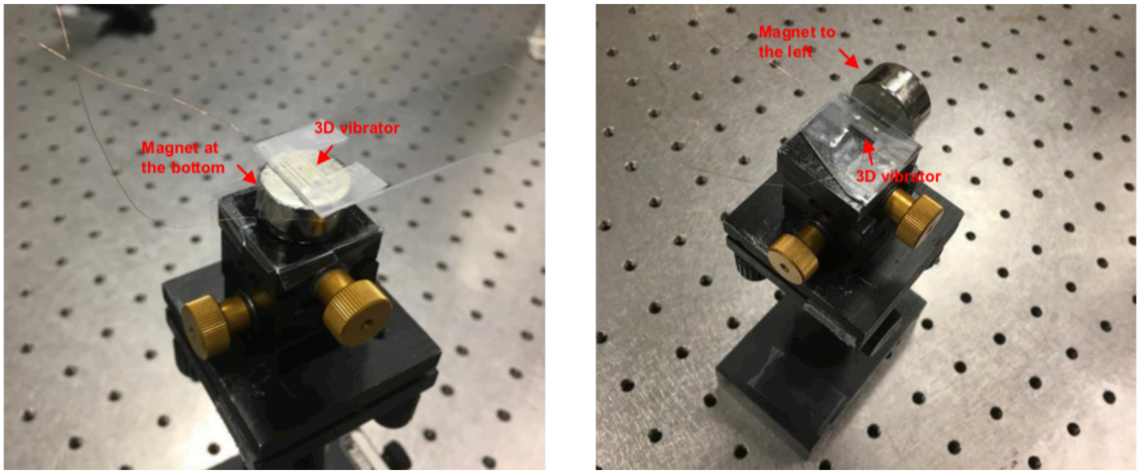

Figure 7.9 Optical image of strategic placement of the disc magnet (left) at the bottom of the 3D vibrator, and (right) to the left of the 3D vibrator.

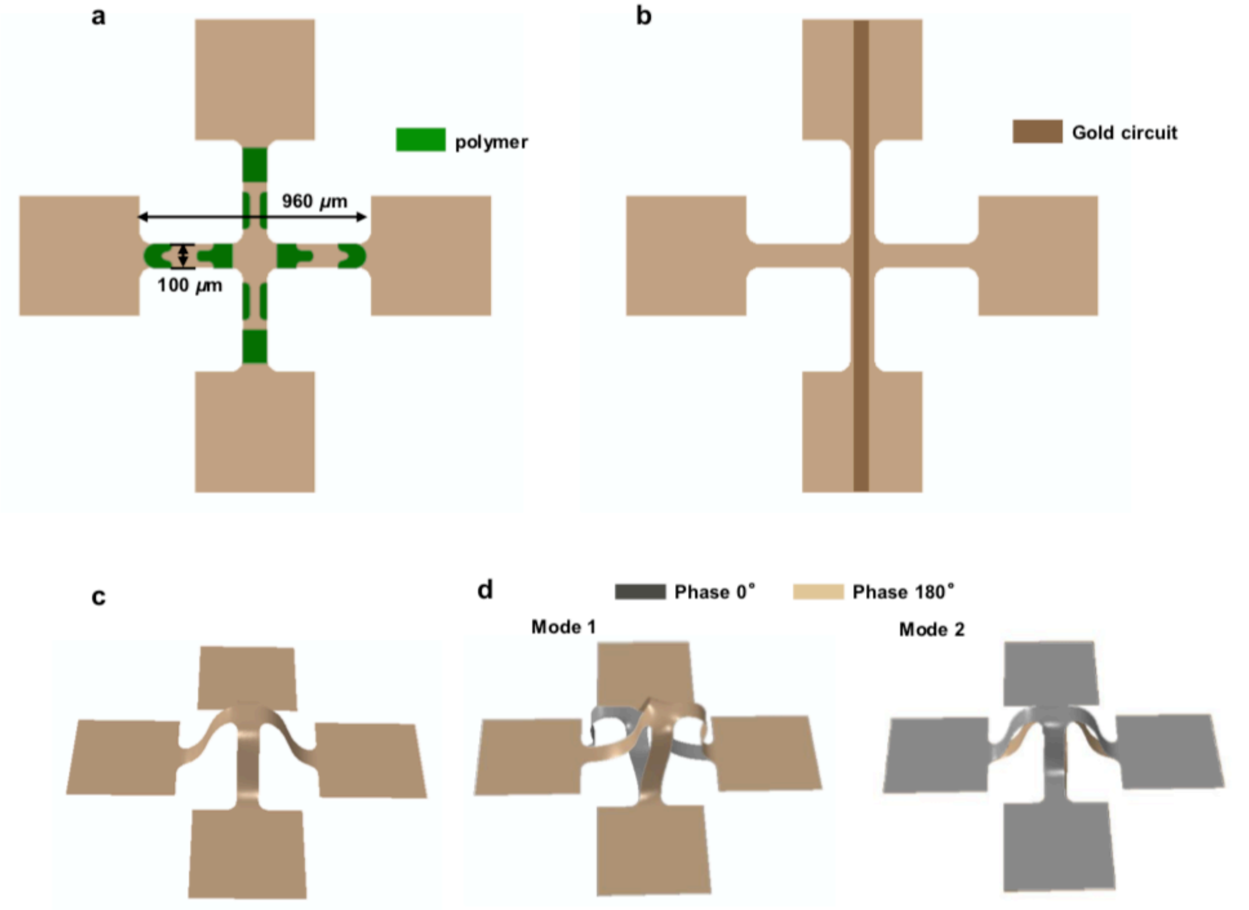

Figure 7.10 (a) the polymer pattern, (b) the gold circuit pattern, and FEA illustration of (c) the buckled 3D shape and (d) the two vibration modes for simultaneous detections of polymer modulus and density.

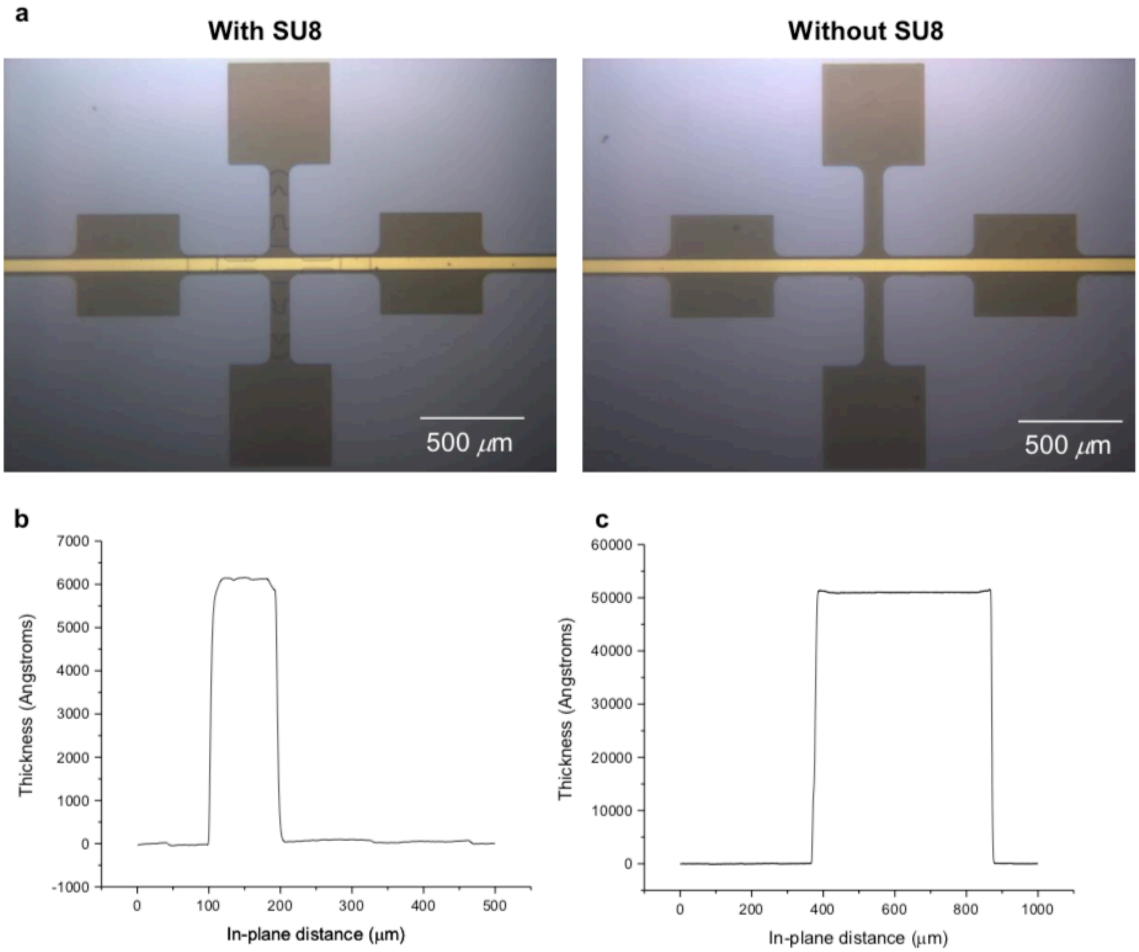

SU8 thickness ~ 610 nm

PI thickness ~ 5100 nm

Figure 7.11 (a) Optical images of the planar vibrator with (left) and without (right) SU8. (b)-(c) Thickness measurements of (b) SU8 and (c) PI using surface profilometry.

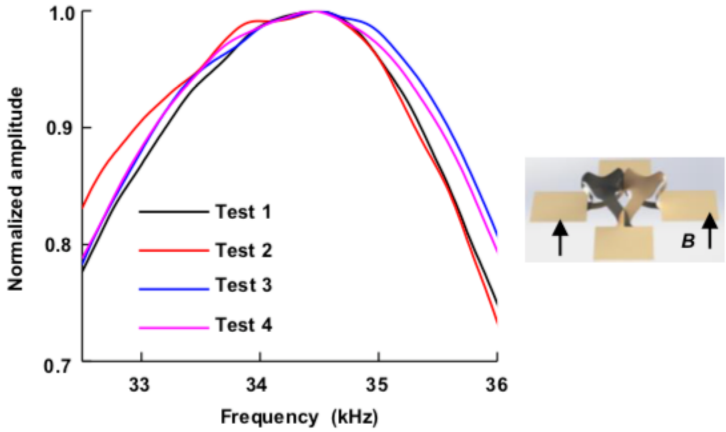

Figure 7.12 Four repeated measurement of the same sample to determine the experimental uncertainty.

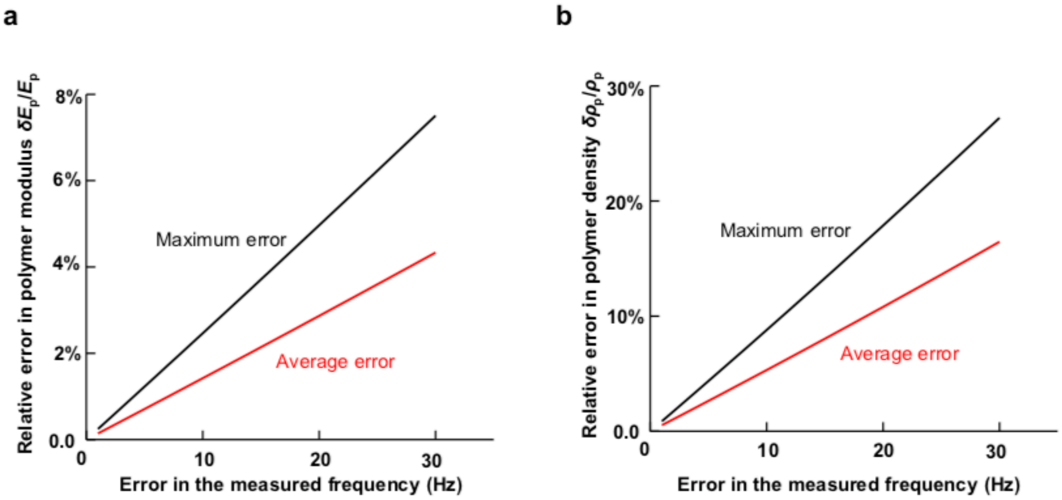

Figure 7.13 Results of accuracy analysis for (a) the polymer modulus and (b) the polymer density, based on the 3D vibratory platform in Figure 7.2.

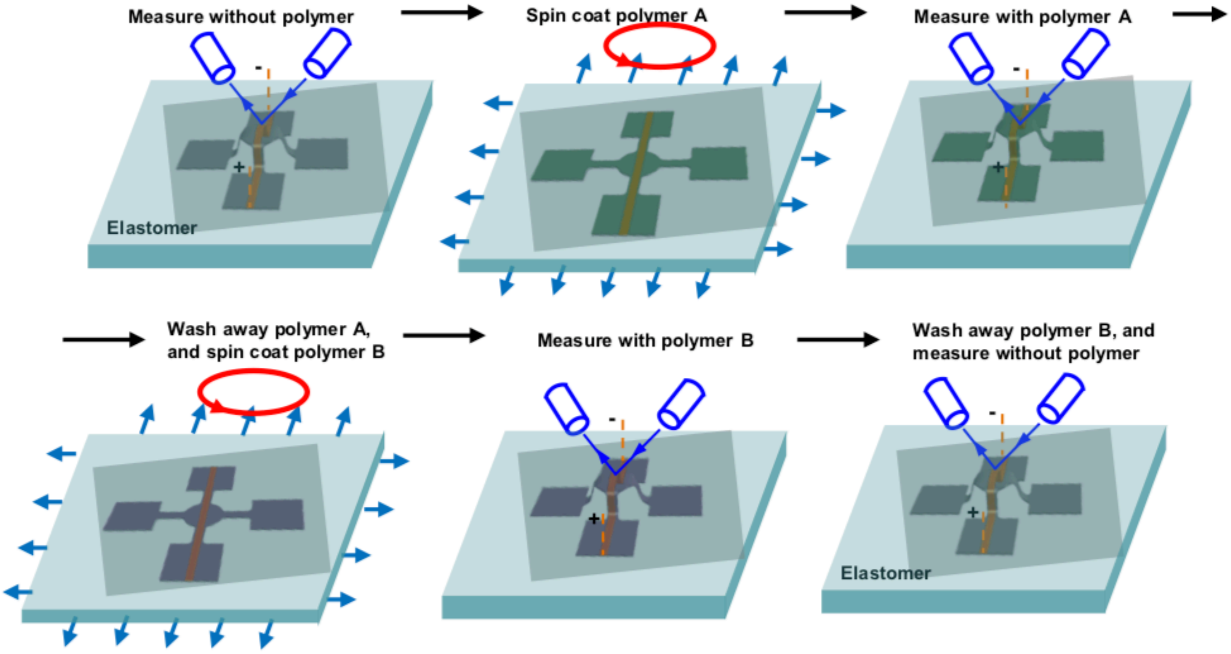

Figure 7.14 Schematic illustration of repetitive use of the 3D vibrator.

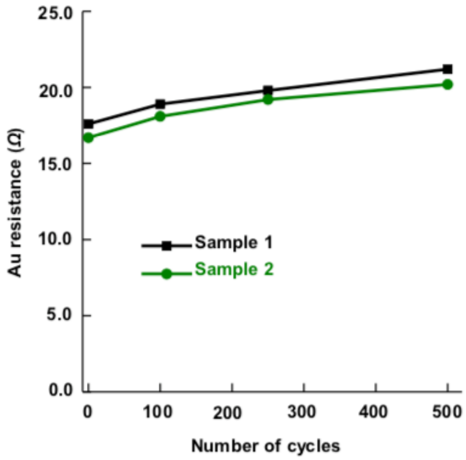

Figure 7.15 Measured changes in resistance of gold when the 3D vibrator is subjected 500 cycles of stretching/release.

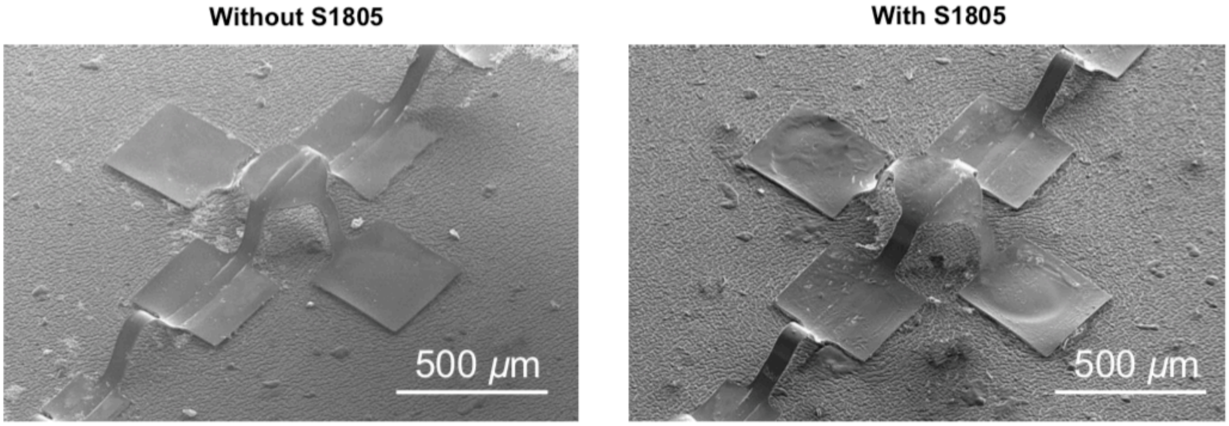

Figure 7.16 Scanning electron microscope images of the 3D vibrator before and after S1805 is spin coated.

.

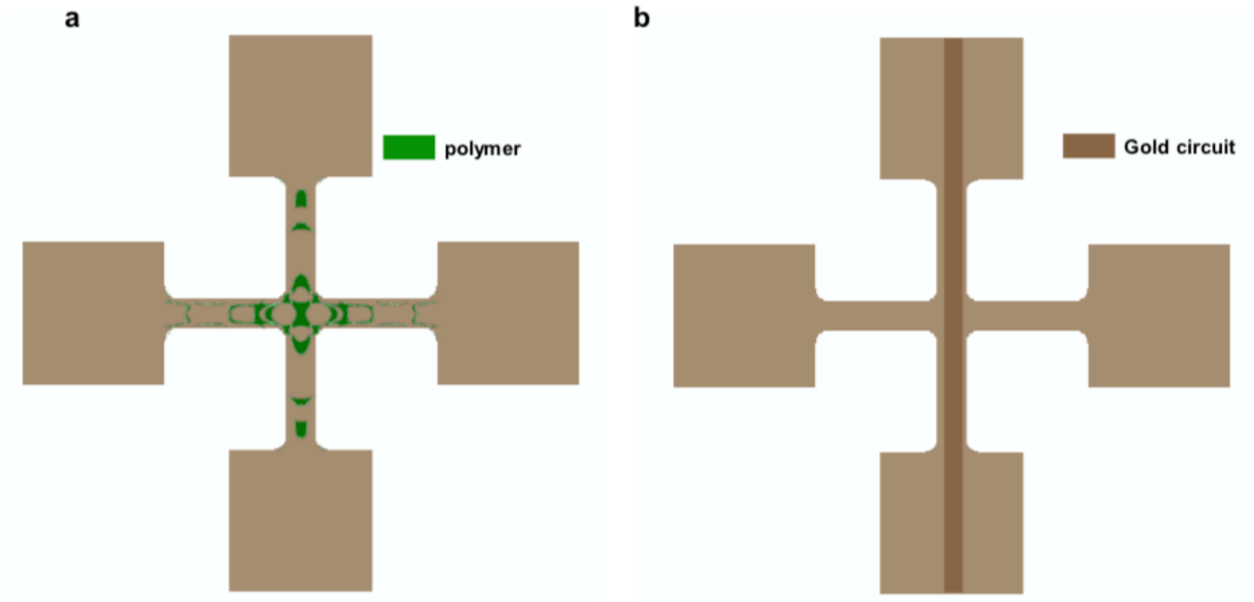

Figure 7.17 FEA results of (a) the polymer pattern and (b) the gold circuit pattern for simultaneous measurement of the transverse and the longitudinal moduli of the transversely isotropic material.

7.5 References

1. Jensen, K.; Kim, K.; Zettl, A. An Atomic-Resolution Nanomechanical Mass Sensor. *Nat. Nanotechnol.* **2008**, *3*, 533-537.
2. Yang, Y. T.; Callegari, C.; Feng, X. L.; Ekinci, K. L.; Roukes, M. L. Zeptogram-Scale Nanomechanical Mass Sensing. *Nano Lett.* **2006**, *6*, 583-586.
3. Chaste, J.; Eichler, A.; Moser, J.; Ceballos, G.; Rurali, R.; Bachtold, A. A Nanomechanical Mass Sensor with Yoctogram Resolution. *Nat. Nanotechnol.* **2012**, *7*, 301-304.
4. Xiong, Q.; Duarte, N.; Tadigadapa, S.; Eklund, P. C. Force-Deflection Spectroscopy: A New Method to Determine the Young’s Modulus of Nanofilaments. *Nano Lett.* **2006**, *6*, 1904-1909.
5. Christopher, G. F.; Yoo, J. M.; Dagalakis, N.; Hudson, S. D.; Migler, K. B. Development of a MEMS Based Dynamic Rheometer. *Lab Chip* **2010**, *10*, 2749-2757.
6. Zhang, X. C.; Myers, E. B.; Sader, J. E.; Roukes, M. L. Nanomechanical Torsional Resonators for Frequency-Shift Infrared Thermal Sensing. *Nano Lett.* **2013**, *13*, 1528-1534.
7. Choi, W. J.; Jeon, Y.; Jeong, J. H.; Sood, R.; Kim, S. G. Energy Harvesting MEMS Device Based on Thin Film Piezoelectric Cantilevers. *J. Electroceram.* **2006**, *17*, 543-548.

8. Liu, J.-Q.; Fang, H.-B.; Xu, Z.-Y.; Mao, X.-H.; Shen, X.-C.; Chen, D.; Liao, H.; Cai, B.-C. A MEMS-Based Piezoelectric Power Generator Array for Vibration Energy Harvesting. *Microelectron. J.* **2008**, *39*, 802-806.
9. Fang, H.-B.; Liu, J.-Q.; Xu, Z.-Y.; Dong, L.; Wang, L.; Chen, D.; Cai, B.-C.; Liu, Y. Fabrication and Performance of MEMS-Based Piezoelectric Power Generator for Vibration Energy Harvesting. *Microelectron. J.* **2006**, *37*, 1280-1284.
10. Yang, S.; Zhao, X.; Sharma, P. Avoiding the Pull-in Instability of a Dielectric Elastomer Film and the Potential for Increased Actuation and Energy Harvesting. *Soft Matter* **2017**, *13*, 4552-4558.
11. Alameh, Z.; Yang, S.; Deng, Q.; Sharma, P. Emergent Magnetoelectricity in Soft Materials, Instability, and Wireless Energy Harvesting. *Soft Matter* **2018**, *14*, 5856-5868.
12. Yao, S.; Myers, A.; Malhotra, A.; Lin, F.; Bozkurt, A.; Muth, J. F.; Zhu, Y. A Wearable Hydration Sensor with Conformal Nanowire Electrodes. *Adv. Healthcare Mater.* **2017**, *6*, 1601159.
13. Yao, S.; Swetha, P.; Zhu, Y. Nanomaterial-Enabled Wearable Sensors for Healthcare. *Adv. Healthcare Mater.* **2018**, *7*, 1700889.
14. Shian, S.; Bertoldi, K.; Clarke, D. R. Dielectric Elastomer Based “Grippers” for Soft Robotics. *Adv. Mater.***2015**, *27*, 6814-6819.
15. Kumar, K.; Liu, J.; Christianson, C.; Ali, M.; Tolley, M. T.; Aizenberg, J.; Ingber, D. E.; Weaver, J. C.; Bertoldi, K. A Biologically Inspired, Functionally Graded End Effector for Soft Robotics Applications. *Soft Robot.* **2017**, *4*, 317-323.
16. Dufour, I.; Maali, A.; Amarouchene, Y.; Ayela, C.; Caillard, B.; Darwiche, A.; Guirardel, M.; Kellay, H.; Lemaire, E.; Mathieu, F.; Pellet, C.; Saya, D.; Youssry, M.; Nicu, L.; Colin, A. The Microcantilever: A Versatile Tool for Measuring the Rheological Properties of Complex Fluids. *J. Sens.* **2012**, *2012*, 719898.
17. Belov, M.; Quitoriano, N. J.; Sharma, S.; Hiebert, W. K.; Kamins, T. I.; Evoy, S. Mechanical Resonance of Clamped Silicon Nanowires Measured by Optical Interferometry. *J. Appl. Phys.* **2008**, *103*, 074304.
18. Seo, J. H.; Brand, O. High Q-Factor in-Plane-Mode Resonant Microsensor Platform for Gaseous/Liquid Environment. *J. Microelectromech. Syst.* **2008**, *17*, 483-493.

19. Menzel, A.; Waffenschmidt, T. A Microsphere-based Remodeling Formulation for Anisotropic Biological Tissues. *Philos. Trans. R. Soc., A* **2009**, *367*, 3499-3523.
20. *Mechanics of Biological Tissue*; Holzapfel, G. A.; Ogden, R. W., Eds.; Springer-Verlag: Berlin, **2006**.
21. Gennisson, J. L.; Deffieux, T.; Macé, E.; Montaldo, G.; Fink, M.; Tanter, M. Viscoelastic and Anisotropic Mechanical Properties of *in vivo* Muscle Tissue Assessed by Supersonic Shear Imaging. *Ultrasound Med. Bio.* **2010**, *36*, 789-801.
22. Tan, J. C.; Merrill, C. A.; Orton, J. B.; Cheetham, A. K. Anisotropic Mechanical Properties of Polymorphic Hybrid Inorganic–Organic Framework Materials with Different Dimensionalities. *Acta Mater.* **2009**, *57*, 3481-3496.
23. Kim, G. H. Electrospun PCL Nanofibers with Anisotropic Mechanical Properties as a Biomedical Scaffold. *Biomed. Mater.* **2008**, *3*, 025010.
24. Haque, M. A.; Kamita, G.; Kurokawa, T.; Tsujii, K.; Gong, J. P. Unidirectional Alignment of Lamellar Bilayer in Hydrogel: One-Dimensional Swelling, Anisotropic Modulus, and Stress/Strain Tunable Structural Color. *Adv. Mater.* **2010**, *22*, 5110-5114.
25. Minnich, A. J. Phonon Heat Conduction in Layered Anisotropic Crystals. *Phys. Rev. B: Condens. Matter Mater. Phys.* **2015**, *91*, 085206.
26. Minnich, A. J. Exploring the Extremes of Heat Conduction in Anisotropic Materials. *Nanoscale Microscale Thermophys. Eng.* **2016**, *20*, 1-21.
27. Wang, Z.; Lee, J.; He, K.; Shan, J.; Feng, P. X. L. Embracing Structural Nonidealities and Asymmetries in Two-Dimensional Nanomechanical Resonators. *Sci. Rep.* **2015**, *4*, 3919-3926.
28. Moore, S. I.; Ruppert, M. G.; Yong, Y. K. Multimodal Cantilevers with Novel Piezoelectric Layer Topology for Sensitivity Enhancement. *Beilstein J. Nanotechnol.* **2017**, *8*, 358-371.
29. Ilic, B.; Krylov, S.; Craighead, H. G. Young's Modulus and Density Measurements of Thin Atomic Layer Deposited Films Using Resonant Nanomechanics. *J. Appl. Phys.* **2010**, *108* (4), 044317.
30. Ning, X.; Wang, H.; Yu, X.; Soares, J. A.; Yan, Z.; Nan, K.; Velarde, G.; Xue, Y.; Sun, R.; Dong, Q.; Luan, H.; Lee, C. M.; Chempakasseril, A.; Han, M.; Wang, Y.; Li, L.; Huang, Y.; Zhang, Y.; Rogers, J. A. 3D Tunable, Multiscale, and Multistable Vibrational Micro-Platforms Assembled by Compressive Buckling. *Adv. Funct. Mater.* **2017**, *27*, 1605914.

31. Wang, H.; Ning, X.; Li, H.; Luan, H.; Xue, Y.; Yu, X.; Fan, Z.; Li, L.; Rogers, J. A.; Zhang, Y.; Huang, Y.Vibration of Mechanically-Assembled 3D Microstructures Formed by Compressive Buckling. *J. Mech. Phys. Solids* **2018**, *112*, 187-208.
32. Vinod, T. P.; Taylor, J. M.; Konda, A.; Morin, S. A. Stretchable Substrates for the Assembly of Polymeric Microstructures. *Small* **2017**, *13*, 1603350.
33. Konda, A.; Rau, A.; Stoller, M. A.; Taylor, J. M.; Salam, A.; Pribil, G. A.; Argyropoulos, C.; Morin, S. A. Soft Microreactors for the Deposition of Conductive Metallic Traces on Planar, Embossed, and Curved Surfaces. *Adv. Funct. Mater.* **2018**, *28*, 1803020.
34. Liao, X.; Xiao, J.; Ni, Y.; Li, C.; Chen, X. Self-Assembly of Islands on Spherical Substrates by Surface Instability. *ACS Nano* **2017**, *11*, 2611-2617.
35. Ma, L.; Peng, J.; Wu, C.; He, L.; Ni, Y. Sphere-To-Tube Transition toward Nanotube Formation: A Universal Route by Inverse Plateau–Rayleigh Instability. *ACS Nano* **2017**, *11*, 2928-2933.
36. Xu, S.; Yan, Z.; Jang, K. I.; Huang, W.; Fu, H.; Kim, J.; Wei, Z.; Flavin, M.; McCracken, J.; Wang, R.; Badea, A.; Liu, Y.; Xiao, D.; Zhou, G.; Lee, J.; Chung, H. U.; Cheng, H.; Ren, W.; Banks, A.; Li, X.Assembly of Micro/Nanomaterials into Complex, Three-Dimensional Architectures by Compressive Buckling. *Science* **2015**, *347*, 154-159.
37. Zhang, Y.; Yan, Z.; Nan, K.; Xiao, D.; Liu, Y.; Luan, H.; Fu, H.; Wang, X.; Yang, Q.; Wang, J.; Ren, W.; Si, H.; Liu, F.; Yang, L.; Li, H.; Wang, J.; Guo, X.; Luo, H.; Wang, L.; Huang, Y.; Rogers, J. A. A Mechanically Driven Form of Kirigami as a Route to 3D Mesostructures in Micro/Nanomembranes. *Proc. Natl. Acad. Sci. U. S. A.*.**2015**, *112*, 11757-11764.
38. Zhang, Y.; Zhang, F.; Yan, Z.; Ma, Q.; Li, X.; Huang, Y.; Rogers, J. A. Printing, Folding and Assembly Methods for Forming 3D Mesostructures in Advanced Materials. *Nat. Rev. Mater.* **2017**, *2*, 17019-17035.
39. Fu, H.; Nan, K.; Bai, W.; Huang, W.; Bai, K.; Lu, L.; Zhou, C.; Liu, Y.; Liu, F.; Wang, J.; Han, M.; Yan, Z.; Luan, H.; Zhang, Y.; Zhang, Y.; Zhao, J.; Cheng, X.; Li, M.; Lee, J. W.; Liu, Y.et al.Morphable 3D Mesostructures and Microelectronic Devices by Multistable Buckling Mechanics. *Nat. Mater.* **2018**, *17*, 268-279.
40. Park, K.; Millet, L. J.; Kim, N.; Li, H.; Jin, X.; Popescu, G.; Aluru, N. R.; Hsia, K. J.; Bashir, R. Measurement of Adherent Cell Mass and Growth. *Proc. Natl. Acad. Sci. U. S. A.* **2010**, *107*, 20691-20696.

41. Krishnan, S.; Shi, Y.; Webb, R. C.; Ma, Y.; Bastien, P.; Crawford, K. E.; Wang, A.; Feng, X.; Manco, M.; Kurniawan, J.; Tir, E.; Huang, Y.; Balooch, G.; Pielak, R. M.; Rogers, J. A. Multimodal Epidermal Devices for Hydration Monitoring. *Microsyst. Nanoeng.* **2017**, *3*, 17014-17025.
42. Chung, S.; Park, S. Effects of Temperature on Mechanical Properties of SU-8 Photoresist Material. *Journal of Mechanical Science and Technology* **2013**, *27*, 2701-2707.
43. Biswas, C. S.; Patel, V. K.; Vishwakarma, N. K.; Tiwari, V. K.; Maiti, B.; Maiti, P.; Kamigaito, M.; Okamoto, Y.; Ray, B. Effects of Tacticity and Molecular Weight of poly (N-isopropylacrylamide) on Its Glass Transition Temperature. *Macromolecules* **2011**, *44*, 5822-5824.
44. Keddie, J. L.; Jones, R. A.; Cory, R. A. Size-Dependent Depression of the Glass Transition Temperature in Polymer Films. *Europhys. Lett.* **1994**, *27*, 59-64.
45. Forrest, J. A.; Dalnoki-Veress, K.; Stevens, J. R.; Dutcher, J. R. Effect of Free Surfaces on the Glass Transition Temperature of Thin Polymer Films. *Phys. Rev. Lett.* **1996**, *77*, 2002-2005.
46. Prucker, O.; Christian, S.; Bock, H.; Rühe, J.; Frank, C. W.; Knoll, W. On the Glass Transition in Ultrathin Polymer Films of Different Molecular Architecture. *Macromol. Chem. Phys.* **1998**, *199*, 1435-1444.
47. Forrest, J. A.; Mattsson, J. Reductions of the Glass Transition Temperature in Thin Polymer Films: Probing the Length Scale of Cooperative Dynamics. *Phys. Rev. E: Stat. Phys., Plasmas, Fluids, Relat. Interdiscip. Top.* **2000**, *61*, 53-56.
48. Forrest, J. A.; Dalnoki-Veress, K. The Glass Transition in Thin Polymer Films. *Adv. Colloid Interface Sci.***2001**, *94*, 167-196.
49. Dalnoki-Veress, K.; Forrest, J. A.; Murray, C.; Gigault, C.; Dutcher, J. R. Molecular Weight Dependence of Reductions in the Glass Transition Temperature of Thin, Freely Standing Polymer Films. *Phys. Rev. E: Stat. Phys., Plasmas, Fluids, Relat. Interdiscip. Top.* **2001**, *63*, 031801.
50. Feng, R.; Farris, R. J. The Characterization of Thermal and Elastic Constants for an Epoxy Photoresist SU8 Coating. *J. Mater. Sci.* **2002**, *37*, 4793-4799.
51. Kujawa, P.; Winnik, F. M. Volumetric Studies of Aqueous Polymer Solutions Using Pressure Perturbation Calorimetry: A New Look at the Temperature-Induced Phase Transition of poly (N-isopropylacrylamide) in Water and D_2O. *Macromolecules* **2001**, *34*, 4130-4135.

52. Antipov, Y. V.; Vygodskii, Y. S. Polymers on the Basis of Epoxy Oligomers and Polyimides. *Moscow International Composites Conference (MICC) 90*; Springer: Dordrecht, **1991**; pp 679-684.
53. Ye, C.; Singh, G.; Wadley, M. L.; Karim, A.; Cavicchi, K. A.; Vogt, B. D. Anisotropic Mechanical Properties of Aligned polystyrene-block-polydimethylsiloxane Thin Films. *Macromolecules* **2013**, *46*, 8608-8615
54. Xue, C.; Yonet-Tanyeri, N.; Brouette, N.; Sferrazza, M.; Braun, P. V.; Leckband, D. E. Protein Adsorption on Poly (N-isopropylacrylamide) Brushes: Dependence on Grafting Density and Chain Collapse. *Langmuir* **2011**, 27, 8810–8818.
55. Supporting Information in: Zhang, Y.; Webb, R. C.; Luo, H.; Xue, Y.; Kurniawan, J.; Cho, N. H.; Krishnan, S.; Li, Y.; Huang, Y.; Rogers, J. A. Theoretical and Experimental Studies of Epidermal Heat Flux Sensors for Measurements of Core Body Temperature. *Adv. Healthc. Mater.* **2016**, 5, 119–127.
56. Lide, David R. Handbook of Chemistry and Physics. 75th Edition. New York: CRC Press, **1996–1997**, 11–41.
57. Ning, X.; Wang, H.; Yu, X.; Soares, J.A.; Yan, Z.; Nan, K.; Velarde, G.; Xue, Y.; Sun, R.; Dong, Q.; Luan, H.; Lee, C. M.; Chempakasseril, A.; Han, M.; Wang, Y.; Li, L.; Huang, Y.; Zhang, Y.; Rogers, J. A. 3D Tunable, Multiscale, and Multistable Vibrational Micro-Platforms Assembled by Compressive Buckling. Adv. Funct. Mater. 2017, 27, 1605914.

CHAPTER 8: AUTONOMIC MOLECULAR TRANSPORT FOR ULTRASENSITIVE SURFACE-ENHANCED INFRARED ABSORPTION SPECTROSCOPY

8.1 Introduction

Detecting molecules at low concentration with high specificity is of great importance for applications ranging from pollution monitoring and biomolecule diagnostics to explosive detection.[1-9] One approach under investigation is surface-enhanced infrared adsorption (SEIRA), which uses resonant metal nanoantennas, to strongly enhance the absorption of a band of IR-active resonant modes in a label-free manner.[10-15] To improve the SEIRA sensor response to analytes, a number of studies have focused on increasing the enhancement factor through the choice of materials, nanoantenna arrangements, and geometries.[16,17] However, the detection of dilute analytes will still be limited by the probability a sufficient number of analytes are present within the SEIRA-enhancement region (or 'hot spot'), which is only within ~100nm of the antenna.[18-21] Therefore, it is attractive to consider an effective way to concentrate target analytes within the SEIRA-enhancement region to optimize sensitivity.

Magnetic and electric fields, and chemically-specific interactions (e.g., host-guest interactions) have been demonstrated as approaches to concentrate molecules into local regions of space.[22-24] However, these approaches either require analytes to be tagged with magnetic or electric-field responsive moieties, or that they participate in specific host-guest binding. Approaches to concentrate molecules without external fields or chemically–specific interactions are limited, but a few examples include the use of catalytically-pumped microfluidic systems,[18] and solvent evaporation on superomniphobic slippery liquid-infused porous surfaces (SLIPS).[7] While these approaches can result in a high analyte collection efficiency, they do not provide chemical specificity, which may be a shortcoming in some cases.

Recently, we demonstrated chemical gradient-driven molecular concentration in a radially functionalized hydrogel gel in which the molecules of interest freely diffuse until reaching the gradient edge, and concentrate as they are attracted to the center of the gradient.[25] Chemical gradients provide molecular collection without external inputs, can be defined to target selected analytes, and can be used to concentrate the analyte of interest to a specific region of space. In the present work, we applied a hydrogel film on top of a 3.0 μm x 80 nm SEIRA sensor. A gradient was then embedded in the hydrogel film to drive the molecules of interest to concentrate in the local vicinity of the SEIRA sensor. A small molecule containing an organophosphate functional group was selected as target molecule to demonstrate the gradient-driven concentration and SEIRA sensing, as it is similar to the structure of highly toxic pesticides and nerve agents.[26-28] We demonstrate that the model analyte was concentrated on the SEIRA sensing region by 15-fold with the use of a cationic radial chemical gradient. Combining the 15-fold concentration enhancement provided by the chemical gradient and the signal enhancement from SEIRA (>6.6-fold), this integrated system can be used to push the detection limit of the chemical species of interest ~100-fold, in a label-free manner.

8.2 Results and discussion

8.2.1 Sample fabrication and analyte selection

Gold nanoantennas were fabricated on calcium difluoride (CaF_2), a low refractive index, infrared-transparent substrate, by electron beam lithography (Figure 8.1a and Section 8.4). The length of the nanoantennas was set to 3.0 μm, the appropriate length to provide strong IR absorption enhancement in the range of 900 cm^{-1} to 1300 cm^{-1} in an aqueous environment, which covers the signature organophosphate P-O-C stretching of the agent of interest at 980 cm^{-1}. The simulated electric field of a single nanoantenna at 980 cm^{-1} indicates >1000 and >4000 electric field enhancement at the rod edge and tip, respectively (Figure 8.1c). To optimize the signal enhancement in each patch, the nanoantennas were arranged in a periodic pattern. Then, discrete nanoantenna patches were aligned in a row, 5 μm apart to spatially resolve the local concentration of the analyte of interest on the sensor surface as a function of time.

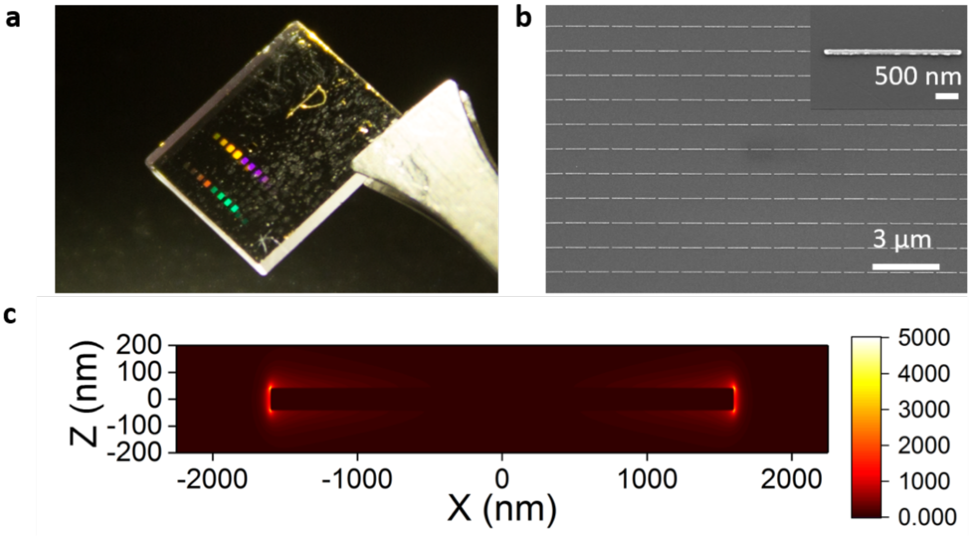

Figure 8.1 Surface-enhanced IR absorption (SEIRA)-active substrate. (a) An optical image of a SEIRA device with two rows of 300×300 µm nanoantenna patches. (b) SEM images of the nanoantenna pattern (inset: higher magnification image). Each nanoantenna is 3.0 µm long. (c) FDTD simulation of a single nanoantenna showing the electromagnetic field enhancement.

4-methylumbelliferyl phosphate (MUP) disodium, an anionic organophosphate, was selected as a model analyte due to its aqueous solubility and relatively low toxicity. It should be noted that compared to SERS, SERIA is more favorable for detecting organophosphates since the infrared absorbances of their signature vibrations are generally stronger than their corresponding Raman scattering. For this reason, FTIR is commonly used to study the degradation reactions of organophosphates (FTIR enables extracting detailed molecular structural information in a label-free fashion).[26]

8.2.2 Signal enhancement capabilities of unmodified nanoantennas

To study the IR signal intensity enhancement capability of the nanoantennas, we exposed the SEIRA chip to MUP solutions of various concentrations. Then, the spectra were compared to attenuated total internal reflection (ATR) infrared spectroscopy collected from similar solutions. The SEIRA-active substrate (in air) exhibited the expected characteristic asymmetric Fano-type line shapes with a maximum at approximately 1210 cm^{-1}. When immersed in water, the resonance bands red-shift about 200 cm^{-1} because of the increased refractive index of the environment. Thus, after exposing the antenna to the MUP solution, the observed peak at 980 cm^{-1} associated with the P-O-C stretch of MUP is in the SEIRA-active spectral region of the substrate. We subtracted the

MUP-free baseline from the MUP spectra and converted the reflectance to absorbance to obtain the corrected absorbance spectra. Comparing the corrected absorbance spectra of SEIRA and ATR in Figure 8.2b-d, we see that the absorbance peak intensity of the P-O-C stretch is linearly related to the solution concentration for SEIRA and ATR, and SEIRA provides a 6.6-fold enhancement over ATR.

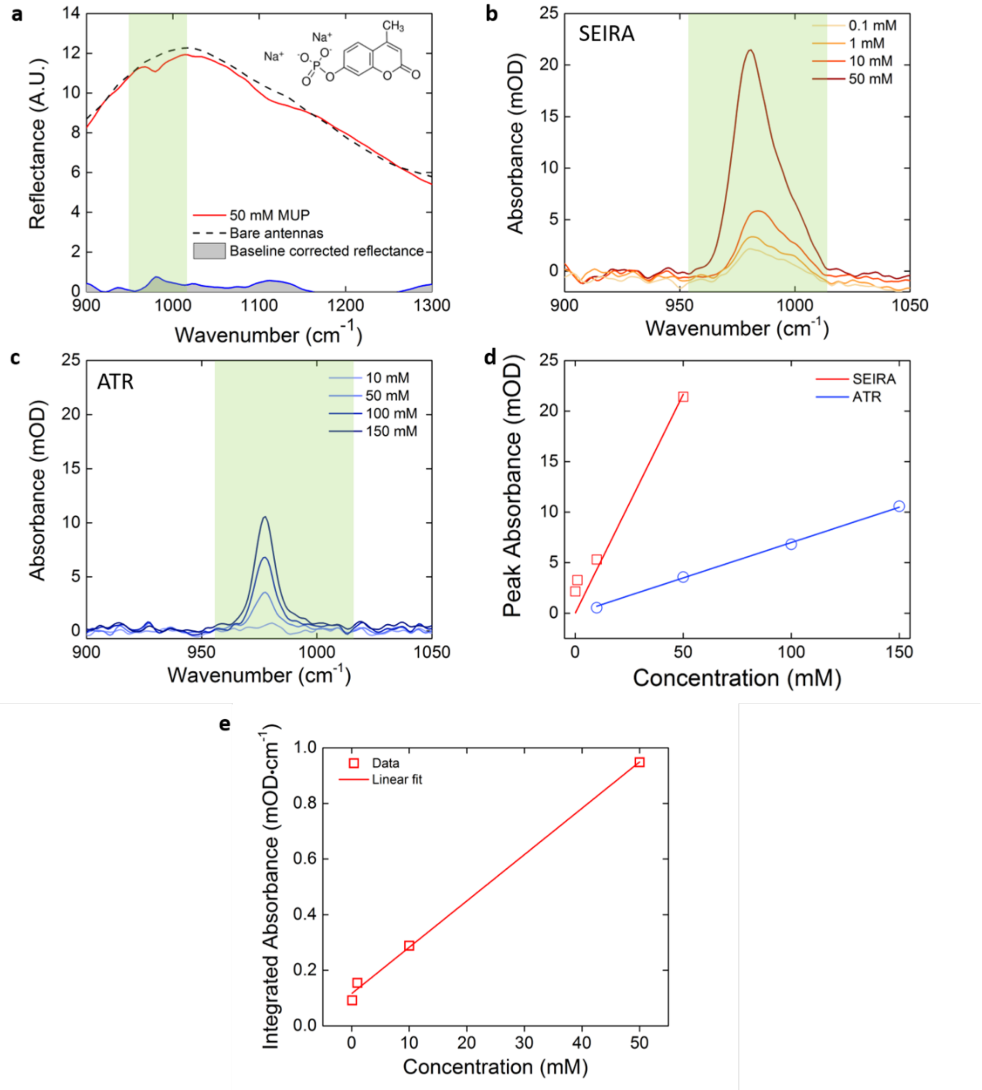

Figure 8.2 SEIRA and ATR spectrum of 4-methylumbelliferyl phosphate disodium and the concentration calibration curve. (a) Reflectance of nanoantenna array immersed in 50 mM MUP in water. (b) Baseline corrected absorbance spectra of 0.1 mM to 50 mM MUP solutions in the range of 900 to 1100 cm^{-1}. Range of the 978 cm^{-1} P-O-C stretching vibration highlighted. (c) ATR baseline-corrected absorbance spectra of 10 mM to 150 mM MUP solutions. (d) SEIRA and ATR absorbance peak maximum vs. MUP concentration. (e) Calibration curve of integrated absorbance in the P-O-C stretching region as a function of concentration.

8.2.3 Fabrication of gradient-modified nanoantennas

Because MUP is negatively charged at pH 7.4, the pH of the buffered hydrogel, a radial positive charge gradient was used to concentrate the MUP analyte. The hydrogel was based on cross-linked polyacrylamide (PAAm); this chemistry was selected due to its mechanical and chemical stability as well as its versatility in chemical post-modification. The PAAm hydrogel first polymerized on the SEIRA chip. A radial carboxylic acid gradient was then embedded within the hydrogel by diffusing a hydrolyzing agent (which converted amide groups to carboxylic acid groups) from a central point. Diamine groups were then conjugated onto the formed carboxylic acid groups, forming the gradient of positive charge, with the center of the gradient aligned with the central antenna patch (Figure 8.3b).

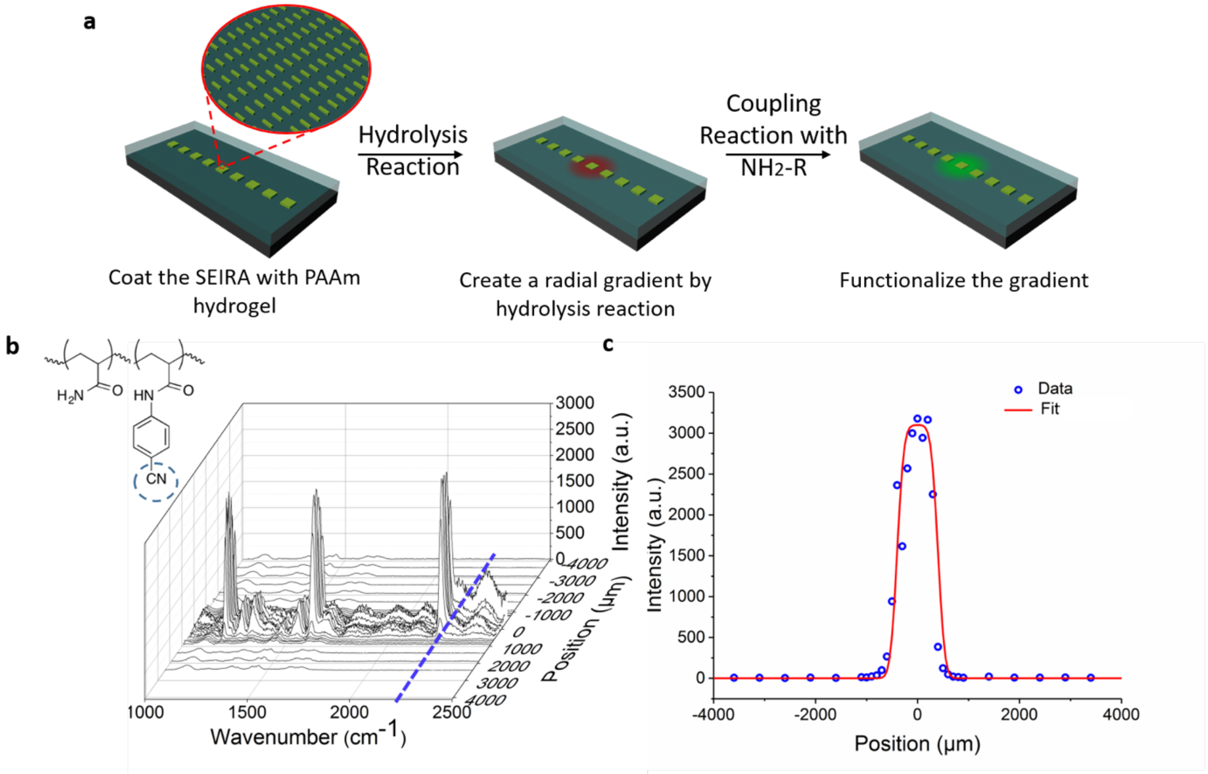

Figure 8.3 Fabrication of PAAm hydrogel with embedded radial chemical gradient on a SEIRA-active substrate. (a) Schematic for constructing radial chemical gradient via hydrolysis followed by amine coupling. (b) Raman map of a line scan across the 4-aminobenzylnitrile conjugated chemical gradient, with the strong cyano Raman peak at 2228 cm^{-1} indicated with a dotted line. (c) The intensity of the 2228 cm^{-1} cyano peak profile along the gradient center. This peak is normalized with a peak at 1100 cm^{-1} that corresponds to the hydrogel carbon backbone.

For the purpose of characterizing the chemical gradient, the diamine was replaced with 4-aminobenzylnitrile in the coupling step. The cyano-appended amine was selected since it has a strong Raman-active resonance at 2228 cm^{-1}, which can be used to profile the chemical gradient. Using a Raman line scan across the gradient (Figure 8.3b and 8.3c), the gradient can be seen to be comprised of two parts, an inner circle region (~700 µm diameter) of relatively constant chemical functionality and a transition ring (~300 µm in width) between the center of the gradient and the gradient-free region of the hydrogel.

8.2.4 Signal enhancement capabilities of gradient-modified nanoantennas

To investigate analyte collection, we recorded the spectrum inside and outside of the positive charge gradient at different time points after applying the MUP solution to the hydrogel surface. The MUP solution was sprayed on dehydrated hydrogels with fixed distance (around 20 cm width and 30 cm height) from different directions for 10 times to mimic an aerosol pesticide or nerve agent dosing event (Figure 8.4a). Samples then were sealed in chambers at 100% humidity to swell the hydrogel and initiate the transport process.

Figure 8.4c and 8.4d show SIERA spectra after dosing 10 mM and 1 mM MUP solutions, respectively. At the 1-hour time point, the peak intensity as measured everywhere is similar, confirming that the sprayed droplets of MUP have initially locally diffused, generating a homogenous dosing of MUP on the hydrogel. From this time forward, baseline corrected P-O-C spectrums exhibit a continuous peak intensity increase inside the gradient and a continuous decrease intensity outside the gradient, indicating accumulation of MUP in the gradient region. As mentioned, the integrated absorbance is linearly related to MUP concentration, enabling conversion of the baseline corrected reflectance spectrum to MUP concentration. To quantify the concentration enhancement of the chemical gradient, we calculate the concentration enhancement ratio (CER), the ratio of the MUP concentration inside the chemical gradient to the concentration outside the chemical gradient. Figure 4 c and d demonstrate that accumulation of MUP within the gradient is initially rapid and then gradually slows down for both the 10 mM and 1 mM MUP dosing. For the sample dosed with 10 mM, the CER is 2 after 3 hours and 4 after 17 hours. The CER is greater for the more dilute 1 mM of MUP solution. The CER is 4 after 3 hours and 15 after 17 hours (the CER saturates by this time). We suspect the final CER is greater for 1 mM MUP than for 10 mM MUP because if sufficient MUP is present, it will neutralize the charged groups in the gradient region of the hydrogel.

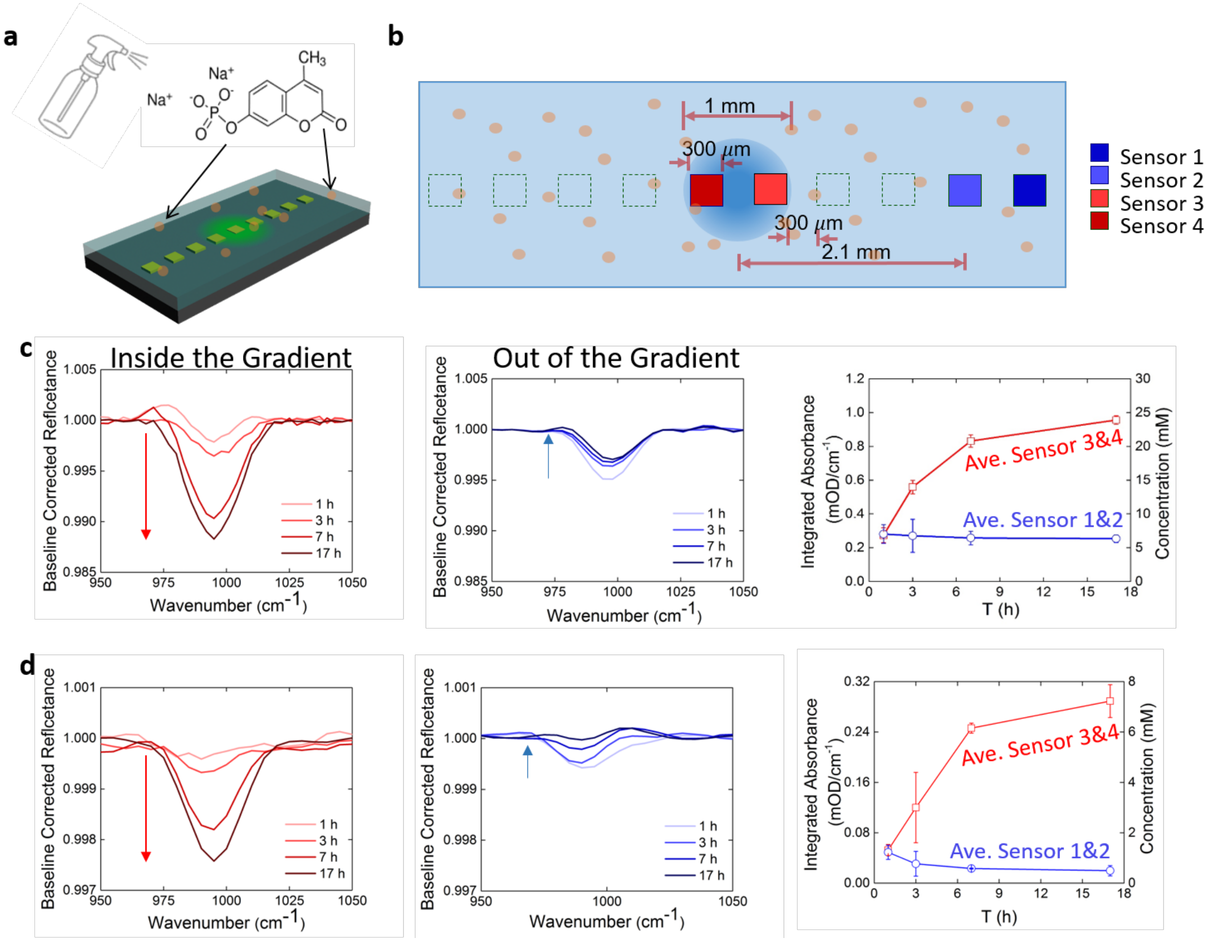

Figure 8.4 Gradient-induced SEIRA sensitivity improvement. (a) MUP aerosol dosing. (b) top view schematic of the radial gradient and nanoantenna patches (only the colored patches were interrogated, the patches in the dotted boxes were present, but not interrogated as collecting spectra from all the SEIRA patches would have reduced the time resolution of the experiment). We selected two patches within the gradient region and two outside of the gradient region to compare the baseline corrected P-O-C stretching vibration spectra at different time points after dosing with (c) 10mM and (d) 1mM MUP solutions.

8.3 Conclusions

A functional hydrogel coating with embedded radial chemical gradient is constructed on the nanoantenna SEIRA chip to focus analytes to the sensing region. A radial gradient with ~1 mm diameter is fabricated with hydrolysis and amide coupling reactions and is characterized by confocal Raman spectroscopy. This procedure is facile, affording a flexible post-functionalization method that is capable of creating gradients of diverse functionality. Directed concentration of the model organophosphate analyte MUP is realized with a positive charge gradient via functionalizing the gradient with diamine molecules. Through comparing the infrared spectra inside and outside the gradient at different time points after spraying MUP aerosol on the hydrogel-coated SEIRA sensor, we observed a continued analyte accumulation in the gradient region. The concentration enhancement effect is stronger after reducing the sprayed MUP solution concentration from 10 mM to 1 mM. A 15-fold concentration enhancement is realized after 17 hours of transport. As the first demonstration of combining the signal enhancement from both the gel embedded chemical gradient with a nanostructured sensor, we showed that improved sensitivity can be realized by employing benefits of both the nanostructure-assisted electric field enhancement and the gradient-driven molecule concentration. We expect that this method can easily be tuned to combine different chemical gradient (e.g. supramolecular interaction gradients, hydrogen bond gradients, or more specific biomolecule gradients), even with other nanosensors (e.g. SERS, microring sensors). Furthermore, through integrating gradients arrays and sensors arrays into one chip, an integrated sensing device that can realize the detection of more complex mixture may be realized.

8.4 Experimental section

8.4.1 Nanofabrication of the SEIRA chip

The single-band gold nanoantenna arrays are patterned on CaF_2 (1×1 cm^2) substrate using electron-beam lithography (Raith eLine). 950 kDa PMMA was spin coated on the CaF_2 substrate (3500 rpm, 55 s), baked for 5 min at 180 ℃ to form a 350 nm resist layer. Then, the sample was exposed to E-beam with a dose of 270 μm/cm^2 under a voltage of 10 kV, developed in MIBK:IPA 1:4 for 1 min, and blow dried by high-purity nitrogen. A 50 nm Au layer was deposited on the sample using electron-beam evaporation (first 0.5 Å/s for 100s to increase adhesion and then 1 Å/s for 450s). After the Au deposition, the sample was immersed in acetone for 1 h and exposed to oxygen plasma to remove excess metal and resist. The height, width, and length of the nanoantenna was 80 nm, 80 nm and 3.0 μm, respectively. The gap between different rows was 5 μm. The electrical magnetic field is simulated using FDTD software Lumerical FDTD-Solution.

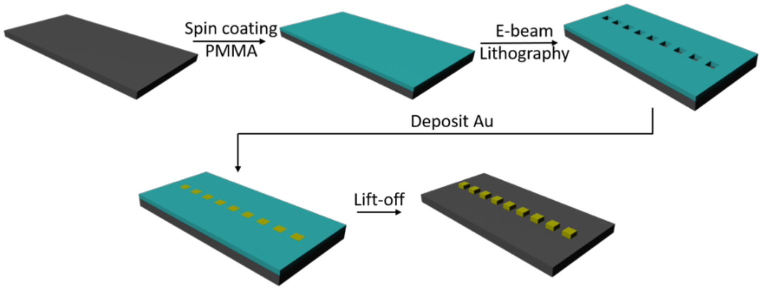

Figure 8.5 Schematic of fabrication process of SEIRA device. Nano-antennas on CaF_2 were fabricated with E-beam lithography and E-beam evaporator.

8.4.2 Coating the SEIRA chip with chemical gradient-embedded hydrogel

Nanoantenna SEIRA chips and silicon wafers were firstly immersed in a 3-(trimethoxysilyl)propyl methacrylate (TMSPMA) solution in THF (0. 2 v/v%) overnight to improve the adhesion between the substrate and the PAAm hydrogel and in trichloro(1H, 1H, 2H, 2H-perfluoroocyl)silane (PFOS) solution in THF (0. 2 v/v%) to enhance the hydrophobicity, respectively. Using a 15 μm thick aluminum foil with a 0.8 × 0.8 cm^2 hole as spacer, a drop (approx. 0.5 ml) of the PAAm polymerization solution (0.02 g diethoxyacetophenone, 0.6 g 37:1 acrylamide/bis-acrylamide, and 10g Millipore water) was applied between the SEIRA chip and the silicon wafer and then polymerized under UV light (365 nm wavelength, 60 Hz, 100W) for 2 h. After peeling off the silicon wafer, the PAAm hydrogel coated SEIRA chip was first dried under ambient condition overnight and then hydrolyzed by pipetting a 0.1 μl hydrolysis solution (1 g N, N, N', N'-tetramethylethylenediamine, 0.09 g sodium chloride, 0.12 g sodium hydroxide, 10 g Millipore water) on top of the central nanoantenna patch. After the hydrolysis reaction, the hydrogel-coated SEIRA chip was immersed in the coupling solution (EDC 0.112 g, N, N-dimethylethylenediamine 0.0516 g, pH 4.7 MES buffer solution 15 g and sodium chloride 0.132 g) for 24 h to construct the positive charge gradient.

8.4.3 Raman characterization of the chemical gradient in hydrogel

Samples for the Raman spectroscopy profile were similar to above samples with positive charge gradient, however, were fabricated on silicon wafers instead of SEIRA chips and were functionalized with 4-aminobenzonitrile (0.069 g) which replaced the diamine in the functionalization solution. Raman confocal imaging microscope (Horiba, 532 nm wavelength laser, 0.5 NA 50× objective) was used to profile the gradient along the diameter. Raman spectra were normalized with the peak at ca. 1100 cm^{-1} which is from the PAAm C-C backbone.

The chemical gradient is formed with the diffusion of the sodium hydroxide hydrolyzation solution. As shown in Figure 8.3, the gradient system is comprised of two parts, the inner plateau region (~700 μm in diameter) of relatively constant intensity and the transition ring (~300 μm in width) connecting the gradient to the exterior region. Since there is a plateau region in the chemical gradient center, we fitted the curve using the diffusion model assuming fixed surface concentration:

$$C(x,t) = \frac{C_s}{2} + \frac{C_s}{2}\,\mathrm{erf}(\pm(\frac{x - x_0}{\sqrt{4Dt}})) \qquad 8.1$$

in which the $C(x,t)$ is the hydrolysis agent concentration along the gradient, C_s is the hydrolysis agent concentration in the center, x is the position, x_0 is the center of the transition region (the x_0 of the left and right transition region should be of comparable absolute value). In the error function, the sign of $(\frac{x-x_0}{\sqrt{4Dt}})$ is positive for the left edge and negative for the right edge.

Using the Confocal Raman Spectroscopy to quantify the chemical gradient, we assume the Raman intensity of the peak 2228 cm^{-1}, which is corresponding to the functionalized nitrile group, is linearly proportional to the concentration distribution of the hydrolysis agent, and thus using the following equation to fit the Raman profile:

$$I(x,t) = \frac{I_S}{2} + \frac{I_S}{2}\,\mathrm{erf}((\pm\frac{x - x_0}{\sqrt{4Dt}})) \qquad 8.2$$

in which the $I(x,t)$ is the Raman 2228 cm^{-1} peak intensity distribution along the chemical gradient, I_S is the one in the central plateau region. After the curve fitting, the I_S is 3100, x_0 of the left and right edge are -350 μm and 350 μm, correspondingly, and the $\sqrt{4Dt}$ is 150 μm, as shown in the Figure 8.3c.

8.4.4 Transport experiment in the gel-coated SEIRA sensor

MUP solutions was applied on the sensor by spraying aerosols from a fixed distance (~20 cm width, ~30 cm height) from 10 different directions. Then, samples were placed in a sealed Petri-dish with 100% humidity to allow hydration during transport. As the transport experiment proceeded for 1h, 3h, 7h, and 17h, FTIR measurements were taken with a liquid-nitrogen-cooled mercury cadmium telluride (MCT) detector using a Bruker Vertex70 spectrometer (512 scans, 40 kHz mirror velocity, 8 cm^{-1} resolution, 0.4 NA dark field objective). The aperture size was adjusted to match the size of the nanoantenna array. Zero order reflectance spectrums were collected using the Bruker Hyperion 3000 IR microscope and were then transformed to Fourier transform infrared (FTIR) with a coupled FTIR spectrometer. At each time point, all measurements were taken within 10 min. The reflectance of the nanoantennas are normalized according to the reflection spectrum of gold mirror layer (with almost 100% reflectivity in the mid-infrared range). The attenuated total reflectance Fourier transform infrared spectroscopy (ATR-FTIR) was taken with a Thermo-Nicolet NEXUS 670 FTIR system (512 scans, 8 cm^{-1} resolution). A θ = 45º ZnSe crystal was selected as the reflectance element with ten internal reflections. The water spectrum was used as reference.

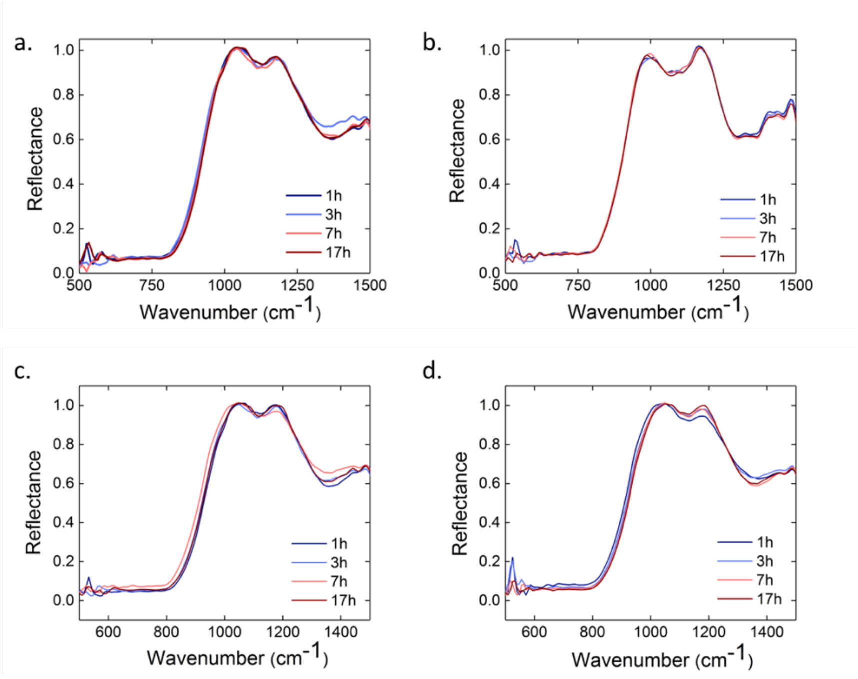

Figure 8.6 FTIR reflectance spectrums of PAAM hydrogel-coated SEIRA with MUP transport process. a) reflectance within the chemical gradient sprayed with 10 mM MUP solution; b) reflectance outside the chemical gradient sprayed with 10 mM MUP solution; c) reflectance within the chemical gradient sprayed with 1 mM MUP solution; d) reflectance outside the chemical gradient sprayed with 1 mM MUP solution;

8.5 References

1. Kelley, S. O.; Mirkin, C. A.; Walt, D. R.; Ismagilov, R. F.; Toner, M.; Sargent, E. H. Advancing the speed, sensitivity and accuracy of biomolecular detection using multi-length-scale engineering. *Nature Nanotechnology* 2014, 9, 969-980.
2. Homola, J. Surface plasmon resonance sensors for detection of chemical and biological species. *Chemical Reviews* 2008, 108, 462-493.
3. Reiner, J. E.; Balijepalli, A.; Robertson, J. W. F.; Campbell, J.; Suehle, J.; Kasianowicz, J. J. Disease Detection and Management via Single Nanopore-Based Sensors. *Chemical Reviews* 2012, 112, 6431-6451.
4. Kosaka, P. M.; Pini, V.; Ruz, J. J.; da Silva, R. A.; Gonzalez, M. U.; Ramos, D.; Calleja, M.; Tamayo, J. Detection of cancer biomarkers in serum using a hybrid mechanical and optoplasmonic nanosensor. *Nature Nanotechnology* 2014, 9, 1047-1053.
5. Ding, S. Y.; Yi, J.; Li, J. F.; Ren, B.; Wu, D. Y.; Panneerselvam, R.; Tian, Z. Q. Nanostructure-based plasmon-enhanced Raman spectroscopy for surface analysis of materials. *Nature Reviews Materials* 2016, 1.
6. Chen, J. M.; Huang, Y. J.; Kannan, P.; Zhang, L.; Lin, Z. Y.; Zhang, J. W.; Chen, T.; Guo, L. H. Flexible and Adhesive Surface Enhance Raman Scattering Active Tape for Rapid Detection of Pesticide Residues in Fruits and Vegetables. *Analytical Chemistry* 2016, 88, 2149-2155.
7. Yang, S. K.; Dai, X. M.; Stogin, B. B.; Wong, T. S. Ultrasensitive surface-enhanced Raman scattering detection in common fluids. *Proceedings of the National Academy of Sciences of the United States of America* 2016, 113, 268-273.
8. Gruenke, N. L.; Cardinal, M. F.; McAnally, M. O.; Frontiera, R. R.; Schatza, G. C.; Van Duyne, R. P. Ultrafast and nonlinear surface-enhanced Raman spectroscopy. *Chemical Society Reviews* 2016, 45, 2263-2290.
9. Mesch, M.; Zhang, C. J.; Braun, P. V.; Giessen, H. Functionalized Hydrogel on Plasmonic Nanoantennas for Noninvasive Glucose Sensing. *Acs Photonics* 2015, 2, 475-480.
10. Luk'yanchuk, B.; Zheludev, N. I.; Maier, S. A.; Halas, N. J.; Nordlander, P.; Giessen, H.; Chong, C. T. The Fano resonance in plasmonic nanostructures and metamaterials. *Nature Materials* 2010, 9, 707-715.
11. Adato, R.; Altug, H. In-situ ultra-sensitive infrared absorption spectroscopy of biomolecule interactions in real time with plasmonic nanoantennas. *Nature Communications* 2013, 4.

12. Adato, R.; Yanik, A. A.; Amsden, J. J.; Kaplan, D. L.; Omenetto, F. G.; Hong, M. K.; Erramilli, S.; Altug, H. Ultra-sensitive vibrational spectroscopy of protein monolayers with plasmonic nanoantenna arrays. *Proceedings of the National Academy of Sciences of the United States of America* 2009, 106, 19227-19232.
13. Neubrech, F.; Pucci, A.; Cornelius, T. W.; Karim, S.; Garcia-Etxarri, A.; Aizpurua, J. Resonant Plasmonic and Vibrational Coupling in a Tailored Nanoantenna for Infrared Detection. *Physical Review Letters* 2008, 101.
14. Aouani, H.; Rahmani, M.; Sipova, H.; Torres, V.; Hegnerova, K.; Beruete, M.; Homola, J.; Hong, M. H.; Navarro-Cia, M.; Maier, S. A. Plasmonic Nanoantennas for Multispectral Surface-Enhanced Spectroscopies. *Journal of Physical Chemistry C* 2013, 117, 18620-18626.
15. Neubrech, F.; Pucci, A. Plasmonic Enhancement of Vibrational Excitations in the Infrared. *Ieee Journal of Selected Topics in Quantum Electronics* 2013, 19.
16. Adato, R.; Aksu, S.; Altug, H. Engineering mid-infrared nanoantennas for surface enhanced infrared absorption spectroscopy. *Materials Today* 2015, 18, 436-446.
17. Neubrech, F.; Huck, C.; Weber, K.; Pucci, A.; Giessen, H. Surface-Enhanced Infrared Spectroscopy Using Resonant Nanoantennas. *Chemical Reviews* 2017, 117, 5110-5145.
18. Das, S.; Shklyaev, O. E.; Altemose, A.; Shum, H.; Ortiz-Rivera, I.; Valdez, L.; Mallouk, T. E.; Balazs, A. C.; Sen, A. Harnessing catalytic pumps for directional delivery of microparticles in microchambers. *Nature Communications* 2017, 8.
19. Sheehan, P. E.; Whitman, L. J. Detection limits for nanoscale biosensors. *Nano Letters* 2005, 5, 803-807.
20. Sitt, A.; Hess, H. Directed Transport by Surface Chemical Potential Gradients for Enhancing Analyte Collection in Nanoscale Sensors. *Nano Letters* 2015, 15, 3341-3350.
21. Neubrech, F.; Beck, S.; Glaser, T.; Hentschel, M.; Giessen, H.; Pucci, A. Spatial Extent of Plasmonic Enhancement of Vibrational Signals in the Infrared. *Acs Nano* 2014, 8, 6250-6258.
22. Gijs, M. A. M. Magnetic bead handling on-chip: new opportunities for analytical applications. *Microfluidics and Nanofluidics* 2004, 1, 22-40.
23. Hlushkou, D.; Perdue, R. K.; Dhopeshwarkar, R.; Crooks, R. M.; Tallarek, U. Electric field gradient focusing in microchannels with embedded bipolar electrode. *Lab on a Chip* 2009, 9, 1903-1913.

24. Escobedo, C.; Brolo, A. G.; Gordon, R.; Sinton, D. Optofluidic Concentration: Plasmonic Nanostructure as Concentrator and Sensor. *Nano Letters* 2012, 12, 1592-1596.
25. Zhang, C. J.; Sitt, A.; Koo, H. J.; Waynant, K. V.; Hess, H.; Pate, B. D.; Braun, P. V. Autonomic Molecular Transport by Polymer Films Containing Programmed Chemical Potential Gradients. *Journal of the American Chemical Society* 2015, 137, 5066-5073.
26. Kim, K.; Tsay, O. G.; Atwood, D. A.; Churchill, D. G. Destruction and Detection of Chemical Warfare Agents. *Chemical Reviews* 2011, 111, 5345-5403.
27. Moss, J. A.; Szczepankiewicz, S. H.; Park, E.; Hoffmann, M. R. Adsorption and photodegradation of dimethyl methylphosphonate vapor at TiO2 surfaces. *Journal of Physical Chemistry B* 2005, 109, 19779-19785.
28. Steiner, W. E.; Clowers, B. H.; Haigh, P. E.; Hill, H. H. Secondary ionization of chemical warfare agent simulants: Atmospheric pressure ion mobility time-of-flight mass spectrometry. *Analytical Chemistry* 2003, 75, 6068-6076.

CHAPTER 9: PROJECT CONCLUSIONS AND FUTURE DIRECTIONS

9.1 Microring resonators for characterizing analyte-brush interactions

Silicon photonic microring resonators are introduced as a new method of monitoring analyte-polymer interactions by tracking of environmental changes (i.e. compositional and volumetric differences) from the perspective of brush-modified sensors that are introduced to changing experimental conditions. These sensors operate by confining light within the microring waveguide via total internal reflection, which is coupled onto the microrings according to an interferometric-based condition with the majority of the active sensing volume within 100 nm of the ring surface.[1] The resonant wavelength can be monitored in real-time and its changes can be plotted against several different conditions, including time, pH, and brush length to extract different types of data. Microring resonators have previously been utilized for the surface-sensitive, refractive index-based detection of biomolecular targets, including proteins,[2] miRNA,[3] and DNA.[4] Additionally, this technology has also been applied to monitor layer-by-layer assembly[5] and chemical reactions occurring at the sensor surface.[6] However, without specific binding or recognition elements, detection capabilities significantly decrease as there is no localization of the analyte within the surface-confined sensing region.

First, we demonstrate that polymer brushes that are grown from the surface can be used to enhance the sensitivity and selectivity through non-covalent molecular interactions.[7] In this work, polymer modification was found to enhance the sensor response in excess of 1000% for some brush-analyte combination, compared to unmodified sensors. Analytes were selected to emphasize the promise of this technology of sensitive detection for toxic and regulated substances. For example, representative targets include 4-methylumbelliferyl phosphate (a simulant for highly toxic organophosphates) and Bisphenol A (an industrial pollutant). The enhancement from intermolecular interactions and solubility effects has potential to be optimized to be highly specific and sensitive for particular classes of target analytes. Alternatively, the presence of differential response for each analyte to different brush systems suggests the potential for array-based target identification. This opens the door for many possibilities of future work to optimize polymeric constructs for specific analytical targets and applications.

Next, we sought to investigate the utility of silicon photonic microring resonators as a platform for the in-situ characterization of polymer brush surfaces. Brush-modified surfaces have led to great advances in surface and interface science, with well-known applications in many different fields. However, the direct measurement of analyte-brush interactions, a key aspect of protective coating and membrane development,[8] remains a challenge. For example, although many works acknowledge or even take advantage of the limited permeability of dense brushes to small molecules or oligomers,[9] those that study these effects focus mostly on brush conformation characterization.[10] In this work, we demonstrated that brush-modified sensors allow for straightforward extraction of various constants, such as partitioning and diffusion coefficients, critical thickness values, and pK_a, as a function of complex variables. Many of these constants can be extracted from the same set of data, greatly increasing the amount of information gained during each experiment. Additionally, the surface sensitive nature of our detection platform provides a good complement to brush-liquid interface sensitive techniques, such as goniometry. In future work, the spatial independence of this platform would allow for the fast combinatorial screening of analyte-brush systems in a multiplexed fashion.

9.2 Design of new degradable materials

A renewed interest in degradable polymers, especially for biomedical and engineering applications has led to an extensive search for new mechanisms to breakdown polymers.[11] Most degradable polymers contain functional groups along their main chain that cleave independently by chemical or photochemical reaction, in which case, the degradation rate remains constant until the trigger or cleavable functionality is consumed. The discovery of self-immolative polymers was particularly exciting because one triggering event is sufficient to activate an entire polymer chain to degrade.[12,13] These systems are stable under ambient conditions until a reactive unit at the polymer end is cleaved, triggering a cascade of fragmentation reactions that proceed sequentially along the polymer chain. More recently, the development of chain-shattering polymers allows materials to spontaneously degrade along the main chain with a triggering event occurring at each monomer unit.[14] Both the self-immolative and chain-shattering approaches do have limitations in degradation rate and require a stoichiometric amount of the triggering agent. We were interested in a less studied approach that can be referred to as an amplified chain-shattering degradation. In this mechanism, a catalytic species accelerates chain cleavage, which in turn generates a full equivalent of the same agent, leading to an exponential degradation cascade.

In this work, we introduce the 3-iodopropyl acetal moiety as a simple cleavable unit that undergoes acid catalyzed hydrolysis to liberate HI and acrolein stoichiometrically. We show that integrating this unit into linear and network polymers gives a class of macromolecules that undergo a new mechanism of degradation with an acid amplified, sigmoidal rate. This trigger- responsive self-amplified degradable polymer undergoes accelerated rate of degradation and agent release.[15] Based on the success of this project, different systems may be developed for the self-amplified release of other reagents as well as other architectures with different rates and byproducts to expand the toolbox for potential applications. In future work, this acid amplifying motif could serve as a unique method for the controlled delivery of protic acid for various biological and chemical applications. Alternatively, these materials may serve as benign carriers that undergo amplified release of biocidal acrolein in acidic solution.

9.3 Fluorescent techniques for investigating protein-polymer interactions

Proteins have proven to have tremendous potential in biological pharmaceuticals and drug targets due to their highly specific and complex set of functions and biocompatibility. Commonly-used materials include silicon for its use in biosensors and biodegradability into orthosilicic acid,[16] metal oxides due to their wide range of structures and optical, electrical, and magnetic properties,[17] polyethylene glycol or zwitterionic organic modifications to encourage nonfouling behaviors,[18] hydrophobic coatings that combat bacterial growth,[19] and hydrogels for protein delivery in tissue engineering.[20] However, a major challenge in exploiting the unique functions of proteins in engineered devices and delivery systems is their compatibility with these materials. Incompatible materials can disrupt protein structures and lead to aggregation, biofouling, or degradation that reduce device performance. Complicating this problem is that protein-polymer interactions are governed by a complex combination of factors including solvation environment, hydrophobic and noncovalent interactions, charge repulsion, and crowding. This challenge motivates the need for in situ approaches for identifying material properties that affect protein function.

In our work, fast relaxation imaging (FReI) is introduced as a novel technique to detect protein unfolding in situ by imaging changes in fluorescence resonance energy transfer (FRET) after temperature jump perturbations.[21] FReI images the influence of material properties on protein stability rather than typical bulk measurements used to assess protein–material compatibility. Our studies interrogated the equilibrium thermodynamic, kinetic, and spatial details of protein unfolding in polyacrylamide hydrogels with different cross-linking density (pore size). To accomplish this, we investigated a crowding sensor protein and phosphoglycerate kinase to quantify the confinement effect of the cross-linked hydrogel and reveal the effect of noncovalent interactions of the protein with the polymer surface. Future applications of FReI could identify design rules for protein-compatible drug carriers, biosensors, or functional biomaterials. The approach can also be extended to other FRET-labeled biomacromolecules, including other proteins or DNA and RNA aptamers that are used in nucleic acid-based sensors and in drug targeting

Additionally, we demonstrate that a biomedically-relevant zwitterionic polymer in solution can interact with proteins directly through utilizing fluorescence techniques.[22] Polymer-dependent changes in the tryptophan fluorescence spectra of three structurally-distinct proteins reveal that the polymer interacts directly with all three proteins and changes both the local polarity near tryptophan residues and the protein conformation. Thermal denaturation studies show that the protein melting temperatures decrease and that protein folding cooperativity increases upon interaction with the polymer. We demonstrate the exact extent of the changes is protein-dependent, as some proteins exhibit increased stability, whereas others experience decreased stability at high polymer concentrations. For immediate future work, future studies could interrogate the effect of grafting density and charge spacing on the structure and amount of adsorbed protein. However, these results suggest that the polymer is not universally protein-repellent and that its efficacy in biotechnological applications will depend on the specific proteins used. As such, our findings open a new area of exploration in polymer physics to determine mechanisms by which biological solutes may interact differently with grafted versus soluble polyzwitterions.

9.4 Resonant MEMS for characterizing polymer films

Microelectromechanical systems (MEMS) are systems that consist of small-scale electrical and mechanical components for specific purposes. Although a universal definition is lacking, MEMS products possess a number of distinctive features: miniature embedded systems, involve one ore many micromachine components, enable higher level functions, integrate smaller functions into one package with greater utility.[23] A subset of MEMS technology are systems with tailored mechanical vibratory resonances. These systems can serve as means for assessing physical properties of ultrathin coatings in sensors and analytical platforms. Most such technologies exist in largely two-dimensional configurations with a limited total number of accessible vibration modes and modal displacements, thereby placing constraints on design options and operational capabilities.

Our work presents a set of concepts in 3D microscale platforms with vibrational resonances excited by Lorentz-force actuation for purposes of measuring properties of thin-film coatings.[24] Nanoscale films including photodefinable epoxy, cresol novolak resin, and polymer brush with nm-scale thicknesses serve as demonstrations of the advantages of these devices for detection of multiple physical properties, such as modulus and density, within a single polymer sample. The stability and reusability of the structure are demonstrated through multiple measurements of polymer samples using a single platform, and *via* integration with thermal actuators, the temperature-dependent physical properties of polymer films are assessed. The findings establish unusual opportunities for interrogation of the physical properties of polymers through advanced MEMS design. Numerical modeling suggests the potential for characterization of anisotropic mechanical properties in single or multilayer films. Additionally, these assembly approaches can be applied to 3D structures with reduced dimensions, increased operating frequencies, and enhanced sensitivity.

9.5 Strategies for ultrasensitive SEIRA

The detection of low-concentration target analytes has long been a challenge for nanoscale sensors: if the desired analyte is only transported across the sensor by diffusion, the probability that a molecule will interact the sensor scales with the solution concentration.[25] There are many relevant chemical agents that must be detected at low concentrations, including organophosphates, pesticides, industrial toxins, and environmental toxins. As such, new devices and technologies are needed that can quickly identify and/or degrade agents into less toxic substances. Surface attraction has been used to drive diffusion against conventional gradients and gravity since the early 90's.[26] In this method, ionic, hydrophobic, or other noncovalent interactions are exploited to bring an analyte closer in space to the sensor to improve both the sensitivity and response time.[27] Depending on the analyte of interest, one general solution is to segregate and concentrate chemical compounds into specific regions on a surface. This can be accomplished by post-modification of a polymer backbone such that the concentration of specific functional groups varies over distance.[28] These embedded chemical potential gradients create interactions with the target molecule and serve as the driving force for molecular transport across the polymer surface.

One approach is surface-enhanced infrared adsorption (SEIRA) to strongly enhance the absorption of a band of IR-active resonant modes in a label-free manner.[29] In this technique, the molecular vibration of interest can be matched with the plasmonic excitation of a resonant nanoantenna, thus enhancing the signal of that vibration. In this work, we demonstrate the use of a polyacrylamide hydrogel film with imbedded radial chemical gradient to locally concentrate analytes in the local vicinity of SEIRA-active nanoantenna to improve the detection limit over that provided by SEIRA. Using an embedded positive charge gradient, a nerve agent simulant 4-methylumbelliferyl phosphate was concentrated 15-fold on top of a SEIRA active array of nanoantenna. The combined effect of molecular concentration and SEIRA resulted in the potential ability to detect the agent of interest at concentrations two orders of magnitude below that provided by ATR using a conventional, gradient-free substrate. Gradient technology has the potential to be further developed for catalytic remediation and detection at points of concentration or for lab-on-a-chip devices that incorporate directional transport. Gradient systems that are innately mobile (i.e. that do not need plasticizer to concentrate on a reasonable time scale) are of particular interest due to their utility in real-world applications.

9.6 References

1. Iqbal, M.; Gleeson, M. A.; Spaugh, B.; Tybor, F.; Gunn, W. G.; Hochberg, M.; Baehr-Jones, T.; Bailey, R. C.; Gunn, L. C. Label-Free Biosensor Arrays Based on Silicon Ring Resonators and High-Speed Optical Scanning Instrumentation. *IEEE J. Sel. Top. Quantum Electron*. **2010**, *10 (3)*, 654−661.
2. Washburn, A. L.; Gunn, L. C.; Bailey, R. C.; Label-Free Quantitation of a Cancer Biomarker in Complex Media Using Silicon Photonic Microring Resonators. *Anal. Chem.* **2009**, *81 (22)*, 9499-9506.
3. Qavi, A. J.; Bailey, R. C. Multiplexed Detection and Label-Free Quantitation of MicroRNAs Using Arrays of Silicon Photonic Microring Resonators. *Angew. Chemie Int. Ed.* **2010**, *49 (27)*, 4608-4611.
4. Qavi, A. J.; Mysz, T. M.; Bailey, R. C. Isothermal Discrimination of Single-Nucleotide Polymorphisms via Real- Time Kinetic Desorption and Label-Free Detection of DNA Using Silicon Photonic Microring Resonator Arrays. *Anal. Chem.* **2011**, *83* (17), 6827-6833.

5. Luchansky, M. S.; Washburn, A. L.; Martin, T. A.; Iqbal, M.; Gunn, L. C.; Bailey, R. C. Characterization of the evanescent field profile and bound mass sensitivity of a label-free silicon photonic microring resonator biosensing platform. *Biosens. Bioelectron.* **2010**, *26 (4)*, 1283-1291.
6. (a) Byeon, J.; Limpoco, F. T.; Bailey, R. C. Efficient Bioconjugation of Protein Capture Agents to Biosensor Surfaces Using Aniline-Catalyzed Hydrazone Ligation. *Langmuir* **2010**, *26 (19)*, 15430-15435. (b) Limpoco, F. T.; Bailey, R. C. Real-Time Monitoring of Surface-Initiated Atom Transfer Radical Polymerization Using Silicon Photonic Microring Resonators: Implications for Combinatorial Screening of Polymer Brush Growth Conditions. *J. Am. Chem. Soc.* **2011**, *133 (38)*, 14864-14867.
7. Stanton, A. L. D.; Serrano, K. A.; Braun, P. V.; Bailey, R. C. Polymer Brush- Modified Microring Resonators for Partition-Enhanced Small Molecule Chemical Detection. *ChemistrySelect* **2017**, *2 (4)*, 1521-1524.
8. (a) Chen, H.; Zhao, C.; Zhang, M.; Chen, Q.; Ma, J.; Zheng, J. Molecular Understanding and Structural-Based Design of Polyacrylamides and Polyacrylates as Antifouling Materials. *Langmuir*, **2016**, *32 (14)*, 3315−3330. (b) Gunkel, G.; Weinhart, M.; Becherer, T.; Haag, R.; Huck, W. T. S. Effect of Polymer Brush Architecture on Antibiofouling Properties. *Biomacromolecules* **2011**, *12 (11)*, 4169−4172. (c) Krishnan, S.; Weinman, C. J.; Ober, C. K. Advances in polymers for anti-biofouling surfaces. *J. Mater. Chem.* **2008**, *18 (29)*, 3405−3413. (d) Stuart, M. A. C.; Huck, W. T. S.; Genzer, J.; Müller, M.; Ober, C.; Stamm, M.; Sukhorukov, G. B.; Szleifer, I.; Tsukruk, V. V.; Urban, M.; Winnik, F.; Zauscher, S.; Luzinov, I.; Minko, S. Emerging applications of stimuli-responsive polymer materials. *Nat. Mater.* **2010**, *9 (2)*, 101−113. (e) Yang, W. J.; Neoh, K.-G.; Kang, E.T.; Teo, S. L.-M.; Rittschof, D. Polymer brush coatings for combating marine biofouling. *Prog. Polym. Sci.* **2014**, *39 (5)*, 1017−1042. (f) Keating, J. J., IV; Imbrogno, J.; Belfort, G. Polymer Brushes for Membrane Separations: A Review. *ACS Appl. Mater. Interfaces* **2016**, *8* (42), 28383−28399.
9. (a) de Groot, G. W.; Santonicola, M. G.; Sugihara, K.; Zambelli, T.; Reimhult, E.; Vörös, J.; Vancso, G. J. Switching Transport through Nanopores with pH-Responsive Polymer Brushes for Controlled Ion Permeability. *ACS Appl. Mater. Interfaces* **2013**, *5 (4)*, 1400-1407. (b) Castro, R. P.; Cohen, Y.; Monbouquette, H. G. The permeability behavior of polyvinylpyrrolidone-modified porous silica membranes. *J. Membrane Sci.* **1993**, *84 (1- 2)*,

151-160. (c) Ivkov, R.; Butler, P. D.; Satija, S. K. Effect of Solvent Flow on a Polymer Brush: A Neutron Reflectivity Study of the Brush Height and Chain Density Profile. *Langmuir* **2001**, *17 (10)*, 2999-3005. (d) Schuh, C.; Ruhe, J. Penetration of Polymer Brushes by Chemical Nonidentical Free Polymers. *Macromolecules*, **2011**, *44*, 3502-3510.

10. (a)Yim,H.;Kent,M.S.;Satija,S.;Mendez,S.;Balamurugan,S.S.;Balamurugan,S.;Lopez,G.P.Evidencefor vertical phase separation in densely grafted, high-molecular-weight poly(N-isopropylacrylamide) brushes in water. *Phys. Rev.* **2005**, *72*, 051801. (b) Baulin, V. A.; Zhulina, E. B.; Halperin, A. Self-consistent field theory of brushes of neutral water-soluble polymers. *J. Phys. Chem.* **2003**, *119*, 10977. (c) Mahalik, J. P.; Sumpter, B. G.; Kumar, R. Vertical Phase Segregation Induced by Dipolar Interactions in Planar Polymer Brushes. *Macromolecules* **2016**, *49 (18)*, 7096-7107.
11. (a) Binauld, S.; Stenzel, M. H. Acid- Degradable Polymers for Drug Delivery: A Decade of Innovation. *Chem. Commun.* **2013**, *49*, 2082-2102. (b) Delplace, V.; Nicolas, J. Degradable Vinyl Polymers for Biomedical Applications. *Nat. Chem.* **2015**, *7*, 771-784. (c) Kamaly, N.; Yameen, B.; Wu, J.; Farokhzad, O. C.Degradable Controlled-Release Polymers and Polymeric Nanoparticles: Mechanisms of Controlling Drug Release. *Chem. Rev.* **2016**, *116*, 2602-2663. (d) Albertsson, A. C.; Hakkarainen, M. Designed to Degrade. *Science* **2017**, *358*, 872-873.
12. (a) Li, S.; Szalai, M. L.; Kevwitch, R. M.; McGrath, D. V. Dendrimer Disassembly by Benzyl Ether Depolymerization. *J. Am. Chem. Soc.* **2003**, *125*, 10516-10517. (b) de Groot, F. M. H.; Albrecht, C.; Koekkoek, R.; Beusker, P. H.; Scheeren, H. W.“Cascade-Release Dendrimers” Liberate All End Groups Upon a Single Triggering Event in the Dendritic Core. *Angew. Chem., Int. Ed.* **2003**, *42*, 4490-4494. (c) Amir, R. J.; Pessah, N.; Shamis, M.; Shabat, D. Self-Immolative Dendrimers. *Angew. Chem., Int. Ed.* **2003**, *42*, 4494-4499.
13. (a) Peterson, G. I.; Larsen, M. B.; Boydston, A. J. Controlled Depolymerization: Stimuli-Responsive Self-Immolative Polymers. *Macromolecules* **2012**, *45*, 7317-7328. (b) Wong, A. D.; DeWit, M. A.; Gillies, E. R. Amplified Release Through the Stimulus Triggered Degradation of Self-Immolative Oligomers, Dendrimers, and Linear Polymers. *Adv. Drug Delivery Rev.* **2012**, *64*, 1031-1045. (c) Wang, H. C.; Zhang, Y. F.; Possanza, C. M.; Zimmerman, S. C.; Cheng, J. J.; Moore, J. S.; Harris, K.; Katz, J. S. Trigger Chemistries for Better Industrial Formulations. *ACS Appl. Mater. Interfaces* **2015**, *7*, 6369-6382.

14. (a) Zhang, Y. F.; Yin, Q.; Yin, L. C.; Ma, L.; Tang, L.; Cheng, J. J. Chain-Shattering Polymeric Therapeutics with On-Demand Drug-Release Capability. *Angew. Chem., Int. Ed.* **2013**, *52*, 6435-6439. (b) Mutlu, H.; Barner-Kowollik, C.Green Chain-Shattering Polymers Based on a Self-Immolative Azobenzene Motif. *Polym. Chem.* **2016**, *7*, 2272-2279.
15. Miller, K. A.; Morado, E. G.; Samanta, S. R.; Walker, B. A.; Nelson, A. Z.; Sen, S.; Tran, D. T.; Whitaker, D. J.; Ewoldt, R. H.; Braun, P. V.; Zimmerman, S. C. Acid-Triggered, Acid-Generating, and Self-Amplifying Degradable Polymers. *J. Am. Chem. Soc.* **2019**, *141 (7)*, 2838-2842.
16. (a) Nadarassan, D. Biomolecule Adsorption and Release from Porous Silicon. In *Handbook of Porous Silicon*; Canham, L; Springer: New York, 2016. (b) Emami, F. S.; Puddu, V.; Berry, R. J.; Varshney, V.; Patwardhan, S. V.; Perry, C. C.; Heinz, H. Prediction of Specific Biomolecule Adsorption on Silica Surfaces as a Function of pH and Particle Size. *Chem. Mater.* **2014**, *26 (19)*, 5725-5734. (c) Brückner, S. I.; Donets, S.; Dianat, A.; Bobeth, M.; Gutiérrez, R.; Gianaurelio, C.; Brunner, E. Probing Silica–Biomolecule Interactions by Solid-State NMR and Molecular Dynamics Simulations. *Langmuir* **2016**, *32 (44)*, 11698-11705. (d) Iqbal, M.; Gleeson, M. A.; Spaugh, B.; Taybor, F.; Gunn, W. G.; Hochberg, M.; Baehr-Jones, T.; Bailey, R. C.; Gunn, L. C. Label-Free Biosensor Arrays Based on Silicon Ring Resonators and High-Speed Optical Scanning Instrumentation. *IEEE J. Sel. Top. Quantum Electron. 16 (3)*, 654-661. (e) Duan, X.; Li, Y.; Rajan, N. K.; Routenberg, D. A.; Modis, Y.; Reed, M. A. Quantification of the affinities and kinetics of protein interactions using silicon nanowire biosensors. *Nat. Nanotechnol.* **2012**, *7 (6)*, 401-407.
17. (a) Limo, M. J.; Sola-Rabada, A.; Bolx, E.; Thota, V.; Westcott, Z.; Puddu, V.; Perry, C. C. Interactions between Metal Oxides and Biomolecules: from Fundamental Understanding to Applications. *Chem. Rev.* **2018**, *118 (22)*, 11118-11193. (b) Patwardhan, S. V.; Patwardhan, G.; Perry, C. C. Interactions of biomolecules with inorganic materials: principles, applications and future prospects. *J. Mater. Chem.* **2007**, *17 (28)*, 2875-2884.
18. (a) Kisley, L.; Serrano, K. A.; Davis, C. M.; Murphy, E. A.; Gruebele, M.; Leckband, D. E. Soluble Zwitterionic Poly(sulfobetaine) Destabilizes Proteins. *Biomacromolecules* **2019**, 1*9 (9)*, 3894-3901. (b) Spicer, C. D.; Davis, B. G. Selective chemical protein modification. *Nat. Comm.* **2014**, *5 (5)*, 4740. (c) Keefe, A. J.; Jiang, S. Poly(zwitterionic)protein conjugates offer increased stability without sacrificing binding affinity or bioactivity. *Nat. Chem.* **2012**,

4 (1), 59-63. (d) Leng, C.; Hung, H.-C.; Sun, S.; Wang, D.; Li, Y.; Jiang, S.; Chen, Z. Probing the Surface Hydration of Nonfouling Zwitterionic and PEG Materials in Contact with Proteins. *ACS Appl. Mater. Interfaces* **2015**, *7 (30)*, 16881-16888. (e) Jin, Q.; Chen, Y.; Wang, Y.; Ji, J. Zwitterionic drug nanocarriers: A biomimetic strategy for drug delivery. *Colloids Surf. B Biointerfaces* **2014**, *124*, 80-86. (f) Veronese, F. M. Peptide and protein PEGylation: a review of problems and solutions. *Biomaterials* **2001**, *22 (5)*, 405-417.

19. (a) Falde, E. J.; Yohe, S. T.; Colson, Y. L.; Grinstaff, M. W. Superhydrophobic Materials for Biomedical Applications. *Biomaterials* **2016**, *104*, 87-103. (b) Novick, S. J.; Dordick, J. S. Protein-containing hydrophobic coatings and films. *Biomaterials* **2002**, *23 (2)*, 441-448. (c) Cox, J. D.; Curry, M. S.; Skirboll, S. K.; Gourley, P. L.; Sasaki, D. Y. Surface passivation of a microfluidic device to glial cell adhesion: a comparison of hydrophobic and hydrophilic SAM coatings. *Biomaterials* **2002**, *23 (3)*, 929-935. (d) Lumsdmon, S. O.; Green, J.; Stieglitz, B. Adsorption of hydrophobin proteins at hydrophobic and hydrophilic interfaces. *Colloids Surf. B* **2005**, *44 (4)*, 172-178.
20. (a) Baker, J. S.; Dudley, L. Y. Biofouling in membrane systems — A review. *Desalination*, **1998**, *118 (1-3)*, 81-89. (b)Vermonden, T.; Censi, R.; Hennink, W. E. Hydrogels for Protein Delivery. *Chem. Rev.* **2012**, *112 (5)*, 2853-2888. (c) Kopeček, J. Hydrogel biomaterials: A smart future? *Biomaterials* **2007**, *28 (34)*, 5185-5192. (d) Censi, R.; Martino, P. D.; Vermonden, T.; Hennink, W. E. Hydrogels for protein delivery in tissue engineering. *J. Control Release* **2012**, *161 (2)*, 680-692. (e) Jonker, A. M.; Löwik, D. W. P. M.; van Hest, J. C. M. Peptide- and Protein-Based Hydrogels. *Chem. Mater.* **2012**, *24 (5)*, 759-773.
21. Kisley, L.; Serrano, K. A.; Kong, X.; Gruebele, M.; Leckband, D. E. Direct Imaging of Protein Stability and Folding Kinetics in Hydrogels. *ACS Appl. Mater. Interfaces* **2017**, *9 (26)*, 21606-21607.
22. Kisley, L.; Serrano, K. A.; Davis, C. M.; Murphy, E. A.; Gruebele, M.; Leckband, D. E. Soluble Zwitterionic Poly(sulfobetaine) Destabilizes Proteins. *Biomacromolecules* **2019**, 1*9 (9)*, 3894-3901.
23. (a) Maluf, N. *An Introduction to Microelectromechanical Systems Engineering*. Artech House: Boston, 2000. (b) Allen, J. J. *Micro Electro Mechanical System Design*. CRC Press: Boca Raton, 2005.

24. Nan, K.; Want, H.; Ning, X.; Miller, K. A.; Wei, C.; Liu, Y.; Li, H.; Xue, Y.; Xie, Z.; Luan, H.; Zhang, Y.; Huang, Y.; Rogers, J. A.; Braun, P. V. Soft Three-Dimensional Microscale Vibratory Platforms for Characterization of Nano-Thin Polymer Films. *ACS Nano* **2019**, *13 (1)*, 449-457.

25. Sheehan, P. E.; Whitman, L. J. Detection Limits for Nanoscale Biosensors. *Nano Lett.* **2005**, *5 (4)*, 803-807.

26. Chaudhury, M. K.; Whitesides, G. M. How to make water run uphill. *Science* **1992**, *256 (5063)*, 1539-1541.

27. (a) Katira, P.; Hess, H. Two-Stage Capture Employing Active Transport Enables Sensitive and Fast Biosensors. *Nano Lett.* **2010**, *10 (2)*, 567-572. (b) Fang, J.; Park, S.; Schlag, L.; Stauden, T.; Pezoldt, J.; Jacobs, H. O. Localized Collection of Airborne Analytes: A Transport Driven Approach to Improve the Response Time of Existing Gas Sensor Designs. *Adv. Funct. Mater.* **2014**, *24 (24)*, 3706-3714.

28. (a) Zhang, C.; Sitt, A.; Koo, H.-J.; Waynant, K. V.; Hess, H.; Pate, B. D.; Braun, P. V. Autonomic Molecular Transport by Polymer Films Containing Programmed Chemical Potential Gradients. *J. Am. Chem. Soc.* **2015**, *137* (15), 5066-5073. (b) Koo, H.-J.; Waynant, K. V.; Zhang, C.; Braun, P. V. Polymer Brushes Patterned with Micrometer-Scale Chemical Gradients Using Laminar Co-Flow. *ACS Appl. Mater. Interfaces* **2014**, *6 (16)*, 14320-14326. (c) Koo, H.-J.; Waynant, K. V.; Zhang, C.; Haasch, R. T.; Braun, P. V. General Method for Forming Micrometer-Scale Lateral Chemical Gradients in Polymer Brushes. *Chem. Mater.* **2014**, *26 (8)*, 2678-2683.

29. (a) Luk'yanchuk, B.; Zheludev, N. I.; Maier, S. A.; Halas, N. J.; Nordlander, P.; Giessen, H.; Chong, C. T. The Fano resonance in plasmonic nanostructures and metamaterials. *Nature Materials* 2010, 9, 707-715. (b) Adato, R.; Altug, H. In-situ ultra-sensitive infrared absorption spectroscopy of biomolecule interactions in real time with plasmonic nanoantennas. *Nature Communications* 2013, 4. (c) Adato, R.; Yanik, A. A.; Amsden, J. J.; Kaplan, D. L.; Omenetto, F. G.; Hong, M. K.; Erramilli, S.; Altug, H. Ultra-sensitive vibrational spectroscopy of protein monolayers with plasmonic nanoantenna arrays. *Proceedings of the National Academy of Sciences of the United States of America* 2009, 106, 19227-19232. (d) Neubrech, F.; Pucci, A.; Cornelius, T. W.; Karim, S.; Garcia-Etxarri, A.; Aizpurua, J. Resonant Plasmonic and Vibrational Coupling in a Tailored Nanoantenna for Infrared Detection. *Physical Review*

Letters 2008, 101. (e) Aouani, H.; Rahmani, M.; Sipova, H.; Torres, V.; Hegnerova, K.; Beruete, M.; Homola, J.; Hong, M. H.; Navarro-Cia, M.; Maier, S. A. Plasmonic Nanoantennas for Multispectral Surface-Enhanced Spectroscopies. *Journal of Physical Chemistry C* 2013, 117, 18620-18626.

APPENDIX: IMPACT OF A PILOT LABORATORY SAFETY TEAM WORKSHOP[1]

A.1 Abstract

Recurring academic laboratory accidents and a lack of consensus about the best approach to chemical safety culture education has led to the development of laboratory safety team (LST) programs at many research institutions in the United States. LSTs are collaborative groups that seek to improve the safety culture within a department or multiple departments. They usually consist of a partnership between departmental faculty, staff, and students and have the goal of providing concrete opportunities for all of these stakeholders to continuously improve safety practices within their department. These programs also offer a supplementary form of safety education that is designed to fit the specific culture and needs of each institution. As these programs have developed in a variety of institutions, best practices for forming and maintaining LSTs have begun to emerge. In order to better understand these best practices, we developed a pilot workshop for the 255th National American Chemical Society Meeting audience to provide attendees with the knowledge and resources to go back to their home institutions and establish LSTs or similar programs. To understand the effectiveness of this pilot workshop, we conducted a small survey of the attendees at the first presentation. Questionnaires before and after the workshop show that the workshop was well received overall. Participants became more confident in their ability to teach others about safety and gained an improved understanding of safety topics and resources. There is also evidence that the workshop changed participants perception on their own career values and their institution's values on laboratory safety. These results are promising and give us hope that programs such as this can be a useful platform for safety education.

A.2 Introduction

Recurring laboratory accidents over the years have drawn attention to the question of whether adequate training in laboratory safety is provided to students and researchers at academic institutions.[1,2] One outcome of this longstanding debate is the suggestion that laboratory safety can potentially be integrated in a chemist's higher education in variety of ways. Examples of potential

---

[1] Reproduced with permission from: Miller, K. A.; Tyler, K. I Impact of a pilot laboratory safety team workshop. *J. Chem. Health Safety*, in press. DOI: 10.1016/j.jchas.2018.12.003. Published online: January 15, 2019. Copyright 2019 Division of Chemical Health and Safety of the American Chemical Society.

approaches include: inclusion throughout the classroom and laboratory curriculum, taught as a separate class, introduced as a seminar topic, by programs within each research group, or a variety of less traditional methods.[3-9] A particular challenge identified in this debate is that safety education involves development of both technical and cultural skills. Traditionally, chemical safety education has focused on the development of technical skills. However, the required technical skills vary widely depending on the chemistries that are being studied. This variety challenges the development of a consistent safety culture within academic departments and leads to a lack of consensus about appropriate safety practices and education requirements. Thus, the question is raised: what can be standardized in safety education, given the distinct needs and culture of each institution?[10]

In this context, laboratory safety teams (LSTs) have emerged across the United States as a potentially effective way for improving safety culture, particularly in institutions with large cohorts of students involved in research.[11,12] These teams offer a supplementary approach to safety education that is designed to fit the specific culture and needs of each institution. LSTs often take the form of a collaborative group of students, faculty, and safety professionals that meet on a regular basis to improve the safety culture in a given department or multiple departments. However, the organizational structure and objectives of the team can vary widely depending on the institution's organizational structure, needs, and resources.

Typical team features can include: appointment of safety representative(s) from research groups in the department, campaigns to raise awareness of safety concerns throughout the department (e.g. safety moments and hallway posters), peer laboratory walkthroughs, providing resources for students to practice research safely (e.g. pre-arranged safety kits and peer consultation), supplemental safety trainings, and an open conversation about safety in the research labs. It is important to note that LSTs do not take responsibility for enforcement of regulatory compliance issues; these teams should instead focus on creation of a culture where safety is seen as fundamental value to every researcher and is included throughout the scientific method.[13-15]

Because academic laboratory safety culture is less consistent than that found in government and industry,[16,17] there has been much recent interest from industry to support the development of LSTs. Not only does industrial involvement in these efforts improve the safety knowledge that industry relies upon, but it also teaches future employees the importance of a safe research culture. As academic/industry collaborations become more prevalant,[11,18] the American Chemical Society

(ACS) has identified a need to support these programs. Leadership development opportunities have been shown to be an effective method to create lasting change in academic institutions.[19,20] For these reasons, we describe the content and outcomes of a pilot workshop designed to equip students with the resources they need to become an advocate for laboratory safety at their home institutions.

A.3 Workshop content

A.3.1 Overview

This three-hour workshop included three educational topics that culminate with an LST planning session (Figure A.1). The purpose of this workshop organization was first to focus on filling gaps in the participant's technical and cultural safety education as well as teaching participants about the general concepts of safe research practices in academic institutions. After ensuring all participants have this solid foundation, they were introduced to the idea of LSTs and given the opportunity to discuss how these safety teams might work at their own institutions. All activities took place in small round table groups for 20-40 minutes each with the assistance of two moderators. After each topic, participants were given the opportunity to ask questions and reflect with the group as a whole.

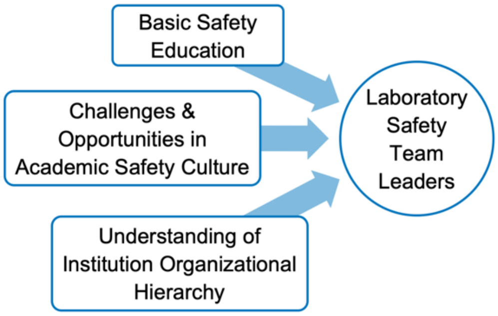

Figure A.1 Workshop strategy for developing laboratory safety team (LST) leaders.

A.3.2 Topic 1: Safety education

A few examples of laboratory accidents were used to open the workshop and emphasize the importance of laboratory safety in academic institutions and how it compares to industrial standards. Participants learned about topics such as hazard assessments, operational risk management, hierarchy of controls, and the model of accident causation. Then, each team discussed hurdles that students may face when performing risk assessments and created scenarios in which laboratory accidents would occur.

A.3.2 Topic 2: Academic safety culture

Academic safety culture is defined as an organization's shared values, assumptions, and beliefs specific to workplace safety. Or, more simply, it is defined as the importance of safety within the organization relative to other priorities.[14] After a discussion of the meaning of safety culture, each participant was assigned to reflect on their own institution's current laboratory safety environment. Participants then shared their opinions on what an ideal safety culture should be, what changes could be made in their current institution, and the limitations of their current institution. Emphasis was placed on relevant occupational safety practices and strategies for organizational change.

A.3.2 Topic 3: Institution organizational hierarchy

The third topic was added to give perspective to students that may not be familiar with the organizational structure of academic institutions. Participants worked together to define the responsibilities and limitations of six groups of people relating to laboratory safety: (1) researchers and students, (2) environmental health and safety professionals, (3) principal investigators, (4) department chairs, (5) vice presidents of research and deans, and (6) presidents, chancellors, or provosts.[14] For example, researchers have the ability to identify day-to-day safety problems within the laboratory but have limited control over funding for safer laboratory equipment.

A.3.2 Topic 4: Laboratory safety teams

The last activity of the workshop focused on developing individualized plans for the creation or improvement of LSTs. Students discussed the history of LSTs, what is currently practiced at their institutions, shared successful programs from other institutions, and formulated plans for their own safety team. For example, what leadership structure should your team have? Who is part of the team leadership? What resources will your team offer students in the department? How will you incentivize good practices? Consideration was also given to cases where other types of safety programs are more appropriate than LSTs.

A.3.2 Survey questions

To assess the value of the workshop to the attendees, two surveys were given (one before and one after the workshop). This study was created to give an understanding of participant opinions before and after attending a safety workshop at the Spring 2018 National ACS Meeting in New Orleans, LA. The analyzed surveys were reviewed and approved by UIUC's Institutional Review Board as appropriate for use with human subjects. There were 22 participants from 15 different institutions that attended the workshop. Participation was open to students, faculty, staff, and safety professionals. For the purpose of this analysis, only the student participants (N = 15) were included in this study. All student participants were actively involved in academic research. We analyzed 52 questions grouped into the following categories: demographics (7, pre-survey only), personal safety (15), safety culture in current program (9), opinions on chemical safety education (10), and workshop evaluation (10, post-survey only). The questions were developed based on the topics covered in the workshop and as well as motivations for student involvement in safety programs.

A.4 Outcomes

A.4.1 Description of participants

Because students self-select to participate in this workshop, initial questions were used to give insight into the studied population (Figure A.2). It should be noted that participants were comprised mostly of graduate students, with a few postdocs and undergraduates interested in academic careers. In addition, participants mostly attended Research 1 Institutions (R1) for their safety training with some participants from Research 2 Institutions (R2) and Primarily Undergraduate Institutions (PUI).[25] Given that LSTs originated to improve the safety culture in research-intensive institutions, it is possible that increased awareness of these programs caused higher attendance rates. However, these results are more likely from a disparity in accessibility to National ACS Meetings. Development of more accessible programs in the future (e.g. webinars or online modules) is necessary to reach and meet the needs of all institutions.

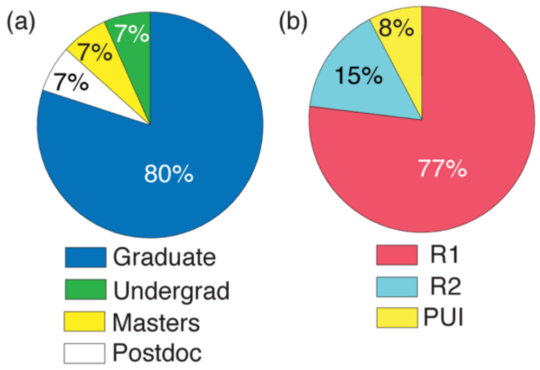

Figure A.2 (a) Breakdown of current education level of participants. (b) Breakdown of institutions where students received a majority of their safety training (self-reported).

Within this population of students, many were interested in starting safety teams at their own institutions. Before the workshop, 93% of participants did not believe they don't have time for laboratory safety and 100% of participants did not believe that they shouldn't be responsible for the safety of others (Figure A.3). Additionally, 80% of participants thought they had good safety practices in the lab and 80% thought they regularly incorporated risk management into the design of their own experiments. Despite these participants having a largely positive safety outlook and practices, 73% still wanted more training. These responses suggest that the participants were a highly motivated group of students and that their current educational programs did not include adequate safety instruction for their purposes.

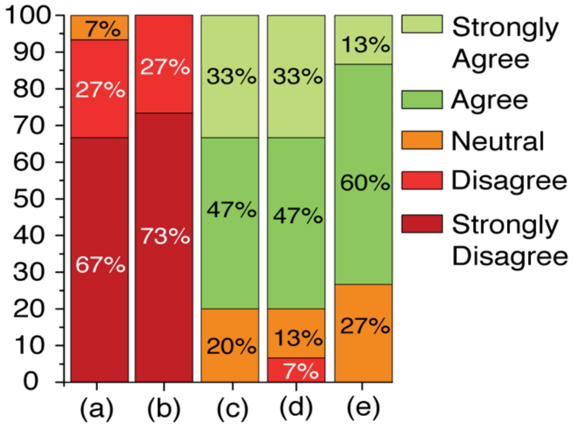

Figure A.3 Respondents' answers to the pre-survey question: (a) "I don't have time to think about chemical safety," (b) "I'm not responsible for the safety of others," (c) "I have good safety practices in the lab," (d) "I regularly incorporate risk management into the design of my own experiments," and (e) "I need more training in chemical safety."

A.4.2 Impact of workshop on participant confidence

Survey results suggest that participants gained valuable resources to take back to their own institutions. When asked what part of the workshop was most beneficial, one student said it was the "role of administration in safety and benefits of establishing university wide safety programs." Other students said, "I was unaware of the different groups on each campus that promote safety" and "I did not realize the admin staff of any institution would ever have a role to play in laboratory safety." Based on *t*-test results and the Cohen's *d* values, we can say that our workshop had a moderate effect on instructing participants on where to seek out more information (Figure A.4a), a large effect on their individual confidence as safety leaders (Figure A.4b), and a large effect on participants' knowledge of what a chemical safety professional does (Figure A.4c). The increase in students' knowledge on where to go to learn about chemical safety (Figure A.4a) was less than expected. However, this may simply be because participants were already relatively knowledgeable about chemical safety resources. It is interesting to note that their opinion of their needed level of safety training (Figure A.4d) did not significantly change. This suggests that even with additional training, these participants still wanted to learn more about chemical safety and continue to improve their laboratory safety culture. Additionally, their comfort in asking their labmates to improve their safety practices (Figure A.4e) increased but did not significantly change, suggesting that these students already had supportive labmates.

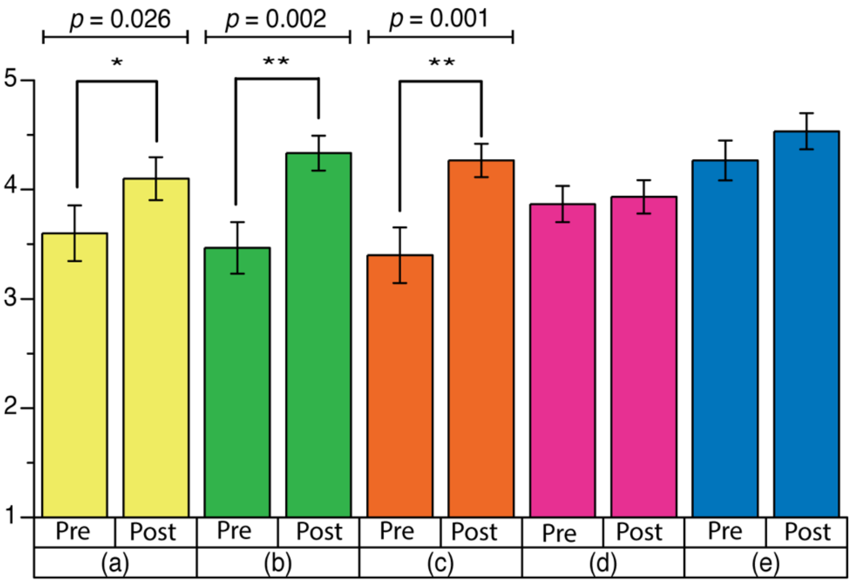

Figure A.4 Respondents' answers to the question: (a) "I know where to go if I want to learn more about chemical safety" ($p = 0.026$, Cohen's $d = 0.56$), (b) "I could teach others about chemical safety ($p = 0.002$, Cohen's $d = 1.1$)," (c) "I am familiar with what a chemical safety professional does" ($p = 0.001$, Cohen's $d = 1.07$), (d) "I need more training in chemical safety," and (e) "I am comfortable encouraging my labmates to improve their safety practices."

Laboratory safety leaders must have confidence to seek out chemical safety knowledge to lead necessary change within their own research groups. When asked who they would be comfortable going to with safety-related questions, participants were most comfortable approaching colleagues (pre-survey Likert scale average of 4.73 ± 0.46), then principal investigators (PI, 4.66 ± 0.62), and least comfortable approaching EH&S professionals (4.40 ± 0.83). From these results and those in Figure A.4a-d, we can postulate that while the workshop helped participants gain confidence in their personal chemical safety knowledge and leadership ability, many were still not comfortable approaching people above their institutional hierarchy. It is possible that the presence of an LST at their institution will help bridge this gap because it will create a supportive and informal environment for students to interact with PI's and EH&S professionals regarding laboratory safety matters.

A.4.3 Change in perception of institution values

Institutional culture can play a large role in enabling students as safety leaders because even the most motivated students can be discouraged by not being able to enact change. For example, if the participants feel that their contributions to safety within their institution are not valued, it would diminish their confidence and motivation to be a leader. Based on *t*-test results and the Cohen's *d* values, we can say that our workshop had a moderate negative effect on what participants thought of their institution's safety values (Figure A.5a), a moderate negative effect on whether they had the resources they need from their institution to practice research safely (Figure A.5b), and a large negative effect on whether participants though their institution had an organized safety program across different labs (Figure A.5c). These results are likely due to the participants new perspective on what can and has been done at other academic institutions to promote a safe research culture. Thus, it is not necessarily negative that students have these changing perceptions because they are now better equipped to make improvements on the safety culture at their own institutions after seeing what changes can be made. As more LSTs develop, it will be important that the students, faculty, safety professionals, and administration recognize their strengths and limitations to create a culture where everyone works together to push for a safe research and laboratory environment. As one student put it, improving safety programs at their own institution means "develop[ing] a safety culture through increasing communication of safety in ALL labs."

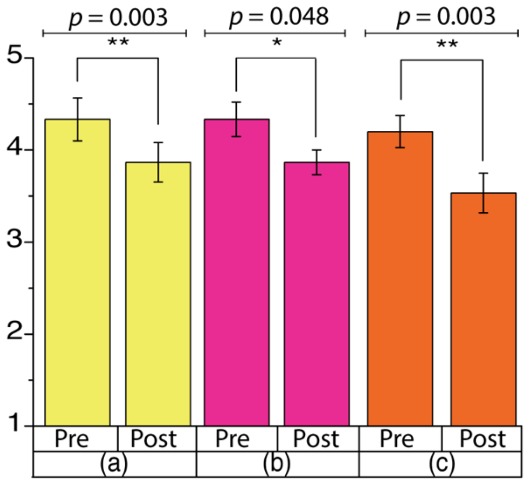

Figure A.5 Respondents' answers to the question: (a) "My institution values laboratory safety" ($p = 0.004$, $d = 0.53$), (b) "I have the resources I need from my institution to practice research safely" ($p = 0.048$, $d = 0.74$), and (c) "My institution has organized chemical safety programs across different labs" ($p = 0.003$, $d = 0.88$).

A.4.4 Career value of laboratory safety

Due to the aforementioned growing interest in student safety training and LST development from industries, we hoped that topics 1 (safety education) and 4 (history and examples of LSTs) of this workshop would emphasize the importance of safety as a core value when entering the workforce. Several questions were asked after the workshop to understand participant opinions regarding the importance of chemical safety for their career (Figure A.6) and all participants saw the value of understanding lab safety, both for their personal career (100%) and for their resumes (100%). We see this as a promising result that speaks to the potential for these students to become successful leaders at their own institutions because understanding why laboratory safety is important will help them teach others. Additionally, while this was not the purpose of the workshop, we also asked about participant interest in chemical safety as a career. Most did not see it as a viable career path, with 33% negative response and 30% neutral response. However, 47% of participants positive response. It is interesting to show that so many of these students have an open mind for safety as a career option and suggests an untapped market for future safety professionals.

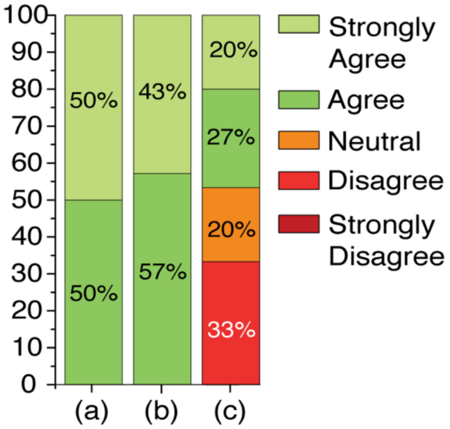

Figure A.6 Respondents' answers to the post-survey question: (a) "Understanding lab safety will get me a job," (b) "I think employers value seeing chemical safety experiences when recruiting," and (c) "I am interested in chemical safety as a career."

A.4.5 Overall workshop success

In planning for future workshops, we asked several questions relating to participant opinions on workshop success (Figure A.7). We found responses that were promising with regards to the longevity of this program. Participants would recommend this workshop to others (93% positive response) and thought the topics were relevant and activities in each topic were useful (100%). Additionally, participants thought that the workshop gave them skills that would help in their career (87%). One student summarized their experience as “I really enjoyed talking with my table about safety issues and how they handled them. I just want to see workshops like this more often.” One area that could be improved is that only 64% of participants thought the workshop helped them develop a clear plan to improve or develop a program at their own institution, with all other participants having a neutral response. A large reason for this is possibly the overwhelming variety of structure and goals of current LSTs. Although we previously mentioned this as positive attribute of LSTs because it will help to fill gaps in institutional shortcomings relating to laboratory safety, it could make starting a new program a daunting task. This problem could be circumvented in the future by developing more interactive resources to help new student leaders navigate these options and chose LST features that are most useful for their own institution (e.g. online modules or decision-making questionnaires).

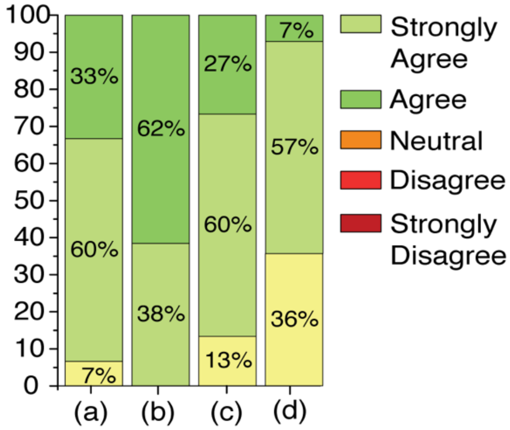

Figure A.7 Respondents’ answers to the post-survey question: (a) “I would recommend this workshop to others,” (b) “Topics were relevant and activities in each topic were useful,” (c) “This workshop gave me skills that will help me in my career,” and (d) “This workshop helped me develop a clear plan to improve or develop a program at my own institution.”

A.4.6 Limitations

While these results are quite promising, there are a few limitations to consider. One is that our sample size (N=15) makes it hard to make large claims. Additionally, our population is selfselected to attend the workshop, meaning they already have a high level of interest in the topic. Results may change if this workshop was a mandatory event at another venue. Along the same line, populations will change every time a workshop is offered and discrepancies between subsequent workshops are possible. These topics are important to consider in later workshop analyses or when applied to studies on other programs.

A.5 Conclusions

We described the reasons for and content of a pilot workshop aimed to develop future leaders of laboratory safety teams. Outcomes of this workshop were investigated through a study via surveys given before and after the workshop. This workshop was well received overall; participants found the workshop useful and would recommend it to others. Results suggest that participants became more confident in their ability to teach others about safety and gained an improved understanding of safety topics and resources. There is also evidence that the workshop changed the participant's perception of their own career values and their institution's values on laboratory safety. These results are promising and give us reason to expect that programs such as this can be a useful platform for safety education and leadership development. Moving forward, it will be critical to encourage open communication and resource-sharing between LST leaders[26,27] because program complexity will be a major hurdle for new LSTs. In addition, interactive resources for safety leaders would be useful for the design of new programs.

A.6 IRB and survey materials

This research was conducted under IRB 18652 at the University of Illinois at Urbana-Champaign. The most recent IRB approval notice is provided below.

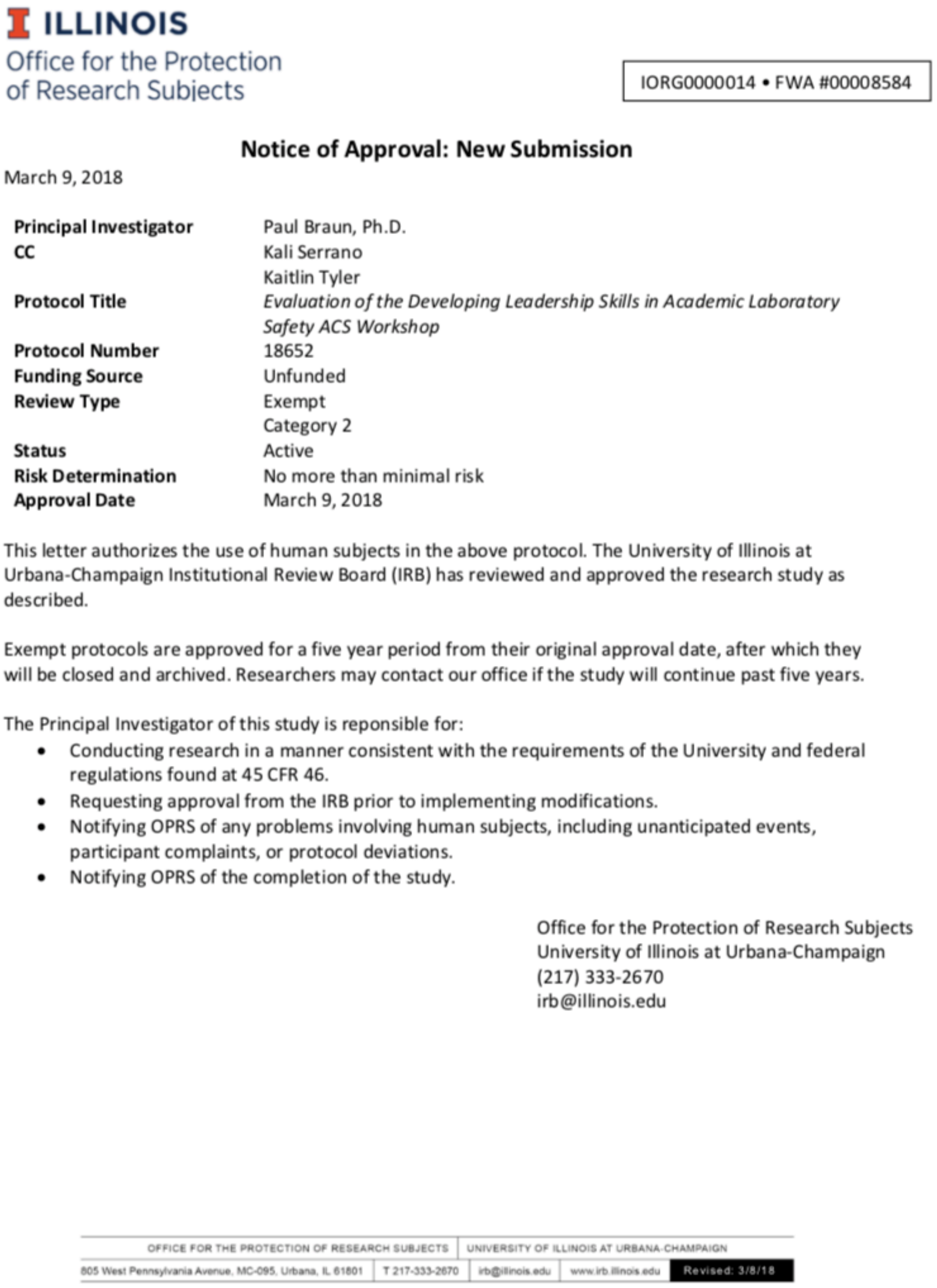

ILLINOIS
Office for the Protection
of Research Subjects

IORG0000014 • FWA #00008584

Notice of Approval: New Submission

March 9, 2018

Principal Investigator	Paul Braun, Ph.D.
CC	Kali Serrano Kaitlin Tyler
Protocol Title	*Evaluation of the Developing Leadership Skills in Academic Laboratory Safety ACS Workshop*
Protocol Number	18652
Funding Source	Unfunded
Review Type	Exempt Category 2
Status	Active
Risk Determination	No more than minimal risk
Approval Date	March 9, 2018

This letter authorizes the use of human subjects in the above protocol. The University of Illinois at Urbana-Champaign Institutional Review Board (IRB) has reviewed and approved the research study as described.

Exempt protocols are approved for a five year period from their original approval date, after which they will be closed and archived. Researchers may contact our office if the study will continue past five years.

The Principal Investigator of this study is reponsible for:

- Conducting research in a manner consistent with the requirements of the University and federal regulations found at 45 CFR 46.
- Requesting approval from the IRB prior to implementing modifications.
- Notifying OPRS of any problems involving human subjects, including unanticipated events, participant complaints, or protocol deviations.
- Notifying OPRS of the completion of the study.

Office for the Protection of Research Subjects
University of Illinois at Urbana-Champaign
(217) 333-2670
irb@illinois.edu

OFFICE FOR THE PROTECTION OF RESEARCH SUBJECTS | UNIVERSITY OF ILLINOIS AT URBANA-CHAMPAIGN
805 West Pennsylvania Avenue, MC-095, Urbana, IL 61801 | T 217-333-2670 | irb@illinois.edu | www.irb.illinois.edu | Revised: 3/8/18

A.7 References

1. Mulcahy, M. B. Y., A.; Gibson, J.; Hildreth, C.; Ashbrook, P.; Izzo, R.; Backus, B. College and university sector response to the U.S. Chemical Safety Board Texas Tech incident report and UCLA laboratory fatality. *J Chem Health Saf* **2013,** *20* (2), 6.
2. Langerman, N. Deaths continue. *J Chem Health Saf* **2011,** *18* (4), 38.
3. Hill, R. H. Undergraduates Need a Safety Education! *J Chem Educ* **2016,** *93* (9), 1495.
4. Staehle, I. O.; Chung, T. S.; Stopin, A.; Vadehra, G. S.; Hsieh, S. I.; Gibson, J. H.; Garcia-Garibay, M. A. An Approach To Enhance the Safety Culture of an Academic Chemistry Research Laboratory by Addressing Behavioral Factors. *J Chem Educ* **2016,** *93* (2), 217.
5. Kumasaki, M.; Shoji, T.; Wu, T. C.; Soontarapa, K.; Arai, M.; Mizutani, T.; Okada, K.; Shimizu, Y.; Sugano, Y. Presenting Safety Topics Using a Graphic Novel, Manga, To Effectively Teach Chemical Safety to Students in Japan, Taiwan, and Thailand. *J Chem Educ* **2018,** *95* (4), 584.
6. Matson, M. L.; Fitzgerald, J. P.; Lin, S. Creating customized, relevant, and engaging laboratory safety videos. *J Chem Educ* **2007,** *84* (10), 1727.
7. Gublo, K. I. A laboratory safety trivia game. *J Chem Educ* **2003,** *80* (4), 425.
8. Moody, A. E.; Freeman, R. G. Chemical safety and scientific ethics in a sophomore chemistry seminar. *J Chem Educ* **1999,** *76* (9), 1224.
9. Livingston, H. K. Safety Consideration in Research Proposals. *J Chem Educ* **1964,** *41* (10), A785.
10. Pitt, M. J. Can Laboratory Safety Be Taught? *J Chem Health Saf* **1988,** *65* (12), A312.
11. McGarry, K. A.; Hurley, K. R.; Volp, K. A.; Hill, I. M.; Merritt, B. A.; Peterson, K. L.; Rudd, P. A.; Erickson, N. C.; Seiler, L. A.; Gupta, P.et al. Student Involvement in Improving the Culture of Safety in Academic Laboratories. *J Chem Educ* **2013,** *90* (11), 1414.
12. Alaimo, P. J.; Langenhan, J. M.; Tanner, M. J.; Ferrenberg, S. M. Safety Teams: An Approach To Engage Students in Laboratory Safety. *J Chem Educ* **2010,** *87* (8), 856.
13. APLU Council on Research Task Force on Laboratory Safety (2016). A Guide to Implementing a Safety Culture in Our Universities. CoR Paper 1. Washington, D. A. o. P.
14. Thorp, H. H. D., D. M.; Bercaw, J. E.; Bergman, R. G.; Deeb, J. M.; Gibbs, L. M.; Goodson, T., III, ; Imada, A. S.; Jeskie, K. B.; Pentelute, B. L.; Roberts, K. H.; Schomaker, J. M.; Young,

A. M.; Friedman, D.; Warden, T. *Safe Science: Promoting a Culture of Safety in Academic Chemical Research*; The National Academies Press: Washington, D.C., 2014.

15. Advancing Safety Culture in the University Laboratory: A report of the Task Force for Advancing the Culture of Laboratory at Stanford University. Accessed December 13, 2018. https://web.stanford.edu/dept/EHS/cgi-bin/lsctf/.
16. Schroder, I.; Huang, D. Y. Q.; Ellis, O.; Gibson, J. H.; Wayne, N. L. Laboratory safety attitudes and practices: A comparison of academic, government, and industry researchers. *J Chem Health Saf* **2016,** *23* (1), 12.
17. Nicholson, D. G. Safety Practices: Industry, Yes - Colleges, ?? *J Chem Educ* **1959,** *36* (8), 377.
18. Huston, E. M.; Milligan, J. A.; Powell, J. R.; Smith, A. M.; Neal, D.; Duval, K. M.; DiNardo, M. A.; Stoddard, C.; Bell, P. A.; Berning, A. W.et al. Development of an Undergraduate Course in Chemical Laboratory Safety through an Academic/Industrial Collaboration. *J Chem Educ* **2018,** *95* (4), 577.
19. Maral P. S. Mousavi, Z. S., Evan L. Anderson, Amanda Stemig-Vindedah, David Golden, Gary Christenson, Katherine Lust, and Philippe Bühlmann. Stress and Mental Health in Graduate School: How Student Empowerment Creates Lasting Change. *J Chem Educ* **2018**.
20. Robert H. Hill, D. C. F. Academic leaders create strong safety cultures in colleges and universities. *J Chem Health Saf* **2013,** *20* (5), 27.
21. Lakens, D. Calculating and reporting effect sizes to facilitate cumulative science: a practical primer for t-tests and ANOVAs. *Front Psychol* **2013,** *4*, 863.
22. Piasta S, Justice L. Cohen's d statistic. In: Salkind N, ed. Encyclopedia of Research Design. Thousand Oaks, CA: Sage Publications; 2010: 181–186.
23. Bergstrom, L.; Ward, E. C.; Finizia, C. Voice rehabilitation for laryngeal cancer patients: Functional outcomes and patient perceptions. *Laryngoscope* **2016,** *126* (9), 2029.
24. Cronbach, L. J. Coefficient Alpha and the Internal Structure of Tests. *Psychometrika* **1951,** *16* (3), 297.
25. The Carnegie classification of institutions of higher learning. Accessed November 27, 2018. http:// classifications.carnegiefoundation.org/.
26. Alexander J. M. Miller, I. A. T. Let's Talk About Safety: Open Communication for Safer Laboratories. *Organometallics* **2018,** *37* (19), 3225.

27. Stuart, R. B.; McEwen, L. R. The Safety "Use Case": Co-Developing Chemical Information Management and Laboratory Safety Skills. *J Chem Educ* **2016,** *93* (3), 516.